

Spin Qubits in Silicon and Germanium

Lawrie, W.I.L.

DOI

[10.4233/uuid:97c4ea24-9672-4e0b-b7a5-e3a48258c871](https://doi.org/10.4233/uuid:97c4ea24-9672-4e0b-b7a5-e3a48258c871)

Publication date

2022

Citation (APA)

Lawrie, W. I. L. (2022). *Spin Qubits in Silicon and Germanium*. [Dissertation (TU Delft), Delft University of Technology]. <https://doi.org/10.4233/uuid:97c4ea24-9672-4e0b-b7a5-e3a48258c871>

Important note

To cite this publication, please use the final published version (if applicable).
Please check the document version above.

Copyright

Other than for strictly personal use, it is not permitted to download, forward or distribute the text or part of it, without the consent of the author(s) and/or copyright holder(s), unless the work is under an open content license such as Creative Commons.

Takedown policy

Please contact us and provide details if you believe this document breaches copyrights.
We will remove access to the work immediately and investigate your claim.

SPIN QUBITS IN SILICON AND GERMANIUM



SPIN QUBITS IN SILICON AND GERMANIUM

Dissertation

for the purpose of obtaining the degree of doctor
at Delft University of Technology,
by the authority of the Rector Magnificus, prof. dr. ir. T.H.J.J. van der Hagen,
chair of the Board for Doctorates,
to be defended publicly on
30 June 2022 at time 12:30 o'clock

by

William Iain Leonard LAWRIE

Master of Science in Physics,
The University of Melbourne, Australia
born in Perth, Australia.

This dissertation has been approved by the promotor.

Composition of the doctoral committee:

Rector Magnificus,	chairperson
Dr. ir. M. Veldhorst,	Delft University of Technology, promotor
Dr. G. Scappucci,	Delft University of Technology, copromotor

Independent members:

Prof. dr. ir. L. DiCarlo,	Delft University of Technology
Prof. dr. E. P. A. M. Bakkers,	Eindhoven University of Technology
Prof. dr. G. Katsaros,	Institute of Science and Technology Austria
Dr. E. Greplova,	Delft University of Technology
Dr. M. Wimmer,	Technical University of Delft, reserve member

Other members:

Dr. J. Helsen,	Centrum Wiskunde & Informatica
----------------	--------------------------------



Keywords: quantum computing, quantum dots, spin qubits, semiconductors, germanium, silicon, electrons, holes, qubit arrays

Printed by: Gildeprint

Copyright © 2022 by W. I. L. Lawrie
Casimir PhD Series, Delft-Leiden 2022-18

ISBN 978-90-8593-529-2

Cover design by William Lawrie

An electronic version of this dissertation is available at

<http://repository.tudelft.nl/>.

CONTENTS

Summary	xi
Samenvatting	xv
1 Introduction	1
1.1 Primer on Quantum Information	2
1.1.1 Quantum Bits, Superposition and Entanglement	2
1.1.2 Quantum gates.	3
1.2 What makes a good quantum bit?.	4
1.3 How does this work fit in?.	6
References	8
2 Electron and Hole Spin Qubits in Semiconductor Quantum Dots	11
2.1 Semiconductors.	12
2.2 Semiconductor Quantum Dots	12
2.2.1 Coloumb Oscillations	13
2.2.2 Charge Sensing	15
2.2.3 Virtual Gates	15
2.3 Spin Qubits	19
2.3.1 Zeeman Splitting.	20
2.3.2 Lamor Precission	20
2.3.3 Qubit State Manipulation	20
2.3.4 Exchange Interaction	21
2.3.5 Two-Qubit Exchange Gates	23
2.3.6 Spin Readout.	24
2.4 Electron spin qubits in Silicon quantum dots	25
2.4.1 Valley Splitting.	25
2.4.2 Electron Spin Resonance.	28
2.5 Hole spin qubits in Germanium quantum dots	28
2.5.1 The Valence Band	29
2.5.2 Strain	30
2.5.3 Lifting Spin Degeneracy	31
2.5.4 Hyperfine Interaction	32
2.5.5 Electric Dipole Spin Resonance	34
2.6 Qualifying a Quantum System	34
2.6.1 Spin Relaxation	35
2.6.2 Dephasing	35
2.6.3 Gate Fidelity	38
References	38

3 Quantum Dot Arrays in Silicon and Germanium	45
3.1 Mobility and Stack by Platform	47
3.2 Integration Scheme	48
3.3 Singly Occupied Quantum Dot Arrays.	52
3.4 Cross Capacitance	53
3.5 Future Perspectives	54
3.6 Conclusion	55
3.7 SiMOS Fabrication Improvements	55
3.7.1 Gate Anneal	55
3.7.2 ALD Window Etch	56
3.8 Extended Fabrication Recipe	56
References	60
Silicon	65
References	65
4 Tuneable Coupling and Isolation of Single Electrons in Silicon Quantum Dots	67
4.1 Introduction	68
4.2 Results and discussion	68
4.2.1 Charge Sensing and Readout.	68
4.2.2 Tunnel Couple Control.	71
4.3 Conclusions.	72
References	72
5 Universal quantum logic in hot silicon qubits	75
5.1 Hot Qubits	76
5.2 Large-scale quantum computing in SiMOS	76
5.3 Single Qubit Control	78
5.4 Two-Qubit Quantum Logic at 1.1 K	79
5.5 Temperature Effects on Quantum Coherence	81
5.6 Methods	82
5.6.1 Experimental setup	82
5.6.2 Single-qubit randomized benchmarking.	82
5.6.3 Two-qubit randomized benchmarking.	83
5.7 Extended Data	84
5.8 Fit of the full exchange spectrum	86
5.9 Noise model and noise fitting	86
5.10 Temperature dependence of the dephasing time	87
References	88
6 Design and integration of single-qubit rotations and two-qubit gates in silicon above one Kelvin	91
6.1 Introduction	92
6.2 Results and discussion	92
6.2.1 Silicon quantum dot device	92
6.2.2 Qubit characterization	93
6.2.3 Hot, fast, and high-fidelity CPHASE gates	94

6.2.4	Hot, fast and high-fidelity SWAP operation.	95
6.2.5	Hot two-qubit gate performance.	98
6.3	Methods	98
6.4	Reconstruction of the spin state probabilities.	98
6.5	Temperature effects on readout and initialization.	99
6.6	Exchange spectrum	100
6.7	Two-qubit gate simulations	100
6.7.1	Physical model.	100
6.7.2	Adiabatic and diabatic CPHASE gates	101
6.7.3	SWAP gate	102
	References	103
Germanium		107
	References	108
7 A Single-Hole Spin Qubit		109
7.1	Introduction	110
7.2	Results	110
7.2.1	Single hole quantum dot and Pauli spin blockade	110
7.2.2	Qubit operation	113
7.3	Discussion	115
7.3.1	Fabrication process	115
7.3.2	Experimental setup	116
7.3.3	Measurement details.	116
7.3.4	Virtual gates	116
7.4	Extended Data	117
	References	120
8 Spin Relaxation Benchmarks and Individual Qubit Addressability for Holes in Quantum Dots		123
8.1	Device and Setup	124
8.2	Spin Blockade for Hole Fillings	127
8.3	Spin Relaxation	127
8.4	Qubit Addressability	129
8.5	Conclusion	130
8.6	Methods	132
8.6.1	Tunnel Rate Analysis.	132
8.6.2	Relative Lever Arm	132
	References	134
9 A Four-Qubit Germanium Quantum Processor		137
9.1	Introduction	138
9.2	A Two-by-Two Qubit Quantum Dot Array	138
9.3	Single Qubit Control	139
9.4	One, Two and Threefold Conditional Rotations	139
9.5	Conditional Phase Gates Between Neighbouring Qubit Pairs	142
9.6	Demonstration of a Four Qubit Greenberger-Horne-Zeilinger State.	145

9.7	Methods	146
9.7.1	Device fabrication	146
9.7.2	Device screening.	146
9.7.3	Experimental setup	146
9.7.4	Virtual gate matrices.	147
9.7.5	Latched readout mechanism.	149
9.7.6	Conditional rotation gates	150
9.7.7	Shift in Rabi frequency due to exchange	151
9.7.8	Fitting of the two-qubit decay data.	152
9.7.9	Specification of the CROT and CZ gate times.	152
	References	157
10	Simultaneous driving of semiconductor spin qubits at the fault-tolerant threshold	161
10.1	Introduction	162
10.2	Results	162
10.2.1	Single Qubit Benchmarking	163
10.2.2	N -copy Randomized Benchmarking.	165
10.3	Conclusion	167
10.4	Methods	167
10.4.1	Device Fabrication.	167
10.4.2	Generation of the Single-Qubit Clifford Set	168
10.4.3	Fitting	168
10.4.4	Simultaneous Elementary Gate Tuning	168
10.5	Initialization and Readout	169
10.6	Clifford Gate Set.	170
10.7	Two-Copy Randomized Benchmarking	171
10.7.1	Structure of the matrix decays	172
10.7.2	Different types of two-copy RB.	172
10.7.3	Even same-system (ES) two-copy RB.	173
10.7.4	Odd same-system (OS) two-copy RB.	174
10.7.5	Even different-system (DS) two-copy RB.	174
10.8	Two-copy RB in practice	174
10.8.1	Lower Bound on Average Fidelity	175
10.8.2	Symmetric and Anti-symmetric input states for two-copy RB	176
10.9	Direct comparison of two-copy benchmarking and two-qubit simultaneous randomized benchmarking.	177
10.9.1	Simulation of the Clifford gate superoperator	178
10.9.2	Simulation of the clifford experiments	179
10.9.3	Comparison between the results.	179
10.10	Summary of N -copy benchmarking data.	182
	References	183

11 Quantum Coherence in Germanium Hole Spin Qubits	185
11.1 Introduction	186
11.2 Results	186
11.2.1 Quantum Coherences	187
11.2.2 Probing the ^{73}Ge Larmor Precession	189
11.2.3 Spin Dephasing due to Hyperfine Noise	190
11.3 Conclusion	192
11.4 Methods	193
11.4.1 Device Fabrication	193
11.4.2 Fitting Methods	193
11.4.3 Readout	193
11.5 Extended Data	194
11.5.1 Hole Spin Qubit g-Factors	194
11.5.2 Observation of ^{73}Ge Larmor Precession at High Field	194
References	195
12 Conclusion & Outlook	197
12.1 Conclusion	198
12.2 What next?	199
12.2.1 In Germanium	200
12.2.2 In Silicon	201
12.2.3 In General	201
References	202
Acknowledgements	203
Curriculum Vitæ	207
List of Publications	209



SUMMARY

Quantum computers based on semiconductor quantum dots are proving promising contenders for large scale quantum information processing. In particular, group IV based semiconductor hosts containing an abundance of nuclear spin-zero isotopes have made considerable headway into fulfilling the requirements of a universal quantum computer. Silicon (Si) and germanium (Ge) are two elements that have played important roles in the history of classical computing, and are now poised to do the same in the future of quantum computation. In this thesis, we advance efforts in developing a quantum computer in both Si, using electron spins in Si-metal-oxide-semiconductor (SiMOS) hosted quantum dots, and hole spins in planar germanium quantum wells (Ge/SiGe).

In chapter 3, we develop fabrication strategies for quantum dot arrays in SiMOS, Si/SiGe and Ge/SiGe platforms. In each case, a fabrication recipe is developed with considerations according to each of the different platforms challenges and opportunities. Using these recipes, we create quantum dot arrays in silicon and germanium, depletable down to single charge occupancy in all cases. Additionally, we study the cross-capacitance of the electrostatic gates on adjacent quantum dots, finding that SiMOS requires the smallest virtual corrections to gate voltages.

Using these fabrication recipes, we then focus on the SiMOS platform, creating devices for quantum information processing. In chapter 4, we show that tunnel couple control is possible between quantum dots in silicon MOS, using dedicated barrier gates. We demonstrate tuneable tunnel rates and tunnel couplings via a barrier gate, showing tunnel rates can be suppressed to below 1 Hz, and tunnel couplings are tuneable between 3 GHz and 13 GHz, overcoming a longstanding challenge for electrons in silicon-MOS quantum dots.

Operation of spin qubits at higher temperatures will permit strategies such as on chip integration of electronics, which may be key for scaling up spin qubits. In chapter 5, we demonstrate a universal set of quantum gates in a pair of SiMOS electron spin qubits, operated at 1.1 K. We find high single qubit fidelities for both qubits of around 99%, and find that dephasing times are not limited by temperature in the measured range, between 300 mK and 1.25 K. Furthermore in chapter 6, we demonstrate a portfolio of two qubit gates in the same device, and construct composite gates that should overcome limitations due to the finite Zeeman energy differences of the qubits. These results mark a milestone in the scale-up of spin qubits.

The results using electron spin qubits in SiMOS show that spin qubits can be operated at higher temperatures, where the cooling power of dilution refrigerators is much higher. SiMOS as a material host however still faces several issues in terms of scale-up. First, the interface disorder results in the unwanted formation of quantum dots, as well as the strong localization of their wavefunctions, making reliable qubit interactions non-trivial. This is reflected by the relatively lower mobility, and higher percolation densities when compared to other platforms as measured in chapter 3. We therefore switch gears to hole spins in Ge/SiGe, advancing the platform through a number of experiments.

Building on the success of the platform, we utilize the fabrication strategies developed in chapter 3 to fabricate quantum dot arrays in Ge/SiGe, which we deplete to single hole occupancy, and demonstrate the first single hole spin qubit in chapter 7. Exploiting the native spin orbit interaction, we achieve coherent, fast, all-electrical driving via electric dipole spin resonance (EDSR) of a single hole spin qubit, and characterize its spin dephasing and relaxation times. We also find that

the g -factor is highly dependent on the electric field environment.

By tuning the coupling between the hole spin qubit and its charge reservoirs, we find that spin relaxation times can be significantly improved, and we measure single hole spin qubit spin lifetimes of 32 ms. We also find that g -factors are influenced significantly by neighbouring gate potentials, providing both an opportunity for ease of qubit addressability, as well as raising the challenge of enhanced charge noise coupling in the platform.

In an effort to reduce charge noise, we fabricated wafers on quantum wells grown deeper below the heterostructure surface. This innovation led to reduced charge noise levels in hole spin qubits and facilitated the work in chapter 9. Here we present a two-by-two array of hole spin qubits, demonstrating universal quantum logic via single qubit manipulations, as well two-qubit CZ and CROT gates between all neighbouring qubit pairs. We further show the expected eight-fold splitting of a qubit resonance frequency as a result of four exchange coupled spins, allowing for both a native Toffoli-like three qubit gate, and even a four qubit controlled rotation gate. To showcase the control of the qubit array, we generate a four-qubit Greenberger-Horne-Zeilinger state in the first ever four qubit algorithm performed on a quantum processor hosted by semiconductor quantum dots.

Quantum computers will require very high operational fidelities, and will likely require the simultaneous operation of many qubits in close proximity, leading to qubit cross-talk. In chapter 10, we examine single qubit gate fidelities using Randomized Benchmarking protocols. We find that single hole spin qubits, when operated individually can exhibit native gate fidelities of 99.990(1)%, marking the state of the art for single qubit operational accuracy in spin qubit platforms. Furthermore, we investigate how cross-talk when operating multiple qubits simultaneously affects single qubit gate fidelities. To do this, we develop a new randomized benchmarking protocol called " N -Copy Benchmarking", where the same Random Clifford sequences are applied simultaneously to each of the N qubit in the experiment. This permits extraction of a single qubit gate fidelity that approximates gate fidelity in the absence of qubit-qubit interactions, for example, residual exchange coupling. We find two-copy native gate fidelities above 99.905(8)%, and four-copy fidelities of 99.34(4)%, indicating that classical crosstalk is a major consideration when considering quantum computing scale up.

Having explicitly investigated hole spin qubit relaxation times and gate fidelities, we also investigated their dephasing times to better understand the processes that limit coherence times. We found that as a function of magnetic field, a $T^{2*} \propto 1/B$ proportionality described the behaviour of spin dephasing between 0.1 T and 1 T magnetic field strengths. This trend is consistent with the expectation that charge noise coupled to the spin eigenstates via the spin-orbit interaction is the limiting noise process for hole spin qubits in Ge/SiGe. We found also that by implementing refocussing pulses, coherence could be extended as high as 504 μ s. To do this, we implemented Carl-Purcell-Meiboom-Gill pulse sequences, of varying numbers of refocussing π -pulses. These pulse sequences exhibit a characteristic filter function based on this number, that effectively reduces low frequency noise effects on qubit coherence, but also enhances certain frequencies noise. We exploit this feature to investigate the sensitivity of hole spins to the ^{73}Ge nuclei present in the quantum well with an abundance of approximately 7.3%. By modelling the traces resulting from CPMG sequences, we extract a hyperfine coupling strength for the hole spins, and estimate a dephasing time limited by hyperfine interaction. We find this time to be within the same order of magnitude as the charge noise limited dephasing time, at an in-plane magnetic field of 0.25 T. From this we conclude that, in light of the rapidity of advancements in planar germanium material quality, isotopic purification will likely become necessary in the near future in order to extend quantum coherence times of hole spins in Ge/SiGe.

William I. L. Lawrie



SAMENVATTING

Kwantum computers gebaseerd op halfgeleider kwantumdots blijken veelbelovende kandidaten voor kwantum-informatie-verwerking op grote schaal. In het bijzonder hebben op groep IV halfgeleider gebaseerde materialen met een overvloed van nucleaire spin-nul isotopen een aanzienlijke vooruitgang doorgemaakt richting het vervullen van de eisen van een universele kwantum computer. Silicium (Si) en germanium (Ge) zijn twee elementen die belangrijke rollen hebben gespeeld in de geschiedenis van klassieke computers, en zijn nu klaar om hetzelfde te doen in de toekomst van kwantum computers. In deze thesis maken we vordering met het ontwikkelen van een kwantum computer in zowel Si, gebruikmakende van elektron spins in Si-metaal-oxide-halfgeleider (SiMOS) genestelde kwantum dots, en gat spins in planaire germanium kwantum putten (Ge/SiGe).

In hoofdstuk 3 ontwikkelen we fabricage strategieën voor kwantum dot rasters in de SiMOS, Si/SiGe en Ge/SiGe platforms. In elke casus is een fabricage recept ontwikkeld waarbij we de uitdagingen en kansen van de verschillende platformen overwegen. Gebruikmakende van deze recepten maken we kwantum dot rasters in silicium en germanium, in ieder geval uitputbaar tot enkele ladings bezetting. Aanvullend daarop bestuderen we de kruis-capaciteit van de electrostatische electrodes op aangrenzende kwantum dots, waarbij we bevinden dat SiMOS de kleinste virtuele correcties op de spanningen nodig heeft.

Gebruikmakende van deze fabricage recepten leggen we dan de focus op het SiMOS platform, waarin we chips voor kwantum informatie verwerking maken. In hoofdstuk 4, laten we zien dat controle over de tunnel koppeling mogelijk is tussen kwantumdots in SiMOS, gebruikmakende van afzonderlijke barrière elektrodes. We laten afstembare tunnel snelheden en tunnel koppelingen zien via een barrière elektrode, waarbij we laten zien dat tunnel snelheden tot onder 1 Hz gedempt kunnen worden, en dat tunnel koppelingen afstembaar tussen 3 GHz en 13 GHz zijn, waarbij een lang-staande uitdaging voor electronen in SiMOS kwantum dots overkomen wordt.

Het functioneren van spin kwantumbits op hogere temperaturen zal strategieën zoals op-chip-integratie van electronica mogelijk maken, hetgeen de sleutel kan zijn voor het opschalen van spin kwantumbits. In hoofdstuk 5 demonstreren we een universele set van kwantum poorten in een paar SiMOS elektron spin kwantumbits, werkend op 1.1 K. We vinden hoge enkel kwantumbit betrouwbaarheden van rond de 99% en vinden dat defaseringstijden in het gemeten bereik (tussen 300 mK en 1.25 K) niet gelimiteerd worden door temperatuur. Bovendien laten we in hoofdstuk 6 een portfolio van twee kwantumbit poorten op dezelfde chip zien, waarbij we samengestelde poorten opbouwen die de limieten kunnen overkomen die gesteld worden als gevolg van het eindige Zeeman energie verschil tussen de kwantumbits. Deze resultaten tonen een belangrijke mijlpaal aan in het opschalen van spin kwantumbits.

De resultaten van elektron spin kwantumbits in SiMOS laten zien dat spin kwantumbits op hogere temperaturen kunnen functioneren, waar het koelvermogen van verdunnings-koelkasten veel groter is. Als materiaal wordt SiMOS echter nog steeds geconfronteerd met meerder problemen wat betreft het opschalen. Allereerst heeft de wanorde op het grensvlak als resultaat dat er ongewenste kwantumdots gevormd worden, zowel als sterke localisatie van hun golf functies,

waardoor betrouwbare kwantumbit interacties bemoeilijkt worden. Dit blijkt uit de relatief lagere mobiliteit en hogere percolatiedichtheden vergeleken met andere platforms zoals gemeten in hoofdstuk 3. Daarom veranderen we koers naar gat spins in Ge/SiGe, waarbij we het platform door een serie experimenten vooruithelpen.

Bouwend op het succes van het platform benutten we de fabricage strategieën die in hoofdstuk 3 ontwikkeld zijn om kwantumdot rasters in Ge/SiGe te fabriceren, welke we uitputten tot bezetting met een enkel gat, en demonstreren de eerste enkelgats-spinkwantumbit in hoofdstuk 7. Door het uitbuiten van de intrinsieke spin-baan interactie behalen we coherente, snelle, puur elektrische aandrijving via elektrische dipool spin resonantie (EDSR) van een enkelgats-spinkwantumbit, en karakteriseren we diens spin defasering en relaxatie tijden. We bevinden ook dat de g -factor sterk afhankelijk is van de elektrische omgeving.

Door het afstemmen van de koppeling tussen de gat-spinkwantumbits en diens ladingsreservoirs komen we erachter dat spin-relaxatietijden sterk verbeterd kunnen worden, en we meten enkelgats-spinkwantumbit spin levensduren van 32 ms. We bevinden ook dat g -factors significant beïnvloed worden door aangrenzende elektrode potentialen, hetgeen zowel voor een kans voor gemakkelijke adresseerbaarheid voor kwantumbits zorgt als voor een uitdaging met betrekking tot versterkte ladingsruis-koppeling in het platform.

In een poging tot het verminderen van ladingsruis fabriceren we wafers met kwantum putten die dieper onder de heterostructuur gegroeid zijn. Deze innovatie leidde tot verminderde ladingsruis-niveaus in gat-spinkwantumbits en faciliteerde het werk in hoofdstuk 9. Hier presenteren we een twee-bij-twee raster van gat-spinkwantumbits, hetgeen universele kwantum logica laat zien via enkele kwantumbits manipulatie, samen met twee-kwantumbit CZ en CROT poorten tussen alle aangrenzende kwantumbit paren. Verder laten we ook de verwachte achtvoudige splitsing van een kwantumbit resonantiefrequentie zien als resultaat van vier wisselwerkings gekoppelde spins, hetgeen zowel een intrinsieke Toffoli-achtige drie kwantumbit poort laat zien als zelfs een vier kwantumbit gecontroleerde rotatie poort. Om de controle over het kwantumbitraster uit te lichten genereren we een vier-kwantumbit Greenberger-Horne-Zeilinger staat in het eerste vier kwantumbits algoritme ooit uitgevoerd op een kwantum processor genesteld in halfgeleider kwantumdots.

Kwantum computers vereisen erg hoge operationele betrouwbaarheid, en zullen waarschijnlijk de gelijktijdige operatie van vele kwantumbits in directie nabijheid, hetgeen leidt tot kwantumbit cross-talk. In hoofdstuk 10 onderzoeken we enkel-kwantumbit poort betrouwbaarheden met Randomized Benchmarking protocollen. We bevinden dat enkel-gat-spinkwantumbits intrinsieke poort betrouwbaarheden van 99.990(1)% kunnen laten zien bij individuele operatie, hetgeen de state of the art voor enkel kwantumbits operationele nauwkeurigheid in spin kwantumbit platformen markeert. Daarbovenop zoeken we uit hoe cross-talk resulterende uit het gelijktijdig opereren van meerder kwantumbits de enkel kwantumbit poort betrouwbaarheid beïnvloed. Om dit te doen ontwikkelen we een nieuw randomized benchmarking protocol genaamd " N -Copy Benchmarking", waarbij dezelfde willekeurige Random Clifford reeks gelijktijdig op elk van de N kwantumbits in het experiment wordt toegepast. Dit stelt ons in staat om de enkel kwantumbit poort betrouwbaarheid te bepalen die benaderd wat de betrouwbaarheid zou zijn bij het ontbreken van kwantumbit-kwantumbit interacties zoals residuële wisselwerkingskoppeling. We bepalen two-copy intrinsieke poort betrouwbaarheden van boven de 99.905(8)%, en four-copy betrouwbaarheden van 99.34(4)%, aangevend dat klassieke cross-talk een belangrijke afweging is bij het opschalen van kwantum computers.

Nu we expliciet gat kwantumbit spin relaxatie tijden en poort betrouwbaarheden onderzocht hebben onderzoeken we ook hun defaseer tijden om beter de processen die coherentie tijden beperken te begrijpen. We vonden dat als functie van magnetisch veld een $T^{2*} \propto 1/B$ evenredigheid het gedrag van de spin defasering beschrijft tussen 0.1 T en 1 T magnetisch veldsterkte. Deze

trend is consistent met de verwachting dat ladingsruis gekoppeld aan spin eigenstaten via spin-baan interactie het limiterende ruis proces voor gat-spin-kwantumbits in Ge/SiGe is. We vonden ook dat door het implementeren van herfocus pulsen coherentie verhoogd kon worden tot wel $504 \mu\text{s}$. Om dit te kunnen doen implementeren we Carl-Purcell-Meiboom-Gill pulse reeksen van verschillende antallen herfocus π -pulsen. Deze pulsreeksen laten een karakteristieke filter functie gebaseerd op die aantal zien, welke effectief lage frequentie ruis effecten op kwantumbit coherentie vermindert, maar ook de ruis op bepaalde frequenties versterkt. We buiten deze eigenschap uit om de gevoeligheid van gat spinkwantumbits voor ^{73}Ge nuclei te onderzoeken, welke aanwezig zijn in de kwantumput voor ongeveer 7.3%. Door het modelleren van de curves als resultaat van CPMG reeksen leiden we een hyperfine koppelings kracht af voor de gat spins, en we benaderen de defaserings tijd gelimiteerd door hyperfine interactie. We vinden dat deze tijd in dezelfde orde-grootte ligt als de ladingsruis gelimiteerde defaserings tijd, bij een in-vlak magnetisch veld van 0.25 T. Hieruit concluderen we dat, in het licht van de snelheid van vooruitgang in planair germanium materiaal kwaliteit, isotopisch purificeren waarschijnlijk in de nabije toekomst nodig wordt om kwantum coherentie tijden van gat spins in Ge/SiGe te verlengen.



Strewth

/stru:θ/

Exclamation

Used to express surprise or dismay.¹

¹Oxford English Dictionary



1

INTRODUCTION

Classical mechanics is the physics of music. Quantum mechanics is the music of physics

Klaus Mølmer

Quantum computing promises to revolutionize the way we process information, and the complexity of the computational tasks we can achieve. The first proposals to utilize quantum systems as a computational resource came about in the early 1980's [1]. It was soon shown that in order to simulate a quantum system efficiently, one would need a computer that evolved according to quantum mechanical laws [2]. Among other important early contributions, these two statements birthed a field of quantum information processing, spurred on by the idea that quantum computers may be able to perform certain tasks much faster than classical ones. Throughout the 1990s, algorithms exploiting the quantum mechanical nature of reality were developed that confirmed this belief, resulting in an immense global effort to build a useful quantum computer.

In this section we review basic quantum information and quantum mechanical principles required for the work in this thesis. We examine the criteria for making a good qubit, and where this work fits into the greater field of quantum computing.

1.1. PRIMER ON QUANTUM INFORMATION

The theory encapsulating the behaviour of quantum systems at the physical level is called *quantum mechanics*. The theory describing how quantum information can be manipulated is called *quantum information theory*. *Quantum computing* involves the processing of information contained within a quantum system. In this chapter, we review the basics of quantum computing utilized in this thesis.

1.1.1. QUANTUM BITS, SUPERPOSITION AND ENTANGLEMENT

The theories of both classical and quantum information rely on the manipulation of data. At its most fundamental unit, this data takes the form of an abstract two level system called a *bit* if classical, and a *qubit* if quantum. The reason for this distinction is because the physical properties of a qubit give rise to additional complexities in the complete description of its state. Figure 1.1

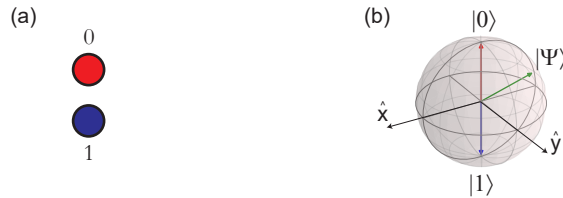


Figure 1.1: Comparison of the properties of classical and quantum bits. The classical bit (left) can be completely described by one piece of information, the value of the variable a . The qubit's state can be represented by an arbitrary vector of unit magnitude $|\Psi\rangle$, on the surface of a sphere. Two complex valued variables a and b describe the state of a single isolated qubit.

compares a description of a classical state to a quantum state. In the former case, a complete description of the state is possible with a single variable, a , which can only take one of two possible discrete values $a \in \{0, 1\}$. The quantum state, while still binary, is much richer. A qubit's state can be depicted as a unit vector using *Dirac notation* as

$$|\Psi\rangle = a|0\rangle + b|1\rangle = \begin{pmatrix} a \\ b \end{pmatrix} \quad (1.1)$$

where $a, b \in \mathbb{C}$, and $|a|^2 + |b|^2 = 1$. When this vector points towards the bottom or top of the sphere, we recover the classical bit states of 0 or 1 respectively. However, an infinite number of states exist in between, reflecting the ability for a quantum state to exist in both states at once. This phenomenon is called *superposition*, and constitutes one of the intrinsically quantum properties that lead to the predicted advantages of quantum computing [3–6].

A second important and advantageous property for quantum computation is the phenomenon of *entanglement*. To illustrate entanglement, let's first consider the state space of a system of two qubits $|\Psi\rangle_1 = \alpha_1|0\rangle + \beta_1|1\rangle$ and $|\Psi\rangle_2 = \alpha_2|0\rangle + \beta_2|1\rangle$. The state space of the *full* quantum system is then

$$|\Psi\rangle_{12} = |\Psi\rangle_1 \otimes |\Psi\rangle_2 = \alpha_1\alpha_2|00\rangle + \alpha_1\beta_2|01\rangle + \beta_1\alpha_2|10\rangle + \beta_1\beta_2|11\rangle = \begin{pmatrix} \alpha_1\alpha_2 \\ \alpha_1\beta_2 \\ \beta_1\alpha_2 \\ \beta_1\beta_2 \end{pmatrix} \quad (1.2)$$

where ' \otimes ' is the tensor product operation, and we have taken the convention $|\psi_1\rangle_1 |\psi_2\rangle_2 = |\psi_1\psi_2\rangle$. Notice that we have to specify *four* separate complex variables to describe a two-qubit quantum

system, whereas a two-bit system could be described with only two real variables. In fact, as a function of the system size N , the amount of information required to represent a quantum system scales as 2^N , while classical systems scale as N . One can quickly see that classical computers will have a hard time simulating quantum systems of even modest sizes, with a system of about 250 qubits requiring more bits than there are estimated atoms in the universe [7].

To illustrate the concept of entanglement, it is useful to classify the state of a system of qubits into two types: *separable* states, and *inseparable* states. Separable states are quantum systems that can be expressed as the product of the individual qubit states. For example, considering the present two-qubit system, $|\Psi\rangle_{12}$ is already by definition a separable state, since it was defined to be the tensor product of two individual qubit states $|\Psi\rangle_{12} = |\Psi\rangle_1 \otimes |\Psi\rangle_2$. Separable states are also called *product* states for this reason. Inseparable states on the other hand, cannot be expressed as the tensor product of two separate quantum systems. Consider the state $|\Psi\rangle_{12} = \frac{1}{\sqrt{2}}(|00\rangle + |11\rangle)$. This state cannot be written as the product of two individual qubit states, and is therefore inseparable. We call a state that is inseparable, an *entangled* state. The physical consequence of a state being entangled, is that the full state information of an individual qubit is not stored locally. The ability to create quantum states with non-local properties lies at the heart of the fields of quantum information and communication.

Another useful representation of a qubit's state, is via its *density matrix*. This is particularly useful when describing systems of noisy, or entangled quantum systems. The density matrix of a qubit state composed of some probabilistic mixture of states $|\psi_j\rangle$ is defined as

$$\rho = \sum_j p_j |\psi_j\rangle \langle \psi_j| \quad (1.3)$$

where the probabilities p_j add up to one. If a quantum state is known, ie. we can always choose some projective measurement that will return the state with complete certainty, then it is said to be a *pure state*. If no such basis exists, such as for qubits who's state's have decohered, or are entangled with other qubits, they are said to be *mixed states*. The density matrix of a quantum state allows us to measure the outcome probability of some system observable \hat{A} simply as $p = \text{Tr}\{\hat{A}\rho\}$ where $\text{Tr}\{\cdot\}$ is the trace of a matrix.

1.1.2. QUANTUM GATES

Operations that change the state of a systems of quantum bits are called gates. For a system of N qubits, a quantum gate can be represented mathematically as $2^N \times 2^N$ matrix. Quantum gates must satisfy the property of *unitarity*, that is, for a gate U , it's inverse must be equal to its conjugate transpose, ie. $U^\dagger U = I$.

To begin, let us consider operations on a single qubit state. Single qubit operations are equivalent to rotations on the Bloch sphere. It is therefore useful to define quantum gates in terms of rotational operators around the mutually orthogonal axes of the Bloch sphere (Fig. 1.1b). Let's define X_θ , Y_θ and Z_θ as rotations of angle θ around the x , y and z axes, where [8]

$$X_\theta = \begin{pmatrix} \cos \frac{\theta}{2} & -i \sin \frac{\theta}{2} \\ -i \sin \frac{\theta}{2} & \cos \frac{\theta}{2} \end{pmatrix} \quad (1.4)$$

$$Y_\theta = \begin{pmatrix} \cos \frac{\theta}{2} & -\sin \frac{\theta}{2} \\ \sin \frac{\theta}{2} & \cos \frac{\theta}{2} \end{pmatrix} \quad (1.5)$$

$$Z_\theta = \begin{pmatrix} e^{-i\frac{\theta}{2}} & 0 \\ 0 & e^{i\frac{\theta}{2}} \end{pmatrix}. \quad (1.6)$$

These gates unlock the full state space of a single qubit. When we set $\theta = \pi$, we recover a special set of quantum gates, known as the Pauli operators

$$X_\pi = \sigma_x = \begin{pmatrix} 0 & 1 \\ 1 & 0 \end{pmatrix} \quad (1.7)$$

$$Y_\pi = \sigma_y = \begin{pmatrix} 0 & i \\ -i & 0 \end{pmatrix} \quad (1.8)$$

$$Z_\pi = \sigma_z = \begin{pmatrix} 1 & 0 \\ 0 & -1 \end{pmatrix}. \quad (1.9)$$

The same principle can be applied for rotations of $\theta = \pi/2$, whose matrices are shown in Figure 1.2. These types of rotations allow the generation of superposition states.

In order to achieve universal access to a two-qubit state space, one needs a two-qubit entangling gate [9]. Here it becomes useful to introduce different types of qubits in quantum computation. We usually refer to a qubit whose state is changed as a *target qubit*, while a qubit whose state determines whether or not action occurs on the target qubit is called a *control qubit* [10].

In this thesis, we work with three main two-qubit entangling gates: The *controlled-NOT* (CNOT), The *controlled-Z* (CZ) and the SWAP. The CNOT gate is a two-qubit gate which performs a σ_x gate on a target qubit, if the control qubit is in the $|1\rangle$ state, and does nothing otherwise. The *controlled-Z* gate is the same, but by applying a σ_z gate on a target qubit. The SWAP gate exchanges the states of the qubits. The SWAP gate does not actually permit universal access to the two qubit state space, however the $\sqrt{\text{SWAP}}$ does. These gates are all shown in Figure 1.2.

Since universal quantum logic is possible using a single two-qubit entangling gate in addition to single qubit rotations, it follows that each of the two-qubit gates presented above can be compiled in terms of a combination of single and two-qubit gates. Furthermore, any arbitrary unitary operation on any number of qubits can be decomposed into only single- and two-qubit quantum gates. This is indeed the case, however sometimes it can be more efficient to utilize a variety of quantum gates when operating a quantum computer. This is particularly prudent since real implementations of qubits are very sensitive to their environments, and can lose their quantum information rapidly. We now turn to the criteria that determine whether a quantum system is suitable as a qubit candidate.

1.2. WHAT MAKES A GOOD QUANTUM BIT?

There are many eligible quantum systems with which to build quantum computers at the hardware level. This might seem overwhelming, but luckily there are some well established guidelines that help us assess whether a particular qubit is suitable or not. These guidelines were published by theoretical physicist David DiVincenzo in 2000 [11], and are have served as the qualitative benchmarks against which to compare quantum computing platforms. There are seven criteria, though these are frequently referred to as '5+2' since the first five pertain to quantum computation, while the final two relate to quantum communication. However, some proposals for quantum computing architectures rely on medium or long range communication elements for their qubits [12], usually on the same chip.

- *A scalable physical system with well characterized qubits*

A well characterized qubit is simply a two level quantum system that is split off from other

Gate	Action	Representation	Matrix Form
Pauli-X/2			$\frac{1}{\sqrt{2}} \begin{pmatrix} 1 & -i \\ -i & 1 \end{pmatrix}$
Pauli-Y/2			$\frac{1}{\sqrt{2}} \begin{pmatrix} 1 & -1 \\ 1 & 1 \end{pmatrix}$
Pauli-Z/2			$\frac{1}{\sqrt{2}} \begin{pmatrix} 1 & 0 \\ 0 & i \end{pmatrix}$
Hadamard			$\frac{1}{\sqrt{2}} \begin{pmatrix} 1 & 1 \\ 1 & -1 \end{pmatrix}$
Controlled-NOT			$\begin{pmatrix} 1 & 0 & 0 & 0 \\ 0 & 1 & 0 & 0 \\ 0 & 0 & 0 & 1 \\ 0 & 0 & 1 & 0 \end{pmatrix}$
Controlled-Z			$\begin{pmatrix} 1 & 0 & 0 & 0 \\ 0 & 1 & 0 & 0 \\ 0 & 0 & 1 & 0 \\ 0 & 0 & 0 & -1 \end{pmatrix}$
SWAP			$\begin{pmatrix} 1 & 0 & 0 & 0 \\ 0 & 0 & 1 & 0 \\ 0 & 1 & 0 & 0 \\ 0 & 0 & 0 & 1 \end{pmatrix}$
Toffoli			$\begin{pmatrix} 1 & 0 & \dots & 0 & 0 \\ 0 & 1 & \dots & 0 & 0 \\ \dots & \dots & \dots & \dots & \dots \\ 0 & 0 & \dots & 0 & 1 \\ 0 & 0 & \dots & 1 & 0 \end{pmatrix}_{8 \times 8}$

Figure 1.2: **Summary of single- two- and three- qubit gates.** Rows represent single- two- and three- qubit gates. The action column shows examples of their action on a single qubit in the Bloch sphere. A arrow indicates an example starting state, while a red arrow indicates the final state. Red arcs indicate the path through state space traced by the qubit over the duration of the gate. The remaining columns show how they are represented in a quantum circuit, and their mathematical matrix structure.

energy states by a reasonable energy. Examples of such a system are the spin eigenstates of a hole or electron in a magnetic field [13], the vibrational modes of ions confined to potential wells [14], and the oscillations of cooper pairs across tunnel junctions between superconducting islands [15]. The requirement for a scalable physical system is an extremely complicated condition, and one that continues to baffle the quantum computing community as the number of qubits on state-of-the-art quantum computers becomes larger. At it's most idealistic, scalability states that for a given platform, there exists a unit-cell such that going from one unit cell to a large number (say 10^9) should introduce no emergent problems. In the case of classical computing, reduction in transistor size, power requirements,

electronic signal control and multiplexing contributed to the scalable nature of the transistor, and are why billions of transistors can be controlled with around a thousand pins on modern CPUs. Generally speaking for quantum computers, a single qubit needs several DC electronic connections, several AC signals, and isolation of the quantum state, leading to an unscalable number of interconnects per qubit [16]. This metric, known as "Rent's Rule", is a good way to disambiguate scalability claims [17].

- *The ability to reliably initialize qubits into a known state*

Quantum computers perform algorithms on qubits. This requires precise knowledge of what the state of the qubit was to begin with. It is not surprising that this is a requirement, however it can be difficult to achieve accurate state initialization. One tactic is to simply wait for a system to relax into its ground state. However this time frame is often impractically long, leading to investigation into other high fidelity state initialization methods.

- *Long relevant coherence times*

Quantum states are delicate - any interaction with unaccounted for physical systems will result in information loss, either due to quantum state relaxation or decoherence. As a result, the timeframes over which information can be reliably stored in a quantum computer must be long enough to endure a given algorithm.

- *A Universal set of quantum gates*

Computing with quantum systems requires the ability to access and exploit its full state space. A set of gates that are able to achieve this is called a universal set. Technically, due to the infinite nature of the state space of a qubit, no finite set of quantum gates exists that is universal. The gate set $\{X_\theta, Y_\theta, Z_\theta, \text{CNOT}\}$ constitutes a universal gate set of infinite size, however arbitrary qubit rotations can in practice be easily performed (see chapters 5 and 9 for example).

- *Measurement capability*

In order to extract information from a quantum algorithm we need to be able to measure the state of a quantum system. Like initialization, quantum measurement fidelities are susceptible to error and must also be reliable. Measurement can be non-trivial in practice, for example, direct measurement of the magnetic moment of an electron spin is difficult. Measurement techniques for spin qubit systems are elaborated upon in Chapter 2.

1.3. HOW DOES THIS WORK FIT IN?

Having seen what makes a good qubit, we are now in a position to place the work contained in this thesis into context. We have seen that there are a multitude of challenges that quantum computing faces, as the field attempts to build processors with increasing numbers of qubits. We have also seen that there are a multitude of approaches to quantum computing, each offering different solutions to the many challenges we face moving forward. As a result, it is a non-trivial task to narrow down which quantum computing implementation is most suitable.

In the sub-field of spin qubits, several diverse qubit candidates exist. However, a certain class of qubits, called *semiconductor quantum dot spin qubits* share a unique advantage, in that they bear a high degree of similarity to the transistor: the physical representation of the bit, upon which modern computers are based. The potential of bootstrapping off the the wealth of knowledge and experience contained within the semiconductor industry is a highly attractive prospect that positions semiconductor spin qubit platforms as promising candidates for quantum computing scale up.

The work in this thesis pertains to experiments on spin qubits defined in silicon and germanium semiconductor hosts. Namely, electron spins defined in silicon quantum dots, and hole spins defined in germanium quantum dots. A particular emphasis is placed on assessing both platforms' suitability for quantum computing efforts, and attempting to draw conclusions about which aspects of each candidate may limit future progress. The structure of the thesis is as follows:

- **Chapter 2** contains a theoretical background required to understand the experiments and conclusions of the chapters that follow it, introducing semiconductor quantum dots, electron spin qubits in silicon, and hole spin qubits in planar germanium. Experimental techniques and setups are also introduced here.
- **Chapter 3** introduces a fabrication strategy for producing quantum dot arrays in group IV based platforms, and examines the advantages of electron spin qubits in silicon metal-oxide semiconductor, as well as silicon quantum wells. This chapter also motivates the operation of qubits at higher temperatures to facilitate cryogenic on-chip integration of electronics, easing scale up requirements.

The next two chapters examine quantum computing using electron spins in SiMOS, with an emphasis on demonstration of qubit operation at high temperature.

- **Chapter 4** shows the first demonstration of a tuneable tunnel-coupling between quantum dots in silicon-MOS, adding a highly versatile new tool to operating qubits in this platform.
- **Chapter 5** covers the first demonstration of universal two-qubit logic at elevated temperatures, showing that high temperature operation of spin qubits is possible. We explore the behaviour of spin dephasing times as a function of temperature, finding little dependence. We also find that single qubit gate fidelities obtained via randomized benchmarking, can exceed 99%, even at 1.1 K.
- **Chapter 6** presents a two-qubit gate portfolio, operated at high temperatures. SWAP, CPHASE and CROT gates are all demonstrated in the same device by utilizing adiabaticity and diabaticity to overcome the finite Zeeman energy difference present between the qubits.

The following chapters are devoted to experiments in planar germanium. Scaling the number of qubits and characterization of their quality are the primary focus points.

- **Chapter 7** demonstrates the first single hole spin qubit, serving as a starting point for all future measurements. We quantify the coherence of the qubit, and demonstrate coherent control of its spin state.
- **Chapter 8** demonstrates long spin relaxation times for single- and few-hole quantum dots, as well as studies the effects of gate voltages on qubit g-factor. These results show that spin relaxation will not be a limiting factor for hole spins defined in planar germanium.
- **Chapter 9** builds on the work in previous chapters, by demonstrating a four-qubit germanium quantum processor, defined in a 2x2 array of hole spin qubits. We show full control of single- and two-qubit operations for nearest neighbour operations in the array, as well as excellent control of qubit pair exchange, allowing for the execution of native 3-qubit Toffoli like and 4-qubit gates CCC-NOT gates. We also demonstrate fast CZ gates between all qubit nearest neighbour pairs, and showcase our qubit control and quality by creating a fully entangled four-qubit GHZ state, marking the state-of-the-art for semiconductor spin qubit quantum computing efforts.
- **Chapter 10** demonstrates the ability to operate up to four qubits simultaneously, while still maintaining good control fidelity. This alleviates some of the requirements placed on spin coherence, since simultaneous qubit operation will reduce qubit idle time. We also report state-of-the-art single qubit control fidelities across all semiconductor quantum dot platforms.

- **Chapter 11** studies the primary cause of spin decoherence in germanium hole spin qubits. We find this to be primarily charge noise, but also find that noise due to the non-zero nuclear spin isotopes of natural germanium causes a significant decohering effect on hole spin qubits, presenting an argument for the isotopic purification of the platform.

The final chapter concludes by discussing future research directions for silicon and germanium spin qubits, clarifying the immanent hurdles of both platforms, and avenues that may open the way to practical quantum devices.

REFERENCES

- [1] Benioff, P. The computer as a physical system: A microscopic quantum mechanical Hamiltonian model of computers as represented by Turing machines. *Journal of Statistical Physics* **22**, 563–591 (1980).
- [2] Feynman, R. P. Simulating physics with computers. *International Journal of Theoretical Physics* **21**, 467–488 (1982).
- [3] Shor, P. W. Algorithms for quantum computation: Discrete logarithms and factoring. In *Proceedings - Annual IEEE Symposium on Foundations of Computer Science, FOCS*, 124–134 (IEEE Computer Society, 1994).
- [4] Grover, L. K. A fast quantum mechanical algorithm for database search. In *Proceedings of the Annual ACM Symposium on Theory of Computing*, vol. Part F1294, 212–219 (Association for Computing Machinery, 1996).
- [5] Deutsch, D. & Jozsa, R. Rapid solution of problems by quantum computer - Deutsch and Jozsa.pdf. *Proceedings of the Royal Society A: Mathematical, Physical and Engineering Sciences* 553–558 (1992).
- [6] Zalka, C. Simulating quantum systems on a quantum computer. *Proceedings of the Royal Society A: Mathematical, Physical and Engineering Sciences* **454**, 313–322 (1998).
- [7] Gott III, J. R. *et al.* A Map of the Universe. *Astrophys. J.* **624**, 463–484 (2005).
- [8] Quantum inspire knowledge base: Rotation operators. URL <https://www.quantum-inspire.com/kbase/rotation-operators/>.
- [9] Williams, C. P. *Explorations in Quantum Computing*. Texts in Computer Science (Springer London, London, 2011), 2 edn. URL <http://link.springer.com/10.1007/978-1-84628-887-6>.
- [10] Nielsen, M. A. & Chuang, I. L. *Quantum Computation and Quantum Information* (Cambridge University Press, 2010).
- [11] DiVincenzo, D. P. The physical implementation of quantum computation. *arXiv 0002077* **48**, 771–783 (2000).
- [12] Vandersypen, L. M. K. *et al.* Interfacing spin qubits in quantum dots and donors—hot, dense, and coherent. *npj Quantum Inf.* **3**, 1–10 (2017).
- [13] Loss, D. & DiVincenzo, D. P. Quantum computation with quantum dots. *Physical Review A - Atomic, Molecular, and Optical Physics* **57**, 120–126 (1998).

- [14] Cirac, J. I. & Zoller, P. Quantum computations with cold trapped ions. *Physical Review Letters* **74**, 4091–4094 (1995).
- [15] Arute, F. *et al.* Quantum supremacy using a programmable superconducting processor. *Nature* **574**, 505–510 (2019).
- [16] Franke, D. P., Clarke, J. S., Vandersypen, L. M. & Veldhorst, M. Rent's rule and extensibility in quantum computing. *Microprocessors and Microsystems* **67**, 1–7 (2019).
- [17] Landman, B. S. & Russo, R. L. On a Pin Versus Block Relationship For Partitions of Logic Graphs. *IEEE Transactions on Computers* **C-20**, 1469–1479 (1971).



2

ELECTRON AND HOLE SPIN QUBITS IN SEMICONDUCTOR QUANTUM DOTS

In this section, we introduce the concepts pertaining to the implementations of quantum bits used throughout the thesis: Spin qubits defined in semiconductor quantum dots. We begin by intuitively introducing quantum dots in planar semiconductor platforms, and the techniques common to the operation of semiconductor quantum dot devices, including charge sensing and virtual gates. We continue by introducing the concept of a spin qubit, and its behaviour in stationary and oscillating magnetic fields, the exchange interaction, how to implement single- and two-qubit gates, and discuss how to perform spin readout. Next we introduce the spin qubit systems of electrons silicon and holes in germanium, defined in quantum dots, reviewing their respective physical considerations. Finally we review noise sources acting on spin qubits in silicon and germanium, and experimental methods used to quantify the performance of a quantum system.

2.1. SEMICONDUCTORS

Crystalline materials in solid state physics can be classified as conductors, semiconductors, or insulators. The main parameters that determine which of these categories a given material falls in to are the *bandgap* E_g , and the *Fermi level* E_F . For a crystalline material without defects, no energy states exist within its bandgap. It is defined as the difference in energy between the highest *valence band* state, and the lowest *conduction band* state, representing how much energy is required to excite a charge carrier from a valence bond, to a free carrier. For insulators, this gap is very large, and transport through them is very difficult. Semiconductors have smaller band gaps, allowing for excitations of electrons from valence to conduction bands. To put this in perspective, the band gaps of the semiconductors silicon and germanium are about 1.1 eV and 0.72 eV respectively [1], while for insulator SiO_2 , depending on growth quality, it can be as high as 9.6 eV. For conductors, the conduction and valence bands overlap, requiring no excitations to generate free carriers. This results in favorable conduction properties. The Fermi level of a material is defined as the energy at which the occupation probability of the next available energy state is one half. For the examples of conductors and semiconductors just described, the Fermi level lies at the intrinsic level, which is in the exact energy center of the bandgap. However, the Fermi level can also be raised or lowered, by introducing a greater density of allowed states via techniques such as doping [2]. Adding dopants to a semiconductor enhances their conduction properties and in extreme limits, can cause transitions between semiconductors and metals [3].

Often, by combining semiconductors, metals, and insulators together, we can create devices that function in practical ways. In this thesis, we focus on three semiconductor heterostructures. Silicon is used as a host material in both metal-oxide-semiconductor (SiMOS) as shown in figure 2.1a, and in Si/SiGe heterostructures as shown in figure 2.1b. In the former case, electrons accumulate at the Si-SiO₂ interface when a positive voltage is applied to a metallic gate deposited above the insulating oxide layer. For Si/SiGe, the band energies of the Si and SiGe layers are different, creating a *quantum well*, where electrons become trapped in the silicon layer. Figure 2.1c shows a Ge/SiGe heterostructure, where a quantum well is also formed that permits trapping of either conduction band electrons or valence band holes. This thesis focuses on hole spins in Ge quantum wells. Here, a negative potential is required to accumulate holes in the quantum well.

2.2. SEMICONDUCTOR QUANTUM DOTS

In semiconductors, quantum dots are clusters of charge carriers that are spatially confined in such a way that their energies become measurably quantized [4]. The confinement depends on the geometry of the host medium, however the work in this thesis pertains to the case where quantum dots are defined in a planar geometry (Fig 2.2). The cross-sectional view shows charges (white circles) accumulating at a semiconductor-insulator interface, below metallic gates (dark grey). These gates are electrostatically biased to attract charges, overcoming the repulsive energy between the individual charges. This forms a small island of charge in the semiconductor bulk, constituting a quantum dot. It's important to note that the depictions of quantum dots in this chapter are intended to cater to a classical intuition. In reality, the way that charges arrange themselves in quantum dots is complex and for a more thorough and accurate description, consult ref. [4]. Figure 2.2c shows a simulation of the arrangement of charges within a circular quantum dot of radius 25 nm. Each geometry is two-fold degenerate due to spin, which we will come to in 2.3.

In order to confine quantum dots in practice, it is usually necessary to have several metallic gates in order to create a well controlled potential profile. Figure 2.2 shows a typical strategy em-

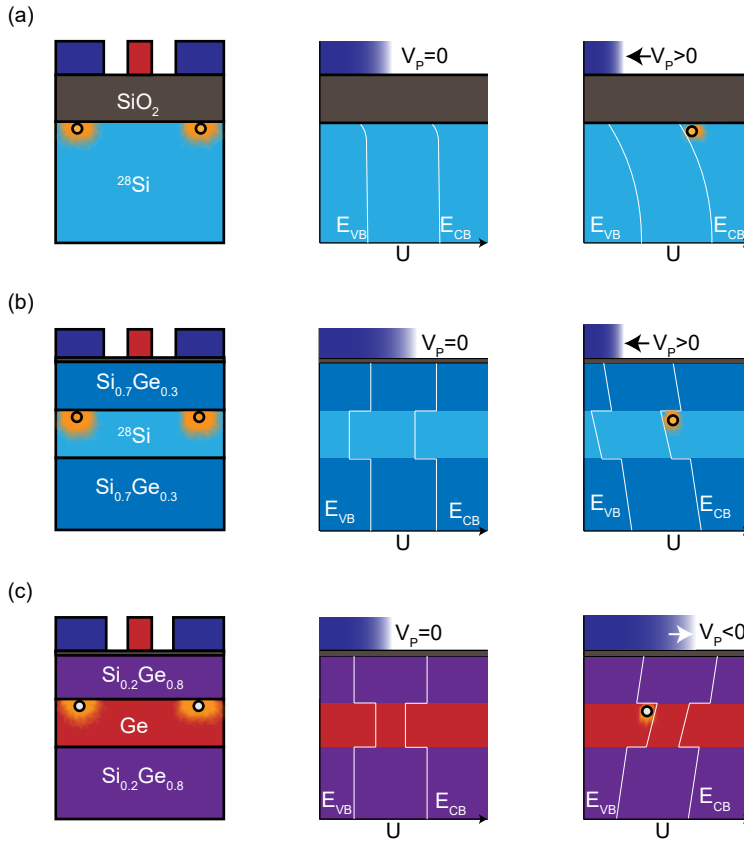


Figure 2.1: **Summary of the semiconductor heterostructures studied in this thesis.** (a) Silicon-MOS. Electrons are confined to the Si-SiO₂ interface. In equilibrium, conduction and valence bands bend slightly due to strain induced by the semiconductor-oxide lattice mismatch. When a positive voltage V_p is applied to a metallic gate, electrons accumulate. (b) Si/SiGe heterostructures. Electrons accumulate in the Si quantum well, when a positive voltage is applied. (c) Ge/SiGe heterostructures. The nature of the materials parameters permit electrons or holes to become trapped inside a Ge quantum well. However we focus on holes in this case. When a negative potential is applied, holes become confined in the valence band within the quantum well.

ployed in the design of nanoscale devices, whereby charges are attracted beneath a *plunger gate* (blue), and repulsed by flanking *barrier gates* (red).

2.2.1. COULOMB OSCILLATIONS

In order to load a quantum dot with charges, a nearby reservoir must be coupled to it. Reservoirs are regions in the semiconductor bulk with a practically infinite number of charges. Figure 2.4 shows how reservoirs can be used to controllably load charges into a quantum dot. Two reservoirs (green) contact the semiconductor bulk through windows in the insulator. They are controllably coupled to the quantum dot via the barrier gate voltages. We can imagine an experiment where one measures the current between the two reservoir leads, which we will call source (the left lead) and drain (the right lead). By setting the chemical potential of the source higher than that of the

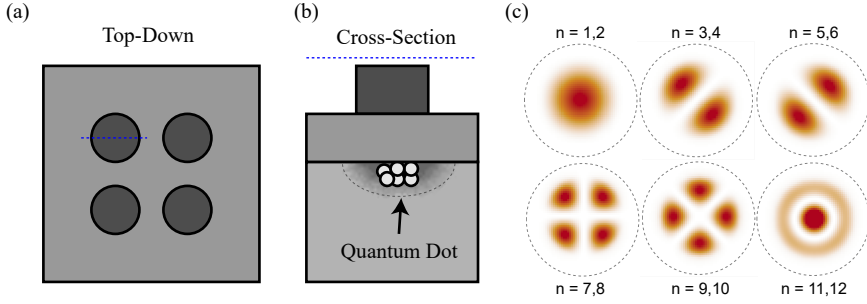


Figure 2.2: **Planar semiconductor quantum dots.** (a) A top down view shows darker circles representing metallic gates, in an array on the insulating surface of a semiconductor wafer. These gates control the potentials that allow for the accumulation and depletion of charges that form quantum dots. (b) The Cross-sectional view shows charges accumulating in the semiconductor bulk underneath the metallic gates, constituting quantum dots. (c) More realistic depiction of the first 12 wavefunctions of spin-1/2 charges distributed in a quantum dot defined by a circular potential of radius 25 nm. Simulated using KWANT [5]

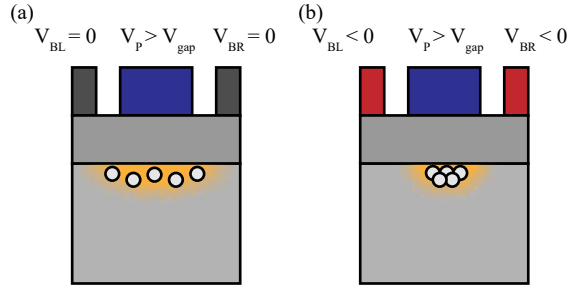


Figure 2.3: **Confinement of quantum dots.** (a) A voltage is applied to the plunger gate (blue) resulting in charges becoming confined to the interface of the semiconductor bulk and insulator. The charges are still mostly unconfined in the lateral dimension. (b) Repulsive voltages are applied to the barrier gates (red). This causes lateral confinement of the quantum dot, underneath the plunger gate.

drain $\mu_S > \mu_D$, we create a source-drain bias $V_{SD} = \alpha(\mu_S - \mu_D)$ where α is the lever arm, such that it is favorable for current to flow [6]. The quantum dot also has a chemical potential μ_{dot} dictated by the voltage on the plunger gate V_p . Unlike the reservoir, the quantum dot has discrete allowed energy levels, in this case dictated by the number of charges it contains. The chemical potential of the N 'th charge occupation of a quantum dot is defined as $\mu_N = \mu_{N-1} + E_{\text{add}}$. If $\mu_S \geq \mu_N$, then a charge will tunnel from the source onto the quantum dot such that there are N charges. Similarly, if $\mu_D \leq \mu_N$, a charge from the quantum dot will tunnel into the drain, leaving $N - 1$ charges. In order for current to flow between the source-drain leads, an available quantum dot state must exist within the bias window such that $\mu_S < \mu_N < \mu_D$. The left panels show the situation where no allowed charge occupation state exists within the bias window. Resultantly, no current flows for this plunger gate voltage (red star). This situation is called "Coulomb blockade". The right panels show the case where the plunger gate voltage has tuned the chemical potential of the quantum dot such that $\mu_D < \mu_N < \mu_S$, allowing current to flow, and resulting in a sharp current peak (blue star). The sharpness of the current peaks in the lower panel due to the lifting of Coulomb blockade is a very useful tool when sensing the motion of nearby charges, as we will now see.

2.2.2. CHARGE SENSING

The abrupt nature of the sharp transitions between current flow and Coloumb blockade in a quantum dot provides a useful tool in quantum devices, known as charge sensing. Charge sensing is the ability to detect when a quantum dot changes occupancy. That is, when a charge is added or removed from the quantum dot. It is important to know the charge occupation of a quantum dot, since it is common practice to define a qubit as the spin of a single charge particle (more of this in section 2.3). It is also useful for a technique called spin-to-charge conversion, used in the reading out of a qubit's spin state, which will be discussed later. For now, we will consider the general concept of charge sensing.

Consider a system, where a quantum dot coupled to two reservoirs (like the case above) is defined, close to another quantum dot coupled to a different reservoir. This is shown in figure 2.5. We will call the former system a *charge sensor*. Here, we assume that current cannot flow between the charge sensor and the quantum dot, rather they are capacitively coupled. We also assume for ease of explanation that there is no capacitive coupling of the gates to the quantum dots, except via their respective plunger gates. The breaking of this assumption will be explained later in the context of 'virtual gates'. Let us assume that the charge sensor is currently tuned in such a way that there is an allowed energy level of the sensor quantum dot inside the source-drain bias window. This means that current is flowing between the leads. Let us also assume that the other quantum dot has an occupation N . If we now sweep the plunger gate controlling the chemical potential of this quantum dot, we will reach a regime where it is energetically favourable for a new charge to tunnel into the dot, bringing the occupation to $N + 1$. If this happens, the capacitance of this dot will change and therefore due to it's capcative coupling to the sensor dot, so too will the chemical potential of the charge sensor, leading to a change in current. Since the Coloumb peaks of the quantum sensor are sharp, this allows us a sufficiently large differential signal between charge states to deterministically fill a quantum dot to an arbitrary occupancy.

2.2.3. VIRTUAL GATES

This principle can be extended to sensing multiple quantum dots. The bottom panels of figure 2.5 show a double-dot charge sensing configuration. Here, a second quantum dot is also capacitively coupled to the charge sensor. Figure 2.5f is called a *charge stability diagram* (CSD), and shows the charge occupation of the two quantum dots as a function of V_{P1} and V_{P2} . Note that the charge transitions of one dot are not dependent on the value of the other dot. This is a result of the assumption that there is no capacitive coupling between the quantum dots. In reality, there will be some dependence of the chemical potential of a quantum dot on the gate voltages in the device. This motivates the use of virtual gates, a practice where multiple gate voltages are changed at once to alter a given quantum dots chemical potential, without affecting others in the system. Consider the device in Figure 2.6a, where a double quantum dot system is defined with two plunger gates P_1 and P_2 , separated by a barrier gate B_{12} . The charge state of the system is detected by a charge sensor. We want to define virtual gates \tilde{V}_{P1} , \tilde{V}_{P2} , \tilde{V}_{B12} , as a function of the real gate voltages V_{P1} , V_{P2} , V_{B12} such that a change in the virtual gate voltage does not affect the position of the charge transition lines of the dots unintentionally. Therefore we define changes in the virtual gates as [7]:

$$\begin{pmatrix} \tilde{V}_{P1} \\ \tilde{V}_{B12} \\ \tilde{V}_{P2} \end{pmatrix} = \begin{pmatrix} 1 & \alpha_{12} & \alpha_{13} \\ 0 & 1 & 0 \\ \alpha_{31} & \alpha_{32} & 1 \end{pmatrix} \begin{pmatrix} V_{P1} \\ V_{B12} \\ V_{P2} \end{pmatrix} \quad (2.1)$$

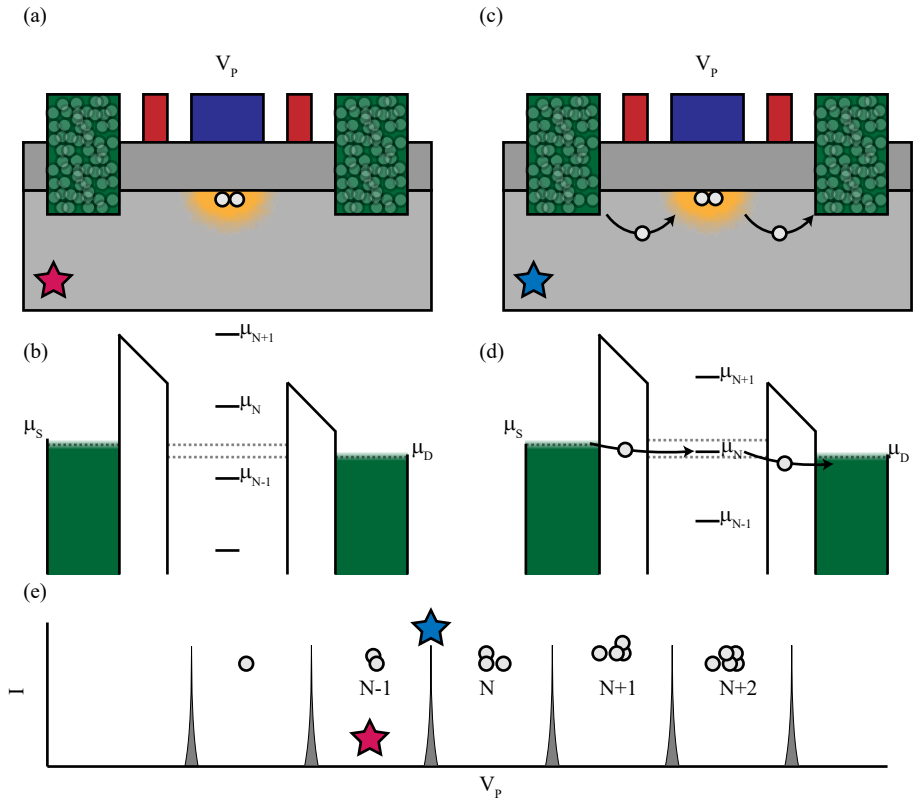


Figure 2.4: **Quantum dot energy levels and transport.** Green indicates a reservoir that is tunnel coupled to the quantum dot defined under the plunger gate (blue). Two reservoirs exist on the left and right of the quantum dot, called source and drain respectively. The source and drain leads are biased such that $\mu_S > \mu_D$ promoting current flow between the leads if Coulomb blockade is lifted. Left panels indicate a state of Coulomb blockade, where current cannot flow between the source-drain leads since no states exist within the source-drain bias window. When the plunger gate is tuned slightly, the energy level μ_N can be brought into the bias window permitting current to flow. This happens at regularly spaced peaks in energy based on the addition energy of the quantum dot and the lever arm of the plunger gate.

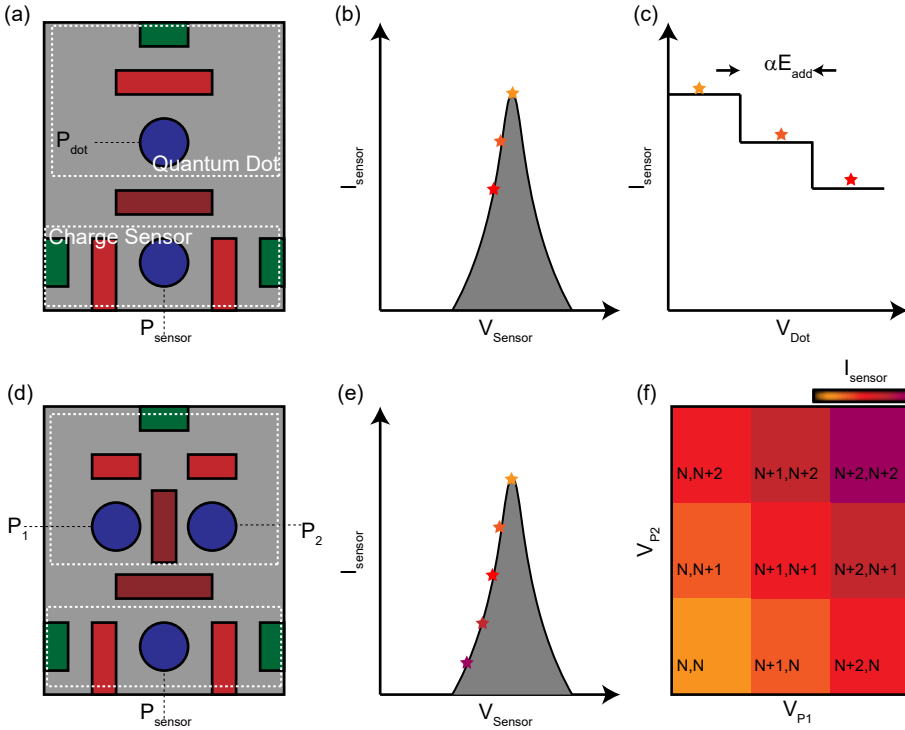


Figure 2.5: **Charge sensing in single- and double- quantum dots.** (a,b,c) correspond to a charge sensor sensing the charge occupation of a single quantum dot. The chemical potential of sensor μ_{sensor} and dot μ_{dot} are controlled by V_{sensor} and V_{dot} respectively. The charge sensor is capacitively coupled to quantum dot, such that μ_{sensor} depends on the charge occupation of the quantum dot. We assume system is tuned such that there are N charges in the quantum dot, and that the charge sensor current is maximised on top of a Coulomb peak (yellow star). Changes in the voltage on an increase in V_{dot} of more than αE_{add} where α is the plunger-dot lever arm and E_{add} is the addition energy of then quantum dot, will result in a change in the quantum dot occupancy. Via capacitive coupling, this will affect μ_{sensor} and a different current will flow (orange star). Therefore, sensor current corresponds to a direct measure of charge occupancy. (d,e,f) show the case where a sensor senses two dots. Here, one plunger for each dot is used to control the chemical potentials. A two-dimensional sweep of the plunger gates results in a pattern of many different currents passing through the dot, corresponding to different charge occupancy's.

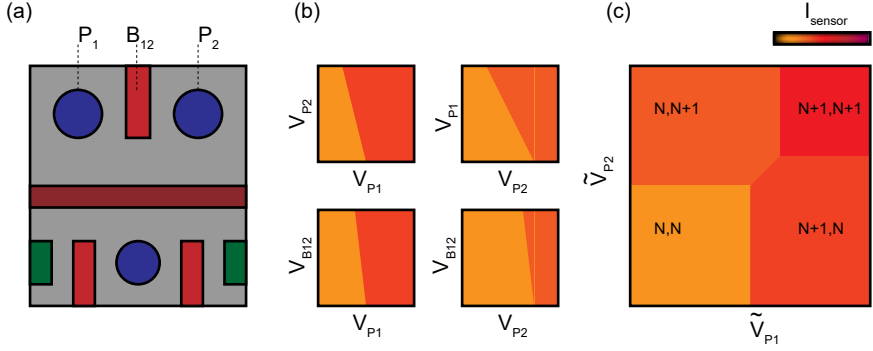


Figure 2.6: **Virtual gate matrices.** (a) Double dot system defined by voltages on real gates V_{P1} , V_{P2} , V_{B12} . Charge state of the double dot system is determined by the charge sensor below. (b) Tracking the shift in energy of a charge transition under P1 (left) or P2 (right) as a function of other gates in the system. (c) Charge stability diagram sweeping the virtual plungers \tilde{V}_{P1} and \tilde{V}_{P2} .

where $\alpha_{ij} = \delta V_j / \delta V_i$ is the change in voltage of the charge transition under real gate i due to a change of V_j on real gate j . The diagonals of this matrix are of course unity, and the entries for the barrier gates are set to zero, since there is (hopefully) not a quantum dot under these gates. Constructing a charge stability diagram by sweeping virtual gates \tilde{V}_{P1} and \tilde{V}_{P2} instead, would yield the charge stability diagram in Fig 2.6c, where the virtual gates have influence on the chemical potential only of their respective quantum dots. It is common practice to define charge transitions with respect to a different virtual gate space, called detuning-energy ($\epsilon - U$) space. For a given double-dot system containing a set number of charges n , one can define a detuning axis perpendicular to the charge anticrossings such that varying the detuning (effectively creating a difference in real plunger gate voltages up to a lever arm) results in different distributions of the n charges amongst the quantum dots. U can then be thought of as the chemical potential of the quantum dot. Figure 2.7a shows charge stability diagrams in the two different virtual gate spaces.

Quantum dots can couple, such that they mutually effect their energies. Notice that a change in charge occupation results in a slight shift in the charge transition (See Fig. 2.6c). This is due to the additional mutual capacitance that exists between the dots themselves, hence the dots are capacitively coupled together. Another form of coupling between dots is called tunnel coupling, which is related to the overlap of wavefunction of adjacent quantum dots, leading to tunneling of charges between dots. The quantum dot device in figure 2.6a has a barrier gate B₁₂, which is intended to control the tunnel coupling between quantum dots. With energy, detuning, charge occupation and tunnel coupling defined, qualitatively, we can model and simulate simplistic multi-quantum dot systems. Consider a double quantum dot system such as the one in figure 2.6a. If we assume charge occupation is the only important quantum number, then the eigenstates of such a system will be $\sum_{i,j} |n_i, n_j\rangle$ where $n_{i,j} \in \mathbb{N}$ represents the number of charges on a quantum dot. The Hamiltonian describing the system can be written in terms of an on-site energy H_E , an inter-dot coupling Hamiltonian H_t , an internal Coloumb repulsion term H_U and an inter-dot Coloumb repulsion term H_V [8].

$$H = H_E + H_t + H_U + H_V = \sum_i \epsilon_i \hat{n}_i - \sum_{i \neq j} t_{ij} (\hat{c}_i^\dagger \hat{c}_j + h.c.) + \sum_i \frac{U_i}{2} \hat{n}_i (\hat{n}_i - 1) + \sum_{i \neq j} V_{ij} \hat{n}_i \hat{n}_j \quad (2.2)$$

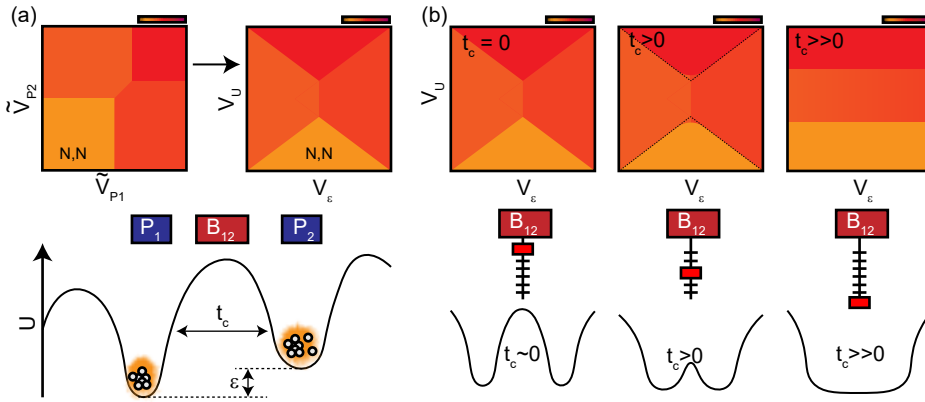


Figure 2.7: **Detuning-Energy Virtual Gates and Tunnel Coupling.** (a) Conversion from virtual plunger gate space to energy-detuning space. In the latter, the detuning axis V_e represents the skew in chemical potentials of the two dots, which is related to the difference in plunger gate voltages. The energy axis V_U represents the eigenenergies of the charge occupation levels of the system. (b) Tunnel coupling and its effect on the charge stability diagrams. In the limit of zero tunnel coupling, the barrier between quantum dots is high, and so there is no mixing of energy levels near the charge anticrossing resulting in rigid charge transition lines. For moderate tunnel coupling, the barrier is lowered and state mixing occurs, resulting in bending of the charge transition lines near the anticrossing. In the limit of high tunnel coupling, an effective single quantum dot is formed.

where \hat{n}_i is the number operator on the i 'th quantum dot ($\hat{n}_i |n_i, n_j\rangle = n_i |n_i, n_j\rangle$), \hat{c} and \hat{c}^\dagger are the annihilation and creation operators, U_i sets the strength of the internal Coloumb repulsion of the i 'th quantum dot, and V_{ij} sets the strength of the inter-dot Coloumb repulsion between the i 'th and j 'th quantum dots.

We have now derived the Hamiltonian for a system of quantum dots, filled with charges. This is sufficient to build a first-order intuition about the dynamics of quantum dots, but does not provide us with a useful qubit in which to perform quantum computation. The two-level quantum system that we will actually define the quantum information in, will be encoded in the spin quantum number of the charges contained within the quantum dot.

2.3. SPIN QUBITS

According to classical electrodynamics, a spinning charged body will generate a magnetic field similar to a bar magnet, depending on its angular momentum. This analogy is illustrative for quantum mechanics, where an electron in a quantum dot can be described by its spin quantum number. In this section, we examine two level spin-1/2 systems, which constitute the basic building blocks for the qubit implementations in this thesis. A spin-1/2 system, has two eigenstates, commonly referred to as spin-down $|\downarrow\rangle$ and spin-up $|\uparrow\rangle$. We can therefore represent the state of a spin qubit as

$$|\Psi\rangle = \alpha |\downarrow\rangle + \beta |\uparrow\rangle = \begin{pmatrix} \alpha \\ \beta \end{pmatrix} \quad (2.3)$$

with $\alpha, \beta \in \mathbb{C}$ and $|\alpha|^2 + |\beta|^2 = 1$.

2.3.1. ZEEMAN SPLITTING

When a magnetic dipole $\mathbf{M} = \frac{g}{2m}\mathbf{L}$ is placed in an external magnetic field \mathbf{B} , it forms a system with energy $E = -\mathbf{M} \cdot \mathbf{B}$. Spin-1/2 systems are magnetic dipoles, with angular momentum $S_z = \frac{\hbar}{2}\sigma_z$, and thus their energy states can be written analogously, as

$$E = \frac{g\mu_B}{\hbar}\mathbf{S} \cdot \mathbf{B} \quad (2.4)$$

where g is the gyromagnetic ratio of the spin (here assumed to be spatially isotropic), μ_B is the Bohr magneton and \hbar is the reduced Plank's constant. In general, the gyromagnetic ratio is not isotropic in all directions, and is better represented by a g -tensor $\overleftrightarrow{g} = \text{diag}(g_x, g_y, g_z)$, such that equation 2.4 can be rewritten more generally as

$$E = \frac{\mu_B}{\hbar}\mathbf{S} \cdot \overleftrightarrow{g} \cdot \mathbf{B} \quad (2.5)$$

If we now (without loss of generality) assume a magnetic field is applied in the \hat{z} direction, the dot product between magnetic field and spin simplifies, resulting in two energy eigenstates from the two allowed spin angular momenta. The difference in energy between these eigenstates is called the *Zeeman energy*. We can write down a Hamiltonian for the spin-1/2 system in an external magnetic field, as

$$H_Z = \frac{g_z\mu_B B_z}{2}\sigma_z. \quad (2.6)$$

2.3.2. LAMOR PRECISSION

If we consider the case where the spin vector is not perfectly aligned to the external magnetic field, for example a system prepared in the state $|\psi_0\rangle = 1/\sqrt{2}(|\uparrow\rangle + |\downarrow\rangle)$, ie. the cardinal \hat{x} -axis on equator of the Bloch sphere, then the time evolution of the system will be given by $|\psi(t)\rangle = \exp[iH_Z t/\hbar]|\psi_0\rangle$. If, for example, we examine the behaviour of the projection of the S_x spin component, evaluating $\langle S_x \rangle = \langle \psi(t) | S_x | \psi(t) \rangle$, we will observe oscillatory behaviour, according to

$$\langle S_x \rangle = \frac{\hbar}{2} \cos\left(\frac{g_z\mu_B B_z}{\hbar} t\right) \quad (2.7)$$

indicating that the spin vector will precess with a frequency

$$\omega_z = \frac{g_z\mu_B B_z}{\hbar} \quad (2.8)$$

known as the *Lamor precession frequency* [9]. Note that in the case that the system was prepared in an eigenstate, the spin would still precess at this frequency, however there would be no change to the spin observables as time evolves.

2.3.3. QUBIT STATE MANIPULATION

Rotations between the $|\downarrow\rangle$ and $|\uparrow\rangle$ eigenstates of the qubit can be performed by applying an oscillating magnetic field at the resonance frequency of the qubits, perpendicular to the stationary Zeeman field. The driving Hamiltonian H_{AC} can be written in terms of a AC magnetic field of strength B_{AC} applied in the \hat{x} axis of the Bloch sphere

$$H_{AC} = \frac{\mu_B}{2} \begin{pmatrix} 0 & g_x B_{AC} \left((A_{IQ})e^{-i\omega_a t} + (A_{IQ}^*)e^{i\omega_a t} \right) \\ g_x B_{AC} \left((A_{IQ})e^{-i\omega_a t} + (A_{IQ}^*)e^{i\omega_a t} \right) & 0 \end{pmatrix} \quad (2.9)$$

where ω_a is the applied microwave frequency, and $A_{IQ} = I + iQ$ represents the composition of in-phase (I) and quadrature (Q) components of the microwave signal. The total Hamiltonian of the driven system $H = H_Z + H_{AC}$, for magnetic field $\mathbf{B} = (B_{AC}, 0, B_z)$ becomes

$$H = \frac{\mu_B}{2} \begin{pmatrix} g_z B_z & g_x B_{AC} \left((A_{IQ})e^{-i\omega_a t} + (A_{IQ}^*)e^{i\omega_a t} \right) \\ g_x B_{AC} \left((A_{IQ})e^{-i\omega_a t} + (A_{IQ}^*)e^{i\omega_a t} \right) & g_z B_z \end{pmatrix} \quad (2.10)$$

In its current form, this Hamiltonian describes the qubit's state in the lab frame, meaning its dynamics are seen as a spin vector is precessing around the externally applied magnetic field while rotating between eigenstates as a result of an AC magnetic field. This is inconvenient to visualise and treat mathematically. Therefore, to analyze qubit dynamics, it is prudent to transform this Hamiltonian to a rotating frame describing the interaction between the qubit and microwave field, but not the spin precession. This is done through a transformation $H_{RF} = U H U^\dagger - i\hbar \frac{\partial U}{\partial t} U^\dagger$ giving a rotating frame Hamiltonian

$$H_{RF} = \frac{\hbar}{2} \begin{pmatrix} \omega_z - \omega_a & \omega_x (A_{IQ}^*) + \omega_x (A_{IQ}) e^{-2i\omega_a t} \\ \omega_x (A_{IQ}) + \omega_x (A_{IQ}^*) e^{2i\omega_a t} & -\omega_z + \omega_a \end{pmatrix}. \quad (2.11)$$

Here, $U = e^{iH_Z t/\hbar}$ is the time evolution unitary of the stationary Hamiltonian, and $\omega_{x(y)} = g_{x(y)} \mu_B B_{x(y)} / \hbar$. Since the terms $e^{\pm 2i\omega_a t}$ are fast oscillations, they will time-average out to zero over meaningful operation timescales. Discarding these terms is called the Rotating Wave Approximation (RWA) [10] and gives a final Hamiltonian

$$H = \frac{\hbar}{2} \begin{pmatrix} \omega_z - \omega_a & \omega_x (A_{IQ}^*) \\ \omega_x (A_{IQ}) & \omega_a - \omega_z \end{pmatrix}. \quad (2.12)$$

It is not difficult to see how this Hamiltonian then decomposes into its respective Pauli operators. Clearly by choosing $I = 1$ and $Q = 0$ for the microwave, we will rotate the qubit state around the \hat{x} -axis of the Bloch sphere, and by choosing $I = 0$ and $Q = 1$, we will perform \hat{y} -axis rotations, providing us with a complete set of single qubit operations.

The time evolution of this Hamiltonian (assume $I = 1$, $Q = 0$) acting on an initial state $|\psi_0\rangle$ then gives the system dynamics of a spin-1/2 particle in a magnetic field, being driven by an oscillating magnetic field

$$|\psi(t)\rangle = U^\dagger \exp\left\{-\frac{iHt}{\hbar}\right\} U |\psi_0\rangle \quad (2.13)$$

For the example of an initial state $|\psi_0\rangle = |\uparrow\rangle$, we can find the spin-up probability $p_\uparrow = \langle \uparrow | \psi(t) \rangle$ to be

$$p_\uparrow = \frac{\omega_x^2}{\omega_x^2 + (\omega_a - \omega_z)^2} \sin^2\left(\frac{\sqrt{\omega_x^2 + (\omega_a - \omega_z)^2}}{2\hbar} t\right). \quad (2.14)$$

The quantity $\omega_a - \omega_z$ is called the *detuning*, and represents how far from resonance the driving microwave field is from the Larmor precession of the qubit. The oscillatory evolution of a qubit state due to a driving field is called a *Rabi oscillation*. We can see the effect of the detuning of a driving pulse on the quantum state evolution of a qubit in Figure 2.8.

2.3.4. EXCHANGE INTERACTION

We have now seen how a single spin qubit can be manipulated, using an AC-magnetic field. In order to perform two-qubit gates, spin qubits need a form of coupling such that their states can be come entangled. This occurs natively as a result of the *exchange interaction*, which manifests

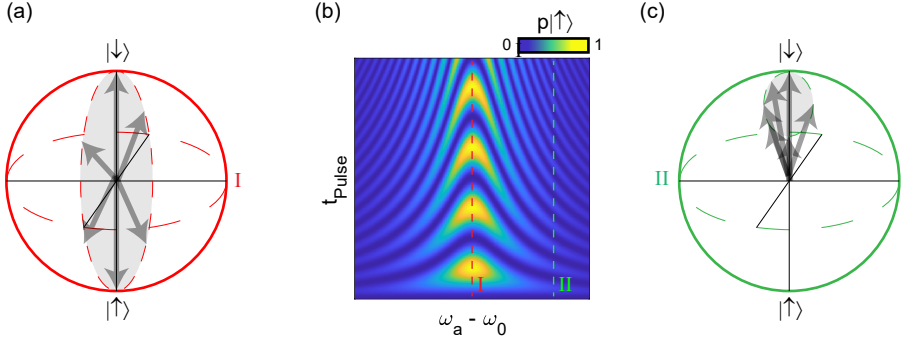


Figure 2.8: **Rabi Rotations of a Spin Qubit.** (a) and (c) Correspond to specific cases where the detuning frequency is zero, and non-zero respectively. In the former case, perfect oscillations between the north and south poles of the Bloch sphere occur at the Rabi speed. In the latter case, the detuned microwave frequency causes faster rotations between the initial state and the final state, which is no longer the $|\uparrow\rangle$ state. (b) Rabi Chevron patterns, showing the behavior of the qubit state for a driving pulse time t , and a detuning $\omega_a - \omega_z$.

due to the indistinguishability of electrons. An effective exchange interaction arises in double quantum dot systems due to the coupling between the singlet states. To illustrate this, consider the the Fermi-Hubbard model (See equation 2.2, but add spin to the summation of on-site energy) for a double quantum dot occupied by two spins. Without considering orbital states, the relevant basis states are given by $\{|\downarrow\downarrow\rangle, |\downarrow\uparrow\rangle, |\uparrow\downarrow\rangle, |\uparrow\uparrow\rangle, |S(2,0)\rangle, |S(0,2)\rangle\}$. For an on-site interaction energy U , energy detuning ϵ with respect to the (1,1) and (0,2) charge anticrossings (see section 2.2.3), and tunnel coupling t_0 , we can write the 6x6 Hamiltonian as [11]

$$H = \begin{pmatrix} \frac{E_1+E_2}{2} & 0 & 0 & 0 & 0 & 0 \\ 0 & \frac{E_1-E_2}{2} & 0 & 0 & t_0 & t_0 \\ 0 & 0 & \frac{E_2-E_1}{2} & 0 & -t_0 & -t_0 \\ 0 & 0 & 0 & -\frac{E_1+E_2}{2} & 0 & 0 \\ 0 & t_0 & -t_0 & 0 & U-\epsilon & 0 \\ 0 & t_0 & -t_0 & 0 & 0 & U+\epsilon \end{pmatrix}. \quad (2.15)$$

where $E_{1(2)}$ is the Zeeman energy of the qubit in the left(right) quantum dot. This Hamiltonian can be rebroadcast into one that only considers effective interactions between the lowest four energy eigenstates, assuming that $U \pm \epsilon > t_0 > 0$. This is done via a Schreiffer-Wolf transformation [12, 13], and yields an effective Hamiltonian in the two qubit subspace $\{|\downarrow\downarrow\rangle, |\downarrow\uparrow\rangle, |\uparrow\downarrow\rangle, |\uparrow\uparrow\rangle\}$ [11, 14]

$$H = \begin{pmatrix} \frac{E_1+E_2}{2} & 0 & 0 & 0 \\ 0 & \frac{E_1-E_2}{2} - \frac{J}{2} & \frac{J}{2} & 0 \\ 0 & \frac{J}{2} & \frac{E_2-E_1}{2} - \frac{J}{2} & 0 \\ 0 & 0 & 0 & -\frac{E_1+E_2}{2} \end{pmatrix} \quad (2.16)$$

where J is the effective exchange interaction, defined as

$$J = \frac{t_0^2}{U-\epsilon+(E_1-E_2)/2} + \frac{t_0^2}{U+\epsilon+(E_2-E_1)/2}. \quad (2.17)$$

Controlling J in this Hamiltonian is integral to designing two-qubit gate operations.

2.3.5. TWO-QUBIT EXCHANGE GATES

There are three main two-qubit gates based on the exchange interaction, that occur in different regimes of exchange interaction strength J compared to Zeeman energy difference $\Delta E_z = |E_1 - E_2|$. In the limit of high exchange such that $J/\Delta E_z \gg 1$, one can approximate the Hamiltonian using the anti-parallel spin states such that

$$H = \begin{pmatrix} -J/2 & J/2 \\ J/2 & -J/2 \end{pmatrix} \quad (2.18)$$

Therefore, by turning on the exchange interaction, the qubits will exchange states at a rate exactly dictated by the size of J . If one pulses the exchange for a time $t = 1/(2J)$, a $\sqrt{\text{SWAP}}$ gate will occur, which is a universal two-qubit gate. Depending on the achievable exchange interaction, SWAP gates can be executed in very fast times. One problem with SWAP style gates however, is that any finite Zeeman energy difference between qubits will result in an imperfect state exchange, which limits the achievable accuracy. One can overcome this in two ways. The first is to perform a SWAP gate by pulsing the exchange between the two qubits at their Zeeman energy difference frequency, cancelling unwanted rotations due to a finite Zeeman energy difference. This is called a *resonant SWAP* gate [15]. Alternatively, composite pulses can be constructed with timing considerations that overcome these issues [16].

A second type of two-qubit exchange gate, is the controlled-phase gate (C-Phase), which occurs in the regime where $J/\Delta E_z \ll 1$. In this regime, the anti-parallel spin states will acquire phase at a different rate, relative to the parallel spin states. The unitary describing a C-Phase gate is

$$U_{\text{CPHASE}} = \begin{pmatrix} 1 & 0 & 0 & 0 \\ 0 & 1 & 0 & 0 \\ 0 & 0 & 1 & 0 \\ 0 & 0 & 0 & e^{i\phi} \end{pmatrix} \quad (2.19)$$

By timing the phase accumulation such that $\phi = \pi$, the gate will perform a controlled-Z rotation, another universal two-qubit gate. CZ-gates can also be performed in very fast times, and have been shown with fidelities above 99% [17]. Errors from residual exchange can result in unwanted SWAP oscillations, however these can either be mitigated by ensuring constant adiabaticity when pulsing J , or by timing the gate with the periodicity of the SWAP oscillation.

The final two-qubit exchange gate is known as a controlled rotation (CROT) gate. It occurs since increasing the exchange interaction between two qubits, lowers the anti-parallel state energies without lowering the parallel state energies, resulting in a splitting of each qubit's resonance frequency, dependent on the state of the other.

$$f_{|\downarrow\downarrow\rangle \rightarrow |\uparrow\downarrow\rangle} = \bar{E}_z - \sqrt{J^2 + \Delta E_z^2}/2 - J/2 \quad (2.20)$$

$$f_{|\uparrow\uparrow\rangle \rightarrow |\uparrow\uparrow\rangle} = \bar{E}_z - \sqrt{J^2 + \Delta E_z^2}/2 + J/2 \quad (2.21)$$

$$f_{|\downarrow\downarrow\rangle \rightarrow |\downarrow\downarrow\rangle} = \bar{E}_z + \sqrt{J^2 + \Delta E_z^2}/2 - J/2 \quad (2.22)$$

$$f_{|\uparrow\uparrow\rangle \rightarrow |\uparrow\uparrow\rangle} = \bar{E}_z + \sqrt{J^2 + \Delta E_z^2}/2 + J/2 \quad (2.23)$$

where $\bar{E}_z = (E_1 + E_2)/2$. Due to the frequency differences, controlled rotations can be performed on one qubit based on the states of the others. Controlled rotations have two main challenges. The first is the achievable driving speed, which is limited by the single qubit gate rotations speed. This speed is not necessarily low, however gates whose speed is based on the size of the exchange

interaction like SWAP and CZ gates are typically much faster. The second challenge is that since CROT's are typically performed in the low-exchange regime, the gates must be carefully shaped such that cross-talk effects are taken into account to prevent unwanted transitions between other states. Fidelities as high as 98% have been reported for controlled rotation gates in silicon MOS [18], and above 99% in Si/SiGe [19].

2.3.6. SPIN READOUT

With the concepts of two-level spin systems and of quantum dots under our belts, we can now address an important requirement in building a quantum computer: readout. Readout is the final operation performed on a quantum computer, whereby a qubit state is measured, collapsing the wavefunction of the quantum state after computation. In order to read out the spin state of a qubit in a quantum dot, one must somehow map the spin degree of freedom onto a charge state, such that the readout signal is large enough. We do this since the magnetic moment of a spin is typically much too small to measure directly. Instead, the process of *spin-to-charge conversion* allows readout of a charge state via a charge sensor or reflected phase of a microwave signal [20].

There are two main types of spin-to-charge conversion for semiconductor spin qubits. The first is known as Elzermann readout, and involves spin selective tunnelling of a charge between a quantum dot and a reservoir [21]. Here, the Zeeman energy splitting of a qubit's spin states are tuned such that they straddle the Fermi-level of a nearby reservoir. In this way, during readout, a spin up state will tunnel from the dot into the reservoir, resulting in a jump in the sensor current. After some time, a spin down state will tunnel back into the dot, causing the current to change back. This process is summarised in figure 2.9a. The deterministic filling of a spin-down state also provides a useful initialization mechanism for the qubit. Elzermann readout has been used extensively in early spin qubit experiments [22–24], however it has some major pitfalls. Firstly, it relies on large Zeeman splittings. If this is not possible for reasonable magnetic field strengths, then there will be readout errors. Additionally, the unloading and loading occurs at a random time, placing constraints on readout bandwidth. Finally, the reservoir must be close to zero-temperature, or the thermal broadening of the Fermi-energy will also lead to readout errors. This makes it an incompatible strategy for high temperature qubit operation [25], and therefore we will examine an alternative readout method.

The Pauli exclusion principle prevents two fermions from existing with the exact same quantum numbers. In a quantum dot, two spins cannot occupy the same quantum dot ground state if they share the same spin. This facilitates a spin-to-charge conversion technique called *Pauli spin blockade* (PSB). In PSB, a spin state in one quantum dot is read out using the spin state of another quantum dot. The term *measurement qubit* refers to the qubit whose state we want to read out, and the term *helper qubit* refers to the qubit whose state is used for readout. Typically, we know what the helper qubit spin state is prior to measurement, allowing for direct readout of the measurement qubit. To illustrate PSB, consider a quantum double dot system, where a single spin qubit defined in a quantum dot has completed some arbitrary quantum operation, and is now ready for measurement. The helper qubit is known to be in the spin down state. By tilting the detuning between the two quantum dots such that it becomes energetically favorable for two-electrons to exist in the helper quantum dot, the measurement qubit will tunnel in only if it was in the spin up state, since two spin down states are not permitted to co-exist in the same quantum dot. The current detected by the charge sensor will therefore either detect a (2,0) configuration ($I_{\text{Unblocked}}$) or a (1,1) configuration (I_{Blocked}). Figure 2.9b summarises the PSB protocol.

The above examples have been presented in a (mostly) platform agnostic way. In other words,

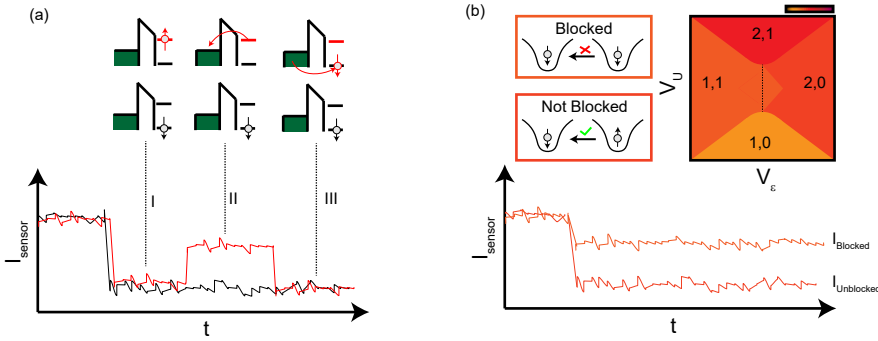


Figure 2.9: **Spin-to-charge conversion of a spin qubit.** (a) Elzerman readout. Spin state energy levels are tuned such that they straddle the Fermi level of a reservoir. Only a spin up state can tunnel into the reservoir (red trace), resulting in a sensor signal. A spin down qubit can then tunnel back into the quantum dot, resulting in a sensor change, and a spin down initialization of the qubit. Spin down qubits cannot tunnel into the reservoir as there are no free states below its chemical potential (black trace), therefore no current change occurs in the sensor. (b) Pauli Spin Blockade readout. An helper qubit (left dot) is used to read out the spin state of a measurement qubit (right dot). Preparing the helper qubit in a spin down state allows spin selective tunnelling from the measurement dot to the helper dot, based on the measurement qubit's state. Choosing a readout point in the spin blockade window (triangle in the CSD), one can observe a difference in current response when the measurement qubit is spin up or spin down. Note that sensor currents in (a) and (b) are only sketches, and are not real or simulated data.

we are yet to apply our concept of spin qubits to the case of electrons in silicon, or holes in germanium. Therefore, the current discussion will shift gears to talk about the In the following sections, we examine the specific physics of both electrons in silicon, and holes in germanium.

2.4. ELECTRON SPIN QUBITS IN SILICON QUANTUM DOTS

The electron is a fundamental, negatively charged particle. It is also a spin-1/2 particle, making it a logical qubit candidate. It is also therefore crucial to quantum computation, that an electron's spin degree of freedom exists in an environment where unwanted interactions are minimized. Silicon, in contrast to group III-V materials like GaAs, contains a low abundance of spin non-zero nuclei, making it an attractive candidate for quantum computation. Additionally, silicon can be isotopically purified [26], effectively eliminating unwanted interactions between nuclear and electron spins. The utilization of isotopically purified silicon as a host for electron spin qubits substantially improved the time for which quantum information can be stored [22, 27], and has therefore drastically increased the platforms viability. Improvements in the quality of the silicon-oxide [28], and material growth have also led to a very quiet environment in which to host qubits, earning the Si-MOS platform the prestigious title of 'the semiconductor vacuum' [29].

2.4.1. VALLEY SPLITTING

In order to understand the behaviour of electron spin qubits in silicon quantum dots, we can begin by examining the band structure of silicon. The conduction band of silicon contains a minimum about 85 % along the energy dispersion line between the Γ -point and X -point [30]. In the case of an electron in bulk silicon, this minimum, called a valley, will occur at the same energy for each cardinal axis in momentum space, leading to a six-fold degenerate energy spectrum (Figure 2.10b

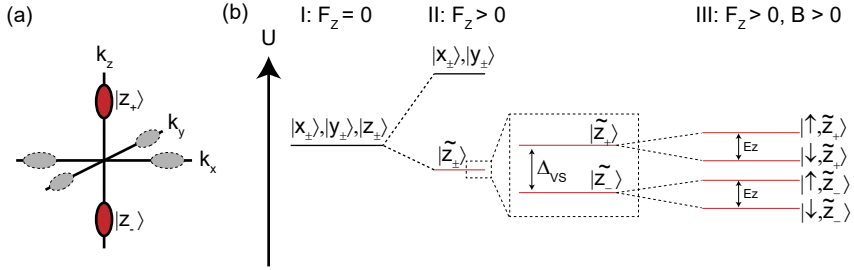


Figure 2.10: **Energy structure of Silicon quantum dots due to valleys.** (a) Conduction band electrons in the silicon bulk experience an energy minima in each direction in k -space between the Γ -point and X -point [30]. (b) I: A 6-fold valley degeneracy exists for conduction band electrons in bulk silicon. II: the application of an electric field in the out-of-plane \hat{z} direction results in the splitting of this degeneracy into two-lower lying \hat{z} valleys and four degenerate states in the in-plane directions at much higher energies [31]. These two lower lying valley states are mixed by the strong interface confinement, resulting in new eigenstates $|\tilde{z}_{\pm}\rangle$ split by an energy Δ_{VS} called the valley splitting [32]. III: The application of a magnetic field results in the lifting of spin degeneracy, resulting in four lowest energy eigenstates, the lowest two of which, $|\downarrow, \tilde{z}_{-}\rangle$ and $|\uparrow, \tilde{z}_{-}\rangle$, we use qubit encoding.

I) [30]. When we confine an electron at an interface to form a quantum dot with an electric field F_z in the \hat{z} direction, the electron will experience a much higher effective mass in the confinement direction than within the plane of the quantum well, splitting the degeneracy into a four-fold degeneracy containing the four $(\pm k_x, \pm k_y)$ valleys with a high energy, leaving the two lowest energy valleys in the \hat{k}_z direction [31] (Figure 2.10b II). The presence of an electric field also results in the mixture of these valleys, such that their eigenstates are combinations of the bulk $|z_{\pm}\rangle$ valleys [33]. These lower two valley eigenstates $|\tilde{z}_{\pm}\rangle$ are split by an energy gap Δ_{VS} , called the *valley splitting*. In SiMOS and Si/SiGe platforms the singular nature of the interfaces at which electrons are confined has a major impact on the size of Δ_{VS} [34]. The size of Δ_{VS} is typically between 0.03-0.3 meV in Si/SiGe[35, 36], and between about 0.1-1 meV in SiMOS [23, 37] with evidence of tuneability via electrostatic gates [23, 38]. These values are comparable to typical Zeeman energies of electron spins in silicon and as a result, strategies to deal with the valley states in silicon are integral to achieving good electron spin qubits.

Consider a single electron spin defined in a silicon quantum dot. The four lowest energy eigenstates will now be given by it's spin and valley degrees of freedom, such that $|1\rangle = |\downarrow, \tilde{z}_{-}\rangle$, $|2\rangle = |\uparrow, \tilde{z}_{-}\rangle$, $|3\rangle = |\downarrow, \tilde{z}_{+}\rangle$ and $|4\rangle = |\uparrow, \tilde{z}_{+}\rangle$. Opposite valley states can couple via the spin orbit interaction, such that the states [39]

$$|\tilde{2}\rangle = \left(\frac{1-a}{2}\right)^{1/2} |2\rangle - \left(\frac{1+a}{2}\right)^{1/2} |3\rangle, \quad (2.24)$$

$$|\tilde{3}\rangle = \left(\frac{1+a}{2}\right)^{1/2} |2\rangle + \left(\frac{1-a}{2}\right)^{1/2} |3\rangle \quad (2.25)$$

describe the energy eigenstates, where $a = -(\Delta_{VS} - \omega_Z) / \sqrt{(\Delta_{VS} - \omega_Z)^2 - \Delta^2}$ for coupling Δ and Zeeman energy ω_Z . Figure 2.11a shows how these four lowest energy spin-valley eigenstates behave as a function of magnetic field. We can see that above a critical magnetic field, the spin eigenstates no longer define the lowest energy eigenstates of the system. At magnetic fields close to this critical value, spin-valley mixing causes significantly enhanced spin relaxation times [39]. The

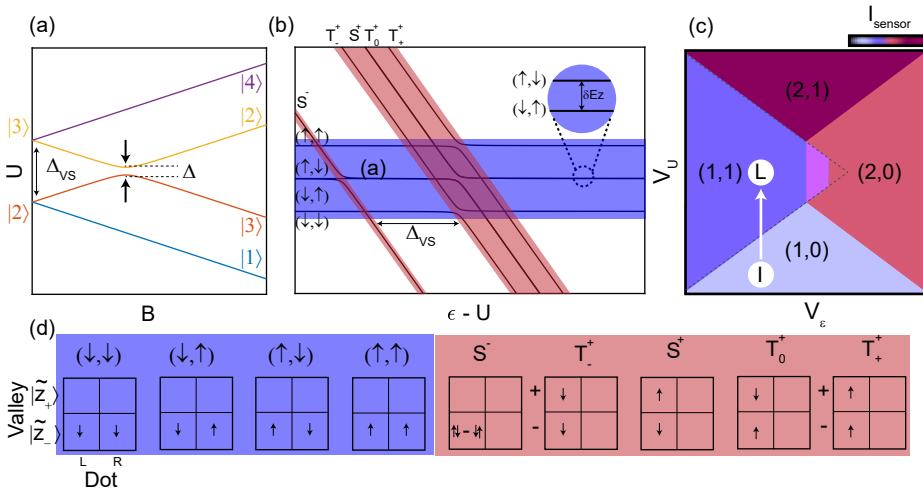


Figure 2.11: **Impact of valley splitting for electron spin qubits in silicon quantum dots.** (a) Four lowest energy levels of a single electron spin in a quantum dot as a function of applied magnetic field. |1>, |2>, |3>, and |4>, represent $|\downarrow, \bar{z}_-\rangle$, $|\uparrow, \bar{z}_-\rangle$, $|\downarrow, \bar{z}_+\rangle$, $|\uparrow, \bar{z}_+\rangle$ respectively. Spin-valley mixing can occur due to a finite spin-orbit interaction, leading to a coupling of size Δ at a critical magnetic field [38]. Above this magnetic field, the spin states no longer define the lowest energy qubit states. Additionally, close to this field, spin relaxation rates are rapidly enhanced [39]. (b) Valley splitting affects ability to read out a spin state. First nine energy levels of two electron spins in a quantum double dot system. Blue or red shading indicates a preferred (1,1) or (2,0) charge configuration respectively. Spin blockade readout is affected by the presence of Valley states as readout is only possible within the detuning window ϵ_{VS} before the first excited valley state T_{\pm}^{\pm} crosses the (1,1) state, resulting in ambiguity of spin state readout above this detuning value. [40] (c) Effect of valley splitting on spin readout at spin blockade enabled anticrossings. During a spin-blockade readout sequence, a random spin state is loaded into the left dot by moving from I to L. The right dot is initialized in the spin down state. The readout point is then swept across the parameter space shown in the charge stability diagram. Valley splitting truncates the readout window, limiting available readout parameter space, and affecting readout fidelity [39]. (d) Summary of state labelling for (b).

presence of valley states also affects Pauli Spin blockade readout. To illustrate this, we can simulate a double quantum dot system in silicon, with a total of two electrons. Here we simulate the first nine spin-valley eigenstates considering the (1,1)-(2,0) anticrossing. Figure 2.11b shows the resulting energy eigenstates as a function of detuning ϵ between the dots. The readout window for a spin blockade style measurement is limited to the detuning space ϵ_{VS} , between the lowest valley S_{20} and first excited valley T_- states. Figure 2.11c shows how a spin blockade readout sequence behaves as a result of valleys. The pulse sequence to produce such a measurement involves initialization of a spin down electron in the right dot, followed by the loading of a random spin in the left dot. The readout window is then swept and the resulting sensor current is recorded. The spin blockade window is truncated due to the valley splitting. This has the consequence of both reducing the parameter space in which one can read out spin states, and also reduces the fidelity of the readout itself. It is therefore crucial for electron spin qubits in silicon to achieve valley splittings significantly larger than the Zeeman energies of the qubits. Strategies to reliably increase valley splittings, particularly in the Si/SiGe platform have been investigated, including, as mentioned, electric tuning [23, 38], and by introducing small amounts of Ge into the quantum well, which has been shown to help increase valley splittings [41].

2.4.2. ELECTRON SPIN RESONANCE

Performing quantum gates on electron spin qubits relies on delivering oscillating magnetic fields perpendicular to the quantization axis. This can be achieved in different ways, however for now, we will examine the technique of electron spin resonance (ESR) since it is the spin driving technique used for all experiments in this thesis on electron spin qubits. ESR involves the delivery of an oscillating magnetic field to a qubit, by sending an AC-current through a nearby antenna. Achievable single qubit gate times using this method are typically on the order of 1 MHz, and very high control fidelities have been obtained [22]. From a device point of view, this antenna must dissipate minimal heat, therefore aluminium (Al), niobium titanium nitride (NbTiN), and other superconducting materials are usually chosen for its fabrication. Additionally, in order to minimize loss, it must be designed with impedance matching in mind, often resulting in large, bulky structures [42]. This means it is difficult to implement more than a single antennae in a device, which raises the concern of individual qubit addressability. Typically in SiMOS, variations in the Silicon-Oxide interface result in highly varying g-factors, and therefore individually addressable qubits. However in Si/SiGe, disorder is typically much lower, and qubit g-factors are closer. This problem can be mitigated by designing micro-magnets such that the Zeeman differences between qubits are enlarged, however the introduction of a spatially varying magnetic field enhances the coupling of charge noise to the qubit eigenstates, resulting in lower relaxation and coherence times. The use of micromagnets also permits the design of artificial spin-orbit coupling, that allows for electrical driving of the qubit using electric dipole spin resonance (EDSR). This technique will be expanded on when considering qubit manipulation using holes in germanium.

2.5. HOLE SPIN QUBITS IN GERMANIUM QUANTUM DOTS

When an electron in the valence band receives enough energy to excite to the conduction band of a semiconductor, it leaves behind a hole. Holes are pseudoparticles, that can be thought of as positively charged particles that can move throughout a semiconductor, and crucially, are suitable qubit candidates. Valence band holes exhibit p -like Bloch wave vectors, which is a consequence of their $l = 1$ azimuthal quantum number. This means that their wavefunctions have no overlap with nuclear sites in their host, eliminating the contact hyperfine contribution to dephasing (see section 2.5.4), but more importantly, facilitates a spin orbit coupling $\delta_{SO} \mathbf{L} \cdot \mathbf{S}$ between the spin $\hbar \mathbf{S}$ and orbital $\hbar \mathbf{L}$ angular momentum of the hole [43]. The following sections derive the properties of

hole spins in planar germanium quantum dots.

2.5.1. THE VALENCE BAND

The topmost valence band for bulk germanium would be six-fold degenerate at the Γ -point, in the absence of a spin-orbit interaction [44]. The presence of a spin-orbit interaction lifts these degeneracies, which is important for creating a well defined two-level spin system to use as a qubit. To derive the spin orbit effects, we therefore want to understand the effect of the spin orbit operator on the first valence band $\delta_{\text{SO}}\mathbf{L}\cdot\mathbf{S}|\Psi\rangle$. Spin orbit coupling results in a Hamiltonian that no longer commutes with \mathbf{S} or \mathbf{L} , which are therefore no longer good quantum numbers. The total angular momentum however, $\mathbf{J} = \mathbf{S} + \mathbf{L}$ is a good quantum number. We can take the square of \mathbf{J} , and rearrange to find that $\mathbf{L}\cdot\mathbf{S} = 1/2\mathbf{J}^2 - \mathbf{L}^2 - \mathbf{S}^2$. We know that $\mathbf{L}^2|\Psi\rangle = \hbar^2 l(l+1)|\Psi\rangle$, $\mathbf{S}^2|\Psi\rangle = \hbar^2 s(s+1)|\Psi\rangle$, and $\mathbf{J}^2|\Psi\rangle = \hbar^2 j(j+1)|\Psi\rangle$, leaving us with the expression

$$\delta_{\text{SO}}\mathbf{L}\cdot\mathbf{S}|\Psi\rangle = \frac{\hbar^2\delta_{\text{SO}}}{2}(j(j+1) - l(l+1) - s(s+1))|\Psi\rangle. \quad (2.26)$$

since m_s and m_l are not good quantum numbers, we cannot say anything about them, except that they can either be parallel or anti-parallel leading to $j = 1/2$ or $j = 3/2$. We can immediately assign $l = 1$ and $s = 1/2$ since these are properties of the band we are considering, allowing us to calculate the eigenenergies of the above equation as $\delta_{\text{SO}}/2$ for $j = 3/2$ and $-\delta_{\text{SO}}$ for $j = 1/2$. The projections of j therefore give rise to a four fold degenerate band at energy $\delta_{\text{SO}}/2$ and a two fold degenerate band at energy $-\delta_{\text{SO}}$. The difference in energy between these sets of bands is called the spin orbit gap $\Delta_0 = 3\delta_{\text{SO}}/2$, and is defined at the Γ -point, where $k_x = k_y = k_z = 0$ [45]. In germanium, $\Delta_0 \approx 0.3$ eV, which separates it sufficiently from the $j = 3/2$ bands.

The energy dispersion of these bands around the Γ -point can be modelled using a Luttinger-Kohn (LK) Hamiltonian [46]. The LK Hamiltonian in general can be applied to a multitude of semiconductors, however for semiconductors with high inversion symmetry, it can be written in a simplified way by making the spherical approximation according to the eigenstates $|m_j\rangle \in \{|-3/2\rangle, |-1/2\rangle, |1/2\rangle, |3/2\rangle\}$ [47]

$$H_{\text{LK}} = \begin{pmatrix} P+Q & L & M & 0 \\ L^* & P-Q & 0 & M \\ M^* & 0 & P-Q & -L \\ 0 & M^* & -L^* & P+Q \end{pmatrix} \quad (2.27)$$

where

$$P = -\frac{\hbar^2}{2m_0}\gamma_1 k^2 \quad (2.28)$$

$$Q = \frac{\hbar^2}{2m_0}\gamma_s(2k_z^2 - k_x^2 - k_y^2) \quad (2.29)$$

$$L = \frac{\hbar^2}{2m_0}2\sqrt{3}\gamma_s k_- k_z \quad (2.30)$$

$$M = \frac{\hbar^2}{2m_0}\sqrt{3}\gamma_s k_-^2 \quad (2.31)$$

with $k^2 = \mathbf{k}\cdot\mathbf{k}$ and \mathbf{k} the wave vector, m_0 the free electron mass, $k_{\pm} = k_x \pm ik_y$, and γ_1 and $\gamma_s = (2\gamma_2 + 3\gamma_3)/5$ the Luttinger parameters [48]. This hamiltonian yields two sets of two-fold degenerate eigenenergies, $E_{HH} = -\hbar^2 k^2/2m_{HH}$ and $E_{LH} = -\hbar^2 k^2/2m_{LH}$, belonging to the $|m_j\rangle = |\pm 3/2\rangle$ and $|m_j\rangle = |\pm 1/2\rangle$ eigenstates respectively, where $m_{HH} = m_0/(\gamma_1 - 2\gamma_s)$ and $m_{LH} = m_0/(\gamma_1 + 2\gamma_s)$.

The subscripts 'LH' and 'HH' stand for light hole and heavy hole respectively, and are labelled as such since the substitution of the relevant Luttinger parameters for Ge yield $m_{HH} = 0.33m_0$ and $m_{LH} = 0.04m_0$. We can immediately see that away from the Γ -point, the energy dispersion of these LH and HH bands will be different, though they remain degenerate at $|k| = 0$.

2

The system we have defined in the above scenario corresponds to hole states in the valence band, in germanium bulk. However the system we want knowledge about is how hole states behave in a quantum dot, specifically in a confinement potential and in the quantum well of a Ge/SiGe heterostructure. To begin, let's examine a hole confined in a hard wall potential, as might be expected at the interfaces of a quantum well. The strong confinement in the \hat{z} -direction leads to a quantization of momentum such that $k_z = \pi n/L_z$ where n corresponds to the excitation harmonic number, and L_z is the width of the quantum dot. We will introduce another assumption here, whereby the off-diagonal terms in equation 2.27 are negligible when considering the macroscopic energy dispersion of the heavy hole light hole bands near the Γ -point, which turns out to be a good approximation for quantum wells grown on the high symmetry [001] crystallographic axis [44, 45] as is the case for the quantum wells used throughout this thesis [49, 50]. As a result, the eigenenergies E_{HH} and E_{LH} are shifted to

$$E_{HH} = -\frac{\hbar^2}{2m_0} \left(k_{\parallel}^2 (\gamma_1 - 2\gamma_s) + \frac{n_{HH}\pi^2}{L_z^2} (\gamma_1 - 2\gamma_s) \right) \quad (2.32)$$

$$E_{LH} = -\frac{\hbar^2}{2m_0} \left(k_{\parallel}^2 (\gamma_1 + 2\gamma_s) + \frac{n_{LH}\pi^2}{L_z^2} (\gamma_1 + 2\gamma_s) \right) \quad (2.33)$$

where $k_{\parallel}^2 = \mathbf{k}_{\parallel} \cdot \mathbf{k}_{\parallel} = k_x^2 + k_y^2$, and we have approximated that the sub-band excitations in the confinement potential of the LH and HH states are not coupled such that they can be described by their own quantum numbers n_{LH} and n_{HH} respectively. The above equations have an important consequence for energy dispersion when considering the planar wavevectors \mathbf{k}_{\parallel} in that even at $\mathbf{k}_{\parallel} = (0, 0)$, there is an energy gap separating the LH and HH states of

$$\Delta_{LH,HH} = \frac{2\gamma_s \hbar^2 \pi^2}{m_0 L_z^2} \quad (2.34)$$

which therefore lifts the LH-HH degeneracy. This energy splitting is important for ensuring that the two-level quantum system is well defined and isolated from other states. A second interesting consequence is that re-evaluating the effective light hole and heavy hole masses yields in a somewhat confusing result in that $m_{HH} < m_{LH}$.

2.5.2. STRAIN

The sandwiching of a Germanium quantum well between two SiGe layers imparts a strain on the quantum well due to the slight lattice constant mismatch of the two different semiconductors. The degree of the lattice mismatch and therefore strain, is controlled by the relative composition x of Si and Ge in the $\text{Si}_x\text{Ge}_{1-x}$ layers. The effect of strain on energy dispersion relations requires additional treatment of the Hamiltonian that the previous LK Hamiltonian does not take into account. The strain tensor in a material in general a 3x3 matrix with elements ϵ_{ij} where $i, j \in \{x, y, z\}$ represent the cartesian coordinates. For the case of a strained, planar quantum well, the strain is uni-axial [49], allowing for a simplification of the tensor such that $\epsilon_{xx} = \epsilon_{yy}$, and off-diagonal elements vanish such that $\epsilon_{ij} = 0$ if $i \neq j$. Additionally, the strain quite small, and approximately linear, allowing one to write $\epsilon_{zz} = -2(C_{12}/C_{11})\epsilon_{xx}$ where $C_{11} = 129.2$ GPa and $C_{12} = 47.9$ GPa are stiffness coefficients in Ge [51]. The value of ϵ_{xx} is a function of the lattice mismatch, and can be

approximated $\epsilon_{xx} = (a(x) - a_0)/a_0$ where a_0 is the relaxed lattice constant of the Ge quantum well, and $a(x)$ is that of the $\text{Si}_x\text{Ge}_{1-x}$ layers [52].

In this form, the LK Hamiltonian can easily adapt for strain by adjusting augmenting the matrices [53]

$$P \rightarrow P + P_\epsilon \quad (2.35)$$

$$Q \rightarrow Q + Q_\epsilon \quad (2.36)$$

where

$$P_\epsilon = a_\nu (\epsilon_{xx} + \epsilon_{yy} + \epsilon_{zz}) \quad (2.37)$$

$$Q_\epsilon = b_\nu / 2 (\epsilon_{xx} + \epsilon_{yy} - 2\epsilon_{zz}) \quad (2.38)$$

with $a_\nu = 2.0$ eV and $b_\nu = -2.16$ eV are deformation potentials [54]. The value of $\epsilon_{xx} = -0.0063$ is used as it comes from calculations pertaining to the exact quantum wells used in this thesis [49]. The negative value of this strain indicates that it is compressive in the plane of the quantum well. It is immediately apparent that strain of this type will lead to a shift in E_{HH} upwards, and E_{LH} downwards, both of magnitude Q_ϵ . This increases the splitting of the two bands by $\Delta_{LH,HH}^\epsilon = 2Q_\epsilon \approx 49$ meV.

2.5.3. LIFTING SPIN DEGENERACY

At this point, we have a material platform that hosts a well defined, and well separated spin qubit, in the form of the heavy-hole bands. However, these bands are currently degenerate in spin and our model does not yet explain their behaviour when this degeneracy is lifted, let alone how to do this. A good starting point is to examine the spin orbit interaction and its effect on the spin states, particularly those corresponding to the heavy holes.

Spin orbit interaction can manifest in a quantum system that exhibits structural inversion asymmetry (SIA) or bulk inversion asymmetry (BIA) [45]. The latter effect describes lattices that are not the same under point reflection, for example zinc-blende structures like GaAs. Germanium however is symmetric under bulk inversion, and therefore does not exhibit a spin-orbit interaction due to BIA (called a Dresselhaus-type spin orbit interaction) [55]. SIA, however, can occur due to the confinement potential of the quantum well and the metallic gates used to define the quantum dot. This type of spin orbit interaction is called a Rashba spin orbit interaction [56], and acts on the heavy-hole spin manifold according to the Hamiltonian [57]

$$H_{R,SO} = i\alpha_1(k_+\sigma_+ - k_-\sigma_-) + i\alpha_2(k_+^3\sigma_- - k_-^3\sigma_+) + i\alpha_3(k_+\sigma_+ - k_-\sigma_-)k^2. \quad (2.39)$$

Here, $\sigma_\pm = \sigma_x \pm i\sigma_y$, and α_i are the i 'th order Rashba parameters that dictate the strength of the interaction due to various symmetries in H_{LK} . For crystals grown along the high symmetry axis, α_1 and α_3 are typically small compared to α_2 , when making the assumption that H_{LK} is effectively spherical in symmetry [47]. Thus the α_2 term is primarily responsible for lifting spin degeneracy within the heavy hole and light hole manifolds when considering their energy dispersion, in the absence of a magnetic field.

We now come to the behaviour of the spin eigenstates under an externally applied magnetic field. For holes in the upmost valence band, this is given by a Zeeman Hamiltonian of the form [48]

$$H_Z = -2\kappa\mu_B\mathbf{B} \cdot \mathbf{J} - 2q\mu_B\mathbf{B} \cdot \mathbf{J}^3 \quad (2.40)$$

where κ and q are Luttinger parameters. If we restrict ourselves to the case of heavy holes, then the above simplifies to

$$H_Z = -\left(3\kappa + \frac{27}{4}q\right)\mu_B B_z \sigma_z - \frac{3}{2}q\mu_B (B_x \sigma_x - B_y \sigma_y). \quad (2.41)$$

We can see immediately that the effect of an applied magnetic field will differ greatly depending on its orientation. For the in-plane directions, the effective g-factor is isotropic ($g_x = g_y = g_{\parallel} = 3q$). However out of plane, we have $g_z = g_{\perp} = 6\kappa + 13.5q$. Taking typical values of these Luttinger parameters, we find $g_{\parallel} \approx 0.2$ and $g_{\perp} \approx 21.4$ [58]. The experiments conducted on hole spin qubits in germanium in this thesis are performed using a (mostly) in plane magnetic field. In this case, the Zeeman splitting of the heavy hole-like states is perturbed by a spin-orbit term given by [59–61]

$$H_{SO,Z} = \frac{3\gamma_s \kappa \mu_B}{m_0 \Delta_{HH,LH}} \left(B_- k_-^2 \sigma_+ + B_+ k_+^2 \sigma_- \right) \quad (2.42)$$

where $B_{\pm} = B_x \pm iB_y$. Interestingly, the dependence of this term on $\Delta_{HH,LH}$, which depends on the confinement potential, results in an electrically-tuneable g-factor, a valuable tool when considering qubit addressability. However, the dependence of the eigenenergies of hole spin qubits on electric fields makes susceptible to charge noise, which turns out to be a major source of decoherence for the Ge/SiGe platform.

2.5.4. HYPERFINE INTERACTION

The spin and orbital angular momentum degrees of freedom in a hole qubit can interact directly with other spin and orbital degrees of freedom in their environment. Naturally, this process is integral to the operation of a quantum computer to generate entanglement or shuttle information etc. However, this process can also occur between spin systems in an undesirable way. In semiconductors, a major source of unwanted information loss occurs due to the presence of non-zero spin nuclear isotopes of the host material. This interaction between nuclear spins and qubits is called the Hyperfine interaction.

Semiconductor hosts such as GaAs have a 100% nuclear non-zero spin population, which makes storing quantum information a non-trivial matter. Group IV based platforms such as silicon and germanium however, have relatively low compositions of spin non-zero isotopes (in natural silicon, about 4.7 % and in natural germanium about 7.8 %). However, these populations still play a role in limiting coherence times of qubits defined in these platforms. The hyperfine interaction between a spin qubit (hole or electron) and a nuclear spin bath can be written down generally as

$$H_{Hf} = \sum_j A_k \mathbf{S} \cdot \mathbf{I}_k \quad (2.43)$$

where A_k is the hyperfine interaction strength between the hole and the k 'th nuclei in the bath, \mathbf{S} is the qubit spin and \mathbf{I}_k is the spin of the k 'th nucleus. The strength of this interaction A_k is material dependent, and also depends on the degrees of freedom available to the qubit. To illustrate this, we can write down the three separate hyperfine interaction mechanism Hamiltonians available to an electron or hole when coupling to the k 'th nuclear spin (assuming a single non-zero nuclear spin

species) [62]

$$h_1^k = \frac{\mu_0}{4\pi} \frac{8\pi}{3} \gamma_s \gamma_k \delta(\mathbf{r}_k) \mathbf{S} \cdot \mathbf{I}_k \quad (2.44)$$

$$h_2^k = \frac{\mu_0}{4\pi} \gamma_s \gamma_k \frac{3(\mathbf{n}_k \cdot \mathbf{S})(\mathbf{n}_k \cdot \mathbf{I}_k) - \mathbf{S} \cdot \mathbf{I}_k}{r_k^3(1 + d/r_k)} \quad (2.45)$$

$$h_3^k = \frac{\mu_0}{4\pi} \gamma_s \gamma_k \frac{\mathbf{L}_k \cdot \mathbf{I}_k}{r_k^3(1 + d/r_k)} \quad (2.46)$$

where $\gamma_s = 2\mu_B$, $\gamma_k = g_k\mu_N$, μ_B is the Bohr magneton, g_k is the nuclear g-factor, μ_N is the nuclear magneton, $\mathbf{r}_k = \mathbf{r} - \mathbf{R}_k$ is the electron-spin position operator relative to the nucleus, $d \approx Z \times 1.5 \times 10^{-15}$ m is a length describing nuclear dimensions, Z is the nuclear charge, $\mathbf{n}_k = \mathbf{r}_k/r_k$, and \mathbf{S} and $\mathbf{L}_k = \mathbf{r}_k \times \mathbf{p}$ are the spin and orbital angular momentum operators of the qubit respectively. These correspond respectively to a direct contact hyperfine interaction, a dipole-dipole type coupling, and a coupling of the orbital angular momentum of the qubit to the nuclear spin. In the case of an electron in the lowest conduction band, the spherical symmetry of the Bloch wavefunctions eliminates the possibility of a dipole-dipole like interaction, and since there is no orbital angular momentum, we have $h_2^k = h_3^k = 0$, such the the hyperfine interaction of electrons is purely due to the overlap of the qubit and nuclear wavefunctions. In the case of a hole, p-like symmetry results in nodes at nuclear spin sites such that $h_1^k = 0$, while the other two mechanisms are possible. The elimination of h_1^k type couplings have led to the prediction that the hyperfine interactions for hole spins will have negligible contributions. However the resulting terms as a direct consequence of Bloch wavefunctions with p-like symmetry still contribute non-negligibly. We can see that (following ref. [62]) the ratio of the hyperfine coupling strength for holes and electrons in a given material can be approximated by

$$\frac{A_h}{A_e} = \frac{1}{5} \left(\frac{Z_{\text{eff}}(\kappa, 4p)}{Z_{\text{eff}}(\kappa, 4s)} \right)^3 \quad (2.47)$$

where $Z_{\text{eff}}(\kappa, 4p(4s))$ describes the effective screening potential experienced by holes (electrons) in $4p(4s)$ atomic orbitals of nuclear species κ . Taking these values for the ^{73}Ge nuclear spin from ref. [63], we can see that $A_h/A_e \approx 0.12$. This indicates that while less, hyperfine coupling in hole spin qubits is still a relevant contribution to the noise processes inhibiting their operation.

Unlike electrons, the hyperfine interaction for holes can be highly anisotropic. The interaction of holes in the quasi-two dimensional limit (such as holes confined in quantum dots within a quantum well) takes on an Ising-like form

$$H_{Hf} = \sum_k A_k^h s_z I_k^z \quad (2.48)$$

Such that only the z-components of the hole and nuclear spins couple strongly. This anisotropy has some implications regarding optimal magnetic field alignment, since $A_{||} \ll A_{\perp}$, where perpendicular in this case indicates perpendicular to the plane of the quantum well. By aligning a magnetic field in plane, the strong out-of-plane hyperfine coupling term is suppressed due to the Ising like nature of H_{Hf} . This is investigated in length in Chapter 11.

The non-zero nuclear spin isotope of germanium, ^{73}Ge , has a spin $I = 9/2$ quantum number. Nuclear spins with quantum numbers greater than spin-1/2 can exhibit a nuclear quadrupole interaction, that shifts the nuclear energy levels of the satellite transitions [64]. Therefore when

describing a ^{73}Ge nuclear spin bath, one must consider an additional term in the nuclear Hamiltonian

$$H_{\text{nuc}} = -\sum_k \gamma_I B_z I_k^z + \frac{\omega_Q}{2} \sum_k (I_k^z)^2 \quad (2.49)$$

where γ_I is the Larmor precession frequency of ^{73}Ge and ω_Q is the quadrupolar interaction strength. In bulk, magnetic resonance experiments have measured $\omega_Q \approx 100$ Hz [65], however this term is sensitive to local electric fields, therefore the strain in the quantum well can drastically enlarge the magnitude [66].

2.5.5. ELECTRIC DIPOLE SPIN RESONANCE

The spin orbit interaction experienced by holes in Ge/SiGe facilitates a coupling of electric field oscillations to the spin of the hole qubit. Driving a hole spin in this way is called electric dipole spin resonance (EDSR), and allows for very fast manipulation speeds of spin qubits compared to conventional ESR. EDSR is typically achieved by modulating the electric potential of the metallic gates close to the spin qubits in a semiconductor device, causing the qubit oscillate within its confinement potential. The spin orbit interaction results in the hole seeing an effective AC-magnetic field, resulting in spin rotations.

Exciting spin transitions between the heavy-hole eigenstates $|0, 0, \pm 3/2\rangle$ (where the indices correspond to excited state orbital n , azimuthal quantum number l and spin m_J) cannot be achieved by a magnetic dipole interaction, since $\Delta m_J = 3$. Transitions become possible, however, in the picture where the spin flip occurs via a virtual transition to the first excited state orbital of the quantum dot ($n = 1$) in the confinement potential [60]. The AC-electric field provides this change, and since it also moves the qubit within the confinement potential itself, the spin orbit interaction facilitates spin flips. This requires a term in the spin orbit Hamiltonian that permits a change in the orbital excitation of $\Delta n = 1$, which is only found in the cubic-symmetric a_3 term in equation 2.39 [52].

Driving via EDSR in the presence of a spin-orbit interaction usually allows for much faster qubit manipulations than achievable with ESR [67]. ESR strip-lines are also limited by superconducting critical currents dictated by their design and material. On the other hand, oscillating electric fields can be readily achieved by modulating the electrostatic potentials on metallic gates already present on a device (such as plunger or barrier gates), circumventing the need for additional bulky structures such as microwave antennas. However, the dependence of a systems eigenstates on electric field fluctuations enhances the coupling of charge noise to the system, resulting in a trade-off between fast driving and quantum coherence.

2.6. QUALIFYING A QUANTUM SYSTEM

Quantum systems are constantly interacting and exchanging energy (and therefore information) with other quantum systems around them. The trick is to isolate qubits such that they only interact with other qubits when desired, and as little as possible with the outside world. Unfortunately this is never completely possible, and therefore it is important to know the timescales over which one can reliably store information in, or operate on qubits in a quantum computer. Information loss can occur in a number of ways. In the case of a single qubit, information loss can be separated into two processes, called spin-relaxation, and dephasing.

2.6.1. SPIN RELAXATION

Spin relaxation is quantified by a timescale called T^1 . It represents the time that a qubit can remain in its higher energy state, before relaxing to its ground state. Relaxation of this type occurs due to noise that couples perpendicular to the quantization axis of the qubit. For electrons in silicon qubits, this typically occurs due to charge noise in the surrounding 2DEG's and metallic gates [68, 69]. This charge noise couples to the spin degree of freedom weakly via the spin-orbit coupling, resulting in spin-relaxation [39]. Due to this relatively weak effect, spin relaxation times of more than a second have been measured in silicon quantum dots [38, 70]. The large spin orbit coupling of holes in Ge/SiGe results in a stronger effect with respect to the case of silicon, and therefore hole spin relaxation times have been limited to a few hundred microseconds [71, 72]. We demonstrate a drastic improvement to this timescale in chapter 8.

In order to measure spin relaxation of a single qubit, one must initialize a qubit in its higher energy spin state. One then waits for a time, and then reads out the final state of the spin. By repeating this process over many measurements and averaging the traces, a characteristic decay will occur related to the probability of finding the spin still in its $|\uparrow\rangle$ state (See Figure 2.12a). Performing this measurement as a function of wait time yields an exponential decay with characteristic decay time T^1 . Long spin relaxation times are necessary to the operation of a quantum computer, however they are typically not the limiting timescale for spin qubits in general.

2.6.2. DEPHASING

Dephasing is the loss of phase coherence of a qubit. When a qubit is brought to a superposition state, noise that couples to the quantization axis of the qubit will perturb the eigenstates of the system, which will in turn cause the qubit to acquire phase at a different rate. This can happen in the presence of a fluctuating nuclear spin bath via the hyperfine interaction, or due to charge noise coupling to the spin eigenstates via the spin-orbit interaction. These processes destroy the phase information of the qubit, and are currently the limiting mechanism for qubit scale up.

To measure dephasing, we define a timescale T^2 . This timescale is upper bounded by T^1 since a relaxation process while in a superposition also does not preserve phase coherence, however in spin qubits, it is always experimentally measured to be much lower. We define the 'free-induction-decay' timescale T^{2*} to be the rate at which phase coherence is lost. This is measured by preparing the qubit in the $|\downarrow\rangle$ state, then bringing it to the state $1/\sqrt{2}(|\downarrow\rangle + i|\uparrow\rangle)$ by applying an $X_{\pi/2}$ pulse, waiting for a time, then applying a $X_{-\pi/2}$ pulse to return it to the $|\downarrow\rangle$ state, and reading out the final spin state (See Figure 2.12b). Averaging these measurements for different wait times results in an exponential decay with characteristic time T^{2*} . It is typical to apply the pulses with a small but precise detuning, as it aids in the accuracy of the resulting fit. The resulting decay becomes an exponential envelope modulated by a sinusoid of the form

$$P_{|\downarrow\rangle} = A \sin(2\pi f\tau + \phi) \exp\left\{-\tau/T^{2*}\right\} \quad (2.50)$$

where A represents the difference in readout value between the $|\downarrow\rangle$ and fully decohered states, f is the oscillation frequency of the sinusoid due to the detuning, ϕ allows for a phase offset, and τ is the wait time. This pulse sequence is called a Ramsey sequence.

Noise acting on a qubit comes from different sources. One such noise source, which in itself is very general and contains many comprising noise sources, is charge noise. Charge noise typically follows a $1/\omega^\alpha$ spectral density [73]. If the noise acting on a qubit is constant over some time, then it is possible to recover phase coherence using refocussing pulses [74]. One pulse sequence that

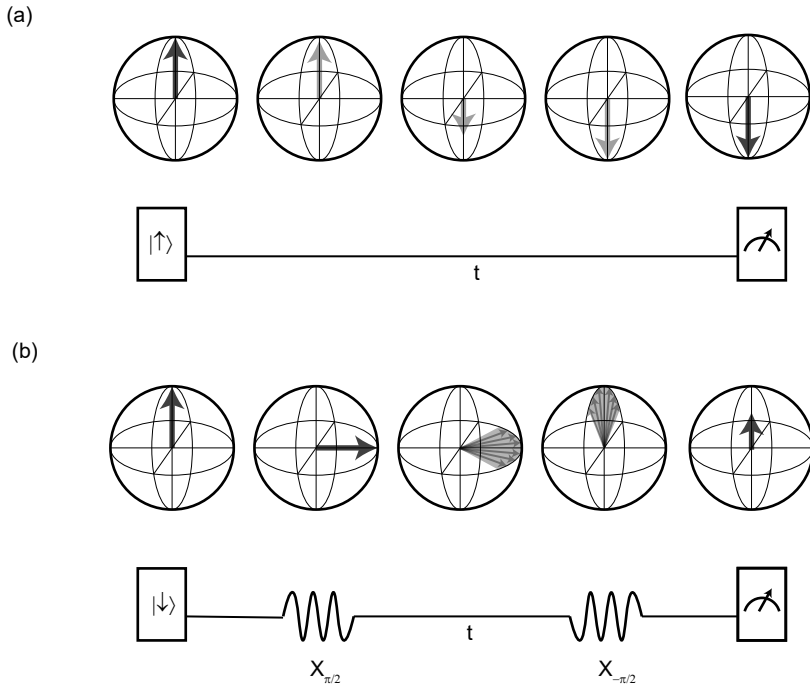


Figure 2.12: **Spin relaxation and spin dephasing measurements.** (a) A spin relaxation measurement occurs by preparing the qubit in the spin-up state, then waiting a time t , before measuring it. Over time, noise in the system will cause the spin to relax to its ground state, resulting in an exponential decay as a function of t . The decay constant of this exponential is called the spin relaxation time, or T^1 . (b) Spin dephasing rates can be measured using Ramsey pulse sequence. The spin state is prepared in the $|\downarrow\rangle$ state. Then, it is brought to the equator of the Bloch sphere by an $X_{\pi/2}$ pulse, where it is left to freely precess for a time t , before being projected back onto the z -axis of the Bloch sphere, and read out in the σ_z Pauli basis. Dephasing of the quantum state due to various noise sources will result in imperfect state recovery, resulting in an exponential decay with characteristic decay constant T^{2*} .

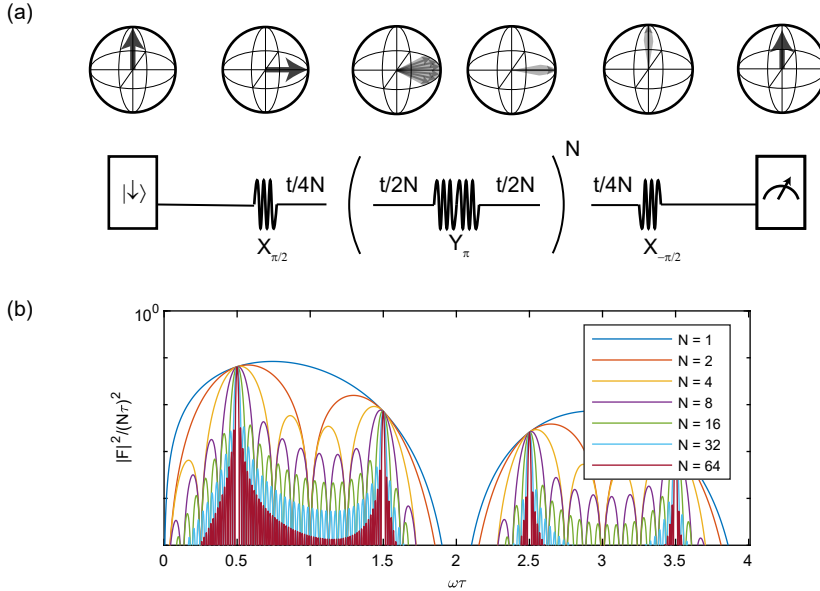


Figure 2.13: **CPMG pulse sequence and filter functions.** A CPMG pulse begins like a Ramsey pulse sequence, by bringing the spin state to the equator. However, the time t over which the spin would then freely precess, is divided up into smaller time partitions, with equally spaced Y_{π} pulses separating them. These pulses invert the parity of the noise acting on the qubit, such that for quasi-static noise, the effect is reversed and the qubit phase is recovered. By dividing a time t up into smaller and smaller intervals with refocussing pulses, the ceiling of noise frequency considered to be 'quasi-static' is raised, resulting in an extended coherence time, quantified by $T^{2,CPMG}$, the characteristic decay rate of the resulting exponential. (b) The CPMG pulse sequence is effectively a filter function, that transmits certain frequencies of noise. The filter function transmission function is plotted for different numbers of refocussing pulses N .

extends phase coherence is called a Hahn spin echo pulse sequence, and is performed by applying an extra X_{π} pulse half way through the wait time of a Ramsey sequence. The resulting decay will yield a different time scale T^{2H} , longer than T^{2*} since the qubit is less sensitive to charge noise. One can think of the pulse sequence as a filter function that reduces sensitivity of the qubit to low frequency noise. For a Hahn echo sequence, this filter function is given by [75]

$$F_H(\omega\tau) = 8 \sin^4(\pi\omega\tau/2) \tag{2.51}$$

for a pulse sequence of length τ , and noise frequency ω .

This technique can be extended by adding additional refocussing pulses in the same time interval at regular partitions. This is called a Carl-Purcell-Meiboom-Gill (CPMG) sequence (Fig. 2.13a), and has the effect of further increasing the band of noise frequency that a qubit is insensitive to. It has a filter function given by [75]

$$F_{CPMG}(N_{\pi}, \omega\tau) = \frac{8}{\pi\omega^2} \sin^4(\omega\tau/4) \frac{\sin^2(N_{\pi}\omega\tau/2)}{\cos^2(\omega\tau/2)} \tag{2.52}$$

where N_{π} represents the number of refocussing pulses in the sequence. Several filter functions are plotted in Fig. 2.12b for various N_{π} .

Using refocussing techniques, one can effectively extend quantum coherence far beyond its free induction decay value. In general, for a spectral density of noise given by $S(\omega)$, the coherence of a qubit undergoing a CPMG pulse sequence after a time τ will behave as [76, 77]

$$C(N\pi, \tau) = \exp\left(-\int_{-\infty}^{\infty} d\omega \frac{S(\omega)}{\omega^2} F(N\pi, \omega\tau)\right). \quad (2.53)$$

As a final note, CPMG filter functions can also be used to narrow sensitivity to a particular frequency of noise, making them useful tools to explore the various noise sources acting upon them. We will see this in chapter 11, where we use CPMG pulse sequences to analyse and quantify the effect of the ^{73}Ge nuclear spin on the coherence of hole spin qubits defined in Ge/SiGe.

2.6.3. GATE FIDELITY

Noise sources that occur in semiconductor devices will limit the timescales over which a quantum computer can be reliably operated, and therefore reduce their overall effectiveness. Additionally, quantum computers can also be affected by systematic mistakes due to errors in the calibration of the resonance frequency of the qubits, errors in the pulse times, cross-talk between qubits etc. Both environmental noise sources and systematic errors reduce the effectiveness of a quantum computer's ability to execute quantum gates. It is useful to know the average error rates of these quantum gates, since they effectively determine the achievable complexity of the quantum algorithms that can be executed on a quantum processor.

One widely used technique to extract the error rates of a quantum processor is Randomized Benchmarking [78]. Randomized benchmarking utilizes the Clifford group, which is a set of unitary operations that map elements of the Pauli group to other elements of the Pauli group. In randomized benchmarking, the general procedure goes according to:

- (1) prepare the quantum system in a known state $|\psi_0\rangle$,
- (2) perform a sequence of $N - 1$ operations selected at random from the Clifford group,
- (3) perform a *recovery* operation (also a Clifford) that returns the system to the original state $|\psi_0\rangle$ and finally,
- (4) calculate the return probability of the final state $\langle\Psi_f|\Psi_I\rangle$ to the original state.

By repeating this sequence for increasing N , error rates will cause a reduction in the return probability, resulting in a decay from which the circuit level error rate can be calculated. Randomized benchmarking produces an average error rate, however error rates may be different as different error channels exist for different quantum operations. Therefore it is important to benchmark with a large enough random subset of Clifford gates such that the errors are effectively averaged out. There are 24 single qubit Cliffords (C_1), 11540 two-qubit Cliffords (C_2), 92897280 three-qubit Cliffords (C_3). This can make it non-trivial to perform randomized benchmarking for larger numbers of qubits, however these considerations don't apply in this thesis, as only single qubit randomized benchmarking is performed.

REFERENCES

- [1] Thornton, S. T. & Rex, A. F. *Modern physics for scientists and engineers* (Saunders College Pub., Fort Worth, 1993).
- [2] Yu, P. Y. & Cardona, M. *Fundamentals of semiconductors physics and materials properties* (Springer, 2010).
- [3] Alexander, M. N. & Holcomb, D. F. The semiconductor-to-metal transition in n-type silicon. *Solid State Commun.* **6**, 355–358 (1968).

- [4] Hanson, R., Kouwenhoven, L. P., Petta, J. R., Tarucha, S. & Vandersypen, L. M. Spins in few-electron quantum dots. *Reviews of Modern Physics* **79**, 1217–1265 (2007).
- [5] Groth, C. W., Wimmer, M., Akhmerov, A. R. & Waintal, X. Kwant: A software package for quantum transport. *New J. Phys.* **16**, 063065 (2014).
- [6] Van der Wiel, W. G. *et al.* Electron transport through double quantum dots. *Reviews of Modern Physics* **75**, 1–22 (2003).
- [7] Volk, C. *et al.* Loading a quantum-dot based “Qubyte” register. *npj Quantum Information* **5**, 1–8 (2019).
- [8] Hensgens, T. *et al.* Quantum simulation of a Fermi-Hubbard model using a semiconductor quantum dot array. *Nature* **548**, 70–73 (2017).
- [9] Levitt, M. H. *Spin dynamics : basics of nuclear magnetic resonance* (John Wiley & Sons, 2008).
- [10] Wu, Y. & Yang, X. Strong-coupling theory of periodically driven two-level systems. *Physical Review Letters* **98**, 013601 (2007).
- [11] Burkard, G., Loss, D. & DiVincenzo, D. P. Coupled quantum dots as quantum gates. *Physical Review B* **59**, 2070 (1999).
- [12] Golovach, V. N., Borhani, M. & Loss, D. Electric-dipole-induced spin resonance in quantum dots. *Phys. Rev. B* **74**, 165319 (2006).
- [13] Schrieffer, J. R. & Wolff, P. A. Relation between the Anderson and Kondo Hamiltonians. *Phys. Rev.* **149**, 491–492 (1966).
- [14] Meunier, T., Calado, V. E. & Vandersypen, L. M. K. Efficient controlled-phase gate for single-spin qubits in quantum dots. *Phys. Rev. B* **83**, 121403 (2011).
- [15] Sigillito, A. J., Gullans, M. J., Edge, L. E., Borselli, M. & Petta, J. R. Coherent transfer of quantum information in a silicon double quantum dot using resonant SWAP gates. *npj Quantum Information* **5**, 1–7 (2019).
- [16] Petit, L. *et al.* High-fidelity two-qubit gates in silicon above one Kelvin. *arXiv 2007.09034* (2020).
- [17] Xue, X. *et al.* Quantum logic with spin qubits crossing the surface code threshold. *Nature* **601**, 343–347 (2022).
- [18] Huang, W. *et al.* Fidelity benchmarks for two-qubit gates in silicon. *Nature* **569**, 532–536 (2019).
- [19] Noiri, A. *et al.* Fast universal quantum control above the fault-tolerance threshold in silicon. *Nature* **2022 601:7893** **601**, 338–342 (2021).
- [20] Zheng, G. *et al.* Rapid gate-based spin read-out in silicon using an on-chip resonator. *Nature Nanotechnology* **14**, 742–746 (2019).
- [21] Eizerman, J. M. *et al.* Single-shot read-out of an individual electron spin in a quantum dot. *Nature* **430**, 431–435 (2004).

- [22] Veldhorst, M. *et al.* An addressable quantum dot qubit with fault-tolerant control-fidelity. *Nature Nanotechnology* **9**, 981–985 (2014).
- [23] Veldhorst, M. *et al.* A two-qubit logic gate in silicon. *Nature* **526**, 410–414 (2015).
- [24] Watson, T. F. *et al.* A programmable two-qubit quantum processor in silicon. *Nature* **555**, 633–637 (2018).
- [25] Vandersypen, L. M. K. *et al.* Interfacing spin qubits in quantum dots and donors—hot, dense, and coherent. *npj Quantum Information* **3**, 1–10 (2017).
- [26] Itoh, K. M. & Watanabe, H. Isotope engineering of silicon and diamond for quantum computing and sensing applications. *MRS Communications* **4**, 143–157 (2014).
- [27] Yoneda, J. *et al.* A quantum-dot spin qubit with coherence limited by charge noise and fidelity higher than 99.9%. *Nature Nanotechnology* **13**, 102–106 (2018).
- [28] Sabbagh, D. *et al.* Quantum Transport Properties of Industrial Si 28 / Si O2 28. *Physical Review Applied* **12**, 014013 (2019).
- [29] Steger, M. *et al.* Quantum information storage for over 180 s using donor spins in a 28Si "semiconductor vacuum". *Science* **336**, 1280–1283 (2012).
- [30] Phillips, J. C. Band structure of silicon, germanium, and related semiconductors. *Phys. Rev.* **125**, 1931–1936 (1962).
- [31] Ando, T., Fowler, A. B. & Stern, F. Electronic properties of two-dimensional systems. *Reviews of Modern Physics* **54**, 437–672 (1982).
- [32] Sham, L. J. & Nakayama, M. Effective-mass approximation in the presence of an interface. *Physical Review B* **20**, 734–747 (1979).
- [33] Ruskov, R., Veldhorst, M., Dzurak, A. S. & Tahan, C. Electron g-factor of valley states in realistic silicon quantum dots. *Physical Review B* **98**, 245424 (2018).
- [34] Friesen, M., Chutia, S., Tahan, C. & Coppersmith, S. N. Valley splitting theory of SiGe/Si/SiGe quantum wells. *Physical Review B* **75** (2007).
- [35] Borjans, F., Zajac, D. M., Hazard, T. M. & Petta, J. R. Single-Spin Relaxation in a Synthetic Spin-Orbit Field. *Physical Review Applied* **11**, 044063 (2019).
- [36] Zajac, D. M., Hazard, T. M., Mi, X., Wang, K. & Petta, J. R. A reconfigurable gate architecture for Si/SiGe quantum dots. *Applied Physics Letters* **106**, 223507 (2015).
- [37] Yang, C. H. *et al.* Orbital and valley state spectra of a few-electron silicon quantum dot. *Physical Review B* **86**, 115319 (2012).
- [38] Yang, C. H. *et al.* Spin-valley lifetimes in a silicon quantum dot with tunable valley splitting. *Nature Communications* **4** (2013).
- [39] Petit, L. *et al.* Spin Lifetime and Charge Noise in Hot Silicon Quantum Dot Qubits. *Physical Review Letters* **121**, 076801 (2018).
- [40] Tagliaferri, M. L. *et al.* Impact of valley phase and splitting on readout of silicon spin qubits. *Physical Review B* **97**, 245412 (2018).

- [41] Wuetz, B. P. *et al.* Atomic fluctuations lifting the energy degeneracy in Si/SiGe quantum dots (2021).
- [42] Dehollain, J. P. *et al.* Nanoscale broadband transmission lines for spin qubit control. *Nanotechnology* **24**, 015202 (2013).
- [43] Nolting, W. & Ramakanth, A. *Quantum theory of magnetism* (Springer Berlin Heidelberg, 2009).
- [44] Scappucci, G. *et al.* The germanium quantum information route. *Nature Reviews Materials* (2020).
- [45] Winkler, R. SpinOrbit Coupling Effects in Two-Dimensional Electron and Hole Systems. 6 Inversion-Asymmetry-Induced Spin Splitting. *Semiconductors* **129**, 69–129 (2003).
- [46] Luttinger, J. M. & Kohn, W. Motion of Electrons and Holes in Perturbed Periodic Fields. *Physical Review* **97**, 869–883 (1955).
- [47] Baldereschi, A. & Lipari, N. O. Spherical model of shallow acceptor states in semiconductors. *Physical Review B* **8**, 2697–2709 (1973).
- [48] Luttinger, J. M. Quantum theory of cyclotron resonance in semiconductors: General theory. *Physical Review* **102**, 1030–1041 (1956).
- [49] Sammak, A. *et al.* Shallow and Undoped Germanium Quantum Wells: A Playground for Spin and Hybrid Quantum Technology. *Advanced Functional Materials* **29**, 1807613 (2019).
- [50] Lodari, M. *et al.* Low percolation density and charge noise with holes in germanium. *Materials for Quantum Technology* **1**, 011002 (2020).
- [51] Wortman, J. J. & Evans, R. A. Young's modulus, shear modulus, and poisson's ratio in silicon and germanium. *Journal of Applied Physics* **36**, 153–156 (1965).
- [52] Terrazos, L. A. *et al.* Theory of hole-spin qubits in strained germanium quantum dots. *Physical Review B* **103**, 125201 (2021).
- [53] Bir, G. L. & Pikus, G. E. *Symmetry and Strain- Induced effects in Semiconductors. Translated from Russian by P. Shelnitz* (Wiley, New York, 1974).
- [54] Fischetti, M. V. & Laux, S. E. Band structure, deformation potentials, and carrier mobility in strained Si Ge, and SiGe alloys. *Journal of Applied Physics* **80**, 2234–2252 (1996).
- [55] Dresselhaus, G. Spin-orbit coupling effects in zinc blende structures. *Physical Review* **100**, 580–586 (1955).
- [56] Rashba, E. Properties of semiconductors with an extremum loop. 1. Cyclotron and combinational resonance in a magnetic field perpendicular to the plane of the loop. *Sov. Phys. Solid State* **2**, 1109–1122 (1960).
- [57] Marcellina, E., Hamilton, A. R., Winkler, R. & Culcer, D. Spin-orbit interactions in inversion-asymmetric two-dimensional hole systems: A variational analysis. *Physical Review B* **95**, 075305 (2017).
- [58] Lawaetz, P. Valence-band parameters in cubic semiconductors. *Physical Review B* **4**, 3460–3467 (1971).

- [59] Nichele, F. *et al.* Characterization of spin-orbit interactions of GaAs heavy holes using a quantum point contact. *Physical Review Letters* **113** (2014).
- [60] Bulaev, D. V. & Loss, D. Electric dipole spin resonance for heavy holes in quantum dots. *Physical Review Letters* **98** (2007).
- [61] Chesi, S. & Giuliani, G. F. Exchange energy and generalized polarization in the presence of spin-orbit coupling in two dimensions. *Physical Review B* **75** (2007).
- [62] Fischer, J., Coish, W. A., Bulaev, D. V. & Loss, D. Spin decoherence of a heavy hole coupled to nuclear spins in a quantum dot. *Physical Review B* **78**, 155329 (2008).
- [63] Clementi, E. & Raimondi, D. L. Atomic screening constants from SCF functions. *The Journal of Chemical Physics* **38**, 2686–2689 (1963).
- [64] Slichter, C. P. Electric Quadrupole Effects. 485–502 (Springer, Berlin, Heidelberg, 1990). URL https://link-springer-com.tudelft.idm.oclc.org/chapter/10.1007/978-3-662-09441-9_10.
- [65] Verkhovskii, S. V. *et al.* Quadrupole Effects on ^{73}Ge NMR Spectra in Isotopically Controlled Ge Single Crystals. *Zeitschrift für Naturforschung - Section A Journal of Physical Sciences* **55**, 105–110 (2000).
- [66] Yusa, G., Muraki, K., Takashina, K., Hashimoto, K. & Hirayama, Y. Controlled multiple quantum coherence of nuclear spins in a nanometre-scale device. *Nature* **434**, 1001–1005 (2005).
- [67] Froning, F. N. *et al.* Ultrafast hole spin qubit with gate-tunable spin-orbit switch functionality. *Nature Nanotechnology* **16**, 308–312 (2021).
- [68] Struck, T. *et al.* Low-frequency spin qubit energy splitting noise in highly purified $^{28}\text{Si}/\text{SiGe}$. *npj Quantum Information* **6**, 1–7 (2020).
- [69] Nakajima, T. *et al.* Coherence of a Driven Electron Spin Qubit Actively Decoupled from Quasistatic Noise. *Physical Review X* **10** (2020).
- [70] Simmons, C. B. *et al.* Tunable spin loading and T1 of a silicon spin qubit measured by single-shot readout. *Physical Review Letters* **106** (2011).
- [71] Vukušić, L. *et al.* Single-Shot Readout of Hole Spins in Ge. *Nano Letters* **18**, 7141–7145 (2018).
- [72] Hu, Y., Kuemmeth, F., Lieber, C. M. & Marcus, C. M. Hole spin relaxation in Ge-Si core-shell nanowire qubits. *Nature Nanotechnology* **7**, 47–50 (2012).
- [73] Paladino, E., Galperin, Y., Falci, G. & Altshuler, B. L. $1/f$ noise: Implications for solid-state quantum information. *Reviews of Modern Physics* **86**, 361–418 (2014).
- [74] Viola, L. & Lloyd, S. Dynamical suppression of decoherence in two-state quantum systems. *Physical Review A - Atomic, Molecular, and Optical Physics* **58**, 2733–2744 (1998).
- [75] Cywiński, Ł., Lutchyn, R. M., Nave, C. P. & Das Sarma, S. How to enhance dephasing time in superconducting qubits. *Physical Review B* **77**, 174509 (2008).
- [76] Uhrig, G. S. Exact results on dynamical decoupling by π pulses in quantum information processes. *New Journal of Physics* **10**, 083024 (2008).

- [77] Uhrig, G. S. Keeping a quantum bit alive by optimized π -pulse sequences. *Physical Review Letters* **98**, 100504 (2007).
- [78] Knill, E. *et al.* Randomized benchmarking of quantum gates. *Physical Review A - Atomic, Molecular, and Optical Physics* **77** (2008).



3

QUANTUM DOT ARRAYS IN SILICON AND GERMANIUM

Electrons and holes confined in quantum dots define excellent building blocks for quantum emergence, simulation, and computation. Silicon and germanium are compatible with standard semiconductor manufacturing and contain stable isotopes with zero nuclear spin, thereby serving as excellent host for spins with long quantum coherence. Here, we demonstrate quantum dot arrays in silicon metal-oxide-semiconductor (SiMOS), strained silicon (Si/SiGe), and strained germanium (Ge/SiGe). We fabricate using a multi-layer technique to achieve tightly confined quantum dots and compare integration processes. While SiMOS can benefit from a larger temperature budget and Ge/SiGe can make ohmic contact to metals, the overlapping gate structure to define the quantum dots can be based on a nearly identical integration. We realize charge sensing in each platform, for the first time in Ge/SiGe, and demonstrate fully functional linear and two-dimensional arrays where all quantum dots can be depleted to the last charge state. In Si/SiGe, we tune a quintuple quantum dot using the N+1 method to simultaneously reach the few electron regime for each quantum dot. We compare capacitive cross talk and find it to be the smallest in SiMOS, relevant for the tuning of quantum dot arrays. We put these results into perspective for quantum technology and identify industrial qubits, hybrid technology, automated tuning, and two-dimensional qubit arrays as four key trajectories that, when combined, enable fault-tolerant quantum computation.

Parts of this chapter have been published in Appl. Phys. Lett. 116 (8), 080501 [1].

Quantum dots have been a leading candidate for quantum computation for more than two decades [2]. Furthermore, they have matured recently as an excellent playground for quantum simulation [3] and have been proposed for the design of new states of matter [4, 5]. Pioneering studies in group III-V semiconductors led to proof-of-principles including the coherent control of electron spins [6, 7], rudimentary quantum simulations [8], and signatures of emergent states such as Majorana fermions [9]. The group IV semiconductors silicon and germanium have the opportunity to advance these concepts to a practical level due to their compatibility with standard semiconductor manufacturing [10] and the availability of isotopes with zero nuclear spin, increasing quantum coherence for single spins by four orders of magnitude [11]. Furthermore, heterostructures built from silicon and germanium also offer a large parameter space in which to engineer novel quantum electronic devices [12–14].

An initial advancement towards silicon quantum electronics [12] was the design of an integration scheme based on overlapping gates to build silicon metal-oxide-semiconductor (SiMOS) quantum dots [15]. This technique was later adopted in strained silicon (Si/SiGe) [16] and refined by incorporating metals with small grain size and atomic layer deposition (ALD) for layer-to-layer isolation [17] and to enable tunable coupling between single electrons in SiMOS [18]. These developments in fabrication have led to a great body of results, including high-fidelity qubit operation [19, 20] and two-qubit logic [21–23]. Controlling holes in silicon has been more challenging due to type II band alignment in strained silicon, limiting experiments to SiMOS [24–26]. Strained germanium on the other hand [13, 27, 28] exhibits type I band alignment and is thereby a viable platform in which not only electrons but also holes with light effective mass [29] can be confined [30] and coherently controlled [31].

Here, we present the fabrication and operation of quantum dots in silicon and germanium, in linear and two-dimensional arrays. We compare integration schemes and find that while each platform has unique aspects and opportunities, the core fabrication of overlapping gates defining the nano-electronic devices is remarkably similar, thereby further accelerating the overall progress in group IV semiconductor quantum dots. In each case, fabrication starts from a silicon substrate, and integration is compatible with standard semiconductor technology. We leverage off the ohmic contact between quantum dots in Ge/SiGe and metals [32] to avoid the need for ion implantation and to provide means for novel hybrid systems. We show stability diagrams obtained by charge sensing and report double quantum dots in SiMOS, Si/SiGe, and Ge/SiGe that can be depleted to the last charge state. Fabrication is most demanding in SiMOS due to requirements on feature size, but we also find that the resulting devices have the smallest cross capacitance, simplifying tuning and operation. We put these results in perspective and outline a road map for quantum technology based on group IV semiconductor platforms.

Figure 3.1a schematically shows the SiMOS, Si/SiGe, and Ge/SiGe wafer stacks used in this study. The SiMOS 300 mm wafers are grown in an industrial complementary metal oxide semiconductor (CMOS) fab [14, 18, 33], while the Si/SiGe and Ge/SiGe four-inch wafers are grown using an RP-CVD reactor (ASM Epsilon 2000) [13]. Each platform is grown on a p-type natural Si wafer. The SiMOS structure consists of 1 μm intrinsic natural silicon (^1Si) followed by 100 nm ^{28}Si (800 ppm purity) and 10 nm SiO_2 [14]. The Si/SiGe heterostructure begins with a linearly graded $\text{Si}_{1-x}\text{Ge}_x$ layer, where x ranges from 0 to 0.3. A relaxed $\text{Si}_{0.7}\text{Ge}_{0.3}$ layer of 300 nm lies below the 10 nm ^{28}Si (800 ppm purity) quantum well which itself is separated from the 2 nm Si capping layer by a second 30 nm relaxed $\text{Si}_{0.7}\text{Ge}_{0.3}$ spacer layer. The Ge/SiGe wafer stack starts with 1.4 μm of Ge and 900 nm of reverse graded $\text{Si}_{1-x}\text{Ge}_x$ where x ranges from 1 to 0.8. This lies below a 160 nm $\text{Si}_{0.2}\text{Ge}_{0.8}$ spacer layer, a 16 nm Ge quantum well under compressive strain, a second $\text{Si}_{0.2}\text{Ge}_{0.8}$ layer of 22 nm and finally a thin Si cap of 1 nm [13].

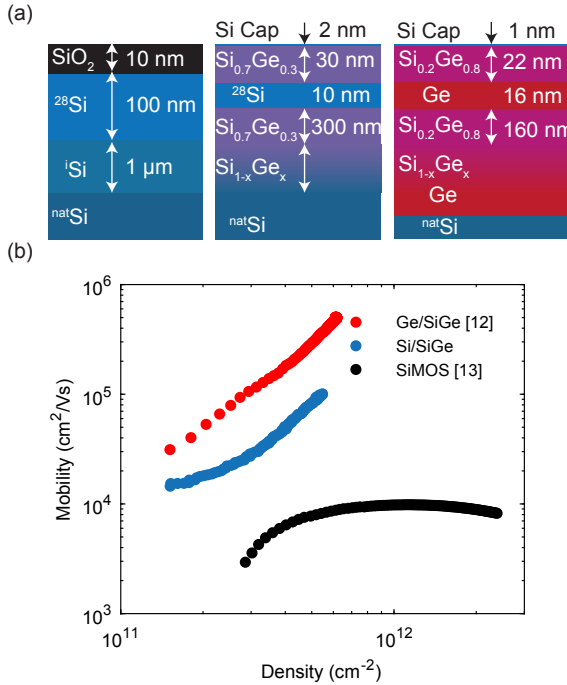


Figure 3.1: Wafer stack schematics and mobility as a function of carrier density. (a) From left to right, SiMOS, Si/SiGe, and Ge/SiGe wafers stacks. For SiMOS, a ^{28}Si epilayer with 10 nm thermal oxide is grown on a 1 μm intrinsic natural Si buffer layer. The Si/SiGe heterostructure consists of a 1.5 μm linearly graded SiGe layer, a relaxed 300 nm SiGe spacer, a 10 nm ^{28}Si quantum well, a 30 nm SiGe spacer, and a 2 nm Si cap. The Ge/SiGe heterostructure consists of 900 nm reverse graded SiGe layer, a relaxed 160 nm SiGe spacer, a 16 nm Ge quantum well, a 22 nm SiGe spacer, and a 1 nm Si cap. (b) Mobility as a function of carrier density measured in each platform. For Ge/SiGe, the peak mobility is greater than $5 \times 10^5 \text{ cm}^2/\text{Vs}$ and the critical density is $1.15 \times 10^{11} \text{ cm}^{-2}$ [13]. The same measurements for Si/SiGe wafers give a peak mobility of $1 \times 10^5 \text{ cm}^2/\text{Vs}$ and a critical density of $1.2 \times 10^{11} \text{ cm}^{-2}$. SiMOS data taken from [14] shows a mobility of $1 \times 10^4 \text{ cm}^2/\text{Vs}$ and a higher critical density of $2.5 \times 10^{11} \text{ cm}^{-2}$.

3.1. MOBILITY AND STACK BY PLATFORM


Figure 3.1b shows a carrier mobility versus density characterization of the three platforms. Hall bar structures were fabricated on coupons cut from the center of each wafer. Maximum mobility and critical density are extracted at 1.7 K. SiMOS 300 mm processed wafers give a peak mobility value of $1 \times 10^4 \text{ cm}^2/\text{Vs}$, as well as a critical density of about $1.75 \times 10^{11} \text{ cm}^{-2}$ as shown in another work [14]. At higher densities, SiMOS mobilities fall off due to surface roughness scattering effects [34–36]. In Si/SiGe, we observe a lower critical density of $1.2 \times 10^{11} \text{ cm}^{-2}$ and a significantly higher maximum mobility exceeding $1 \times 10^5 \text{ cm}^2/\text{Vs}$. Similar studies conducted on natural Si/SiGe grown in an industrial CMOS fab yielded mobilities of $4.2 \times 10^5 \text{ cm}^2/\text{Vs}$ [37]. This quality improvement observed by moving toward industrial CMOS fab also suggests encouraging prospects for Ge/SiGe, already exhibiting a high maximum mobility of $5 \times 10^5 \text{ cm}^2/\text{Vs}$ and critical density of $1.15 \times 10^{11} \text{ cm}^{-2}$ despite being grown in an academic cleanroom via RP-CVD [13].

Temperature	SiMOS	Si/SiGe	Ge/SiGe
Thermal Budget	1000 °C	750 °C	500 °C

Ohmics	SiMOS	Si/SiGe	Ge/SiGe
Dopant	P ⁺	P ⁺	-
Metal	Ti:Pt	Ti:Pt	Al
Annealing	1000 °C, 30 s	700 °C, 30 s	300 °C, 1h

Field Oxide	SiMOS	Si/SiGe	Ge/SiGe
Oxide Window	✓	(1)	(1)

Stack	All Platforms
Bondpads	SiN 150 nm
Gate Layer	Ti:Pt
Isolation	Al ₂ O ₃ ALD



Control	SiMOS	Si/SiGe	Ge/SiGe
mw-Antenna	✓	✓	-
Micromagnet	✓	✓	-
Spin-Orbit	(2)	-	✓

Figure 3.2: Overview of fabrication scheme for SiMOS, Si/SiGe and Ge/SiGe quantum dots. The thermal budget of each material prior to gate stack deposition is estimated based on the limiting mechanism of each platform as discussed in the text. In all cases, gates are fabricated from Pd metal with a thin (3 nm) Ti adhesion layer, with layer-to-layer isolation performed via atomic layer deposition (ALD) of Al₂O₃. These two steps can be looped at appropriate thicknesses to form the multi-layer structure. (1) We note the possibility of such an etch exists for the remaining platforms in the case of a Schottky gate architecture (2) We note that spin-orbit based driving of electrons in SiMOS has been demonstrated for singlet-triplet qubits [38] and proposed for single spin qubits [39].

3.2. INTEGRATION SCHEME

Figure 6.1 summarises the integration scheme utilized for each platform. The thermal budget is estimated based on the respective limiting mechanisms. For SiMOS, thermal processing is limited by the self-diffusion of natural silicon from the substrate into the ²⁸Si epilayer. From the self diffusion constants measured by Bracht et al. [40], we estimate the point at which the residual ²⁹Si concentration within 1 nm of the Si-SiO₂ interface increases by 1 ppm occurs at 1000 °C for time scales above 1 hour, for furnace anneals in a pure argon atmosphere. Consequently, this allows for extensive thermal treatment and annealing of samples. This is highly advantageous, as we have observed that a 15 minute anneal in forming gas at 400 °C after the deposition of every gate layer greatly improves the quality of metallic features with smallest critical dimensions (see Supplementary material section Ia for detailed comparison). In addition, a final end-of-line anneal is conducted to eliminate processing damage at 400 °C in forming gas for 30 minutes. In the cases of Si/SiGe and Ge/SiGe, the thermal budget is limited by strain relaxation of the quantum wells, thus the maximum processing thermal budget is given qualitatively by the temperature at which the quantum wells were grown. This is 750 °C for strained Si and 500 °C for strained Ge [13].

The design of ohmic contacts is tailored to the specific requirements of the device. For both Si platforms, ohmic contact is made via high fluence P ion implantation followed by evaporation of Ti:Pt metallic contacts, creating n⁺⁺ doped, low resistance channels. The oxide (SiO₂) is

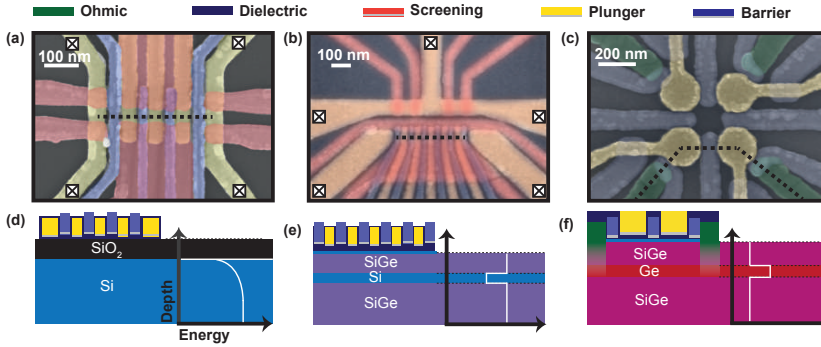


Figure 3.3: Scanning electron microscope images and corresponding device schematics with band bending diagrams, substrate and gate stack for each of the devices. Dotted lines in (a-c) indicate the cross-section through the quantum dot channel illustrated in (d-f) respectively, and crossed boxes indicate gates that overlap with implanted regions to form ohmic contacts. The plunger gates (yellow), the barrier gates (blue) and the screening gates (red) define the quantum dots. (a) SiMOS triple quantum dot linear array. Two SETs function as charge sensors and as reservoirs for the quantum dots on either side of the array (b) Si/SiGe quintuple quantum dot linear array. Two SETs (top) are used for charge sensing. (c) Ge/SiGe (2x2) quadruple quantum dot array. Each quantum dot is tunnel coupled to a metallic lead (green). Measurement can be performed in transport, or using charge-sensing by forming a sensor quantum dot under one channel to sense a double quantum dot in the opposite channel. (d,e,f) Cross-section and bandstructure of metal, dielectric (black) and semiconductor (d) SiMOS, (e) Si/SiGe and (f) Ge/SiGe.

etched locally directly before metal deposition using buffered hydrofluoric acid (BHF). In the case of Si/SiGe, stray capacitance is minimized to ensure maximum power is dissipated in the variable resistance of the sensing quantum dot for RF-readout. Germanium can make direct ohmic contact to metals [32], avoiding the need for implants. We deposit Al and anneal at 300 °C for 1 hour in vacuum to assist in Al diffusion into the quantum well. The Al ohmic contact is defined close to the quantum dots, resulting in a very low resistance channel ideally suited for RF circuits and enabling a tunnel contact that can even be made superconducting [41]. The implementation does however lower the thermal budget of further processing.

Fabrication of each device utilizes a titanium-palladium (Ti:Pd) gate stack with 3 nm of Ti deposited for each layer to assist with adhesion. Pd makes a good gate metal due to its small grain size [17]. Unlike the commonly used material Al, Pd does not self-oxidise and ALD can be used to define sharp dielectric interfaces. For the SiMOS and Si/SiGe devices shown in Fig. 3.3, we utilize a three layer gate stack that we refer to as the screening layer, the plunger layer and the barrier layer. In order to assist climbing of overlapping gate features, the initial layer is deposited at 20 nm total thickness, while subsequent layers at 40 nm. The layers are isolated from one another via ALD of Al₂O₃ at 7 nm thickness. We measure the breakdown electric field of the Al₂O₃ to be greater than 6 MV/cm, allowing potentials of greater than 4 V to be applied between adjacent gates. To leverage off the high quality industrial CMOS fabrication facilities, we begin fabrication of SiMOS devices on wafers including a 10 nm SiO₂ oxide already grown. To further reduce the likelihood of leakage from gate to substrate, we first grow a thick 10 nm Al₂O₃ blanket layer over the entirety of the substrate. Advantageously, one can etch Al₂O₃ on thermally grown SiO₂ selectively, allowing the definition of a 20x20 μm² area where the quantum dot system is defined, which we have measured to significantly reduce low-frequency drifts deduced from charge occupation stability [42] (see Supplementary material section Ib for comparison).

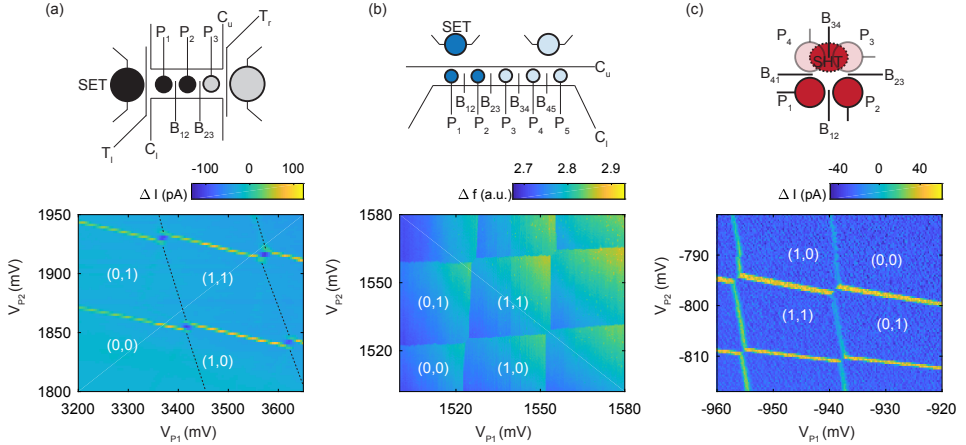


Figure 3.4: Charge stability diagrams of double quantum dots depleted to the single electron/hole regime for the three platforms. (a) SiMOS double quantum dot. Charge addition lines under P_1 are not visible due to low tunnel rate from reservoir. Map taken at 0.44 K using lock-in charge sensing. The excitation is placed on the inter-dot gate B_{12} . (b) Si/SiGe double quantum dot formed under the first two plungers, sensed by the nearest charge sensor via RF-reflectometry utilizing a resonant LC circuit at 84 MHz. Here, the plunger gate voltages are in virtual gate space correcting for weak cross capacitive coupling. (c) Ge/SiGe depleted to the single hole regime. A large single quantum dot is formed under P_3 , B_{34} and P_4 , by adjusting the tunnel barrier voltage B_{34} , and is used to sense a double quantum dot under P_1 and P_2 . The lock-in excitation is placed on the inter-dot tunnel barrier B_{12} .

The final deposition step is the qubit control layer. The spin-orbit coupling for holes in germanium enables qubit operation by simply applying microwave pulses to the quantum dot gates [31, 44] and no further processing is required. In silicon, qubit driving can be realized by integrating on-chip striplines [7, 11], which we fabricate using Al or NbTiN, or micromagnets [45], which we integrate using Ti:Co. Quantum dots in Si/SiGe generally have a larger and more mobile electron wave function as compared to SiMOS and thereby benefit most from a micromagnet integration for fast qubit driving.

A schematic of each material and associated device is shown in Fig. 3.3 and labelling of the relevant gates are shown in Fig. 3.4. The SiMOS device is a three-layer, triple quantum dot structure with dedicated plungers (P_{1-3}), inter-dot barriers (B_{12} , B_{23}) and dot-reservoir barriers (T_l , T_r).

Two large metallic gates (C_l , C_u) deposited in the initial layer and kept at constant potential serve to confine the quantum dots in one lateral dimension. They also serve to screen charge noise resulting from fluctuations near the quantum dot array.

Two single electron transistors (SETs) are positioned at either side of the quantum dot array, and function as charge sensors for spin and charge readout. The Si/SiGe device is a quintuple quantum dot linear array written in three layers utilizing a similar architecture to that of the SiMOS device. The quantum dot array contains five plunger gates (P_{1-5}) with inter-dot barriers (B_{12-45}) and dot-reservoir barriers. Here too, the quantum dots are confined laterally and screened from charge noise by two confinement gates. Two SETs are positioned parallel to the quantum dot channel. The Ge/SiGe device is a 2x2 quadruple quantum dot array written in two layers. Gates (P_{1-4}) are positioned anti-clockwise in the array and define the potential of the quantum dots. Each pair

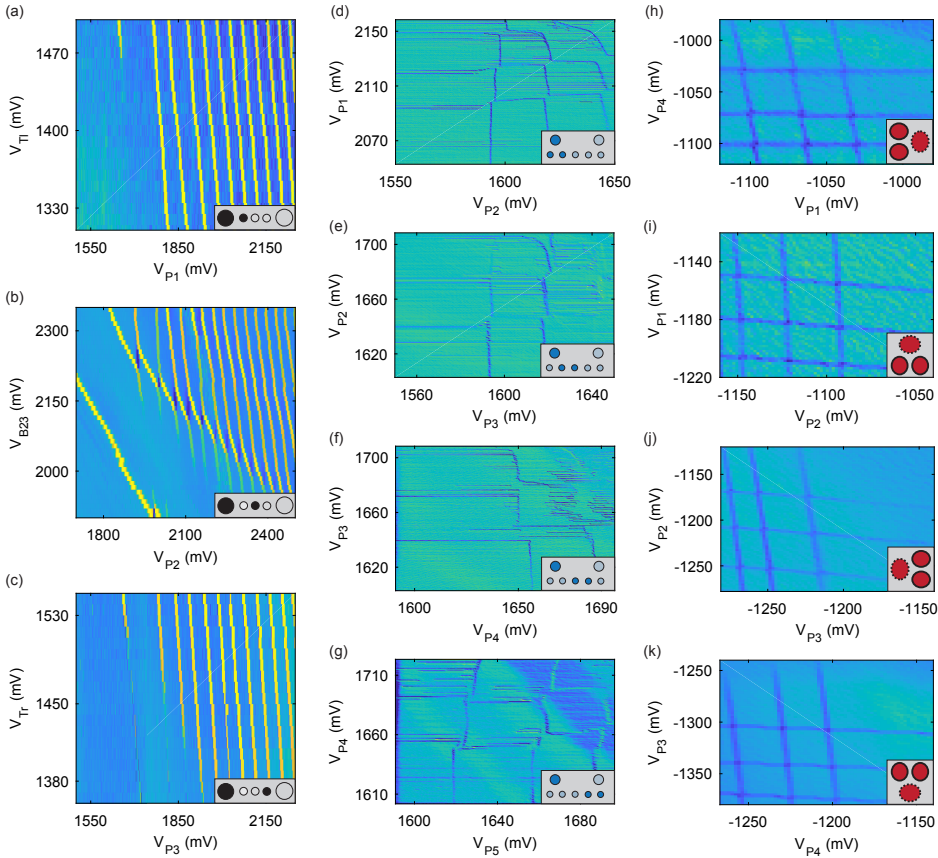


Figure 3.5: Quantum dot arrays in SiMOS, Si/SiGe and Ge/SiGe. (a-c) SiMOS triple quantum dot device stability diagrams. Each single quantum dot is formed under its respective plunger gate upon which an excitation is placed for lock-in charge sensing. Each quantum dot is depleted to the single charge state. (b) Shows the crossing of the adjacent quantum dot under P_3 , through which the quantum dot is loaded. (d-g) Si/SiGe double quantum dots tuned up sequentially using the N+1 method [43] to the single electron regime. True plunger gate voltages are plotted, though virtual gates are swept containing small corrections to adjacent barriers and plungers. Each double quantum dot pair is sensed using RF-reflectometry. The same SET is used for readout in each case, as indicated by the relative signals as each double quantum dot pair is formed farther from the charge sensor. (g) The data has been filtered to remove 50 Hz background noise for data clarity. (h-k) Ge/SiGe 2x2 array double quantum dots formed in each possible configuration. In each case, a charge sensor is formed in the parallel channel by raising the inter-dot coupling to form a large single quantum dot with high hole occupancy. Each charge stability diagrams shows RF-sensing of double quantum dots depleted to the last hole occupancy, in the low tunnel-coupled regime.

of adjacent quantum dots share a barrier gate (B_{12-41}) capable of tuning inter-dot tunnel coupling. Coupling of each quantum dot to its reservoir can be controlled via a barrier gate. This device can be operated as a quadruple quantum dot system in transport mode, but for the present work we intentionally tune the inter-dot barrier to form a single hole transistor (SHT) along a dot channel that we subsequently use for charge sensing of the double quantum dot along the opposite channel. For more information about device specific fabrication, see Supplementary material

section II.

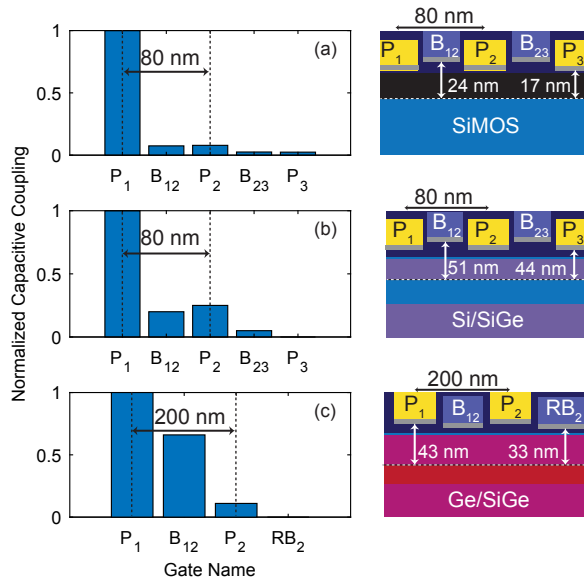


Figure 3.6: Cross capacitance to neighbouring gates of a quantum dot in the single charge occupancy regime under gate P_1 in each platform. For SiMOS (a), we observe immediate falloff of cross coupling due to the tight quantum dot confinement present in SiMOS devices. Here the inter-dot pitches matches that of Si/SiGe at 80 nm. For Si/SiGe (b), we see significant cross-coupling between adjacent plungers and barrier gates. Here the plunger gates are written before the barrier layer and have an inter-dot pitch of 80 nm. Ge/SiGe (c) reveals as expected a slower fall-off of cross coupling. We attribute this to the larger plunger gate design, made possible by lower hole effective mass. In this case, the plunger gates P_1 and P_2 are written in the layer above the barrier gates B_{12} and RB_2 , decreasing coupling to their respective quantum dots. The plunger to plunger pitch is 200 nm. Each cross-sectional cartoon shows plunger pitch and distance between each relevant gate layer to the center of the quantum well.

3.3. SINGLY OCCUPIED QUANTUM DOT ARRAYS

To demonstrate the success of this largely unified integration scheme, we show that we can create stable quantum dots in each platform. Figure 3.4 shows charge stability diagrams for tunnel-coupled double quantum dots, measured by performing charge sensing. Lock-in techniques are used in the case of SiMOS and Ge/SiGe, where an excitation is placed on an inter-dot barrier gate B_{12} in each case, and the trans-conductance of the source-drain channel is measured. We use compensation to remain at a sensitive point of the SET/SHT Coulomb peaks [46]. In the case of Si/SiGe, charge readout is performed using RF-reflectometry techniques. A $3 \mu\text{H}$ kinetic inductor is bonded to the sample source which forms a resonant LC circuit when combined with parasitic capacitance to ground. In each case we measure a charge stability diagram and show that we can deplete down to the (0,0) electron/hole charge configuration. This is done by ensuring that the load rate of each quantum dot is sufficiently high, and depleting to the first charge state of each

quantum dot by sweeping the associated plunger gate, until no further charge transition lines are detected (for details in tuning to the last state see our previous works [18, 47]). While operation in the single electron regime in silicon has been routinely achieved before, this work shows the first demonstration of the single hole regime using charge sensing of holes in Ge/SiGe. We attribute the slight difference in slope of the first and second charge addition lines in Fig. 3.4c to a shift in the position of the quantum dot relative to the inter-dot tunnel barrier.

In Fig 3.5. we demonstrate that quantum dots can be formed under each dedicated plunger gate. For Fig. 3.5 (a-c), in each SiMOS quantum dot, lock-in charge sensing is performed by placing an excitation on the respective plunger gates, while trans-conductance in the nearby SET channel is measured. In each case, the first charge transition is visible. For quantum dots formed under plungers P_{2-3} , electron loading is from the right SET which constitutes a reservoir. For the quantum dot under P_1 , loading is from the left SET via the gate T_l . The Si/SiGe quintuple quantum dot system in Fig 5(d-g) is tuned using the N+1 strategy [43], reaching the few-electron regime simultaneously for all quantum dots. In Fig. 3.5 we show stability diagrams, in each of which we scan two virtual plunger gates which allow to controllably load a single electron into each quantum dot. Double quantum dots are formed between each set of adjacent plungers, and sensed using RF-reflectometry like in Fig. 3.4b using the left SET for all configurations. As expected, observable signal from charge transition lines fades as the quantum dot pairs are formed farther away from the SET. The derivative of the reflected signal is plotted, and shows the (0,0) charge occupancy for each charge stability diagram. For every double quantum dot, loading occurs via the left accumulation gate, leading to latching effects and low tunnel rates in the quantum dots formed farther away from the reservoir. Figure 3.5 (h-k) shows charge sensing operation of the 2x2 quantum dot array fabricated in Ge/SiGe. In each case, a sensing quantum dot is formed in the channel parallel to the double quantum dot by opening the inter-dot barrier such that a large single quantum dot is formed. In the opposite channel, the inter-dot barrier is closed, forming a double quantum dot system in the low tunnel coupled regime.

3.4. CROSS CAPACITANCE

A significant challenge for larger quantum dot arrays will manifest in tuning. The presence of large capacitive crosstalk in GaAs has led to development of virtual gates and approaches to tune larger systems [43, 48]. To assess the relevance of these approaches for silicon and germanium structures we measure cross capacitance as show in Fig. 3.6. To obtain the cross coupling, we measure the slope of the charge addition lines with respect to each gate and normalize by a cross coupling of unity for the plunger gate associated with the respective quantum dot. Each slope is taken for the first charge transition and in the low tunnel-coupled regime. In SiMOS, cross coupling is almost negligible, as expected from quantum dots located only 17 nm (10 nm SiO₂ and 7 nm Al₂O₃) below the electrostatic gates. This compares favourably to the cross coupling observed in Si/SiGe, where falloff is significantly slower despite sharing equal gate pitch to the SiMOS array. While the cross coupling in the Ge/SiGe system is the largest and extends over multiple neighbouring gates, it still falls off significantly faster than quantum dots defined in GaAs [43]. For Ge/SiGe, we also observe that the barrier gates have a relatively stronger lever arm to the quantum dots as compared to the plunger gates, due to definition in lower layers of the multi-layer stack. Summarizing, we conclude that for SiMOS tuning is most straightforward considering capacitive cross talk only, while each platform compares favourably to GaAs using an open gate layout [43].

With the ability to fabricate quantum dot devices in several group IV based platforms using a unified fabrication scheme, we look ahead to identify future challenges and opportunities related to

quantum information processing with semiconductor quantum dot spin qubits.

3.5. FUTURE PERSPECTIVES

Moving forwards, we identify four focus areas for the community that through shared co-development, will launch the field into new and practical ground.

Most quantum devices are fabricated in academic cleanrooms, where the turnaround and feedback from measurement to design and fabrication is fast. However as designs for various types of quantum dot devices converge, an opportunity exists to leverage off the excellent material quality [14, 37, 49] and processing facilities of industrial fabrication lines. Devices fabricated on industrially-grown 300 mm wafers have led to CMOS fab spin qubits [26], tuneable tunnel coupling between single electrons in SiMOS [18] and two-qubit gate operations beyond one Kelvin [50]. Furthering symbiotic partnerships with industry may prove highly beneficial for the development of uniform quantum dots. The adoption of group IV based semiconductor platforms beyond SiMOS such as strained Si and Ge as well as full 300 mm device fabrication lines would accelerate progress in the field of semiconductor quantum dot based quantum computing, like it has in other fields[51].

Many quantum systems have been studied as qubit candidates for quantum information processing. It has also become clear that each of these quantum systems hold specific properties suited to the various requirements of quantum computation[52]. As a result, emerging research has targeted the combination of qubit implementation to leverage off specific advantages and improve qubit quality. These hybrid directions are extensive, including the coupling of spin to light allowing for long range interactions as has been shown on silicon based platforms[53–56], or the coupling of spins to systems that reliably conserve the quantum state, such as topologically protected qubits[57–60]. Here, holes in Ge/SiGe make an excellent candidate for hybrid spin-Majorana qubits, thanks to the Fermi level pinning at the valence band, allowing for tunnel-coupled contacts to superconductors [31]. An important milestone towards demonstrating such a hybrid qubit in Ge/SiGe will be to achieve hard gap superconductivity. This has already been demonstrated in Ge/SiGe core shell nanowires[61, 62], thus providing scope for planar structures. Such a hard gap would be the first step toward defining isolated zero energy states, key in many proposals for hybrid technology [63].

As quantum devices grow in number of physical qubits, so too do the complexities related to tuning them. As a result, a great body of work on the automated tuning of quantum devices has emerged in the last few years in an attempt to address this concern. Due to the extremely low disorder of the material, these efforts were pioneered in GaAs based quantum dots, demonstrating automated tuning to the single electron regime [48, 64] and controllable interdot tunnel coupling [65]. However quantum dot arrays have also emerged more recently in Si/SiGe [66] and computer automated single electron regime tune-up protocols therein[67, 68]. Moreover, with the demonstrations of SiMOS, Si/SiGe, and Ge/SiGe quantum dots in this work, further development of automated tuning protocols will be necessary for the exploration of larger quantum dot systems. In particular the automated tuning of interdot tunnel couplings and protocols for 2D arrays will be critical. Furthermore, high fidelity operation of qubits in large scale quantum devices will require precise operation at exact exchange interaction, resonance frequencies and Rabi frequencies, accounting for potential drifts in these parameters over time. Tune up protocols will therefore have to go beyond charge state control, handling qubit operation also.

Scale up of the number of qubits on a quantum device requires the design and implementation of extensible two-dimensional qubit arrays. However, the wiring and fanout for each qubit at large numbers is impractical and there is a need to engineer architectures that obey Rent's rule [69]. Additionally, the limited cooling power of dilution refrigerators at mK temperatures poses a serious challenge for the scalability of quantum systems [10]. As a result, proposals for shared control using crossbar architectures [70, 71] and on chip classical electronics [10] have been put forward, as well as work on the operation of qubits at high temperatures [50, 72] to mitigate the cooling power requirements of dilution refrigerators. 2D scalability will also require improved operation of larger quantum devices. This includes the ability to tune all quantum dot couplings and to shuttle spin states coherently around a lattice, placing strict requirements on the uniformity of quantum dots. This positions Si/SiGe and Ge/SiGe as favourable platforms due to their very low disorder. A milestone in 2D scalability would be the routine ability to reach single charge occupancy in arbitrary quantum dots using the same cross-capacitance matrix for each quantum dot as this would enable shared control for scalable quantum operation as is proposed in crossbar architectures [71]. We observe Si/SiGe double quantum dots that can be tuned to the (1,1) charge state using identical plunger gates (e.g. Fig. 3.4b), but further progress is essential to enable shared control in large arrays. Solutions to these outstanding hurdles will be crucial to further develop extensible qubit unit cells and therefore scale quantum devices into practically useful regimes.

3.6. CONCLUSION

In conclusion we presented a cross-platform integration scheme for multi-layer quantum dot arrays in group-IV semiconductor hosts. We fabricated linear and 2D arrays of quantum dots in the group IV platforms SiMOS, Si/SiGe and Ge/SiGe. We demonstrated single electron and hole occupancy in double quantum dots confirmed by charge sensing. We showed stable quantum dots under each plunger gate in a SiMOS triple quantum dot linear array, depleteable to the final charge state. In Si/SiGe, we demonstrated tune-up of a quintuple quantum dot array utilizing the N+1 method, successfully reaching the few electron regime in each quantum dot simultaneously. Moreover, we formed and sensed double quantum dots in the single hole regime in each configuration of a 2x2 quadruple quantum dot array in Ge/SiGe. We furthermore compared the capacitive cross talk between quantum dots and gates. We find that the cross capacitance can be small and therefore argue that future work on strategies for the initial tuning of quantum dot arrays should address disorder rather than capacitive cross talk, in particular for SiMOS quantum dots. We envision that our integration scheme for fabricating quantum dot arrays in SiMOS, Si/SiGe, and Ge/SiGe will boost collective development and enable the realization of devices capable of simulating and computing with quantum information.

We envision that our realization of an integration scheme to build quantum dots in SiMOS, Si/SiGe, and Ge/SiGe will boost the collective development toward large quantum dot arrays to build, simulate, and compute with quantum information.

3.7. SiMOS FABRICATION IMPROVEMENTS

3.7.1. GATE ANNEAL

In silicon MOS, anneals are generally used to repair damage caused by e-beam exposure and to improve the structural quality of metal gates. We find that for SiMOS quantum dot devices, the quality of the gates can be improved by the incorporation of a forming gas anneal at 400 °C for 15 min after each gate deposition. Figure 3.7(a) shows a scanning electron microscope (SEM) image of a device for which the anneal was implemented. Figures 3.7(b)-(g) show SEM and Atomic Force

Microscopy (AFM) images for two gate layers of a SiMOS device. We observe a large reduction of surface roughness and sidewall height, which improves even further the homogeneity and yield of the metallic gates.

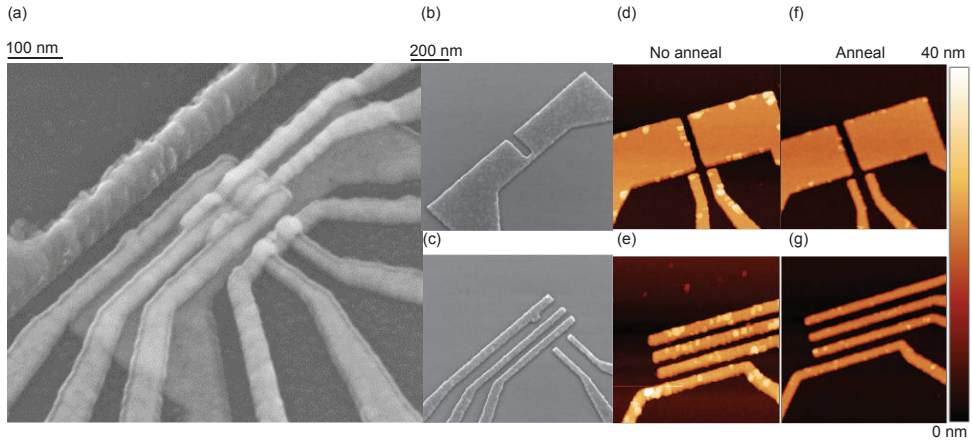


Figure 3.7: (a,b,c) SEM images taken under a 30° angle of (a) full device fabricated with a gate anneal. (b,c) Separate layers after a gate anneal. (d,e,f,g) AFM images of separate gate layers before (d,e) and after (f,g) a gate anneal. The anneal results in a smoother surface with less grains and sidewalls.

3.7.2. ALD WINDOW ETCH

Incorporating atomic layer deposition (ALD) of Al_2O_3 into the gate stack introduces further sources of charge noise [42] making it undesirable in the active region of spin qubits. On the other hand, it is necessary to prevent inter-gate leakage when utilizing a Ti:Pd multi-layer gate stack, as well as leakage to substrate. In the case of SiMOS, fabrication begins on a 10 nm SiO_2 dielectric grown across the substrate. While high in quality, due to the sheer area overlap of gate fan-out, there is a non-negligible probability that a gate may overlap with a region of damaged dielectric. To prevent leakage of gate layers to substrate in our SiMOS stack, we find an initial blanket layer of Al_2O_3 is necessary. An etching process (see section 3.8 regarding fabrication details) with a high selectivity of Al_2O_3 over SiO_2 allows us to locally remove this layer in the active region. Figure 3.8 shows charge stability diagrams of two identically processed quantum dot devices in SiMOS where Al_2O_3 was present or where an oxide window was etched. Without etching, charge noise causes significant fluctuations in the quantum dot potential, which can be observed from the constantly shifting charge addition lines in Fig. 3.8a. Instead, when an oxide window is etched, we observe stable transitions, see Fig. 3.8b. We attribute this stability to the removal of the ALD layer beneath the first gate layer. We note that this behaviour is reproducible in and consistent with other SiMOS quantum dot devices fabricated with and without the removal of the initial ALD layer in the quantum dot active region.

3.8. EXTENDED FABRICATION RECIPE

Here we present the full fabrication process for each platform, specifically for the devices fabricated and studied in the work.

In the case of SiMOS, fabrication begins on a natural silicon wafer, with 1 μm of intrinsic silicon

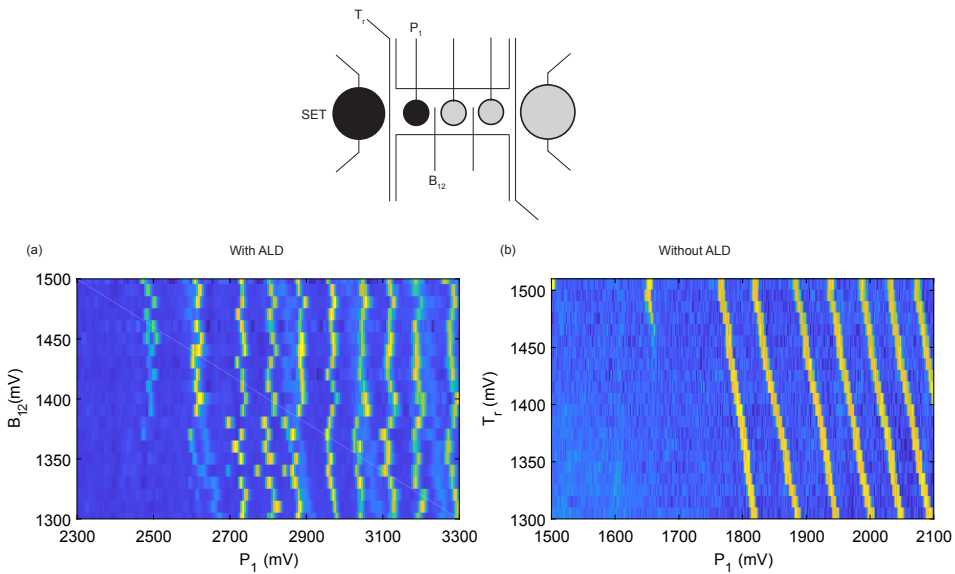


Figure 3.8: Charge stability diagrams via lock-in charge sensing of identically processed quantum dot devices in SiMOS, with the exception of an oxide window etch step. (a) Typical stability behaviour of a single quantum dot with a layer of Al_2O_3 beneath the screening layer. (b) Device processed with oxide window etch step. Stability markedly improves over previous case.

	SIMOS	Si/SiGe	Ge/SiGe
Deposit marker layer 1 Material M	W markers EBL	Etched markers Optical Litho	-
Open implant windows at energy E, fluence n	$E = 6 \text{ keV}, n = 1 \times 10^{16} \text{ cm}^{-2}$	$E = 20 \text{ keV}, n = 5 \times 10^{15} \text{ cm}^{-2}$	-
Anneal and activate at temperature T, time t in an RTP, nitrogen atmos- phere	$T = 1000 \text{ C}, t = 30 \text{ s}$	$T = 700 \text{ C}, t = 30 \text{ s}$	-
Define and write second marker layer Ti:Pt (5.55 nm)	✓	✓	✓
HF etch, imidiately before evaporation of Ohmics (material M) at thickness t	M = Ti:Pt $t = 5.55 \text{ nm}$	M = Ti:Pt $t = 5.55 \text{ nm}$	M = Al $t = 30 \text{ nm}$
1 h vacuum anneal at 300 °C Gate Isolation ALD Al_2O_3 thickness t	$t = 10 \text{ nm}$	$t = 5 \text{ nm}$	$t = 10 \text{ nm}$
Transene etch ALD in active window 50 °C	✓	-	-
Deposit gate stack in layers L at thicknesses t_i with gate anneal $T = 400 \text{ °C}$, 15 mins in Forming gas. Interlayer isolation ALD thickness t.	$t_{\text{scr}} = 3:17 \text{ nm}$ $t_{\text{pig}} = 3:37 \text{ nm}$ $t_{\text{bar}} = 3:37 \text{ nm}$ $t_{\text{ALD}} = 7 \text{ nm}$ Gate anneal ✓	$t_{\text{scr}} = 3:17 \text{ nm}$ $t_{\text{pig}} = 3:37 \text{ nm}$ $t_{\text{bar}} = 3:37 \text{ nm}$ $t_{\text{ALD}} = 7 \text{ nm}$ Gate anneal x	$t_{\text{scr}} = 3:17 \text{ nm}$ $t_{\text{bar}} = 3:37 \text{ nm}$ $t_{\text{pig}} = 10 \text{ nm}$ $t_{\text{ALD}} = 10 \text{ nm}$ Gate anneal x
Deposit qubit control layer Micromagnet or MW Antenna Thickness t, material M	Antenna M = Al $t = 100 \text{ nm}$	Micromagnet M = Ti:Co $t = 5:200 \text{ nm}$	-
End of Line Anneal $T = 400 \text{ °C}$, 30 mins Forming gas.	✓	-	x

Figure 3.9: Full fabrication recipe for the three platforms presented in this work. Ticks represent a used and compatible process, dashes represent a not-used but not necessarily incompatible process, and crosses indicate an unused and incompatible process.

grown, followed by 100 nm epilayer ^{28}Si , and a 10 nm thermally grown oxide [14]. First, tungsten (W) markers are patterned, which are used to define implant windows via electron beam lithography (EBL). After exposure, phosphorus ions (P^+) at 6 keV are implanted to create highly negatively doped (n^{++}) regions in each die. An activation anneal is conducted in a rapid thermal processor (RTP) at 1000 °C for 30 seconds. A buffered hydro-fluoric (BHF) etch removes oxide in bond-pad areas, where Ti:Pt (5:55 nm) metallic contacts are deposited, creating ohmic contacts. A second layer of Ti:Pt markers are also written in this step. Next, a blanket Al_2O_3 ALD layer of 10 nm is grown across the entire sample. A small $20 \times 20 \mu\text{m}^2$ area is exposed and etched away in the vicinity of the quantum dot formation area. This improves dot stability (see Fig. 3.8). Large rounded rectangular regions are then exposed in regions where wirebonding is expected, and 150 nm of SiN is sputtered. These create safer bondpads with which to bond to, reducing leakage and improving device yield. The SiMOS device presented in the work utilizes a three layer Ti:Pd gate stack. (3:17, 3:37, 3:37 nm). After each layer, the device is annealed in a RTP furnace for 15 minutes at 400 °C in forming gas, then a layer of ALD is grown at 7 nm thickness. Next, the qubit control layer is deposited. This can either be an Al or NbTiN antenna of 100 nm thickness for Electron spin resonance driving, or a Ti:Co micromagnet (5:195 nm) for Electron dipole spin resonance. The final step is an end of line anneal at 400 °C for 30 minutes in forming gas in a RTP.

The Si/SiGe 5 dot linear array begins on a natural silicon substrate. A linearly graded $\text{Si}_{1-x}\text{Ge}_x$ layer is deposited where x ranges from 0 to 0.3. A relaxed $\text{Si}_{0.7}\text{Ge}_{0.3}$ layer of 300 nm lies below the 10 nm ^{28}Si (800 ppm purity) quantum well which itself is separated from the 2 nm Si capping layer by a second 30 nm relaxed $\text{Si}_{0.7}\text{Ge}_{0.3}$ spacer layer. The initial marker layer is written using optical lithography and is formed by etching away the SiO_2 . Next, a BHF dip removes native oxide selectively where ohmic contacts of Ti:Pt (5:55 nm) are evaporated, alongside a second set of markers. Gate stack fabrication of the device is almost identical to that of SiMOS. It is a 3-layer Ti:Pd stack of the same thicknesses, interlayer isolated via 7 nm of Al_2O_3 . However, we do not employ a gate anneal between gate layers, despite this technically being possible within the context of thermal budget. For control, both striplines and micromagnets are available, however we prefer the electrical driving option since electron wavefunctions in Si/SiGe tend to be more mobile and hence EDSR provides a route to faster driving. We do not conduct an end of line anneal on SiGe devices.

For the fabrication of the Ge/SiGe 2x2 array, we begin with a natural silicon substrate, upon which 1.4 μm of Ge and 900 nm of reverse graded $\text{Si}_{1-x}\text{Ge}_x$ where x ranges from 1 to 0.8 is grown. This lies below a 160 nm $\text{Si}_{0.2}\text{Ge}_{0.8}$ spacer layer, a 16 nm Ge quantum well under compressive strain, a second $\text{Si}_{0.2}\text{Ge}_{0.8}$ layer of 22 nm and finally a thin Si cap of 1 nm [13]. Ti:Pt EBL markers are then defined for future alignment. A short HF acid etch is conducted immediately before depositing 30 nm Al on regions where ohmic contact is desired. An advantage of the Ge/SiGe platform is the possibility of ohmic formation extremely close (within ≈ 100 nm) of the quantum dot. Devices are then placed under vacuum for 1 h at 300 °C causing Al to diffuse through the heterostructure into the quantum well forming ohmic contact. Atomic Layer Deposition is then performed covering the sample in a 10 nm Al_2O_3 blanket. The gate stack consists of two layers, barrier and plunger. The barrier layer is deposited at 20 nm total thickness utilizing the Ti:Pd stack (3:17 nm). The plunger layer is deposited at 40 nm total thickness (3:37 nm). No further processing is required as the large intrinsic Spin-Orbit coupling of holes in Ge/SiGe provides a native electric driving mechanism [31].

REFERENCES

- [1] Lawrie, W. I. L. *et al.* Quantum Dot Arrays in Silicon and Germanium. *Applied Physics Letters* **116**, 080501 (2020).
- [2] Loss, D. & DiVincenzo, D. P. Quantum computation with quantum dots. *Physical Review A - Atomic, Molecular, and Optical Physics* **57**, 120–126 (1998).
- [3] Hensgens, T. *et al.* Quantum simulation of a Fermi-Hubbard model using a semiconductor quantum dot array. *Nature* **548**, 70–73 (2017).
- [4] Leijnse, M. & Flensberg, K. Scheme to measure Majorana fermion lifetimes using a quantum dot. *Physical Review B* **84**, 140501 (2011).
- [5] Sau, J. D. & Sarma, S. D. Realizing a robust practical Majorana chain in a quantum-dot-superconductor linear array. *Nature Communications* **3**, 964 (2012).
- [6] Petta, J. R. *et al.* Coherent Manipulation of Electron Spins in Semiconductor Quantum Dots. *Science* **309**, 2180–2184 (2005).
- [7] Koppens, F. H. *et al.* Driven coherent oscillations of a single electron spin in a quantum dot. *Nature* **442**, 766–771 (2006).
- [8] Dehollain, J. P. *et al.* *Nature* .
- [9] Mourik, V. *et al.* Signatures of majorana fermions in hybrid superconductor-semiconductor nanowire devices. *Science* **336**, 1003–1007 (2012).
- [10] Vandersypen, L. M. K. *et al.* Interfacing spin qubits in quantum dots and donors - hot, dense and coherent. *npj Quantum Information* **3**, 34 (2016).
- [11] Veldhorst, M. *et al.* An addressable quantum dot qubit with fault-tolerant control-fidelity. *Nature Nanotechnology* **9**, 981–985 (2014).
- [12] Zwanenburg, F. A. *et al.* Silicon quantum electronics. *Reviews of Modern Physics* **85**, 961–1019 (2013).
- [13] Sammak, A. *et al.* Shallow and Undoped Germanium Quantum Wells: A Playground for Spin and Hybrid Quantum Technology. *Advanced Functional Materials* **29**, 1807613 (2019).
- [14] Sabbagh, D. *et al.* Quantum Transport Properties of Industrial Si 28 / Si O 2 28 . *Physical Review Applied* **12** (2019).
- [15] Angus, S. J., Ferguson, A. J., Dzurak, A. S. & Clark, R. G. Gate-defined quantum dots in intrinsic silicon. *Nano Letters* **7**, 2051–2055 (2007).
- [16] Zajac, D. M., Hazard, T. M., Mi, X., Wang, K. & Petta, J. R. A reconfigurable gate architecture for Si/SiGe quantum dots. *Applied Physics Letters* **106**, 223507 (2015).
- [17] Brauns, M., Amitonov, S. V., Spruijtenburg, P. C. & Zwanenburg, F. A. Palladium gates for reproducible quantum dots in silicon. *Scientific Reports* **8**, 5690 (2018).
- [18] Eenink, H. G. J. *et al.* Tunable coupling and isolation of single electrons in silicon quantum dots. *Nano Letters* **19**, 8653–8657 (2019).

- [19] Yang, C. H. *et al.* Silicon qubit fidelities approaching incoherent noise limits via pulse engineering. *Nature Electronics* **2**, 151–158 (2019).
- [20] Yoneda, J. *et al.* A quantum-dot spin qubit with coherence limited by charge noise and fidelity higher than 99.9%. *Nature Nanotechnology* **13**, 102–106 (2018).
- [21] Veldhorst, M. *et al.* A two-qubit logic gate in silicon. *Nature* **526**, 410–414 (2015).
- [22] Zajac, D. M. *et al.* Resonantly driven CNOT gate for electron spins. *Science* **359**, 439–442 (2018).
- [23] Watson, T. F. *et al.* A programmable two-qubit quantum processor in silicon. *Nature* **555**, 633–637 (2018).
- [24] Spruijtenburg, P. C. *et al.* Single-hole tunneling through a two-dimensional hole gas in intrinsic silicon. *Applied Physics Letters* **102**, 192105 (2013).
- [25] Liles, S. D. *et al.* Spin and orbital structure of the first six holes in a silicon metal-oxide-semiconductor quantum dot. *Nature Communications* **9**, 3255 (2018).
- [26] Maurand, R. *et al.* A CMOS silicon spin qubit. *Nature Communications* **7**, 13575 (2016).
- [27] Failla, M. *et al.* Terahertz quantum Hall effect for spin-split heavy-hole gases in strained Ge quantum wells. *New Journal of Physics* **18**, 113036 (2016).
- [28] Su, Y. H., Chuang, Y., Liu, C. Y., Li, J. Y. & Lu, T. M. Effects of surface tunneling of two-dimensional hole gases in undoped Ge/GeSi heterostructures. *Physical Review Materials* **1**, 044601 (2017).
- [29] Lodari, M. *et al.* Light effective hole mass in undoped Ge/SiGe quantum wells. *Physical Review B* **100**, 041304 (2019).
- [30] Hendrickx, N. W. *et al.* Gate-controlled quantum dots and superconductivity in planar germanium. *Nature Communications* **9**, 2835 (2018).
- [31] Hendrickx, N. W., Franke, D. P., Sammak, A., Scappucci, G. & Veldhorst, M. Fast two-qubit logic with holes in germanium (2019).
- [32] Dimoulas, A., Tsipas, P., Sotiropoulos, A. & Evangelou, E. K. Fermi-level pinning and charge neutrality level in germanium. *Applied Physics Letters* **89**, 252110 (2006).
- [33] Petit, L. *et al.* Spin Lifetime and Charge Noise in Hot Silicon Quantum Dot Qubits. *Physical Review Letters* **121**, 076801 (2018).
- [34] Ando, T., Fowler, A. B. & Stern, F. Electronic properties of two-dimensional systems. *Reviews of Modern Physics* **54**, 437–672 (1982).
- [35] Gold, A. & Dolgoplov, V. T. Temperature dependence of the conductivity for the two-dimensional electron gas: Analytical results for low temperatures. *Physical Review B* **33**, 1076–1084 (1986).
- [36] Kruihof, G. H., Klapwijk, T. M. & Bakker, S. Temperature and interface-roughness dependence of the electron mobility in high-mobility Si(100) inversion layers below 4.2 K. *Physical Review B* **43**, 6642–6649 (1991).

- [37] Wuetz, B. P. *et al.* Multiplexed quantum transport using commercial off-the-shelf CMOS at sub-kelvin temperatures. *arXiv 1907.11816* (2019).
- [38] Jock, R. M. *et al.* A silicon metal-oxide-semiconductor electron spin-orbit qubit. *Nature Communications* **9**, 1768 (2018).
- [39] Huang, W., Veldhorst, M., Zimmerman, N. M., Dzurak, A. S. & Culcer, D. Electrically driven spin qubit based on valley mixing. *Physical Review B* **95**, 075403 (2017).
- [40] Bracht, H., Haller, E. E. & Clark-Phelps, R. Silicon self-diffusion in isotope heterostructures. *Physical Review Letters* **81**, 393–396 (1998).
- [41] Hendrickx, N. W. *et al.* Ballistic supercurrent discretization and micrometer-long Josephson coupling in germanium. *Physical Review B* **99**, 075435 (2019).
- [42] Connors, E. J., Nelson, J., Qiao, H., Edge, L. F. & Nichol, J. M. Low-frequency charge noise in Si/SiGe quantum dots. *Physical Review B* **100**, 165305 (2019).
- [43] Volk, C. *et al.* Loading a quantum-dot based "Qubyte" register. *npj Quantum Information* **5**, 29 (2019).
- [44] Watzinger, H. *et al.* A germanium hole spin qubit. *Nature Communications* **9**, 3902 (2018).
- [45] Kawakami, E. *et al.* Electrical control of a long-lived spin qubit in a Si/SiGe quantum dot. *Nature Nanotechnology* **9**, 666–670 (2014).
- [46] Yang, C. H., Lim, W. H., Zwanenburg, F. A. & Dzurak, A. S. Dynamically controlled charge sensing of a few-electron silicon quantum dot. *AIP Advances* **1**, 042111 (2011).
- [47] Hendrickx, N. W. *et al.* *Nature Communications* .
- [48] Baart, T. A. *et al.* Single-spin CCD. *Nature Nanotechnology* **11**, 330–334 (2016).
- [49] Mazzocchi, V. *et al.* 99.992% 28 Si CVD-grown epilayer on 300 mm substrates for large scale integration of silicon spin qubits. *Journal of Crystal Growth* **509**, 1–7 (2019).
- [50] Petit, L. *et al.* *Nature* .
- [51] Arute, F. *et al.* Supplementary information for "Quantum supremacy using a programmable superconducting processor". *Nature* **574**, 505 (2019).
- [52] DiVincenzo, D. P. The physical implementation of quantum computation. *Fortschritte der Physik* **48**, 771–783 (2000).
- [53] Mi, X. *et al.* A coherent spin-photon interface in silicon. *Nature* **555**, 599–603 (2018).
- [54] Samkharadze, N. *et al.* Strong spin-photon coupling in silicon. *Science* **359**, 1123–1127 (2018).
- [55] Landig, A. J. *et al.* Coherent spin-photon coupling using a resonant exchange qubit. *Nature* **560**, 179–184 (2018).
- [56] Borjans, F., Croot, X. G., Mi, X., Gullans, M. J. & Petta, J. R. Resonant microwave-mediated interactions between distant electron spins. *Nature* (2019).
- [57] Leijnse, M. & Flensberg, K. Hybrid topological-spin qubit systems for two-qubit-spin gates. *Physical Review B* **86** (2012).

- [58] Sarma, S. D., Freedman, M. & Nayak, C. Topologically protected qubits from a possible non-abelian fractional quantum hall state. *Physical Review Letters* **94** (2005).
- [59] Hyart, T. *et al.* Flux-controlled quantum computation with Majorana fermions. *Physical Review B* **88** (2013).
- [60] Hoffman, S., Schrade, C., Klinovaja, J. & Loss, D. Universal quantum computation with hybrid spin-Majorana qubits. *Physical Review B* **94** (2016).
- [61] Xiang, J., Vidan, A., Tinkham, M., Westervelt, R. M. & Lieber, C. M. Ge/Si nanowire mesoscopic josephson junctions. *Nature Nanotechnology* **1**, 208–213 (2006).
- [62] Ridderbos, J. *et al.* Hard superconducting gap and diffusion-induced superconductors in Ge-Si nanowires. *Nano Letters* [acs.nanolett.9b03438](https://doi.org/10.1021/acs.nanolett.9b03438) (2019).
- [63] Alicea, J. New directions in the pursuit of Majorana fermions in solid state systems. *Reports on Progress in Physics* **75** (2012).
- [64] Botzem, T. *et al.* Tuning Methods for Semiconductor Spin Qubits. *Physical Review Applied* **10**, 54026 (2018).
- [65] Van Diepen, C. J. *et al.* Automated tuning of inter-dot tunnel coupling in double quantum dots. *Applied Physics Letters* **113**, 33101 (2018).
- [66] Mills, A. R. *et al.* Computer-automated tuning procedures for semiconductor quantum dot arrays. *Applied Physics Letters* **115**, 113501 (2019).
- [67] Mills, A. R. *et al.* Shuttling a single charge across a one-dimensional array of silicon quantum dots. *Nature Communications* **10** (2019).
- [68] Kalantre, S. S. *et al.* Machine learning techniques for state recognition and auto-tuning in quantum dots. *npj Quantum Information* **5** (2019).
- [69] Franke, D. P., Clarke, J. S., Vandersypen, L. M. & Veldhorst, M. Rent's rule and extensibility in quantum computing. *Microprocessors and Microsystems* **67**, 1–7 (2019).
- [70] Veldhorst, M., Eenink, H. G., Yang, C. H. & Dzurak, A. S. Silicon CMOS architecture for a spin-based quantum computer. *Nature Communications* **8** (2017).
- [71] Li, R. *et al.* A crossbar network for silicon quantum dot qubits. *Science Advances* **4**, eaar3960 (2018).
- [72] Yang, C. H. *et al.* Operation of a silicon quantum processor unit cell above one kelvin. *nature* **580**, 350–354 (2020).



SILICON

Silicon is a semiconductor material that has been the driving force behind Moore's law - the doubling of the number of transistors on a chip every two years - since the 1960's. It is therefore no surprise that it is a thoroughly studied material, with a tremendous wealth of knowledge available regarding its material properties, and processing techniques. This abundance of experience makes silicon an excellent material to investigate as a quantum computing platform.

Realizing qubits in silicon can be done in different ways. However the metal-oxide-semiconductor format is perhaps most industrially compatible, given it is also how modern transistors are created. Therefore realizing quantum bits in a SiMOS platform would be highly advantageous when considering the potential to bootstrap off existing industrial infrastructure.

Indeed, electron spin qubits in SiMOS quantum dots have proven highly successful qubit candidates, demonstrating spin relaxation times longer than a second [1], dephasing times as high as 120 μ s [2], single qubit Clifford gate fidelities as high as 99.967 % [3], and two qubit gate fidelities up to 98 % [4]. However, some challenges, for SiMOS and for spin qubits in general remain outstanding.

Firstly, the relatively low electron mobility at the Si-SiO₂ interface suggests a high interface trap density, that can lead to unwanted quantum dot formation and highly immobile wavefunctions. These traits can complicate qubit-qubit interactions. In other words, tunnel couple control using dedicated barrier gates has been difficult to realise in SiMOS quantum dot devices. Chapter 4 explicitly addresses this limitation, by employing the fabrication techniques presented in Chapter 3, a SiMOS double quantum dot device is realised with tuneable tunnel coupling.

A second major challenge pertaining to all spin qubit platforms is scale-up. On average, every qubit in contemporary semiconductor devices require multiple electrostatic gates, and a microwave signal, which must route from the device (in a dilution refrigerator) to room temperature via wire looms, and low loss cables capable of transmitting high frequency signals. This is a manageable problem for a few qubits, but for the large numbers required for useful quantum computing, this interconnect problem is completely intractable. As a result, it has been suggested that the electronics be defined on-chip alongside arrays of qubits in an interspersed, modular fashion [5]. While helping with the interconnect problem, this methodology would result in large amounts of heat being dispersed, far beyond the cooling power of conventional dilution refrigerators. As a result, it would be highly advantageous to operate qubits at higher temperatures, where the cooling power is much higher. In chapter 5, we demonstrate the universal operation of a two-qubit quantum processor at temperatures above 1 K, a significant milestone for scalable spin qubit quantum processors.

REFERENCES

- [1] Zwerver, A. M. J. *et al.* Qubits made by advanced semiconductor manufacturing. *arXiv* 2101.1265 (2021).
- [2] Veldhorst, M. *et al.* An addressable quantum dot qubit with fault-tolerant control-fidelity. *Nature Nanotechnology* **9**, 981–985 (2014).

- [3] Yang, C. H. *et al.* Silicon qubit fidelities approaching incoherent noise limits via pulse engineering. *Nature Electronics* **2**, 151–158 (2019).
- [4] Huang, W. *et al.* Fidelity benchmarks for two-qubit gates in silicon. *Nature* **569**, 532–536 (2019).
- [5] Vandersypen, L. M. K. *et al.* Interfacing spin qubits in quantum dots and donors—hot, dense, and coherent. *npj Quantum Information* **3**, 1–10 (2017).

4

TUNEABLE COUPLING AND ISOLATION OF SINGLE ELECTRONS IN SILICON QUANTUM DOTS

Extremely long coherence times, excellent single-qubit gate fidelities and two-qubit logic have been demonstrated with silicon metal-oxide-semiconductor spin qubits, making it one of the leading platforms for quantum information processing. Despite this, a long-standing challenge has been the demonstration of tunable tunnel coupling between single electrons. Here we overcome this hurdle with gate-defined quantum dots and show couplings that can be tuned on and off for quantum operation. We use charge sensing to discriminate between the (2,0) and (1,1) charge states of a double quantum dot and show high charge sensitivity. We demonstrate tunable coupling up to 13 GHz, obtained by fitting charge polarization lines, and tunable tunnel rates down to below 1 Hz, deduced from the random telegraph signal. The demonstration of tunable coupling between single electrons in silicon provides significant scope for high-fidelity two-qubit logic toward quantum information processing with standard manufacturing.

Parts of this chapter have been published in Nano Lett. 19 (12) 8653-8657.

4.1. INTRODUCTION

Quantum computation with quantum dots has been proposed using qubits defined on the spin states of one [1], two [2] or more [3, 4] electrons. In all these proposals, a crucial element required to realize a universal quantum gate set is the exchange interaction between electrons. The exchange interaction is set by the tunnel coupling and detuning, and gaining precise control over these parameters enables to define and operate qubits at their optimal points [5–8]. Excellent control has already been reported in GaAs [5, 6, 9], strained silicon [10, 11], and more recently in strained germanium [12, 13]. Reaching this level of control in silicon metal-oxide-semiconductor (SiMOS) quantum dots is highly desired as this platform has a high potential for complete integration with classical manufacturing technology [14–16]. However, current two-qubit logic with single spins in SiMOS is based on controlling the exchange using the detuning only [17] or is executed at fixed exchange interaction [18].

In SiMOS, a first step toward the required control to materialize architectures for large-scale quantum computation [1, 19–24] has been the demonstration of tunable coupling in a double quantum dot system operated in the many-electron regime, where gaining control is more accessible owing to the larger electron wave function [25, 26]. More recently, exchange-controlled two-qubit operations have been shown with three-electron quantum dots [27]. However, tunnel couplings between single electrons that can be switched off and turned on for qubit operation still remain to be shown in SiMOS.

In this work we show a high degree of control over the tunnel coupling of single electrons residing in two gate-defined quantum dots in a SiMOS device. The system is stable and no unintentional quantum dots are observed. We are able to measure charge transitions using a sensitive single-electron-transistor (SET) as charge sensor, and characterize the system in the single-electron regime. From a comparison of charge stability diagrams of weakly and strongly coupled double quantum dots, we conclude that we control the tunnel coupling by changing quantum dot location. We show that we can effectively decouple the double quantum dot from its reservoir and control the inter-dot tunnel coupling of the isolated system with a dedicated barrier gate. We quantify the tunability of the coupling by analyzing charge polarisation lines and random telegraph signals and find tunnel couplings up to 13 GHz and tunnel rates down to below 1 Hz.

4.2. RESULTS AND DISCUSSION

Figure 4.1a shows a scanning electron micrograph (SEM) of a SiMOS device nominally identical to the one measured. A high quality wafer is realized [14] with a 100 nm ^{28}Si epilayer, removing nuclear spin interactions to obtain spins with long quantum coherence [28], covered by 10 nm thermally grown SiO_2 . Ohmic contacts are made by defining highly doped n^{++} regions by phosphorus-ion implantation. We use an overlapping gate integration scheme [29] and use palladium (Pd) gates, which have the beneficial property of small grain size [30]. The gates are electrically isolated by an Al_2O_3 layer grown by atomic layer deposition. The sample is annealed at 400 °C in a hydrogen atmosphere to repair e-beam induced damage to the silicon oxide and to reduce the charge trap density [31, 32].

4.2.1. CHARGE SENSING AND READOUT

Figure 4.1b shows the current through the SET, electrostatically defined using gates ST, LB and RB, that is used as charge sensor and as an electron reservoir. The highly regular peak spacing indicates a well defined quantum dot with a constant charging energy. We form a double quantum dot between the confinement barriers CL and CR, using the gates P_1 and P_2 to tune the quantum dot potentials. B_L and B_R are used to control the tunnel coupling between the quantum dots and from the quantum dots to the SET, respectively.

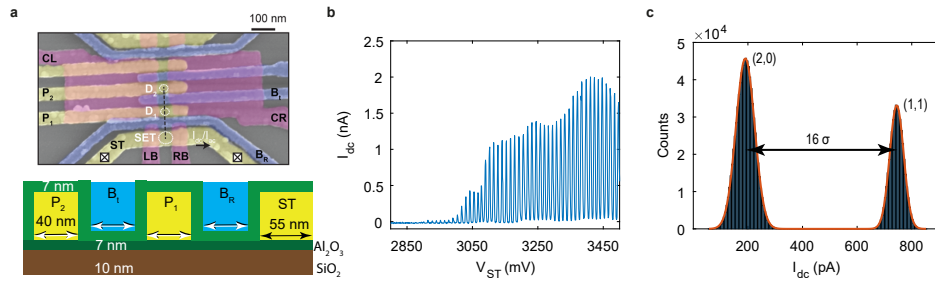


Figure 4.1: Device layout and SET characterisation. **a** False-colour scanning electron micrograph (SEM) of a device identical to the one measured. Purple, yellow and blue colourings correspond to the first, second and third metal layers respectively. Circles indicate the intended location of the quantum dots D_1 and D_2 and the single-electron-transistor (SET). The quantum dots are defined using gate electrodes P_1 and P_2 , confined laterally using CL and CR . B_t controls the tunnel coupling between the quantum dots and B_R the tunnel coupling to the SET. **b** Transport current I_{dc} versus top gate voltage V_{ST} of the SET defined using gate electrodes ST , LB and RB . Regular spacing of Coulomb peaks indicates a well defined quantum dot, ideal for charge sensing. **c** Histogram of the charge sensor current as a response to $(2,0)$ - $(1,1)$ tunneling events. The counts are extracted from 4655 single-shot traces with integration time $t_i = 82 \mu s$, measurement bandwidth 0-50 kHz, and bin size $b = 5 \text{ pA}$. The peaks are fitted with a double Gaussian with $\sigma_{(2,0)} = 34.1 \text{ pA}$ and $\sigma_{(1,1)} = 25.5 \text{ pA}$, giving a peak spacing of over $16 \sigma_{(2,0)}$.

We characterize the charge readout sensitivity by recording the random telegraph signal (RTS) originating from the tunneling of the electrons between the $(2,0)$ and $(1,1)$ charge states with $\Gamma_c \approx 48 \text{ Hz}$, with Γ_c the inter-dot tunnel rate. The fidelity of the $(2,0)$ - $(1,1)$ charge readout is often limited by the sensitivity of the charge sensor to inter-dot transitions. We have designed and positioned the SET with respect to the double quantum dot in such a way that this sensitivity is maximized. Figure 4.1c shows a histogram of the readout signal obtained, using an integration time $\tau = 82 \mu s$. We fit the counts with a double Gaussian curve with $\mu_{(2,0),(1,1)}$ and $\sigma_{(2,0),(1,1)}$ the mean and standard deviation of the Gaussian distributions corresponding to the two charge states. We find $\Delta\mu_{(2,0)-(1,1)} > 16 \sigma_{(2,0)}$ corresponding to an excellent discrimination between the $(2,0)$ and $(1,1)$ charge states.

To precisely measure charge transitions, we implement charge sensing using a lock-in amplifier and apply a square wave excitation at $f_{ac} = 77 \text{ Hz}$ on the gate B_t . Figure 4.2a and 4.2b show the double quantum dot charge stability diagrams of the charge sensor response as a function of V_{P_2} and V_{P_1} for weak ($V_{B_t} = 2.9 \text{ V}$) and strong ($V_{B_t} = 3.6 \text{ V}$) coupling. Horizontal and vertical blue lines indicate the loading of an additional electron from the SET to quantum dots D_1 (located under the gate P_1) and D_2 (located under P_2) respectively, while diagonal yellow lines indicate electron transitions between the two quantum dots. We do not observe more charge transitions at voltages lower than the measured range, and we conclude that the double quantum dot is in the single electron regime. In order to highlight the difference between weak and strong coupling, Fig. 4.2c and 4.2d show higher resolution maps of the $(2,0)$ - $(1,1)$ anticrossing.

When we set a weak inter-dot coupling, charge addition lines of D_2 are barely visible in the charge stability diagram, because of the low tunnel rate between D_2 and the reservoir. This indicates that the tunnel rate is significantly smaller than the excitation frequency applied to the gate, taking into account the increased tunnel rate caused by inelastic tunneling. Similarly, at the $(2,0)$ - $(1,1)$ inter-dot transition, no transitions between the quantum dots can be observed because of the low inter-dot coupling. The loading of the first electron in D_2 can only be observed from the shift of the D_1 charge addition line, caused by the mutual capacitance E_m of the two quantum

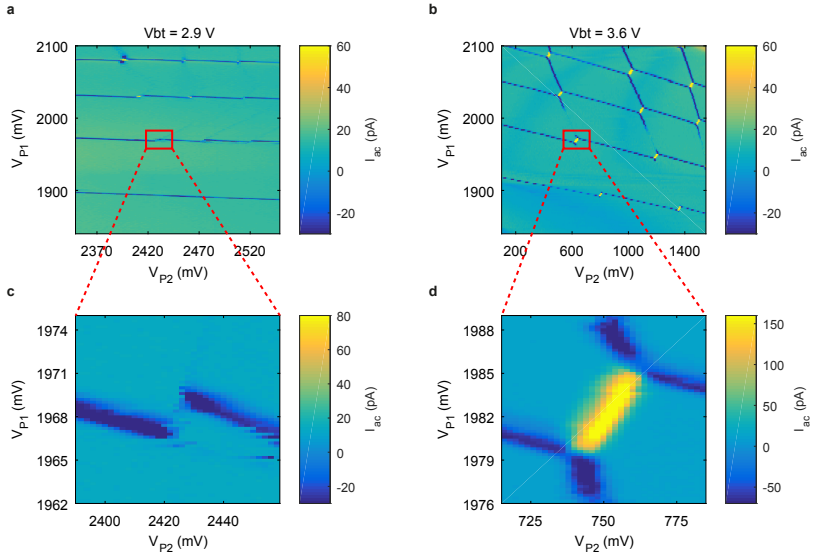


Figure 4.2: Double quantum dot charge stability diagrams. **a, b** Charge stability diagrams of the charge sensor response I_{ac} as a function of voltages V_{P2} and V_{P1} of a double quantum dot for weak (**a**, $V_{Bt} = 2.9$ V) and strong (**b**, $V_{Bt} = 3.6$ V) coupling. Electrons are loaded from the SET. Transitions with a tunnel rate $\Gamma < f_{ac}$ are not visible. **c, d** High resolution zoom in of the $(2,0)$ - $(1,1)$ anticrossing for both weak (**c**) and strong (**d**) tunnel coupling.

dots. Only in the multi-electron regime where the quantum dot wave functions are larger and have more overlap, the coupling is sufficiently high to observe charge transition lines.

When the inter-dot coupling is strong, charge addition lines belonging to D_2 are visible near the anticrossings and at high V_{P1} , where Γ_{R2} is increased. Additionally, t_c and E_m are increased and we observe a honeycomb shaped charge stability diagram, with clearly visible inter-dot transition lines, even when only a single electron is loaded on each quantum dot.

We estimate the relative location and size of the quantum dots from the gate voltage differences $\Delta V_{P1(2)}$ needed to load the second electron with respect to the first electron. We additionally use the cross-capacitances $\alpha_{r1(2)}$ of the plunger gates, determined by measuring the shift in $V_{P1(2)}$ of the charge transition line of the first electron in $D_{1(2)}$ as a function of a step in $V_{P2(1)}$, where $\alpha_{r1(2)}$ is the ratio between the shift and the step.

When the coupling is weak, we find $\Delta V_{P1} \approx 70$ mV, $\alpha_{r1} < 0.05$ for D_1 and $\Delta V_{P2} \approx 50$ mV, $\alpha_{r2} \approx 0.33$ for D_2 . We conclude that we have a system of two weakly coupled quantum dots located under P_1 and P_2 .

We analyse how the locations of D_1 and D_2 change from the changes in ΔV_P and α_r . For D_1 , both ΔV_{P1} and α_{r1} are almost independent of the coupling. For D_2 , ΔV_{P2} increases by a factor 11, from $\Delta V_{P2} \approx 50$ mV for weak coupling to $\Delta V_{P2} \approx 550$ mV for strong coupling, while α_{r2} increases by a factor 5, from 0.3 to 1.5. The increase in α_{r2} can be explained by a change in the location of D_2 toward the gate P_1 , to a position partly below the gate B_t . This change of quantum dot location will decrease the lever arm and this is likely the cause of the increase in ΔV_{P2} . We conclude that tuning from weak to strong coupling causes the location of D_2 to change from a position mostly under P_2 to a position partly below B_t , while D_1 is stationary under P_1 .

By reducing V_{BR} , the tunnel rate Γ_R between the the SET reservoir and the quantum dots can

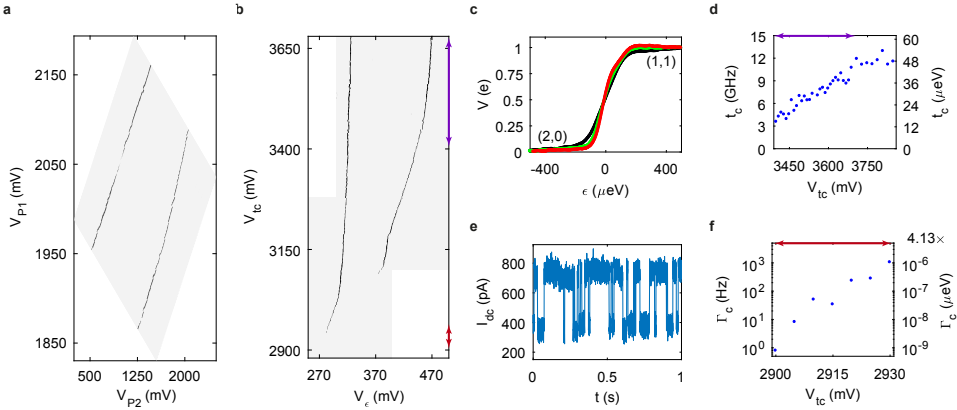


Figure 4.3: Demonstration of tunable tunnel coupling. **a** Map of the isolated (2,0)-(1,1) and (1,1)-(0,2) anti-crossings as a function of V_{P2} and V_{P1} . No additional electrons are loaded into the quantum dot islands due to a negligible Γ_R . **b** Map of the (2,0)-(1,1) and (1,1)-(0,2) anticrossings as a function of detuning and barrier voltage. The relative lever arm between V_{tc} and V_ϵ changes at lower barrier voltages, due to a change in quantum dot location. The orange and purple arrows indicate the regime in which the tunnel coupling was determined using RTS and polarisation line measurements respectively. **c** Polarization lines (excess charge V as a function of detuning ϵ) across the anticrossing for high t_c (black, $V_{tc} = 3.85$ V), intermediate t_c (green, $V_{tc} = 3.6$ V) and relatively low t_c (red, $V_{tc} = 3.4$ V). **d** Extracted t_c from polarization lines as a function of V_{tc} , where we find tunable t_c up to 13 GHz. **e** RTS for weak coupling $V_{tc} = 2.910$ V. **f** Extracted Γ_c from RTS measurements as a function of V_{tc} demonstrating tunable tunnel rates down to below 1Hz.

be reduced and the loading and unloading of electrons can be prevented, resulting in an isolated quantum dot system [27, 33]. Because the reservoir is connected to room temperature electronics, decoupling the quantum dot from it may provide the advantage of reduced noise [34]. Figure 4.3a shows the (2,0)-(1,1) and (1,1)-(0,2) anticrossings as a function of V_{P2} and V_{P1} for strong coupling. Only inter-dot transition lines are present over a wide range of voltages, much larger than the ΔV_P extracted in the previous section. This implies that no additional electrons are loaded, as a result of a negligible coupling to the reservoir. The ability to control the inter-dot transitions of a double quantum dot without loading additional electrons provides good prospects for the operation of quantum dot arrays that are only remotely coupled to reservoirs, as proposed in quantum information architectures [19, 21, 22].

4.2.2. TUNNEL COUPLE CONTROL

We control the tunnel coupling t_c with the gate B_T . To compensate for the influence of V_{Bt} on detuning ϵ and on-site potential U , we implement virtual gates using a cross-capacitance matrix [35] and convert V_{P2} , V_{P1} and V_{Bt} to ϵ , U and t_c . Figure 4.3b shows the (2,0)-(1,1) and (1,1)-(0,2) anticrossings as a function of the new set of virtual gates V_ϵ and V_{tc} . For both transitions the inter-dot line vanishes at low V_{tc} , meaning that the coupling has been largely switched off. We observe that for the (1,1)-(0,2) anticrossing, the transition line disappears at $V_{tc} < 3.1$ V, while for the (2,0)-(1,1) anticrossing this happens for $V_{tc} < 2.95$ V. The variation may come from a small asymmetry in the system.

We tune the double quantum dot to a significantly coupled regime and quantitatively analyze the system by taking charge polarization lines. Figure 4.3c shows charge polarization lines at high, intermediate and relatively low tunnel couplings within this regime. We measure the charge sensor

response V as a function of detuning ϵ and fit the data according to a model that includes cross-talk of ϵ to the charge sensor and the influence of the quantum dot charge state on the charge sensor sensitivity [9, 36]. From the thermal broadening of the polarization line at low tunnel coupling, we extract the lever arm of V_ϵ for the detuning axis $\alpha_\epsilon \approx 0.04$ eV/mV, by assuming the electron temperature to be equal to the fridge temperature of 0.44 K. Figure 4.3d shows a t_c proportional to V_{tc} from approximately 3 to 13 GHz, demonstrating tunable tunnel coupling in the strong coupling regime.

At lower tunnel couplings, the thermal broadening of the polarization line prevents accurate fitting. Instead, to obtain the inter-dot tunnel rate Γ_c , we measure RTS (Fig. 4.3e) at the (2,0)-(1,1) transition and fit the counts C of a histogram of the tunnel times T to $C = Ae^{-\Gamma_c T}$, where A is a constant to normalise the counts. Furthermore we tune the system to be in the elastic tunneling regime, with V_ϵ such that $\Gamma_{c(2,0)-(1,1)} \approx \Gamma_{c(1,1)-(2,0)}$ [37]. This tunnel rate is proportional to the tunnel coupling, but in the weak coupling regime, $\Gamma_c \neq t_c$ due to localisation of the charge [38–40]. Figure 4.3f shows the obtained Γ_c as a function of V_{tc} from 1 kHz down to below 1 Hz. We note that we can further reduce this tunnel rate to even smaller rates simply by further reducing this gate voltage.

4.3. CONCLUSIONS

We have demonstrated control over the tunnel coupling of single electrons residing in a double quantum dot in silicon. The inter-dot coupling of the (2,0)-(1,1) charge transition can be controlled by a barrier gate which changes quantum dot location. We have demonstrated control over the tunnel coupling in the strong coupling regime from 3 to 13 GHz, as well as control over the tunnel rate in the weak coupling regime from 1 kHz to below 1 Hz. Achieving this degree of control in an isolated system constitutes a crucial step toward independent control over detuning and tunnel coupling for operation at the charge symmetry point [5, 6], and reaching the control required for large-scale quantum computation with quantum dots [1, 19–24]. While SiMOS systems are often said to be severely limited by disorder, the excellent control shown here provides great prospects to operate larger arrays fabricated using conventional semiconductor technology.

REFERENCES

- [1] Loss, D. & DiVincenzo, D. P. Quantum computation with quantum dots. *Physical Review A* **57**, 120 (1998).
- [2] Levy, J. Universal quantum computation with spin-1/2 pairs and Heisenberg exchange. *Physical Review Letters* **89**, 147902 (2002).
- [3] DiVincenzo, D. P., Bacon, D., Kempe, J., Burkard, G. & Whaley, K. B. Universal quantum computation with the exchange interaction. *Nature* **408**, 339 (2000).
- [4] Shi, Z. *et al.* Fast hybrid silicon double-quantum-dot qubit. *Physical review letters* **108**, 140503 (2012).
- [5] Martins, F. *et al.* Noise suppression using symmetric exchange gates in spin qubits. *Physical review letters* **116**, 116801 (2016).
- [6] Reed, M. D. *et al.* Reduced sensitivity to charge noise in semiconductor spin qubits via symmetric operation. *Physical review letters* **116**, 110402 (2016).
- [7] Taylor, J. M., Srinivasa, V. & Medford, J. Electrically protected resonant exchange qubits in triple quantum dots. *Physical review letters* **111**, 050502 (2013).

- [8] Kim, D. *et al.* Quantum control and process tomography of a semiconductor quantum dot hybrid qubit. *Nature* **511**, 70 (2014).
- [9] Hensgens, T., T. and Fujita *et al.* Quantum simulation of a Fermi–Hubbard model using a semiconductor quantum dot array. *Nature* **548**, 70 (2017).
- [10] Borselli, M. G. *et al.* Undoped accumulation-mode Si/SiGe quantum dots. *Nanotechnology* **26**, 375202 (2015).
- [11] Zajac, D. M. *et al.* Resonantly driven CNOT gate for electron spins. *Science* **359**, 439–442 (2018).
- [12] Hendrickx, N. W. *et al.* Gate-controlled quantum dots and superconductivity in planar germanium. *Nature communications* **9**, 2835 (2018).
- [13] Hendrickx, N. W., Franke, D. P., Sammak, A., Scappucci, G. & Veldhorst, M. Fast two-qubit logic with holes in germanium. *arXiv 1904.11443* (2019).
- [14] Sabbagh, D. e. a. Quantum Transport Properties of Industrial Si 28 / Si O 2 28 . *Physical Review Applied* **12** (2019).
- [15] Mazzocchi, V. *et al.* 99.992% 28Si CVD-grown epilayer on 300 mm substrates for large scale integration of silicon spin qubits. *Journal of Crystal Growth* **509**, 1–7 (2019).
- [16] Maurand, R. *et al.* A CMOS silicon spin qubit. *Nature Communications* **7**, 13575 (2016).
- [17] Veldhorst, M. *et al.* A two-qubit logic gate in silicon. *Nature* **526**, 410–414 (2015).
- [18] Huang, W. *et al.* Fidelity benchmarks for two-qubit gates in silicon. *Nature* **569**, 532–536 (2019).
- [19] Veldhorst, M., Eenink, H. G. J., Yang, C. H. & Dzurak, A. S. Silicon CMOS architecture for a spin-based quantum computer. *Nature Communications* **8**, 1766 (2017).
- [20] Vandersypen, L. M. K. *et al.* Interfacing spin qubits in quantum dots and donors—hot, dense, and coherent. *npj Quantum Information* **3** (2017).
- [21] Li, R. *et al.* A crossbar network for silicon quantum dot qubits. *Science advances* **4**, eaar3960 (2018).
- [22] Taylor, J. M. *et al.* Fault-tolerant architecture for quantum computation using electrically controlled semiconductor spins. *Nature Physics* **1**, 177 (2005).
- [23] Friesen, M., Biswas, A., Hu, X. & Lidar, D. Efficient multiqubit entanglement via a spin bus. *Physical review letters* **98**, 230503 (2007).
- [24] Trauzettel, B., Bulaev, D. V., Loss, D. & Burkard, G. Spin qubits in graphene quantum dots. *Nature Physics* **3**, 192 (2007).
- [25] Tracy, L. A. *et al.* Double quantum dot with tunable coupling in an enhancement-mode silicon metal-oxide semiconductor device with lateral geometry. *Applied Physics Letters* **97**, 192110 (2010).
- [26] Lai, N. S. *et al.* Pauli spin blockade in a highly tunable silicon double quantum dot. *Scientific reports* **1** (2011).

- [27] Yang, C. H. *et al.* Silicon quantum processor unit cell operation above one Kelvin. *arXiv:1902.09126* (2019).
- [28] Veldhorst, M. *et al.* An addressable quantum dot qubit with fault-tolerant control-fidelity. *Nature Nanotechnology* **9**, 981–985 (2014).
- [29] Angus, S. J., Ferguson, A. J., Dzurak, A. S. & Clark, R. G. Gate-defined quantum dots in intrinsic silicon. *Nano Letters* **7**, 2051–2055 (2007).
- [30] Brauns, M., Amitonov, S. V., Spruijtenburg, P. C. & Zwanenburg, F. A. Palladium gates for reproducible quantum dots in silicon. *Scientific reports* **8**, 5690 (2018).
- [31] Kim, J. S., Tyryshkin, A. M. & Lyon, S. A. Annealing shallow Si/SiO₂ interface traps in electron-beam irradiated high-mobility metal-oxide-silicon transistors. *Applied Physics Letters* **110**, 123505 (2017).
- [32] Nordberg, E. P. *et al.* Enhancement-mode double-top-gated metal-oxide-semiconductor nanostructures with tunable lateral geometry. *Physical Review B* **80**, 115331 (2009).
- [33] Bertrand, B. *et al.* Quantum manipulation of two-electron spin states in isolated double quantum dots. *Physical review letters* **115**, 096801 (2015).
- [34] Rossi, A., Ferrus, T. & Williams, D. A. Electron temperature in electrically isolated Si double quantum dots. *Applied Physics Letters* **100**, 133503 (2012).
- [35] Baart, T. A. *et al.* Single-spin CCD. *Nature Nanotechnology* **11**, 330 (2016).
- [36] DiCarlo, L. *et al.* Differential charge sensing and charge delocalization in a tunable double quantum dot. *Physical review letters* **92**, 226801 (2004).
- [37] Tarucha, S. *et al.* Elastic and inelastic single electron tunneling in coupled two dot system. *Microelectronic engineering* **47**, 101–105 (1999).
- [38] Braakman, F. R., Barthelemy, P., Reichl, C., Wegscheider, W. & Vandersypen, L. M. K. Long-distance coherent coupling in a quantum dot array. *Nature Nanotechnology* **8**, 432 (2013).
- [39] Gamble, J. K., Friesen, M., Coppersmith, S. N. & Hu, X. Two-electron dephasing in single Si and GaAs quantum dots. *Physical Review B* **86**, 035302 (2012).
- [40] Korotkov, A. N. Continuous quantum measurement of a double dot. *Physical Review B* **60**, 5737 (1999).

5

UNIVERSAL QUANTUM LOGIC IN HOT SILICON QUBITS

Quantum computation requires many qubits that can be coherently controlled and coupled to each other [1]. Qubits that are defined using lithographic techniques are often argued to be promising platforms for scalability, since they can be implemented using semiconductor fabrication technology [2–5]. However, leading solid-state approaches function only at temperatures below 100 mK, where cooling power is extremely limited, and this severely impacts the perspective for practical quantum computation. Recent works on spins in silicon have shown steps towards a platform that can be operated at higher temperatures by demonstrating long spin lifetimes [6], gate-based spin readout [7], and coherent single-spin control [8]. However, a high-temperature two-qubit logic gate still needs to be demonstrated. Here we show that silicon quantum dots can have sufficient thermal robustness to enable the execution of a universal gate set above one Kelvin. We obtain single-qubit control via electron-spin-resonance (ESR) and readout using Pauli spin blockade. We show individual coherent control of two qubits and measure single-qubit fidelities up to 99.3 %. We demonstrate tunability of the exchange interaction between the two spins from 0.5 up to 18 MHz and use this to execute coherent two-qubit controlled rotations (CROT). The demonstration of ‘hot’ and universal quantum logic in a semiconductor platform paves the way for quantum integrated circuits hosting the quantum hardware and their control circuitry all on the same chip, providing a scalable approach towards practical quantum information.

Parts of this chapter have been published in Nature 580 (7803), 355-359 and arXiv:2007.09034 [cond-mat.mes-hall]

5.1. HOT QUBITS

Spin qubits based on quantum dots are among the most promising candidates for large-scale quantum computation [2, 9, 10]. Quantum coherence can be maintained in these systems for extremely long times [11] by using isotopically enriched silicon (^{28}Si) as the host material [12]. This has enabled the demonstration of single-qubit control with fidelities exceeding 99.9% [13, 14] and the execution of two-qubit logic [15–18]. The potential to build larger systems with quantum dots manifests in the ability to deterministically engineer and optimize qubit locations and interactions using a technology that greatly resembles today's complementary metal-oxide semiconductor (CMOS) manufacturing. Nonetheless, quantum error correction schemes predict that millions to billions of qubits will be needed for practical quantum information [19]. Considering that today's devices make use of more than one terminal per qubit [20], wiring up such large systems remains a formidable task. In order to avoid an interconnect bottleneck, quantum integrated circuits hosting the qubits and their electronic control on the same chip have been proposed [2, 3, 21]. While these architectures provide an elegant way to increase the qubit count to large numbers by leveraging the success of classical integrated circuits, a key question is whether the qubits will be robust against the thermal noise imposed by the power dissipation of the electronics. Demonstrating a universal gate set at elevated temperatures would therefore be a milestone in the effort towards scalable quantum systems. First steps towards this direction have already been taken in an experiment by Yang et al. [8] by demonstrating a device that can be operated as a two-qubit system at a temperature of 40 mK and continues to have good single-qubit properties when the temperature is increased above one Kelvin.

Here, we solve this challenge and combine initialization, readout, single-qubit rotations and two-qubit gates, to demonstrate full two-qubit logic in a quantum circuit operating at 1.1 Kelvin. We furthermore examine the temperature dependence of the quantum coherence which we find, unlike the relaxation process [6], to be hardly affected in a temperature range $T = 0.45 \text{ K} - 1.25 \text{ K}$.

5.2. LARGE-SCALE QUANTUM COMPUTING IN SIMOS

Figure 5.1a conceptually displays a quantum integrated circuit. Inspired by their classical counterpart where only a few control lines are needed to interact with billions of transistors, a quantum integrated circuit hosts the quantum hardware and its electronic control on the same chip to provide a scalable solution [20]. Here we focus on the quantum hardware of such a circuit, which we implement using silicon quantum dots.

Figure 5.1b shows the silicon quantum dot device. The qubits are realized in an isotopically purified ^{28}Si epi-layer with a ^{29}Si residual concentration of 800 ppm. The fabrication of the quantum dot device is based on an overlapping gate-scheme to allow for tightly confined quantum dots [24, 25]. Electrons can be loaded either from the reservoir or from the single-electron-transistor (SET) [22], which is also used for charge sensing. To allow for coherent control over the electron spins, AC currents are applied through the on-chip aluminum microwave antenna.

Figure 5.1c shows a charge stability diagram of the double quantum dot, where the qubits Q1 and Q2 and their coupling are defined by using the gates P1, B12, and P2. Since we can freely choose the occupancy of the two quantum dots we tune to the regime where we obtain optimal exchange coupling, which we find with one and five electrons for Q1 and Q2 respectively. We then operate the system close to the (5,1)-(4,2) charge anticrossing.

Single spins are often initialized via energy-selective tunneling to a nearby reservoir [26]. However, this method requires a Zeeman splitting much higher than the thermal broadening, limiting the fidelity and making the method unpractical for high temperature operation. Instead, Pauli spin blockade offers a convenient mechanism to perform initialization and readout [2, 7], with a relevant energy scale corresponding to the singlet-triplet energy splitting, which is set by the large and

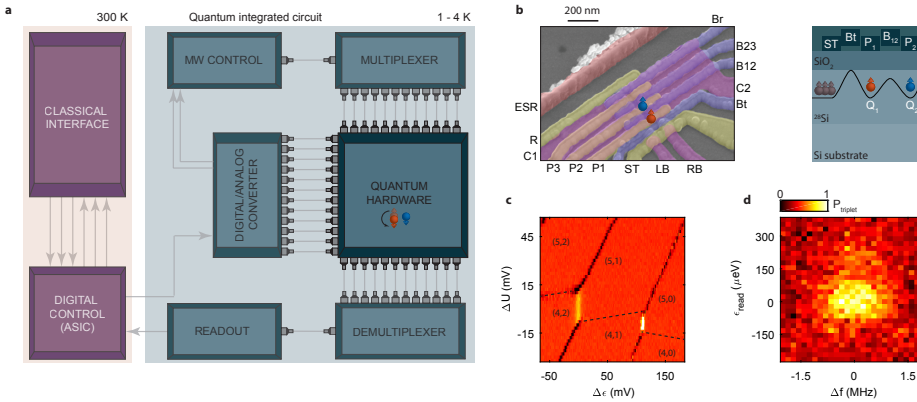


Figure 5.1: Large-scale approach for silicon qubits **a** Quantum integrated circuit as a scalable approach for quantum computing, where the qubits and their control electronics are defined on the same chip. The control functionality that can be integrated is strongly dependent on the available cooling power. When the qubits can be coherently controlled above one Kelvin a broad range of electronics may be integrated, such that communication between room temperature and the coldest stage is limited to only digital signals. Additionally, long distance spin qubit coupling mechanisms would allow to build modular architectures, where widely spaced qubit arrays and local electronics alternate on the same chip, further alleviating fan-out and wiring issues [2]. **b** Scanning Electron Microscope (SEM) image of a quantum device identical to the one measured. Gates P1 and P2 define the two quantum dots and the gate B12 control the inter-dot tunnel coupling. The SET is defined by the top gate ST and the two barriers RB and LB, and it is used both as charge sensor and as reservoir [22], while the tunnel rate is controlled by Bt. The gates C1 and C2 confine the electrons in the three quantum dots. Gates R, Br, P3 and B23 are kept grounded during the experiment. **c** Electron occupancy as a function of detuning energy between the two quantum dots e and on-site repulsion energy U . The data have been centered at the (4,2)-(5,1) anticrossing. The electron transitions have been measured via a lockin technique [23], by applying an excitation of 133 Hz on gate B12. Both electrons are loaded from the SET, with Q2 having a tunneling rate significantly lower than Q1. **d** Readout signal as a function of readout position ϵ_{read} and microwave frequency applied to Q2. When the readout level is positioned between the singlet-triplet energy splitting and the microwave frequency matches the resonance frequency of Q2, we correctly read out the transition from the state $|\downarrow\uparrow\rangle$ to the blocked state $|\uparrow\uparrow\rangle$.

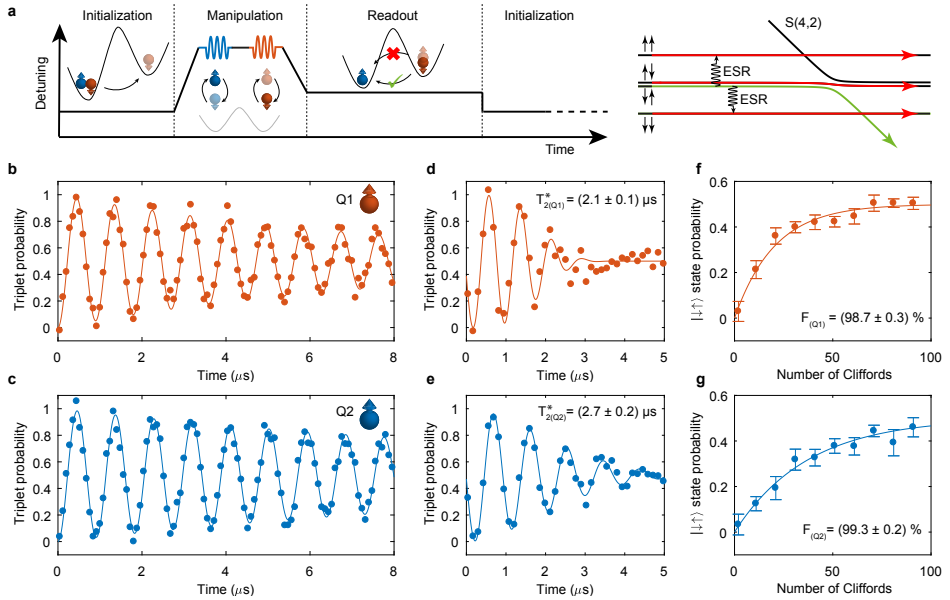


Figure 5.2: **Single-qubit characterization at 1.1 K.** **a** Pulse sequence used for the experiments. Qubits Q1 and Q2 are defined on the spin states of single-electrons, the remaining four electrons in Q2 fill the first levels and do not contribute to the experiment. A voltage ramp allows adiabatic transitions between the (5,1) and (4,2) charge states. Each measurement cycle consists of two of these sequences. The second cycle contains no microwave pulses and it is used as a reference to cancel low-frequency drifts during readout. **b-c** Rabi oscillations for both qubits as a function of the microwave pulse duration. We extract decay time constants $T_{2(Q1)}^{Rabi} = 8 \mu s$ and $T_{2(Q2)}^{Rabi} = 14 \mu s$. **d-e** Decay of the Ramsey fringes for both qubits. The data correspond to the average of four traces where each point is obtained from 500 single-shot traces. **f-g** Randomized benchmarking of the single-qubit gates for both qubits. Each data point is obtained from 500 averages of 20 Clifford sequences, for a total of 10,000 single-shot traces. The fidelity reported refers to the primitive gates, while a Clifford-gate contains on average 1.875 primitive gates. We have normalized the state probabilities to remove the readout errors.

tunable valley splitting energy in silicon metal-oxide-semiconductor (SiMOS) devices [27]. This method is more robust against thermal noise and enables independent optimization of the qubit operation frequency. We choose to set the magnetic field to $B = 0.25$ T, which corresponds to addressable qubits with Larmor frequencies $\nu_{Q1} = 6.949$ GHz and $\nu_{Q2} = 6.958$ GHz in the absence of exchange interaction. This low frequency operation reduces the qubit sensitivity to electrical noise that couples in via the spin-orbit coupling [28]. Additionally it also simplifies the demands on the electronic control circuits and reduces the cable losses.

5.3. SINGLE QUBIT CONTROL

The pulse sequence used in the experiment is schematically shown in Fig. 5.2a. The sequence starts by pulsing deep into the (4,2) charge state, where the spins quickly relax to the singlet state. An adiabatic pulse to the (5,1) regime is applied to initialize the system in the $|\downarrow\uparrow\rangle$ state. At this position in detuning energy ϵ , single- and two-qubit gate operations are performed by applying a microwave burst with variable frequency and duration. The sequence ends by adiabatically pulsing to the anticrossing where readout is performed. The antiparallel spin state with the lowest

energy (which is in this experiment the state $|\downarrow\uparrow\rangle$) couples directly to the singlet (4,2) charge state. The remaining antiparallel spin state ($|\uparrow\downarrow\rangle$) and the two parallel spin states ($|\uparrow\uparrow\rangle, |\downarrow\downarrow\rangle$) couple to the three triplet (4,2) charge states. This allows to map the $|\downarrow\uparrow\rangle$ and the other basis states to different charge configurations ((4,2) or (5,1) states), which can be read out using the SET. As shown in Fig. 5.1d, the optimal readout position can be obtained by sweeping ϵ and applying a π -pulse to Q2. From the detuning lever arm of $\alpha_\epsilon = 0.044$ eV/V, extracted from the thermal broadening of the polarization line, we find a readout window of 155 μ eV where we can efficiently discriminate between the singlet and triplet states.

In this high temperature operation mode, the readout visibility is mainly limited by the broadening of the SET peaks. In order to maximize our sensitivity we subtract a reference signal from each trace, then we average and normalize the resulting signal (for more details on the readout see Fig. 5.5 and 5.6).

Figure 5.2b-g shows the single-qubit characterization of the two-qubit system. We observe clear Rabi oscillations for both qubits (Fig. 5.2b, c) as a function of the microwave burst duration. From the decay of the Ramsey fringes (Fig. 5.2d, e) we extract dephasing times $T_{2(Q1)}^* = 2.1$ μ s and $T_{2(Q2)}^* = 2.7$ μ s, comparable to experiments at similar high temperature [8]. These times are significantly shorter than the longest reported times for ^{28}Si [11], however they are still longer than the dephasing times for natural silicon at base temperature [16, 17]. Furthermore we measure spin lifetimes (see Fig. 5.8) of $T_{1(Q1)} = 2.0$ ms and $T_{1(Q2)} = 3.7$ ms, consistent with values reported in a similar device at a similar operating temperature [6].

We characterize the performance of the single-qubit gates of the two qubits by performing randomized benchmarking [29]. In the manipulation phase we apply sequences of random gates extracted from the Clifford group, followed by a recovery gate that brings the system to the $|\downarrow\downarrow\rangle$ and $|\uparrow\uparrow\rangle$ states for Q1 and Q2 respectively. By fitting the decay of the readout signal as a function of the number of applied gates to an exponential decay we extract qubit fidelities $F_{Q1} = 98.7 \pm 0.3$ % and $F_{Q2} = 99.3 \pm 0.2$ %, with the second one above the fault tolerant threshold.

5.4. TWO-QUBIT QUANTUM LOGIC AT 1.1 K

We now turn to the two-qubit gate characterization. The ability to tune the exchange interaction [9] is the basis to perform two-qubit operations with electrons in quantum dots. By turning on the exchange interaction, either by controlling the detuning energy or the tunnel coupling, the resonance frequencies of each qubit shift depending on the spin state of the other qubit. The central inset in Fig. 6.1a shows this frequency shift for both qubits as a function of the detuning energy between the two quantum dots, with and without a π -pulse applied to flip the spin state of the other qubit. The full exchange spectrum is composed of the transitions f_1 ($|\downarrow\uparrow\rangle \rightarrow |\downarrow\downarrow\rangle$), f_2 ($|\uparrow\uparrow\rangle \rightarrow |\uparrow\downarrow\rangle$), f_3 ($|\downarrow\downarrow\rangle \rightarrow |\uparrow\downarrow\rangle$) and f_4 ($|\downarrow\uparrow\rangle \rightarrow |\uparrow\uparrow\rangle$). The exchange interaction J can be extracted as the differences $f_2 - f_1$ and $f_4 - f_3$, from which we measure tunable J in the range 0.5 - 18 MHz (see Fig. 5.4a). At even larger exchange couplings the readout visibility drastically reduces, which we attribute to a decrease of T_2^* (see Fig 5.4b). By fitting the exchange spectrum (see section 5.8) we extract a tunnel coupling $t_c = 0.8$ GHz and a Zeeman energy difference $\delta E_z = 9.1$ MHz.

Having demonstrated the tunability of the exchange interaction, we use this to demonstrate two-qubit operation. When the exchange is turned on, the resulting shift in resonance frequency can be used to implement state selective ESR transitions (CROT), which are equivalent to a CNOT gate up to single-qubit phases. Figure 6.1a shows controlled oscillations for both qubits, with the control qubit set either to the spin down or spin up state, where we have set the exchange interaction to $J = 2.5$ MHz. When we prepare the state of the control qubit such that the target qubit is in resonance with the external microwave control, we observe clear oscillations of the target qubit as a function of the microwave burst duration, with no significant decay after multiple rotations.

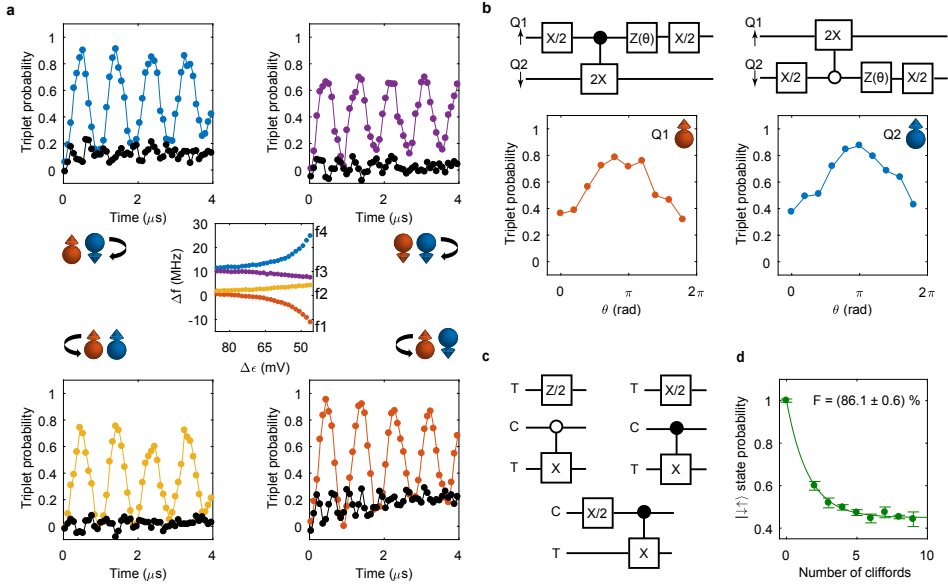


Figure 5.3: **Exchange and two-qubit logic at 1.1 K.** **a** Conditional rotations on all the frequencies f_i , the color code refers to the central inset showing the full exchange diagram obtained from a gaussian fit of the data shown in Fig. 5.7. The frequency offset is 6.948 GHz. The black lines correspond to the same transition f_i , driven with the control qubit in the opposite state. An initialization π -pulse and recovery π -pulse are applied to the control qubit for the sequences where either Q1 is in the spin down state or Q2 is in the spin up state. All Rabi frequencies are set to approximately 1 MHz by adjusting the power of the microwave source to compensate for the frequency dependent attenuation of the fridge line. Even when the exchange interaction is turned on we find the resonance frequencies of both qubits to be stable over the course of several hours (see Fig. 5.9). **b** Phase acquired by the control qubit during a CROT operation. A CROT gate, together with a Z-rotation of $\pi/2$ on the control qubit is equivalent to a CNOT operation. Z gates are implemented by a software change of the reference frame. **c** Primitive gates used to generate the two-qubit Clifford group (11520 gates in total). On average, each Clifford contains 2.5694 primitive gates. Since the Z/2 gates are implemented via a software change of the reference frame, they are not included in the gate count. All gates shown in the figure (except for the Z/2 gate) are implemented with two $\pi/2$ controlled rotations. The compilation scheme is identical to the one in [18]. **d** Decay of the $|\uparrow\uparrow\rangle$ state probability as a function of the number of two-qubit Cliffords applied. A recovery gate returns the system to the $|\uparrow\uparrow\rangle$ state. Since we include the recovery gate in the Cliffords count, the first data point corresponds to $N_{\text{Cliff}} = 2$. Each data point corresponds to the average of 150 random sequences. The fidelity $F = 86.1 \pm 0.6\%$ corresponds to the average fidelity of the primitive gates shown in c. We have normalized the state probabilities to remove the readout errors.

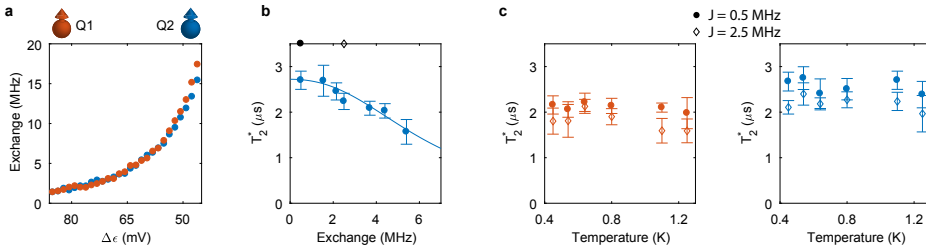


Figure 5.4: **Dephasing dependence on temperature and exchange interaction.** **a** Exchange energy measured as a function of detuning. The data correspond to $f_2 - f_1$ and $f_4 - f_3$ as obtained from Fig. 6.1a. **b** Dephasing time of Q2 as a function of the exchange interaction, fitted with a model taking into account gaussian quasi static noise (see section 5.9). Similar data from Q1 are shown in Fig. 5.10. **c** Temperature dependence of the dephasing time with the exchange interaction set to the minimum obtained by sweeping ϵ ($J = 0.5$ MHz) and with the exchange interaction set to acquire the CROT operations of Fig. 6.1a ($J = 2.5$ MHz).

When we flip the state of the control qubit, the resonance frequency of the target qubit is shifted and the target qubit is not driven by the microwave control.

In order to investigate the coherence of the two-qubit logic, we apply a sequence where we interleave a CROT operation with duration 2π in between two $\pi/2$ single-qubit gates applied to the control qubit with variable phase θ . As shown in Fig. 6.1b, when we invert the second $\pi/2$ pulse ($\theta = \pi$) this cancels out the π phase left by the CROT operation on the control qubit and we correctly measure transitions to the $|\downarrow\downarrow\rangle$ and $|\uparrow\uparrow\rangle$ states. This demonstrates the execution of a coherent CROT, since the control qubit maintains its coherence even when the target qubit is driven.

In order to show the universality of our gate set we also demonstrate two-qubit randomized benchmarking. We apply random gates from the 11520 two-qubit Clifford group, recover the state to the $|\downarrow\uparrow\rangle$ and measure how the singlet probability decays over the number of applied gates. The decay is shown in Fig. 6.1d and the primitive gates used in 6.1c. The lower fidelity ($F = 86.1 \pm 0.6$ %) compared to the single-qubit benchmark can be attributed to the longer time spent by the qubits idling, which causes them to decohere faster. Possible improvements include simultaneous driving of two transitions to reduce idling times, optimized pulse shaping to reduce accidental excitations of nearby transitions and operation at the symmetry point [30, 31].

5.5. TEMPERATURE EFFECTS ON QUANTUM COHERENCE

To further investigate the quantum coherence of the system we measure the decay of the Ramsey fringes for different values of the exchange interaction, see Fig. 5.4b. We find that by increasing the exchange interaction the coherence is reduced, which we explain by the increased qubit sensitivity to electrical noise. We can fit the data with a model (see section 5.9) that includes quasi-static electrical noise coupling in via the exchange interaction and via the Zeeman energy difference between the two qubits. From the fit we extract the fluctuation amplitudes $\delta\epsilon = 21 \mu\text{eV}$ (corresponding to a power spectrum at 1 Hz of $A_\epsilon \approx 6 \mu\text{eV}/\sqrt{\text{Hz}}$) and $\delta E_Z = 400$ kHz. The noise in ϵ is comparable with values extracted at fridge base temperature [32], and consistent with charge noise values extracted from current fluctuation measurements of SETs (see section 5.9 for further information) [6, 33].

To analyze the thermal impact, we characterize the temperature dependence of T_2^* for two values of exchange ($J = 0.5$ MHz and $J = 2.5$ MHz) and we find it to be approximately stable in the range $T = 0.45$ K - 1.25 K (see Fig. 5.4c). While weak dependencies of T_2^* have been reported

in other single-qubit experiments [8], we observe here that the weak temperature dependence is maintained even when the exchange interaction is set to an appreciable value where we can perform two-qubit logic.

The origin of the electrical noise limiting T_2^* can potentially come from extrinsic or intrinsic sources. Although we cannot rule out all extrinsic noise sources, we have confirmed that attenuating the transmission lines does not affect the T_2^* and we thus rule out a direct impact of the waveform generator and the microwave source. When intrinsic charge noise is the dominant contribution, a simple model based on an infinite number of two-level fluctuators (TLFs) predicts a square root dependence of the dephasing rate on the temperature [34]. However, this model assumes a constant activation energy distribution of the TLFs. Deviations from this assumption have been observed in SET measurements, leading to anomalous temperature dependencies [35]. The small size of quantum dots, in particular SiMOS qubits, may lead to only a few TLFs being relevant for the dephasing and these may explain the observed weak temperature dependence (see section 5.10 for more details).

Importantly, the weak dependence of T_2^* on temperature makes silicon qubits remarkably robust against temperature, enabling to execute a universal quantum gate set. The ability to operate lithographically defined qubits above one Kelvin resolves one of the key challenges toward the integration of quantum hardware and control electronics on the same chip. This integration can reduce the number of lines going from room temperature to the device and, at the same time, greatly simplify on-chip wiring, facilitating the realization of quantum integrated circuits for large-scale quantum computation.

5

5.6. METHODS

5.6.1. EXPERIMENTAL SETUP

All measurements are performed in a Bluefors dry dilution refrigerator with a base temperature of $T_{\text{base}} \approx 0.45$ K, operated at $T = 1.1$ K. DC-voltages are applied using battery-powered voltage sources and AC voltages are applied through bias-tee on the sample PCB with a cut-off frequency of 3 Hz. The pulse sequences are generated by an arbitrary waveform generator (AWG) Tektronix AWG5014C, combined with a microwave signal generated by a Keysight PSG8267D vector source. ESR currents are delivered via the PSG8267D using the internal IQ-mixer, driven by two output channels of the AWG. Both qubits can be addressed by setting the vector source to an intermediate frequency and IQ-mixing the signal with a (co)sine wave generated on channels 3 and 4 of the AWG. For the two-qubit randomized benchmarking experiment the pulse sequences are generated by an arbitrary waveform generator Keysight M3202A, that allows for faster waveform uploads. We apply a source-drain bias voltage of $V_{SD} = 0.5$ mV to the single-electron transistor and measure the current using an in-house built transimpedance amplifier.

5.6.2. SINGLE-QUBIT RANDOMIZED BENCHMARKING

The single-qubit Clifford group C_1 consists of 24 rotations. We implement the group using X and Y rotations, using the primitive gates: $\{I, \pm X/2, \pm Y/2, \pm X, \pm Y\}$. On average one Clifford gate contains 1.875 primitive gates. We implement the gates using only frequencies f_1 and f_4 for Q1 and Q2 respectively. The complete list of gates is given in the following table:

Single-qubit Cliffords	
I	
X	
Y	
Y, X	
X/2, Y/2	
X/2, -Y/2	
-X/2, Y/2	
-X/2, -Y/2	
Y/2, X/2	
Y/2, -X/2	
-Y/2, X/2	
-Y/2, -X/2	
X/2	
-X/2	
Y/2	
-Y/2	
-X/2, Y/2, X/2	
-X/2, -Y/2, X/2	
X, Y/2	
X, -Y/2	
Y, X/2	
Y, -X/2	
X/2, Y/2, X/2	
-X/2, Y/2, -X/2	

The phase control needed to implement X and Y rotations is achieved using the internal I-Q mixer of the microwave source. The fidelity reported in Figure 5.2 refers to the average fidelity of the gates in the generator group. All error bars are 1 standard deviation from the mean.

5.6.3. TWO-QUBIT RANDOMIZED BENCHMARKING

The two-qubit Clifford group C_2 consist of 11520 elements c_2 with properties $c_2^\dagger P c_2 \in \pm P$ where P are the Pauli operators. We generate the Clifford gates in our experiment using the set of conditional rotations in Fig. 6.1a where two subsequent conditional rotations implement a primitive gate. We compile the Clifford gates from the set of primitive gates together with virtual $Z/2$ gates on both qubits and search for combinations with the minimal amount of gates. The resulting average Clifford gate consists of 2.5694 primitive gates which are calibrated such that each conditional rotation takes exactly 330 ns, with the exchange interaction set to 3 MHz. To minimize cross-talk, the timing and the exchange interaction are chosen such that the off-resonant pulse is synchronized with the resonant pulse. All error bars are 1 standard deviation from the mean.

5.7. EXTENDED DATA

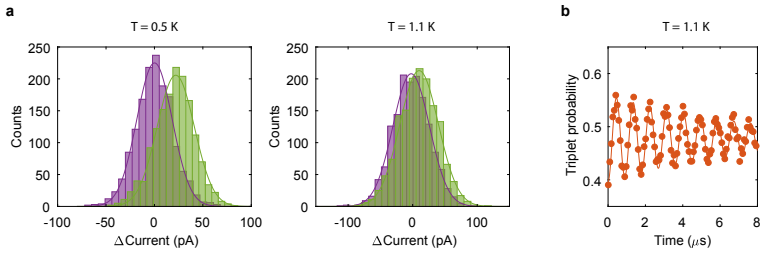


Figure 5.5: **Charge readout and visibility.** **a** Histograms of the readout signal for the singlet and triplet T_- state for two operating temperatures. The sensitivity is reduced at higher temperatures mainly because of the thermal broadening of the Coulomb peaks. The readout signal is obtained by subtracting a reference line, obtained from a sequence where no microwave pulse is applied. The integration time corresponds to $40 \mu\text{s}$. The readout fidelity may be improved by optimizing the charge sensing [36], and by using an RF-reflectometry or dispersive measurement scheme, as shown in [7]. **b** Rabi oscillations of Q1 (see also Fig. 5.2b), obtained by assigning to each single-shot trace the state spin up or spin down, using a threshold obtained from the histograms in **a**. From the data we can extract the visibility, which we find to be $V \approx 0.2$ at $T = 1.1 \text{ K}$.

5

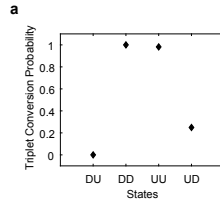


Figure 5.6: **Spin to charge conversion.** **a** Normalized probability that the four two-electron spin states are detected as a triplet state. The probability that the triplet antiparallel spin state is correctly identified as a triplet can be lowered by the non perfect adiabaticity of the pulse and by a faster triplet-singlet relaxation.

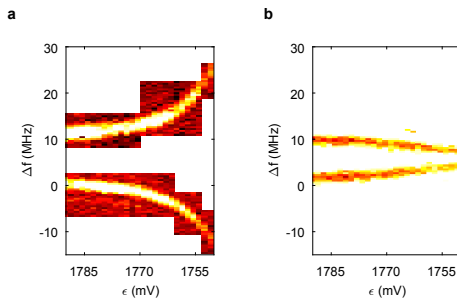


Figure 5.7: **Exchange interaction.** **a-b** Resonance frequency of both qubits as a function of the detuning energy. In **a** we show the transitions f_1 and f_4 , while in **b** we show the transitions f_2 and f_3 . We measure the excited states by ESR controlled spin flips applied to the control qubit.

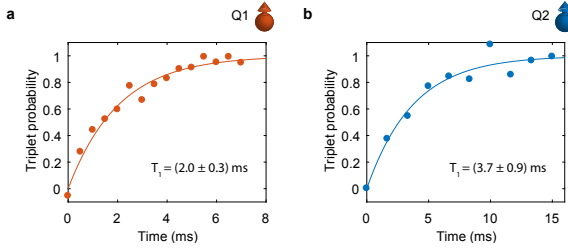


Figure 5.8: **Relaxation times.** **a-b** Single-spin relaxation times of Q1 and Q2. The measurements are performed by fitting the decay of the states $|\downarrow\uparrow\rangle$ and $|\uparrow\downarrow\rangle$ to the $|\downarrow\downarrow\rangle$ state. We extract $T_{1(Q1)} = 2.0$ ms and $T_{1(Q2)} = 3.7$ ms, consistent with [6]. Triplet probabilities have been normalized to remove readout errors.

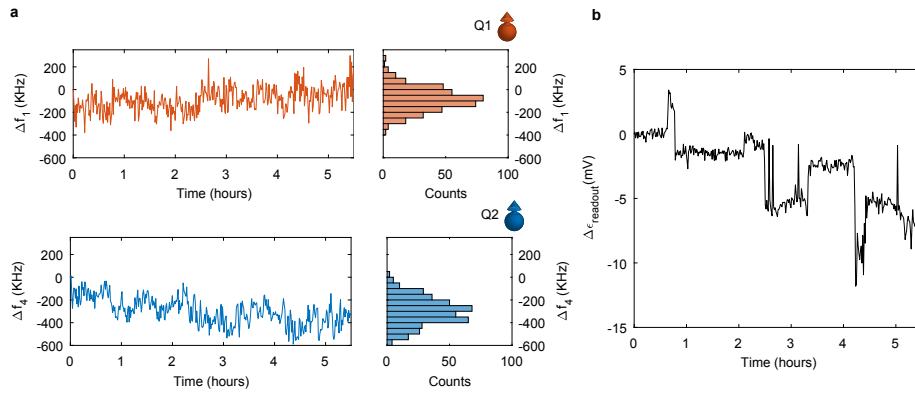


Figure 5.9: **Time dependence of resonance frequencies and readout point.** **a** Time dependences of the resonance frequencies f_1 and f_4 of Q1 and Q2 respectively. The exchange interaction is set to 2.5 MHz. The data have been offset by 6.9491 GHz and 6.9620 GHz for f_1 and f_4 respectively. **b** Time dependence of the readout point obtained by taking a sweep along the detuning axis in a measurement identical to the one shown in Fig. 5.1d. The best readout point is returned with a gaussian fit of the visibility peak.

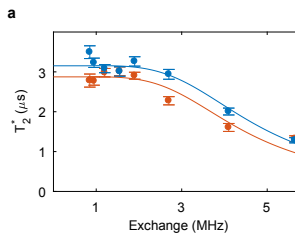


Figure 5.10: **Dephasing times for Q1 and Q2 as a function of exchange interaction.** **a** Dephasing times of Q1 and Q2 as a function of exchange interaction, fitted with the model discussed in section 5.9. Due to a different tuning configuration, the dephasing times are slightly longer than the ones reported in Figure 5.2. In this new configuration we measure a tunnel coupling $t_c = 0.8$ GHz and a Zeeman energy difference $\delta E_Z = 10.6$ MHz.

5.8. FIT OF THE FULL EXCHANGE SPECTRUM

We operate our device in the (5,1) charge occupation regime, close to the (4,2) transition. Considering that the four lowest-energy electrons in the right dot completely freeze out the s-orbital, they do not contribute to the dynamics and thus can be neglected. In the (5,1) charge occupation regime there are four relevant spin states in the lowest valley, $|\uparrow\uparrow\rangle, |\uparrow\downarrow\rangle, |\downarrow\uparrow\rangle, |\downarrow\downarrow\rangle$ which are coupled via tunneling to the (4,2) singlet states $|s(4,2)\rangle$. Therefore, our system can be well-described by the Hubbard Hamiltonian [37]

$$H = \begin{pmatrix} E_z & E_{x,2}^*/2 & E_{x,1}^*/2 & 0 & 0 \\ E_{x,2}/2 & \Delta E_z/2 & 0 & E_{x,2}^*/2 & t_0^* \\ E_{x,1}/2 & 0 & -\Delta E_z/2 & E_{x,1}^*/2 & -t_0^* \\ 0 & E_{x,2}/2 & E_{x,1}/2 & -E_z & 0 \\ 0 & t_0 & -t_0 & 0 & \varepsilon - U \end{pmatrix}, \quad (5.1)$$

where $E_z = \mu_B(g_1 B_{z,1} + g_2 B_{z,2})/2$, $\Delta E_z = \mu_B(g_1 B_{z,1} - g_2 B_{z,2})$, and $E_{x,i} = \mu_B g_i (B_{x,i} + i B_{y,i})$ with $\mathbf{B}_i = (B_{x,i}, B_{y,i}, B_{z,i})^T$ and g_i being the magnetic field and g-factor of quantum dot $i = 1, 2$. Furthermore, t_0 describes the tunnel coupling between the dots, ε is defined as the difference of chemical potentials in quantum dot 1 and 2, and U describes the charging energy of quantum dot 1. The microwave antenna allows us to apply local time-dependent transverse magnetic fields, $E_{x,i} = E_{x,i} + E_{x,i}^{\text{ac}} \cos(2\pi f^{\text{ac}} t + \phi)$, giving rise to electron spin resonance. For large detuning $|\varepsilon - U| \gg t_0$ the system can be approximated by a Heisenberg Hamiltonian [37]

$$H = J(\mathbf{S}_1 \cdot \mathbf{S}_2 - 1/4) + \mu_B g_1 \mathbf{B}_1 \cdot \mathbf{S}_1 + \mu_B g_2 \mathbf{B}_2 \cdot \mathbf{S}_2 \quad (5.2)$$

with the spin operators $\mathbf{S} = (S_x, S_y, S_z)^T$ and the exchange interaction

$$J \approx 2t_0^2/(U - \varepsilon). \quad (5.3)$$

The four resonances observed in the experiment, $f_1 (|\downarrow\uparrow\rangle \rightarrow |\downarrow\downarrow\rangle)$, $f_2 (|\uparrow\uparrow\rangle \rightarrow |\uparrow\downarrow\rangle)$, $f_3 (|\downarrow\downarrow\rangle \rightarrow |\uparrow\downarrow\rangle)$ and $f_4 (|\downarrow\uparrow\rangle \rightarrow |\uparrow\uparrow\rangle)$, are then approximately given by

$$hf_1 = E_z - \sqrt{J^2 + \Delta E_z^2}/2 - J/2 \quad (5.4)$$

$$hf_2 = E_z - \sqrt{J^2 + \Delta E_z^2}/2 + J/2 \quad (5.5)$$

$$hf_3 = E_z + \sqrt{J^2 + \Delta E_z^2}/2 - J/2 \quad (5.6)$$

$$hf_4 = E_z + \sqrt{J^2 + \Delta E_z^2}/2 + J/2. \quad (5.7)$$

In order to extract parameters from the experiment we simultaneously fit $f_2 - f_1 = f_4 - f_3 = J/h$ and $f_4 - f_2 = +f_3 - f_1 = \sqrt{J^2 + \Delta E_z^2}/h$ to extract exchange as a function of detuning, the Zeeman field difference, and the tunneling amplitude. Our best fits yield $t_0 = 0.8 \pm 0.05$ GHz and $\Delta E_z = 9.1 \pm 0.1$ MHz.

5.9. NOISE MODEL AND NOISE FITTING

In this section we derive analytical expressions for the pure dephasing time T_2^* which are then used to extract the noise amplitude. In a Ramsey experiment the qubits are initialized in the $|\uparrow\uparrow\rangle$ state, then brought into a superposition state different for the two qubits: $|Q2+\rangle = (|\downarrow\uparrow\rangle + |\uparrow\uparrow\rangle)/\sqrt{2}$ and $|Q1+\rangle = (|\downarrow\uparrow\rangle + |\downarrow\downarrow\rangle)/\sqrt{2}$, then mapped back after some waiting time, and finally measured.

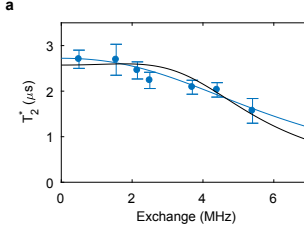


Figure 5.11: **Dependence of the dephasing times on the exchange interaction.** **a** Same data as shown in Fig. 5.4b, with fits accounting for fully correlated (blue line) and fully uncorrelated (black line) noise sources.

The phase $e^{-2\pi i\Phi(\tau)}$ the two qubits acquire during their free evolution is given by their energy difference $\Phi(\tau) = \int_0^\tau dt f_4$ and $\Phi(\tau) = \int_0^\tau dt f_1$. We assume that there are two dominating channels where noise can couple to the qubits, which is assumed to be longitudinal. We assume the noise comes from electrostatic fluctuations, which can couple via the detuning energy through the exchange interaction and through the g-factor modulation and spin-orbit coupling to the difference in Zeeman energy fields. The acquired phase for the two qubits are then given by

$$\Phi_{Q1,(Q2)}(t) = f_{4,(1)} + [\mathcal{D}_\epsilon \delta\epsilon(t) + \mathcal{D}_{\Delta E_z} \delta\Delta E_z(t)], \quad (5.8)$$

where $\mathcal{D}_\epsilon = \partial f_4 / \partial J \times \partial J / \partial \epsilon$ and $\mathcal{D}_{\Delta E_z} = \partial f_4 / \partial \Delta E_z$. The envelope of the Ramsey experiment is then given by the free induction decay [38]

$$2f(\tau) = 1 + \exp \left[-\pi i \langle \Phi(\tau)^2 \rangle \right] \quad (5.9)$$

$$1 + \exp \left[-\pi t^2 \left(\mathcal{D}_\epsilon^2 \sigma_\epsilon^2 + \mathcal{D}_{\Delta E_z}^2 \sigma_{\Delta E_z}^2 + \kappa^2 \mathcal{D}_\epsilon \mathcal{D}_{\Delta E_z} \sigma_\epsilon \sigma_{\Delta E_z} \right) \right] \quad (5.10)$$

under the assumption of Gaussian distributed noise and zero mean $\langle \Phi(\tau) \rangle = 0$. For the second line we assumed quasi-static noise with dispersion $\sigma_\epsilon = \int_{-\infty}^{\infty} S_\epsilon(\omega) d\omega$, where $S(\omega) = \int_{-\infty}^{\infty} \langle \delta\epsilon(t)^2 \rangle e^{-i\omega t} dt$ is the power spectral density of the noise. Similar expressions hold for $\sigma_{\Delta E_z}$. The correlation coefficient is defined $\kappa = \int_{-\infty}^{\infty} K_{\epsilon, \Delta E_z}(\omega) d\omega / (\sigma_\epsilon \sigma_{\Delta E_z})$ with the cross-spectral density $K_{\epsilon, \Delta E_z} = \int_{-\infty}^{\infty} \langle \delta\epsilon(t) \delta\Delta E_z(t) \rangle e^{-i\omega t} dt$. The dephasing time is then given by

$$(T_2^*)^{-1} = \sqrt{\pi} \sqrt{\mathcal{D}_\epsilon^2 \sigma_\epsilon^2 + \mathcal{D}_{\Delta E_z}^2 \sigma_{\Delta E_z}^2 + \kappa^2 \mathcal{D}_\epsilon \mathcal{D}_{\Delta E_z} \sigma_\epsilon \sigma_{\Delta E_z}}. \quad (5.11)$$

We fit the dephasing times as a function of exchange with either a fully uncorrelated noise $\kappa = 0$ or a fully correlated $\kappa = 1$ ansatz. The fits can be seen in Fig. 5.11a. Our best fit yields $\sigma_\epsilon = 21 \mu\text{eV}$, $\sigma_{\Delta E_z} = 400 \text{kHz}$. Assuming that the origin of the noise is $1/f$ and knowing our measurement time, we can convert σ_ϵ to the value of its relative power spectrum at 1 Hz, a metric often reported in literature. We obtain $A_\epsilon \approx 6 \mu\text{eV}/\sqrt{\text{Hz}}$ with $\sigma_\epsilon^2 = A_\epsilon^2 \log(f_{\text{uv}}/f_{\text{ff}})$ [38]. The lower and higher cutoff $f_{\text{ff}} \sim 10^{-2} \text{Hz}$ and $f_{\text{uv}} \sim 10^3 \text{Hz}$ are set by the experiment in the quasistatic approximation.

5.10. TEMPERATURE DEPENDENCE OF THE DEPHASING TIME

In our experiment we observe a weak temperature dependence of T_2^* . This is consistent with the assumption of random telegraphic noise coming from two level fluctuators (TLFs). The power spectral density of a single TLF is given by [34]

$$S(\omega, \nu) = \frac{A}{2 \cosh^2[E/(2k_B T)]} \frac{\nu}{\nu^2 + \omega^2}. \quad (5.12)$$

Here, A is the coupling strength of the fluctuations, E the (activation) energy gap between the two states of the TLF, and ν the switching rate. An explanation for the weak temperature dependence of T_2^* arises from the fact that Eq. 5.12 saturates if $k_B T \gg E$. Assuming that only a few TLFs couple to our system there is only a small probability to find a TLF which has an activation energy E exactly in the temperature range between 0.4 K till 1.2 K. The same arguments hold if instead of a two-level fluctuator an Anderson impurity is the origin of charge noise [39].

On the other hand, if we assume a large ensemble of TLFs a linear temperature dependence [6] is expected assuming that the number of ‘activated’ TLFs increases with temperature. For a large ensemble the noise spectral density reads [34]

$$S(\omega) \propto \int_{2\pi f_{\text{if}}}^{2\pi f_{\text{uv}}} \mathcal{P}(\nu, T) S(\omega, \nu) d\nu, \quad (5.13)$$

where $\mathcal{P}(\nu, T)$ describes the contribution of the process with a switching rate between ν and $\nu + d\nu$, thus, the probability density of a TLFs that contributes to the dephasing process. Assuming a temperature dependent switching rate $\nu = \nu_0 e^{-E/(k_B T)}$ leads to $\mathcal{P}(\nu, T) = \mathcal{P}(E, T) |\partial\nu/\partial E|^{-1}$ and one finds $\mathcal{P}(\nu, T) = \mathcal{P}(E, T) k_B T / \nu$ [34]. Assuming a constant distribution of activation energies, $\mathcal{P}(E, T) = \text{const}$ and inserting this into Eq. 5.13 the characteristic $1/f$ noise with a linear temperature dependence can be reproduced [32],

$$S(\omega) \approx \mathcal{P}(E, T) k_B T \frac{2\pi}{\omega} \equiv \frac{A_\epsilon}{\omega} \quad (5.14)$$

for $2\pi f_{\text{if}} \leq \omega \leq 2\pi f_{\text{uv}}$. However, recent work shows that the assumption of a constant distribution of activation energies $\mathcal{P}(E, T)$ is not entirely valid [35], and this can lead to anomalous temperature dependencies.

REFERENCES

- [1] Ladd, T. D. *et al.* Quantum computers. *Nature* **464**, 45–53 (2010).
- [2] Vandersypen, L. M. K. *et al.* Interfacing spin qubits in quantum dots and donors—hot, dense, and coherent. *npj Quantum Information* **3**, 34 (2017).
- [3] Veldhorst, M., Eenink, H. G. J., Yang, C. H. & Dzurak, A. S. Silicon CMOS architecture for a spin-based quantum computer. *Nat. Commun.* **8**, 1766 (2017).
- [4] Devoret, M. H. & Schoelkopf, R. J. Superconducting circuits for quantum information: an outlook. *Science* **339**, 1169–1174 (2013).
- [5] Neill, C. *et al.* A blueprint for demonstrating quantum supremacy with superconducting qubits. *Science* **360**, 195–199 (2018).
- [6] Petit, L. *et al.* Spin lifetime and charge noise in hot silicon quantum dot qubits. *Physical Review Letters* **121**, 076801 (2018).
- [7] Urdampilleta, M. *et al.* Gate-based high fidelity spin read-out in a cmos device. *Nature Nanotechnology* **14**, 737–741 (2019).
- [8] Yang, C. *et al.* Silicon quantum processor unit cell operation above one kelvin. *arXiv:1902.09126* (2019).
- [9] Loss, D. & DiVincenzo, D. P. Quantum computation with quantum dots. *Phys. Rev. A* **57**, 120–126 (1998).

- [10] Zwanenburg, F. A. *et al.* Silicon quantum electronics. *Rev. Mod. Phys.* **85**, 961–1019 (2013).
- [11] Veldhorst, M. *et al.* An addressable quantum dot qubit with fault-tolerant control-fidelity. *Nat. Nanotech.* **9**, 981–985 (2014).
- [12] Itoh, K. M. & Watanabe, H. Isotope engineering of silicon and diamond for quantum computing and sensing applications. *MRS Commun.* **4**, 143–157 (2014).
- [13] Yoneda, J. *et al.* A quantum-dot spin qubit with coherence limited by charge noise and fidelity higher than 99.9%. *Nature Nanotechnology* **13**, 102–106 (2017).
- [14] Yang, C. *et al.* Silicon qubit fidelities approaching incoherent noise limits via pulse engineering. *Nature Electronics* **2**, 151–158 (2019).
- [15] Veldhorst, M. *et al.* A two-qubit logic gate in silicon. *Nature* **526**, 410–414 (2015).
- [16] Zajac, D. M. *et al.* Resonantly driven CNOT gate for electron spins. *Science* **359**, 439–442 (2018).
- [17] Watson, T. F. *et al.* A programmable two-qubit quantum processor in silicon. *Nature* **555**, 633–637 (2018).
- [18] Huang, W. *et al.* Fidelity benchmarks for two-qubit gates in silicon. *Nature* **569**, 532–536 (2019).
- [19] Fowler, A. G., Mariantoni, M., Martinis, J. M. & Cleland, A. N. Surface codes: Towards practical large-scale quantum computation. *Physical Review A* **86**, 032324 (2012).
- [20] Franke, D. P., Clarke, J. S., Vandersypen, L. M. & Veldhorst, M. Rent's rule and extensibility in quantum computing. *Microprocessors and Microsystems* **67**, 1–7 (2019).
- [21] Li, R. *et al.* A crossbar network for silicon quantum dot qubits. *Science advances* **4**, eaar3960 (2018).
- [22] Morello, A. *et al.* Single-shot readout of an electron spin in silicon. *Nature* **467**, 687–691 (2010).
- [23] Yang, C. H., Lim, W. H., Zwanenburg, F. A. & Dzurak, A. S. Dynamically controlled charge sensing of a few-electron silicon quantum dot. *AIP Advances* **1**, 042111 (2011).
- [24] Lawrie, W. *et al.* Quantum dot arrays in silicon and germanium. *arXiv:1909.06575* (2019).
- [25] Angus, S. J., Ferguson, A. J., Dzurak, A. S. & Clark, R. G. Gate-Defined Quantum Dots in Intrinsic Silicon. *Nano Lett.* **7**, 2051–2055 (2007).
- [26] Elzerman, J. *et al.* Single-shot read-out of an individual electron spin in a quantum dot. *Nature* **430**, 431–435 (2004).
- [27] Yang, C. H. *et al.* Spin-valley lifetimes in a silicon quantum dot with tunable valley splitting. *Nat. Commun.* **4**, 2069 (2013).
- [28] Ruskov, R., Veldhorst, M., Dzurak, A. S. & Tahan, C. Electron g-factor of valley states in realistic silicon quantum dots. *Physical Review B* **98**, 245424 (2018).

- [29] Magesan, E., Gambetta, J. M. & Emerson, J. Scalable and robust randomized benchmarking of quantum processes. *Physical Review Letters* **106**, 180504 (2011).
- [30] Reed, M. *et al.* Reduced sensitivity to charge noise in semiconductor spin qubits via symmetric operation. *Physical review letters* **116**, 110402 (2016).
- [31] Martins, F. *et al.* Noise Suppression Using Symmetric Exchange Gates in Spin Qubits. *Phys. Rev. Lett.* **116**, 116801 (2016).
- [32] Güngördü, U. & Kestner, J. Pulse sequence designed for robust c-phase gates in simos and si/sige double quantum dots. *Physical Review B* **98**, 165301 (2018).
- [33] Freeman, B. M., Schoenfield, J. S. & Jiang, H. Comparison of low frequency charge noise in identically patterned si/sio₂ and si/sige quantum dots. *Applied Physics Letters* **108**, 253108 (2016).
- [34] Paladino, E., Galperin, Y., Falci, G. & Altshuler, B. 1/f noise: Implications for solid-state quantum information. *Reviews of Modern Physics* **86**, 361–418 (2014).
- [35] Connors, E. J., Nelson, J., Qiao, H., Edge, L. F. & Nichol, J. M. Low-frequency charge noise in si/sige quantum dots. *arXiv:1907.07549* (2019).
- [36] Eenink, H. *et al.* Tunable coupling and isolation of single electrons in silicon metal-oxide-semiconductor quantum dots. *Nano letters* **19**, 8653–8657 (2019).
- [37] Burkard, G., Loss, D. & DiVincenzo, D. P. Coupled quantum dots as quantum gates. *Physical Review B* **59**, 2070 (1999).
- [38] Ithier, G. *et al.* Decoherence in a superconducting quantum bit circuit. *Physical Review B* **72**, 134519 (2005).
- [39] Beaudoin, F. & Coish, W. A. Microscopic models for charge-noise-induced dephasing of solid-state qubits. *Physical Review B* **91**, 165432 (2015).

6

DESIGN AND INTEGRATION OF SINGLE-QUBIT ROTATIONS AND TWO-QUBIT GATES IN SILICON ABOVE ONE KELVIN

Spin qubits in quantum dots define an attractive platform for quantum information because of their compatibility with semiconductor manufacturing, their long coherence times, and the ability to operate above one Kelvin. However, despite demonstrations of SWAP oscillations, the integration of this two-qubit gate together with single-qubit control to create a universal gate set as originally proposed for single spins in quantum dots has remained elusive. Here, we show that we can overcome these limitations and execute a multitude of native two-qubit gates, together with single-qubit control, in a single device, reducing the operation overhead to perform quantum algorithms. We demonstrate single-qubit rotations, together with the two-qubit gates CROT, CPHASE and SWAP, on a silicon double quantum dot. Furthermore, we introduce adiabatic and diabatic composite sequences that allow the execution of CPHASE and SWAP gates on the same device, despite the finite Zeeman energy difference. Both two-qubit gates can be executed in less than 100 ns and, by theoretically analyzing the experimental noise sources, we predict control fidelities exceeding 99%, even for operation above one Kelvin.

6.1. INTRODUCTION

Two-qubit gates are at the heart of quantum information science, as they may be used to create entangled states with a complexity beyond what is classically simulatable [1], and ultimately may enable the execution of practically relevant quantum algorithms [2]. Optimizing two-qubit gates is therefore a central aspect across all qubit platforms [3]. In quantum dot systems, two-qubit gates can be naturally implemented using the exchange interaction between spin qubits in neighbouring quantum dots [4]. Pulsing the interaction drives SWAP oscillations, where the spin states in the quantum dots are being exchanged, when the exchange energy is much larger than the Zeeman energy difference of the qubits [4–6], while it results in controlled-phase (CPHASE) oscillations, where only the phase information is exchanged, when the Zeeman energy difference is much larger than the exchange energy [7]. Single-qubit gates need also to be implemented to access the full two-qubit Hilbert space, and this requires distinguishability between the qubits. This is commonly obtained through the spin-orbit coupling [8, 9] or by integrating nanomagnets [10, 11], causing significant Zeeman energy differences. Realizing a high-fidelity SWAP-gate in this scenario would require extremely large values of exchange interaction. For this reason, the CPHASE operation has been the native gate in experimental demonstrations of two-qubit logic when the exchange interaction is pulsed [12–14]. An alternative implementation of two-qubit logic can be realized by driven rotations, which become state dependent in the presence of exchange interaction and can be used to realize controlled-rotation (CROT) operations [15–19]. Driving rotations can also be used to realize a resonant SWAP gate [20], which can be used to perform state swapping. While universal quantum logic can be obtained by combinations of single-qubit rotations and an entangling two-qubit operation [21], the ability to directly execute a multitude of two-qubit gates would reduce the number of operations required to execute practical algorithms.

Here, we demonstrate on the same device the implementation of the CROT, SWAP, and CPHASE, which are all essential gates in quantum computing and error correction applications. SWAP operations can in particular be useful in large quantum dot arrays, providing a mean to achieve beyond nearest-neighbor connectivity. We overcome the limitations imposed by the finite Zeeman energy difference between the qubits by introducing control sequences, which also allows the execution of the CPHASE and the SWAP in short time scales and a predicted high-fidelity. Moreover, we demonstrate these operations at temperatures exceeding one Kelvin. The cooling power at these elevated temperatures is much larger and thereby more compatible with the operation of classical electronics, such that quantum integrated circuits based on standard semiconductor technology become feasible [22–24].

6.2. RESULTS AND DISCUSSION

6.2.1. SILICON QUANTUM DOT DEVICE

The experimental two-qubit system is based on electron spin states confined in a silicon double quantum dot as schematically shown in Fig. 6.1a. The silicon double quantum dot is fabricated using an overlapping gate architecture on a silicon wafer with an isotopically enriched ^{28}Si epilayer of 800 ppm residual concentration of ^{29}Si [19, 25]. In order to obtain an optimal exchange coupling between the electrons, qubits Q1 and Q2 are defined with $N_{Q1} = 1$ and $N_{Q2} = 5$, where N is the charge occupancy. Spin readout is performed at the (1,5)-(2,4) charge anticrossing, where the $|\uparrow\downarrow\rangle$ tunnels to the singlet (2,4) charge state, while the other spin states are blocked because of the Pauli exclusion principle. By using an adiabatic pulse from the (2,4) to the (1,5) region, we initialize the system in the $|\uparrow\downarrow\rangle$ state. Because of the limited sensitivity of the single-electron-transistor (SET) that we use for charge readout, we average the single-shot readout traces and subtract a reference signal. We therefore obtain a current signal, proportional to the probability to have a blocked state. More details about the readout scheme can be found in [19]. We note that the read-

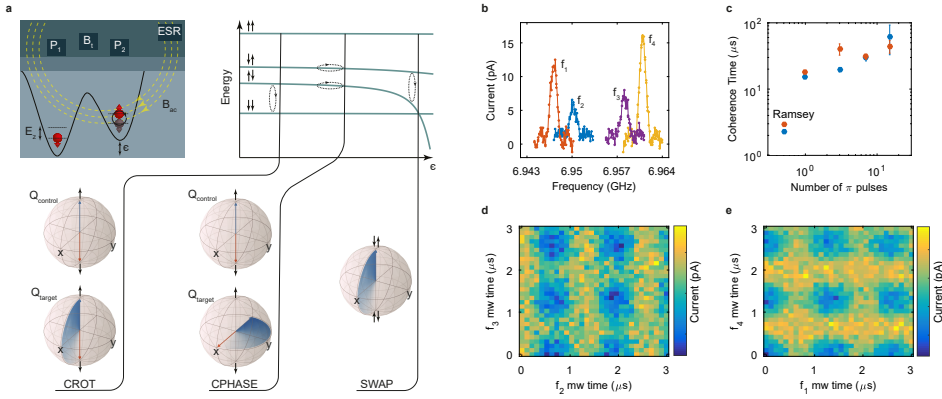


Figure 6.1: Two-qubit gates and quantum coherence of silicon spin qubits operated at a $T = 1.05$ K. **a** Schematic representation of the double quantum dot system. The device is the same as used in [19]. Two plunger gates (P_1 and P_2) and one barrier gate (B_1) are used to control the detuning energy ϵ and the tunnel coupling t between the quantum dots. Spin manipulation occurs via electron-spin-resonance (ESR) using an on-chip microwave line. The energy diagram displays the four electron spin states as a function of ϵ . We exploit both driven rotations and pulsed exchange for coherent control. Controlled rotations (CROTs) can in principle be executed at all points where $J \neq 0$, given that gate times are appropriately set. CPHASE gates are conveniently executed when the exchange interaction is much smaller than the Zeeman energy difference between the qubits, while SWAP oscillations can be realized when the exchange interaction is much larger. **b** Using ESR control we find the four resonance frequencies of the two-qubit system. Here, the exchange interaction is tuned to 3 MHz. The spectrum is composed of the frequencies: f_1 ($|\uparrow\downarrow\rangle \rightarrow |\downarrow\downarrow\rangle$), f_2 ($|\downarrow\downarrow\rangle \rightarrow |\uparrow\downarrow\rangle$), f_3 ($|\uparrow\uparrow\rangle \rightarrow |\downarrow\uparrow\rangle$) and f_4 ($|\uparrow\downarrow\rangle \rightarrow |\uparrow\uparrow\rangle$). **c** Coherence times as a function of the number of refocusing π pulses. Here, the exchange is set to 2 MHz. The plot includes the dephasing times measured through a Ramsey experiment to allow comparison. **d-e** Realization of CROT operations. Rabi oscillations of the target qubit are controlled by the spin state of the control qubit. We find controlled rotations on all the four resonance frequencies f_1, f_2, f_3, f_4 .

out fidelity can be further improved, even at these higher temperatures [26], but here we focus on the coherent control (details on the reconstruction are in section 6.4). We perform spin manipulation via electron spin resonance (ESR) using an on-chip aluminum microwave antenna. All measurements have been performed in a dilution refrigerator at a temperature of $T_{\text{fridge}} = 1.05$ K and with an external magnetic field of $B_{\text{ext}} = 250$ mT.

Readout on Pauli spin blockade is relatively insensitive to temperature, since it does not rely on any external reservoir. However, a finite temperature can still affect qubit readout in the form of an enhanced relaxation [27]. Furthermore, the initialization fidelity can also be lowered due to a non zero population of the excited valley states in the (2,4) charge configuration. By taking into account the two singlet and the three triplet states and estimating a valley splitting of $E_{\text{VS}} = 300 \mu\text{eV}$ from previous works [19, 27], we compute a total population of the ground singlet (2,4) charge state of 87%. This initialization fidelity can be pushed beyond 99% with a valley splitting $E_{\text{VS}} > 550 \mu\text{eV}$ (see section 6.5). Similar valley splitting values have already been measured in Si-MOS samples [9].

6.2.2. QUBIT CHARACTERIZATION

We control the exchange interaction J via the detuning ϵ between the two quantum dots and we measure couplings from $J = 2$ MHz up to $J = 45$ MHz, as shown in Fig. 6.4a. By fitting the exchange spectrum we extract a Zeeman energy difference between the two qubits $\Delta E_z = 11$ MHz, which originates from the the electron g -factor variations due to spin orbit coupling. This frequency

difference is large enough to have a negligible impact on qubit control fidelities. The fitting suggests a negligible dependence of ΔE_z on detuning, further supported by the small magnetic field applied and the absence of external magnetic gradients. Figure 6.1b shows the four resonance frequencies of the two-qubit system when $J = 3$ MHz. At this value of exchange interaction we tune the π -rotation times to be $t_{\text{CROT}} = 660$ ns such that we synchronize the Rabi oscillations of the target transition with the closest off-resonant transition in order to suppress crosstalk [28]. From Ramsey experiments on frequencies f_1 and f_4 we measure dephasing times $T_{2,Q1}^* = 2.3$ μ s and $T_{2,Q2}^* = 2.9$ μ s. The Carr-Purcell-Meiboom-Gill (CPMG) pulse sequence can extend the coherence times, by filtering out the low frequency noise. As shown in Fig. 6.1c, we measure a maximum $T_{2,Q1} = 63$ μ s and $T_{2,Q2} = 44$ μ s when 15 refocusing pulses are applied, setting benchmarks for the coherence time of quantum dot spin qubits at temperatures above one Kelvin.

When the exchange interaction is set to a non-zero value, it is possible to realize the CROT via driven rotations since the resonance frequency of one qubit depends on the state of the other qubit. This CROT gate is a universal two-qubit gate and equivalent to a CNOT gate up to single qubit phases [19]. Figures 6.1d-e show controlled rotations by setting both configurations of target and control qubits.

6.2.3. HOT, FAST, AND HIGH-FIDELITY CPHASE GATES

An alternative way to achieve a universal gate set is through the implementation of the CPHASE gate. Moving in detuning energy toward the (1,5)-(2,4) charge anticrossing lowers the energy of the antiparallel $|\downarrow\uparrow\rangle$ and $|\uparrow\downarrow\rangle$ states with respect to the parallel $|\downarrow\downarrow\rangle$ and $|\uparrow\uparrow\rangle$ spin states. Therefore, pulsing the detuning for a time t results in a phase gate on the target qubit conditional on the spin state of the control qubit. When the total phase $\phi = \phi_{|\downarrow\uparrow\rangle} + \phi_{|\uparrow\downarrow\rangle} = (2n + 1)\pi$ with n integer, a CPHASE gate is realized [7]. A high-fidelity implementation of such a gate requires a Zeeman energy difference between the two qubits much larger than the exchange interaction, in order to suppress the evolution of the exchange gate [4]. This condition is conveniently met in devices with micromagnets [13–15], where the CPHASE is the most natural choice as native two-qubit gate.

In our system, ΔE_z is comparable in magnitude to the accessible J (see section 6.6), due to the small B_{ext} applied. This means that a detuning pulse will also cause the $|\downarrow\uparrow\rangle$ and $|\uparrow\downarrow\rangle$ states to undergo SWAP rotations. While these rotations occur along a tilted angle due to the non-zero ΔE_z , they can still reduce the fidelity of the CPHASE gate. In order to avoid unwanted SWAP rotations we implement an adiabatic detuning pulse, by ramping ϵ to the desired value instead of changing it instantaneously (see schematic in Fig. 6.2j). In this way, a high-fidelity CPHASE gate can still be realized with an arbitrarily small ΔE_z at the cost of a longer gate time. In Fig. 6.2a-c and 6.2d-f we change the duration of a detuning pulse in between a Ramsey-like experiment on Q1, with and without a π pulse applied to Q2. The frequency of the oscillations of Q1 depends strongly on the spin state of Q2, thereby demonstrating a controlled phase operation. Because of the finite Zeeman energy difference, the antiparallel $|\downarrow\uparrow\rangle$ state shifts significantly more in energy than the $|\uparrow\downarrow\rangle$ state. Consequently, the oscillations in Fig. 6.2c are significantly faster than in Fig. 6.2f. Similarly, the decay time in Fig. 6.2e is significantly longer than in Fig. 6.2b because of the lower sensitivity to electrical noise. In Fig. 6.2g-i the pulse time is calibrated such that the total phase $\phi = 3\pi$. We measure this in a Ramsey-like experiment where we probe the phase acquired by the target qubit for different control qubit states. From Fig. 6.2h-i we can observe that the resulting oscillations are nicely out-of-phase, which demonstrates the CPHASE gate. We achieve a gate time $t_{\text{CPHASE}} = 152$ ns, which is mostly limited by the adiabatic ramps which take $t_r = 60$ ns. From a comparison with simulations we find that the contribution of both ramps to the total phase ϕ is approximately 1.7π .

This gate time can be significantly sped up with the implementation of a geometric CPHASE gate, that does not require adiabaticity [29]. For the implementation of this gate we synchronize

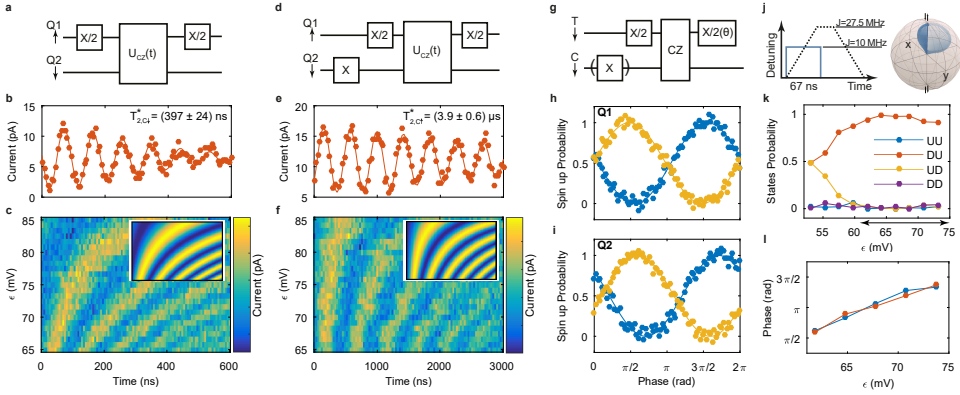


Figure 6.2: **Adiabatic and diabatic CPHASE operation at $T = 1.05$ K.** **b-c, e-f** Conditional phase oscillations by adiabatically pulsing the detuning energy ϵ to increase the exchange interaction J , measured using the quantum circuit in **a, d**. The antiparallel spin states acquire a phase with respect to the parallel states, resulting in coherent oscillations as a function of the duration of the detuning pulse. At smaller detuning values, the exchange interaction increases resulting in faster oscillations. Due to the exchange interaction, the energy difference $E_{\uparrow\uparrow} - E_{\downarrow\downarrow}$ (measured in **b-c**) is smaller than $E_{\uparrow\uparrow} - E_{\downarrow\downarrow}$ (measured in **e-f**), resulting in an acquired phase on the target qubit (T) that is dependent on the state of the control qubit (C). **g** Schematic of the quantum circuit to verify CPHASE operation. The adiabatic detuning pulse of the CPHASE gate is tuned such that the antiparallel spin states acquire a total phase of 3π . The exchange is increased to $J = 27.5$ MHz using a ramp $t_r = 60$ ns and the total gate time is $t_{\text{CPHASE}} = 152$ ns. We verify CPHASE operation by measuring the normalized spin-up probability, obtained through conversion of the readout current, and observe clear antiparallel oscillations (measured in **h-i**). **d** Schematic representation of an adiabatic (dashed black and shown in **g-i**) and a diabatic (solid blue) CPHASE. The diabatic CPHASE is optimized by changing the amplitude of ϵ and measuring probabilities of the four possible spin states in **k**. Due to the finite Zeeman difference ($\Delta E_Z = 11$ MHz) SWAP-interactions are not negligible. However, the exchange can be tuned such that the states undergo rotations of 2π . We tune and optimize this by measuring the phase, projected to the spin states through a $\pi/2$ -pulse on the target qubit. We obtain a diabatic CPHASE for $t_{\text{CPHASE}} = 67$ ns (measured in **k-l**).

the unwanted exchange oscillations with the total gate duration, i.e. our gate performs a CPHASE evolution while the exchange oscillations performs a complete cycle. For a perfectly diabatic pulse the condition for the exchange interaction is:

$$J = (4J_{\text{res}} + \sqrt{3\Delta E_Z^2 + 4J_{\text{res}}^2})/3, \quad (6.1)$$

where J_{res} is the residual exchange interaction at the point where we perform CROT gates (see section 6.7).

Figures 6.2k-l show the experimental implementation of the geometric CPHASE gate. We sweep the amplitude of the detuning pulse and monitor the spin state probabilities (see section 6.4) during exchange oscillations, and the total phase acquired by the antiparallel spin states. We notice that, when $\epsilon \approx 68$ mV, the antiparallel spin states execute a 2π rotation, while acquiring a total phase shift of π . At this value of detuning we measure $J \approx 10$ MHz (see section 6.6) and therefore in agreement with Eq. 6.1. The total gate time is reduced here to $t_{\text{CPHASE}} = 67$ ns.

6.2.4. HOT, FAST AND HIGH-FIDELITY SWAP OPERATION

We now turn to the implementation of a SWAP gate, the originally proposed quantum gate for quantum dots [4]. Despite the experimental demonstration of exchange oscillations [5, 6, 30], its

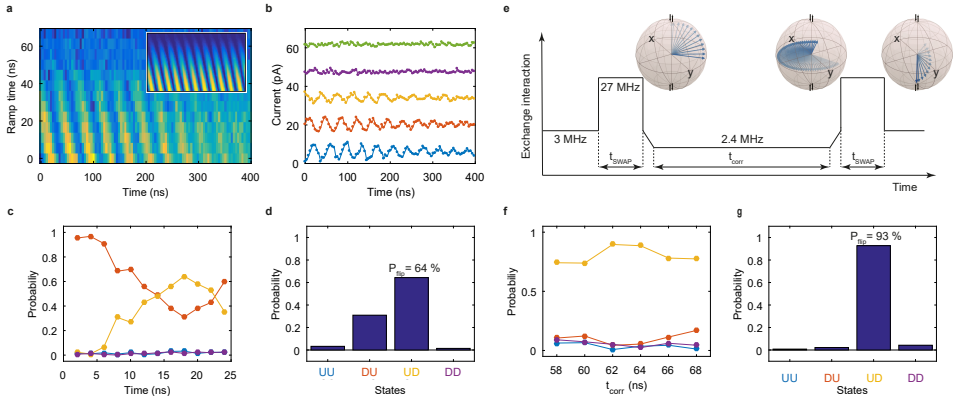


Figure 6.3: Pulsed SWAP and composite exchange pulse for high-fidelity SWAP at $T = 1.05$ K. **a-b** SWAP oscillations as a function of the ramp time for a detuning pulse such that $J = 23$ MHz. When the pulsing becomes adiabatic with respect to variations in J , the exchange oscillations are suppressed. In order to maximize the readout signal we project the $|\downarrow\downarrow\rangle$ to the $|\uparrow\uparrow\rangle$ with a π pulse on E_2 . Traces in **b** correspond to ramp times 0, 16, 33, 49 and 67 ns. We do not consider in these timings the finite bandwidth of the setup. Each trace has been offset by 15 pA for clarity. **c-d** Probabilities of the four spin states as a function of the SWAP interaction time. The states $|\uparrow\uparrow\rangle$ and $|\downarrow\downarrow\rangle$ are not affected, while the states $|\downarrow\uparrow\rangle$ and $|\uparrow\downarrow\rangle$ oscillate. Due to the finite Zeeman difference we achieve a maximum $|\uparrow\downarrow\rangle$ state probability of 64 % for $t_{\text{SWAP}} = 18$ ns. The exchange interaction is set to $J = 27$ MHz. **e** Pulse sequence of the composite SWAP gate to correct for errors coming from the finite Zeeman energy difference. The Bloch spheres on top show the time evolution when starting in the $|\downarrow\downarrow\rangle$ state, with the Bloch vector depicted in nanosecond time steps. We first diabatically pulse the exchange to $J = 27$ MHz, in order to bring the state on the equator of the singlet-triplet Bloch sphere. Then we correct for the phase offset with an adiabatic exchange pulse to $J = 2.4$ MHz. We complete the state flip with another exchange pulse to $J = 27$ MHz. **f** Spin state probability after applying the composite SWAP and as a function of the adiabatic pulse time t_{corr} , from which we find the optimum $t_{\text{corr}} = 62$ ns. **g** Spin state probability after executing the composite SWAP sequence starting from the initial state $|\downarrow\downarrow\rangle$. Compared to the detuning pulse as shown in **d** we find a clear improvement in the spin flip SWAP probability.

implementation together with single-qubit gates is rather challenging because of the requirement of a negligible Zeeman difference between the qubits. In the following we will discuss a protocol that can overcome this problem and allow for a high-fidelity SWAP gate, even in the presence of a finite ΔE_Z .

In order to observe SWAP oscillations, we implement a sequence where we initialize in the $|\downarrow\downarrow\rangle$ state and pulse ϵ for a time t . Clear exchange oscillations between the $|\downarrow\downarrow\rangle$ and the $|\uparrow\uparrow\rangle$ state are visible when the detuning pulse is diabatic (see Fig. 6.3a and 6.3b), where the oscillation frequency is $f_{\text{SWAP}} = \sqrt{J^2 + \Delta E_Z^2}$. As we make the pulse more adiabatic by ramping ϵ , the oscillations disappear and the regime becomes suitable for a CPHASE implementation as discussed before. Even when the detuning pulse is perfectly diabatic, we do not obtain a perfect SWAP due to the finite ΔE_Z . Instead, the spin states rotate in the Bloch sphere around the tilted axis of rotation $\mathbf{r} = (J, 0, \Delta E_Z)^T$, similar to what happens for off-resonant driving. Figure 6.3c and 6.3d show that when starting in the $|\downarrow\downarrow\rangle$ state, a maximum $|\uparrow\downarrow\rangle$ state probability of 64% is obtained in $t_{\text{SWAP}} = 18$ ns, which is in agreement with our simulated predictions (see section 6.7).

Composite pulse sequences [36, 37] can correct for the tilted axis of rotation. It is possible to achieve full population transfer with an exchange sequence consisting of alternating diabatic and adiabatic exchange pulses. The corresponding time evolution operators in the odd parity subspace are:

	Gate time (ns)	$F_{\text{ideal}}(\%)$	$F_{\text{noise}}(\%)$
CROT	660	99.4	89.0
CPHASE	152	99.9	97.8
Diabatic CPHASE	67	99.9	99.4
SWAP	19	84.3	84.2
Composite SWAP	89	99.9	99.4

Table 6.1: **Gate times and simulated fidelities for silicon qubits at $T = 1.05$ K.** Gate times and simulated fidelities for all the two-qubit gates discussed in section 6.2.3, where F_{ideal} represent the fidelity in the absence of noise and F_{noise} takes into account the experimental noise at 1.05 Kelvin. We find high-fidelity two-qubit gates can be obtained in silicon above one Kelvin, by using diabatic CPHASE or composite SWAP sequences. The CROT fidelity is calculated as a conditional π -flip for better comparison. Good agreement is obtained with previous experiments [19], confirming that the simulated noise is an accurate estimate of the real noise. Further improvement in the fidelities of the CROT and the CPHASE may be obtained by incorporating pulse shaping [31–35].

$$U_r = e^{i\Phi_r} e^{i\theta_r \mathbf{r} \cdot \boldsymbol{\sigma}} \quad (6.2)$$

$$U_z = e^{i\Phi_z} e^{i\theta_z \hat{Z}} \quad (6.3)$$

for a diabatic and an adiabatic pulse respectively (see section 6.7). Here $\boldsymbol{\sigma} = (\hat{X}, \hat{Y}, \hat{Z})$ is the vector consisting of the Pauli matrices, $\Phi_{r,z} = J t_{r,z}/2$ the accumulated entangling phase during the pulse, and $\theta_{r,z} = t_{r,z} \sqrt{J^2 + \Delta E_z^2}/2$ the angle of rotation. The condition for a SWAP gate is $U_{\text{tot}} = U_r U_z U_r U_z U_{r_2} \cdots \equiv \hat{X}$. The number of necessary pulses depends on the angle of rotation; obviously a minimal pulse sequence requires $|\Delta E_z| \leq J$. In the typical regime of operation for devices with micromagnets, where $J < \Delta E_z$, a multi-step sequence is required. In the limit $J \ll \Delta E_z$ many steps are necessary and the pulse sequence becomes gradually an ac signal giving rise to the ac-SWAP gate [20]. Furthermore, it is essential to include the global phase which corresponds to a conditional phase evolution in the full two-qubit space and needs to vanish when implementing a SWAP gate. This protocol is highly versatile and can also produce maximally entangling gates, i.e., $\sqrt{\text{SWAP}}$ if $U_{\text{tot}} \equiv i\hat{X}/2$ and $i\text{SWAP}$ for $U_{\text{tot}} \equiv i\hat{X}$. While finding an optimal sequence for such a composition can be done in general following the procedure of [37], here we extend these considerations into a multi-qubit space, which gives rise to additional constraints.

A possible minimal length solution for a SWAP gate is sketched in Fig. 6.3e and the trajectory of the qubit state is seen in the inset. In the experiment, we calibrate the exchange interaction at all stages of the pulse, fix the time of the diabatic pulses to 12 ns and sweep the length of the adiabatic pulse t_{corr} in order to find the best point. Figure 6.3f shows how the four spin probabilities change when sweeping t_{corr} . We find an optimal $t_{\text{corr}} = 62$ ns and the four spin state probabilities for a total pulse duration $t_{\text{SWAP}} = 88$ ns are plotted in Fig. 6.3g. The SWAP probability exceeds 90%, where the remaining error is dominated by miscalibrations, inaccuracies in the gates needed to reconstruct the spin state probabilities, and state-preparation-and-measurement (SPAM) errors. We note here that constructing a SWAP gate out of CPHASEs and CROT gates would result in a gate time significantly slower than the sequence discussed here. A SWAP gate can be compiled using 3 consecutive CROT gates, which would give a total SWAP time of $\approx 2\mu\text{s}$. A SWAP gate compiled from the much faster CPHASE gate requires 11 primitive operations [38], which include 8 single-qubit gates and would therefore give an even larger overhead. Therefore, the composite exchange sequence can improve the gate time by more than one order of magnitude.

6.2.5. HOT TWO-QUBIT GATE PERFORMANCE

In order to assess the performance of our two-qubit gates, we perform time dependent simulations of the Heisenberg hamiltonian, based on the exchange-detuning curve that we measure experimentally (see section 6.6). Additionally, we also take into account the effects of the finite bandwidth of the setup (300 MHz) on the pulse generation. Table 6.1 shows the fidelities associated with the two-qubit gates CROT, CPHASE, and SWAP. Here, F_{ideal} represents the simulated fidelities taking into account the relevant parameters, but neglecting any decoherence. We find $F_{\text{ideal}} > 99\%$ for all gates except the SWAP, which is limited in fidelity by the finite ΔE_z . At the elevated temperatures discussed in this work, thermal noise can impact the gate performances in the form of a larger charge noise amplitude [27], which couple to the spin as an effective magnetic noise via the exchange interaction. Therefore, we have also modelled the decoherence by adding stochastic fluctuations of the detuning, sampled from a $1/f$ noise spectrum (see section 6.7). By fitting the experimental data in Fig 6.2b and 6.2e, we conclude that our model is able to reproduce the decoherence with good agreement. Based on these simulations we determine F_{noise} . The fidelity of the CROT and the CPHASE gate are significantly affected by the noise, due to the relatively long gate times, and we find that the predicted CROT fidelity $F_{\text{noise}} = 89\%$ is close to the experimentally measured fidelity $F = 86\%$ [19]. The SWAP, diabatic CPHASE and composite SWAP are less affected by the noise and in particular we predict that both the diabatic CPHASE and composite SWAP can be executed with fidelities above 99%. While experimental data will be needed to validate these predictions, these results showcases how a multitude of native two-qubit gates can be executed with high-fidelities and remarkable gate speeds. The limiting factor to the fidelities is the charge noise, as we have to significantly pulse the detuning to control the exchange interaction. Significant improvements can be expected by keeping the detuning at zero and instead pulsing the tunnel coupling, as this scheme is to first order insensitive to charge noise.

The ability to execute a diverse set of high-fidelity two-qubit gates define silicon quantum dots as a versatile platform for quantum information. The low magnetic field operation and the small Zeeman energy difference between qubits is furthermore beneficial for the realization of scalable qubit tiles, as it supports high-fidelity shuttlers and on-chip resonators for long-distance qubit links. Moreover, the ability to execute quantum logic at temperatures exceeding one Kelvin provides a pathway to quantum integrated circuits that host both the qubits and their control circuitry for scalable quantum hardware.

6.3. METHODS

The experiments have been performed in a Bluefors refrigerator with a base temperature $T_{\text{base}} \approx 0.45\text{K}$ with a 3 tesla magnet. In the experiments we make use of d.c. voltages and a.c. voltages. The d.c. voltages are supplied via battery-powered voltage sources and filtered through Cu-powder filters and 30 Hz and 150 kHz filters. The a.c. voltages are supplied through a bias-tee that is on the sample printed circuit board with a cut-off frequency of 3 Hz. Pulses are generated by an arbitrary wave form generator (Keysight M3202A) with 14 bit resolution and 1 GS/s. Microwave signals are applied via a Keysight E8267D.

6.4. RECONSTRUCTION OF THE SPIN STATE PROBABILITIES

In order to readout the spin states we average all single-shot readout traces and subtract a reference sequence in which no gates are performed. The corresponding readout signal is therefore a current that is proportional to the probability of having a blocked state. In order to be able to reconstruct the four probability amplitudes $|A|^2, |B|^2, |C|^2, |D|^2$ of an arbitrary state $\psi = A|\uparrow\uparrow\rangle + B|\uparrow\downarrow\rangle + C|\downarrow\uparrow\rangle + D|\downarrow\downarrow\rangle$ it is necessary to know the current signal of the four spin states $\{\alpha \rightarrow |\uparrow\downarrow\rangle, \beta \rightarrow |\uparrow\uparrow\rangle, \gamma \rightarrow |\downarrow\downarrow\rangle, \delta \rightarrow |\downarrow\uparrow\rangle\}$. By initializing the $|\downarrow\uparrow\rangle$ state and then using the four

frequencies f_1, f_2, f_3, f_4 we can reach all spin states and therefore measure the parameters $\alpha, \beta, \gamma, \delta$.

Once we measure the current signals for all spin states we need to gain information about the state ψ . We therefore apply the following sequences and measure the parameters $\phi_0, \phi_1, \phi_2, \phi_3$:

- Sequence: prepare state ψ and then measure. We measure a current ϕ_0 equal to:

$$\phi_0 = |A|^2\beta + |B|^2\delta + |C|^2\alpha + |D|^2\gamma \quad (6.4)$$

- Sequence: prepare state ψ , apply a π pulse on f_4 , and then measure. We measure a current ϕ_1 equal to:

$$\phi_1 = |C|^2\beta + |B|^2\delta + |A|^2\alpha + |D|^2\gamma \quad (6.5)$$

- Sequence: prepare state ψ , apply a π pulse on f_1 , and then measure. We measure a current ϕ_2 equal to:

$$\phi_2 = |A|^2\beta + |B|^2\delta + |D|^2\alpha + |C|^2\gamma \quad (6.6)$$

- Sequence: prepare state ψ , apply a π pulse on f_2 , apply a π pulse on f_4 , and then measure. We measure a current ϕ_3 equal to:

$$\phi_3 = |C|^2\beta + |A|^2\delta + |B|^2\alpha + |D|^2\gamma \quad (6.7)$$

Therefore we have the following system of equations, that we want to solve for the probabilities $|A|^2, |B|^2, |C|^2, |D|^2$:

$$\begin{bmatrix} \beta & \delta & \alpha & \gamma \\ \alpha & \delta & \beta & \gamma \\ \beta & \delta & \gamma & \alpha \\ \delta & \alpha & \beta & \gamma \end{bmatrix} \cdot \begin{bmatrix} |A|^2 \\ |B|^2 \\ |C|^2 \\ |D|^2 \end{bmatrix} = \begin{bmatrix} \phi_0 \\ \phi_1 \\ \phi_2 \\ \phi_3 \end{bmatrix} \quad (6.8)$$

We solve the system by inverting the matrix:

$$\begin{bmatrix} |A|^2 \\ |B|^2 \\ |C|^2 \\ |D|^2 \end{bmatrix} = \begin{bmatrix} \beta & \delta & \alpha & \gamma \\ \alpha & \delta & \beta & \gamma \\ \beta & \delta & \gamma & \alpha \\ \delta & \alpha & \beta & \gamma \end{bmatrix}^{-1} \cdot \begin{bmatrix} \phi_0 \\ \phi_1 \\ \phi_2 \\ \phi_3 \end{bmatrix} \quad (6.9)$$

Finally the resulting amplitudes are normalized. The extracted probabilities correspond to the diagonal parts of the density matrix ρ which may violate $\sum_i \rho_{ii} = 1$ due to measurement and gate errors. In order to ensure the physicality of our results we perform a maximum-likelihood estimation [39] using the diagonal elements of the density matrix.

6.5. TEMPERATURE EFFECTS ON READOUT AND INITIALIZATION

To account for the effect for temperature on the initial and final state we consider that the system is coupled to a thermal bath with temperature $T = 1.05$ K. Under the assumption of thermal equilibrium the initial and final states are then given by the Gibbs state

$$\rho_{\text{th}} = 1/Z \exp(-\beta H_{(0,2)}) \quad (6.10)$$

with the partition function $Z = \text{Tr}\{\exp(-\beta H_{(0,2)})\}$ and the inverse temperature $\beta = (k_B T)^{-1} = 1/(89 \mu\text{eV})$. Since readout and initialization is performed deep in the (0,2) charge regime, the relevant Hamiltonian $H_{(0,2)}$ consists of two electrons in a double quantum dot in the presence

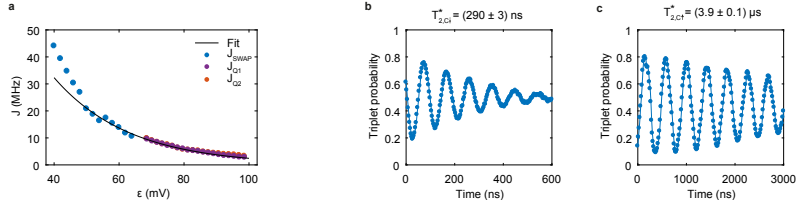


Figure 6.4: **Exchange interaction** **a** Exchange energy as a function of detuning energy. The data points J_{SWAP} have been extracted from the frequency of SWAP oscillations, J_{Q1} and J_{Q2} are obtained from the energy difference between f_1 and f_2 , and f_3 and f_4 respectively. The fit (solid black line) is used for simulations of detuning noise. We observe frequency jumps in the first five points of the data set, and these are therefore neglected in the fitting. **b-c** Simulated data for the sequence used in Fig. 6.2a and 6.2b.

of spin and valley [40]. The two-electron eigenstates in this regime are (approximately) anti-symmetric combinations of spin and valley singlet-triplet states labeled as $|\text{spin, valley}\rangle$. In the basis $\{|S, T_+\rangle, |T_+, S\rangle, |S, T_0\rangle, |T_0, S\rangle, |T_-, S\rangle, |S, T_-\rangle\}$ and neglecting electron-electron interactions the eigenenergies are

$$H_{(0,2)} = \text{diag}(2E_\nu, E_\nu + E_z, E_\nu, E_\nu, E_\nu - E_z, 0), \quad (6.11)$$

where $E_z \approx 29\mu\text{eV}$ is the Zeeman energy in the doubly occupied QD and E_ν is the valley splitting. The valley splitting can be estimated from previous works [19, 27], $E_\nu \approx 300\mu\text{eV}$, giving rise to a ground state probability, Eq. (6.10), of $P_{GS} \approx 87\%$. A thermal ground state probability of $>90\%$ ($>99\%$) can be reached at this elevated temperature with a valley splitting of $E_\nu \gtrsim 327\mu\text{eV}$ ($E_\nu \gtrsim 542\mu\text{eV}$) [9].

6.6. EXCHANGE SPECTRUM

Figure 6.4a shows the exchange spectrum as a function of detuning. When $J < 10\text{MHz}$ we measure the exchange interaction by mapping f_1, f_2, f_3, f_4 as a function of the detuning energy ϵ and then extract J as the difference between f_1 and f_2 , and f_3 and f_4 respectively. When $J > 10\text{MHz}$ we extract the exchange from the frequency of the SWAP oscillations given by $f_{\text{SWAP}} = \sqrt{J^2 + \Delta E_z^2}$.

The best agreement to our data set is obtained by fitting with an exponential dependence [41, 42] $J(\epsilon) = \exp(2\alpha(\epsilon - V_0))$ and constant $\Delta E_z(\epsilon) = \Delta E_z$ with parameters $\alpha = -0.022\ln(\text{MHz})/\text{mV}$, $V_0 = 120\text{mV}$, and $\Delta E_z = 11\text{MHz}$.

6.7. TWO-QUBIT GATE SIMULATIONS

6.7.1. PHYSICAL MODEL

For all the two-qubit gates we obtain the fidelities by numerically solving the time-dependent Schrodinger equation $i\hbar\dot{\Psi}(t) = H(t)\Psi(t)$ using a step size $t = 50\text{ps}$. We have confirmed that a faster sampling rate does not change the simulation results. In order to resemble real setups and to avoid sampling problems we filter all time-dependent signals using a high-pass filter with a cut-off frequency of 300MHz . All simulations are performed using the Heisenberg Hamiltonian

$$H(t) = \Delta E_z(\epsilon)(S_{z,1} - S_{z,2})/2 + J(\epsilon)(\mathbf{S}_1 \cdot \mathbf{S}_2 - 1/4), \quad (6.12)$$

where $\mathbf{S}_i = (S_{x,i}, S_{y,i}, S_{z,i})$ is the spin operator of the electron in quantum dot i . The parameters $\Delta E_z(\epsilon)$ and $J(\epsilon)$ are the qubit frequency difference and the exchange interaction which both depend on the detuning ϵ .

To include the effect of decoherence we add stochastic fluctuations of the detuning, $\epsilon \rightarrow \epsilon + \delta\epsilon(t)$ to each run of the time evolution and average the resulting density matrix. To emulate the effect of $1/f$ charge noise we generate time-dependent fluctuations $\delta\epsilon(t)$ following a $S(\omega) = A_c/f$ spectral density using the method described in Ref. [43, 44]. The amplitude of the noise A_c is set such that it reproduces the decay time of the exchange oscillations measured experimentally. Using the same value of noise we then simulate the Ramsey sequences of Fig. 6.2a and 6.2b and we show the results in Fig. 6.4b and 6.4c. The decay times that we extract are in agreement with the measured decays $T_{2,C\downarrow}^* = (397 \pm 24)$ ns and $T_{2,C\uparrow}^* = (3.9 \pm 0.6)$ μ s, where C refers to the control qubit.

For benchmarking the performance of the simulated gate operations we use the average gate fidelity from QuTiP [45].

6.7.2. ADIABATIC AND DIABATIC CPHASE GATES

Using the Hamiltonian in Eq. 6.12 it is possible to implement a controlled-phase (CPHASE) gate. The conventional approach for the CPHASE implementation is to use a smooth exchange pulse such that the system undergoes an adiabatic time evolution and it accumulates a phase difference between the even $\{|\uparrow\uparrow\rangle, |\downarrow\downarrow\rangle\}$ and odd parity subspace $\{|\uparrow\downarrow\rangle, |\downarrow\uparrow\rangle\}$. The adiabatic time evolution of the system described by the Hamiltonian in Eq. 6.12 is the unitary

$$U_{\text{ad}} = e^{-i\Phi(S_{z,1}S_{z,2}-1/4)} \times e^{-i(\theta_{\text{ad}}-\theta_{\text{res}})(S_{z,1}-S_{z,2})/2} \quad (6.13)$$

with the entangling phase $\Phi = \int_0^t (J(t') - J_{\text{res}}) dt' / \hbar$ and the single-qubit phases

$\theta_{\text{ad}} = \int_0^t \sqrt{\Delta E_Z^2 + J^2(t')} dt' / \hbar$ and $\theta_{\text{res}} = \sqrt{\Delta E_Z^2 + J_{\text{res}}^2} t / \hbar$. Here we explicitly took into consideration that $J(t=0) = J_{\text{res}}$. An adiabatic CPHASE gate is then obtained for $\Phi = (2n+1)\pi$ with n being an integer number. Virtual single-qubit z -gates are then applied to compensate for the single-qubit phase evolution θ_{ad} . Non-adiabatic (diabatic) errors due to a violation of the adiabatic condition enter via spin-flip terms $S_{x,1}S_{x,2} + S_{y,1}S_{y,2}$ and $S_{x,1}S_{y,2} - S_{y,1}S_{x,2}$ and give rise to SWAP oscillations. They can be mitigated using a decoupling scheme [28] or sufficiently long ramp times (see Fig. 6.3a).

Faster CPHASE gates can be realized using diabatic pulses where we synchronize the SWAP oscillation with the CPHASE evolution [29]. The diabatic time evolution of a system described by Eq. 6.12 is given by:

$$U_{\text{dia}} = e^{-i\Phi(S_{z,1}S_{z,2}-1/4)} \times e^{i\theta_{\text{res}}(S_{z,1}-S_{z,2})/2} \left(\cos(\theta_{\text{dia}}) - i \sin(\theta_{\text{dia}}) \frac{\mathbf{r} \cdot \boldsymbol{\sigma}}{|\mathbf{r}|} \right), \quad (6.14)$$

where $\mathbf{r} = (\Delta E_Z \cdot J - \Delta E_Z \cdot J_{\text{res}}, 0, \Delta E_Z^2 + J \cdot J_{\text{res}})$ describes the tilted SWAP rotation, $\theta_{\text{dia}} = \sqrt{\Delta E_Z^2 + J^2} t / \hbar$ the angle of the rotation, and $\boldsymbol{\sigma} = (\hat{X}, \hat{Y}, \hat{Z})$ is the vector consisting of Pauli matrices in the odd parity space

$$\hat{X} = |\uparrow\downarrow\rangle\langle\downarrow\uparrow| + |\downarrow\uparrow\rangle\langle\uparrow\downarrow| \quad (6.15)$$

$$\hat{Y} = -i|\uparrow\downarrow\rangle\langle\downarrow\uparrow| + i|\downarrow\uparrow\rangle\langle\uparrow\downarrow| \quad (6.16)$$

$$\hat{Z} = |\uparrow\downarrow\rangle\langle\uparrow\downarrow| - |\downarrow\uparrow\rangle\langle\downarrow\uparrow| = S_{z,1} - S_{z,2}. \quad (6.17)$$

Note, that we again took into consideration that $J(t=0) = J_{\text{res}}$ and assumed a piece-wise constant exchange pulse of the form

$$J(t) = \begin{cases} J & \text{if } t > 0 \text{ and } t \leq t_{\text{end}} \\ J_{\text{res}} & \text{else} \end{cases}. \quad (6.18)$$

A diabatic CPHASE gate is then given for $\Phi = (2n + 1)\pi$ and $\theta_{\text{dia}} = m\pi$ with m, n being integers. A generic solution for J , which satisfies both constraints, is given by

$$J = \frac{\sqrt{-(2n+1)^2 (\Delta E_Z^2 ((2n+1)^2 - 4m^2) - 4J_{\text{res}}^2 m^2) + 4J_{\text{res}} m^2}}{4m^2 - (2n+1)^2}. \quad (6.19)$$

The formula in equation 6.1 is obtained for $n = 0$ and $m = 1$, while the results in Ref. [29] are obtained for $J_{\text{res}} = 0$.

6.7.3. SWAP GATE

For $\Delta E_Z = J_{\text{res}} = 0$ the time-evolution of Eq. 6.14 gives rise to oscillations between the $|\uparrow\downarrow\rangle$ and $|\downarrow\uparrow\rangle$ states which can be used to implement the classical SWAP and maximally entangling $\sqrt{\text{SWAP}}$ gate [4]. This is not the case for a finite $\Delta E_Z \neq 0$ and $J_{\text{res}} > 0$ and the maximum flip probability is limited to

$$P_{\text{flip}} = |\langle \downarrow\downarrow | U_{\text{dia}} | \uparrow\uparrow \rangle|^2 = \frac{\Delta E_Z^2 (J - J_{\text{res}})^2}{(\Delta E_Z^2 + J^2)(\Delta E_Z^2 + J_{\text{res}})} \quad (6.20)$$

heavily reducing the maximum fidelity. When $J_{\text{res}} = 3$ MHz, $\Delta E_Z = 11$ MHz and $J = 27$ MHz we obtain a maximum flip probability $P_{\text{flip}} = 63\%$ which is a close match to the observed value in Figure 6.3c. From the formula above it is clear that a high-fidelity implementation of a SWAP gate with $J_{\text{res}} = 3$ MHz and $\Delta E_Z = 11$ MHz would require an extremely large exchange interaction, usually not achieved in state-of-the-art experiments in silicon. Furthermore, it is also impossible to implement a high-fidelity entangling $\sqrt{\text{SWAP}}$ in such a way due to the requirement $\sqrt{\text{SWAP}}\sqrt{\text{SWAP}} = \text{SWAP}$.

In order to overcome these issues we decompose our desired SWAP rotation in the odd parity subspace in terms of tilted \mathbf{r} rotations from the diabatic time evolution and \mathbf{z} rotations from the adiabatic phase evolution. We then construct a composite pulse sequence by alternating diabatic and adiabatic pulses which yields our desired operation U_{tot}

$$U_{\text{tot}} = U_{\text{dia}}(t_1, J_1) U_{\text{ad}}(t_2, J_2) U_{\text{dia}}(t_3, J_3) U_{\text{ad}}(t_4, J_4) \cdots \quad (6.21)$$

Here, the tuple (t_i, J_i) defines a diabatic or adiabatic pulse with time t_i and exchange J_i . The total number of pulses for a SWAP are estimated to be $N = 2 \lfloor \frac{90^\circ}{\beta} \rfloor$, where $\lfloor \cdot \rfloor$ is the floor function and β denotes the angle between the vectors \mathbf{r} and $\mathbf{z} = (0, 0, 1)$. Note, that the final U_{ad} operation only needs to correct single qubit phases which in our experiment can be done alternatively using virtual single qubit z -gates.

Enforcing the constraint $\Phi_{\text{tot}} = \Phi_1 + \Phi_2 + \Phi_3 + \Phi_4 + \cdots = m\pi$, with integer m and Φ_i being the entangling phase of the pulse $U_{\text{dia,ad}}(t_i, J_i)$, ensures that the composite pulse yields a SWAP gate. Using instead $\Phi_{\text{tot}} = \Phi_1 + \Phi_2 + \Phi_3 + \Phi_4 + \cdots = m\pi/2$ yields the universal i SWAP gate.

In our experiment we choose a minimal length symmetric composite pulse consisting of two identical diabatic pulses $U_{\text{dia}}(t_1, J_1) = U_{\text{dia}}(t_3, J_3) = U_{\text{r}}(t_{\text{SWAP}}, J)$ and an adiabatic pulse $U_{\text{ad}}(t_2, J_2) = U_{\text{z}}(t_{\text{corr}}, J_{\text{corr}})$ in between, $U_{\text{r}} U_{\text{r}} = \hat{X}$. The first diabatic pulse executes half of the desired SWAP rotation, the adiabatic pulse realizes a rotation in the $X - Y$ -plane, and the second diabatic pulses

finalizes the SWAP rotation. The pulse times are given by the conditions

$$t_{\text{SWAP}} = \frac{2\hbar \sin^{-1}\left(\frac{1}{\sqrt{2P_{\text{flip}}}}\right)}{\sqrt{\Delta E_Z^2 + J^2}}, \quad (6.22)$$

$$\int_{t_{\text{SWAP}}}^{t_{\text{SWAP}} + t_{\text{corr}}} \sqrt{\Delta E_Z^2 + J_{\text{corr}}^2(t')} dt' = 2\hbar \cos^{-1}\left(-\frac{\sqrt{(J^2 - \Delta E_Z^2)(\Delta E_Z^2 - J_{\text{res}}^2) - 4\Delta E_Z^2 J J_{\text{res}}}}{\Delta E_Z(J - J_{\text{res}})}\right) \quad (6.23)$$

and the condition for the entangling phase Φ_{tot} reads

$$2\hbar J t_{\text{SWAP}} + \hbar \int_{t_{\text{SWAP}}}^{t_{\text{SWAP}} + t_{\text{corr}}} J_{\text{corr}}(t') dt' = m\pi. \quad (6.24)$$

Using a numerical search we find that the pulse sequence

$$J_{\text{corr}}(t) = \begin{cases} 2.37 \text{ MHz} \times \frac{t}{t_{\text{ramp}}} & \text{if } t > 0 \text{ and } t \leq t_{\text{ramp}} \\ 2.37 \text{ MHz} & \text{if } t > t_{\text{ramp}} \text{ and } t_{\text{SWAP}} - t_{\text{ramp}} \\ 2.37 \text{ MHz} \times \frac{t - t_{\text{SWAP}} + t_{\text{ramp}}}{t_{\text{ramp}}} & \text{if } t > t_{\text{SWAP}} - t_{\text{ramp}} \text{ and } t \leq t_{\text{SWAP}} \\ 0 & \text{else} \end{cases} \quad (6.25)$$

allows to achieve gate fidelities $F > 99.9\%$.

REFERENCES

- [1] Arute, F. *et al.* Quantum supremacy using a programmable superconducting processor. *Nature* **574**, 505–510 (2019).
- [2] Reiher, M., Wiebe, N., Svore, K. M., Wecker, D. & Troyer, M. Elucidating reaction mechanisms on quantum computers. *Proceedings of the National Academy of Sciences* **114**, 7555–7560 (2017).
- [3] Ladd, T. D. *et al.* Quantum computers. *Nature* **464**, 45–53 (2010).
- [4] Loss, D. & DiVincenzo, D. P. Quantum computation with quantum dots. *Physical Review A* **57**, 120–126 (1998).
- [5] Petta, J. R. *et al.* Coherent Manipulation of Coupled Electron Spins in Semiconductor Quantum Dots. *Science* **309**, 2180–2184 (2005).
- [6] He, Y. *et al.* A two-qubit gate between phosphorus donor electrons in silicon. *Nature* **571**, 371–375 (2019).
- [7] Meunier, T., Calado, V. E. & Vandersypen, L. M. K. Efficient controlled-phase gate for single-spin qubits in quantum dots. *Physical Review B* **83**, 121403 (2011).
- [8] Nowack, K. C., Koppens, F. H. L., Nazarov, Y. V. & Vandersypen, L. Coherent control of a single electron spin with electric fields. *Science* **318**, 1430–1433 (2007).
- [9] Veldhorst, M. *et al.* An addressable quantum dot qubit with fault-tolerant control-fidelity. *Nature Nanotechnology* **9**, 981–985 (2014).

- [10] Kawakami, E. *et al.* Electrical control of a long-lived spin qubit in a Si/SiGe quantum dot. *Nature Nanotechnology* **9**, 666–670 (2014).
- [11] Yoneda, J. *et al.* A quantum-dot spin qubit with coherence limited by charge noise and fidelity higher than 99.9%. *Nature Nanotechnology* **13**, 102 (2018).
- [12] Veldhorst, M. *et al.* A two-qubit logic gate in silicon. *Nature* **526**, 410–414 (2015).
- [13] Watson, T. F. *et al.* A programmable two-qubit quantum processor in silicon. *Nature* **555**, 633–637 (2018).
- [14] Xue, X. *et al.* Benchmarking gate fidelities in a si/sige two-qubit device. *Physical Review X* **9**, 021011 (2019).
- [15] Zajac, D. M. *et al.* Resonantly driven CNOT gate for electron spins. *Science* **359**, 439–442 (2018).
- [16] Huang, W. *et al.* Fidelity benchmarks for two-qubit gates in silicon. *Nature* **569**, 532–536 (2019).
- [17] Hendrickx, N. W., Franke, D. P., Sammak, A., Scappucci, G. & Veldhorst, M. Fast two-qubit logic with holes in germanium. *Nature* **577**, 487–491 (2020).
- [18] Yang, C. H. *et al.* Operation of a silicon quantum processor unit cell above one kelvin. *Nature* **580**, 350–354 (2020).
- [19] Petit, L. *et al.* Universal quantum logic in hot silicon qubits. *Nature* **580**, 355–359 (2020).
- [20] Sigillito, A. J., Gullans, M. J., Edge, L. F., Borselli, M. & Petta, J. R. Coherent transfer of quantum information in a silicon double quantum dot using resonant swap gates. *npj Quantum Information* **5**, 1–7 (2019).
- [21] Barenco, A. *et al.* Elementary gates for quantum computation. *Physical Review A* **52**, 3457 (1995).
- [22] Veldhorst, M., Eenink, H. G. J., Yang, C. H. & Dzurak, A. S. Silicon CMOS architecture for a spin-based quantum computer. *Nature Communication* **8**, 1766 (2017).
- [23] Vandersypen, L. M. K. *et al.* Interfacing spin qubits in quantum dots and donors—hot, dense, and coherent. *npj Quantum Information* **3**, 34 (2017).
- [24] Li, R. *et al.* A crossbar network for silicon quantum dot qubits. *Science Advances* **4**, eaar3960 (2018).
- [25] Lawrie, W. I. L. *et al.* Quantum dot arrays in silicon and germanium. *Applied Physics Letters* **116**, 080501 (2020).
- [26] Urdampilleta, M. *et al.* Gate-based high fidelity spin read-out in a cmos device. *Nature Nanotechnology* **14**, 737–741 (2019).
- [27] Petit, L. *et al.* Spin lifetime and charge noise in hot silicon quantum dot qubits. *Physical Review Letters* **121**, 076801 (2018).
- [28] Russ, M. *et al.* High-fidelity quantum gates in si/sige double quantum dots. *Physical Review B* **97**, 085421 (2018).

- [29] Burkard, G., Loss, D., DiVincenzo, D. P. & Smolin, J. A. Physical optimization of quantum error correction circuits. *Physical Review B* **60**, 11404 (1999).
- [30] Maune, B. M. *et al.* Coherent singlet-triplet oscillations in a silicon-based double quantum dot. *Nature* **481**, 344 (2012).
- [31] Martinis, J. M. & Geller, M. R. Fast adiabatic qubit gates using only σ_z control. *Physical Review A* **90**, 022307 (2014).
- [32] Güngördü, U. & Kestner, J. Pulse sequence designed for robust c-phase gates in simos and si/sige double quantum dots. *Physical Review B* **98**, 165301 (2018).
- [33] Calderon-Vargas, F. *et al.* Fast high-fidelity entangling gates for spin qubits in si double quantum dots. *Physical Review B* **100**, 035304 (2019).
- [34] Güngördü, U. & Kestner, J. Analytically parametrized solutions for robust quantum control using smooth pulses. *Physical Review A* **100**, 062310 (2019).
- [35] Güngördü, U. & Kestner, J. Robust implementation of quantum gates despite always-on exchange coupling in silicon double quantum dots. *Physical Review B* **101**, 155301 (2020).
- [36] Vandersypen, L. M. K. & Chuang, I. L. Nmr techniques for quantum control and computation. *Reviews of Modern Physics* **76**, 1037 (2005).
- [37] Zhang, X.-M., Li, J., Wang, X. & Yung, M.-H. Minimal nonorthogonal gate decomposition for qubits with limited control. *Phys. Rev. A* **99**, 052339 (2019).
- [38] Lee, S. *et al.* The cost of quantum gate primitives. *Journal of Multiple-Valued Logic & Soft Computing* **12** (2006).
- [39] James, D. F. V., Kwiat, P. G., Munro, W. J. & White, A. G. Measurement of qubits. *Physical Review A* **64**, 052312 (2001).
- [40] Jiang, L. *et al.* Coulomb interaction and valley-orbit coupling in si quantum dots. *Phys. Rev. B* **88**, 085311 (2013).
- [41] Dial, O. E. *et al.* Charge noise spectroscopy using coherent exchange oscillations in a singlet-triplet qubit. *Physical Review Letters* **110**, 146804 (2013).
- [42] Cerfontaine, P., Botzem, T., DiVincenzo, D. P. & Bluhm, H. High-fidelity single-qubit gates for two-electron spin qubits in gaas. *Physical Review Letters* **113**, 150501 (2014).
- [43] Koski, J. V. *et al.* Strong photon coupling to the quadrupole moment of an electron in a solid-state qubit. *Nature Physics* **16**, 642–646 (2020).
- [44] Yang, Y.-C., Coppersmith, S. N. & Friesen, M. Achieving high-fidelity single-qubit gates in a strongly driven charge qubit with $1/f$ charge noise. *npj Quantum Information* **5**, 1–6 (2019).
- [45] Johansson, J., Nation, P. & Nori, F. Qutip 2: A python framework for the dynamics of open quantum systems. *Computer Physics Communications* **184**, 1234 (2013).



GERMANIUM

Not to be confused with Geranium

Wikipedia page on Germanium

We shift focus now to different quantum computing platform: Hole qubits in strained planar germanium quantum wells (Ge/SiGe) [1]. It has been predicted for a long time that the spin states of holes in quantum dots could be a promising candidate for quantum computing. The strong spin-orbit interaction facilitates fast, electrical manipulation of qubits [2], removing the need for bulky structures such as micromagnets or co-planar waveguides. In germanium specifically, the Fermi-level is pinned to the valence band for virtually any metallic contact [3], allowing for the creation of p-type Ohmic contact without the need for implantation or annealing. Additionally, the impressive hole mobility and percolation density in germanium quantum wells (See Chapter 3) suggests a very uniform material, particularly when compared to that of electrons in Silicon-MOS [4]. These qualities position hole states in Ge/SiGe as promising qubit candidates for a scalable quantum computing architecture.

Indeed, exciting and rapid progress in the field has been made possible by the combination of these favourable qualities, and pioneering work in silicon platforms. The field of hole spins in planar germanium progressed from the first demonstration of a quantum dot in Ge/SiGe [5] to two qubit logic in transport mode operated many-hole spin qubits in only two years [6].

The following chapters progress the field of quantum computing with hole states in planar germanium quantum wells. We begin, in chapter 7, by demonstrating the first single-hole spin qubit defined in a quantum dot. This experiment revealed that single hole spin qubits can be coherently controlled with Rabi oscillations approaching 100 MHz. It was also shown that the g-factor of such hole spins could be tuned significantly by altering the electrostatic environment around the spins. Chapter 8 addresses the spin-relaxation lifetime of quantum dots, finding that spin lifetime can be extended as high as 32 ms, by limiting dot-reservoir coupling. Further demonstration of an electrically susceptible g-factor is also shown by measuring the change in resonance frequency of each qubit as a function of their plunger gate potentials. The effect of local electric field on resonance frequency is expected as a result of the spin-orbit coupling present for holes in germanium, and is evidence that charge noise is the limiting mechanism for quantum coherence. By adapting the Ge/SiGe heterostructure such that the quantum wells were positioned deeper, we drastically reduced the charge noise experienced by the hole spin qubits, facilitating the work of the following chapters. In Chapter 9, we perform four-qubit logic on a 2x2 array of hole spin qubits, demonstrating controlled rotations on all neighbouring qubit pairs, a native three-qubit i-Toffoli gate, a novel four-qubit gate resembling a CCCNOT form, and perform a four-qubit algorithm in the form of a Greenberger-Horne-Zeilinger state generation. In chapter 10, we characterise the fidelities of single qubit gates on the same 2x2 quantum dot array using randomized benchmarking. We find that the native single qubit gate fidelities can be as high as 99.990(2)%. We also investigate how classical cross-talk affects single qubit fidelities by presenting a novel benchmarking technique called N-copy benchmarking, that separates classical cross-talk noise from quantum cross-talk noise. We find that single-qubit exchange insensitive fidelities for a two-copy benchmarking pair of qubits can be as high as 99.967 %,

while those of four-copy experiments are limited to around 99%. In chapter 11, we investigate the coherence properties of germanium hole spin qubits, analysing their dependence on charge noise and hyperfine interactions. We conclude, based on dephasing time behaviour as a function of applied magnetic field, that charge noise limits coherence in hole spin qubits in the investigated magnetic field regimes. However, we also observe decohering effects on the hole spin due to hyperfine interactions with the residual ^{73}Ge nuclear spins in the quantum well. We study the strengths of these interactions and find that at even at appreciable magnetic field strengths, the hyperfine interaction will limit spin dephasing within an order of magnitude of the charge noise limited values. These findings demonstrate the necessity of isotopic purification of germanium quantum wells, particularly given the present trends of Ge/SiGe material improvement.

REFERENCES

- [1] Scappucci, G. *et al.* The germanium quantum information route. *Nat. Rev. Mater.* (2020).
- [2] Bulaev, D. V. & Loss, D. Electric dipole spin resonance for heavy holes in quantum dots. *Phys. Rev. Lett.* **98**, 097202 (2007).
- [3] Dimoulas, A., Tsipas, P., Sotiropoulos, A. & Evangelou, E. K. Fermi-level pinning and charge neutrality level in germanium. *Appl. Phys. Lett.* **89**, 252110 (2006).
- [4] Lawrie, W. I. L. *et al.* Quantum Dot Arrays in Silicon and Germanium. *Appl. Phys. Lett.* **116**, 080501 (2020).
- [5] Hendrickx, N. W. *et al.* Gate-controlled quantum dots and superconductivity in planar germanium. *Nat. Commun.* **9**, 2835 (2018).
- [6] Hendrickx, N. W., Franke, D. P., Sammak, A., Scappucci, G. & Veldhorst, M. Fast two-qubit logic with holes in germanium. *Nature* **577**, 487–491 (2020).

7

A SINGLE-HOLE SPIN QUBIT

Qubits based on quantum dots have excellent prospects for scalable quantum technology due to their compatibility with standard semiconductor manufacturing. While early research mostly focused on the simpler electron system, recent demonstrations using many-hole quantum dots illustrated the favourable properties holes can offer for fast and scalable quantum control. Here, we establish a single-hole spin qubit in germanium and demonstrate the integration of single-shot readout and quantum control. We deplete a planar germanium double quantum dot to the last hole, confirmed by radio-frequency reflectometry charge sensing, and achieve single-shot spin readout. To demonstrate the integration of the readout and qubit operation, we show Rabi driving on both qubits and find remarkable electric control over their resonance frequencies. Finally, we analyse the spin relaxation time, which we find to exceed one millisecond, setting the benchmark for hole-based spin qubits. The ability to coherently manipulate a single hole spin underpins the quality of strained germanium and defines an excellent starting point for the construction of novel quantum hardware.

7.1. INTRODUCTION

Group-IV semiconductor spin qubits [1] are promising candidates to form the main building block of a quantum computer due to their high potential for scalability towards large 2D-arrays [2–5] and the abundance of net-zero nuclear spin isotopes for long quantum coherence [6, 7]. Over the past decade, all prerequisites for quantum computation were demonstrated on electron spin qubits in silicon, such as single-shot readout of a single electron [8], high-fidelity single-qubit gates [9, 10] and the operation of a two-qubit gate [11–14]. However, hole spins may offer several advantages [15, 16], such as a strong spin-orbit coupling (SOC) and a large excited state energy. Early research demonstrated the feasibility of using the SOC for all-electric driving [17, 18], but these experiments were limited by nuclear spins and the coherent driving of a single hole spin remained an open challenge. More recently, hole spins in group-IV materials have gained attention as a platform for quantum information processing [19–21]. In particular hole states in germanium can provide a high degree of quantum dot tunability [22–24], fast and all-electrical driving [20, 21] and Ohmic contacts to superconductors for hybrids [25, 26]. These experiments culminated in the recent demonstration of full two-qubit logic [21]. While hole spins have been read out in single-shot mode using the Elzerman technique [27], these experiments require magnetic fields impractical for hole qubit operation due to the strongly anisotropic g -factor of hole spins in germanium [28]. Pauli spin blockade readout allows for spin readout independent of the Zeeman splitting of the qubit, leveraging the large excited state energy purely defined by the orbital energy for holes in germanium. Furthermore, achieving these assets on a single-hole spin demonstrates full control over the materials system and allows to tune the quantum dot occupancy at will, optimising the different qubit properties. Moreover, the ability to study a platform at the single-particle level would provide great insight into its physical nature, crucial for holes which originate from a more complicated band structure than electrons [29, 30].

In this work, we make this step and demonstrate single-shot readout and operation of a single hole spin qubit. We grow undoped strained germanium quantum wells [31] and fabricate devices using standard manufacturing techniques [2]. The high mobility and low effective mass [32] allow us to define quantum dots of relatively large size, alleviating the restraints on fabrication. We deplete the quantum dots to their last hole, confirmed by charge sensing using a nearby single hole transistor (SHT). The use of radio-frequency (RF) reflectometry [33–35] enables a good discrimination of the charge state, while maintaining a high measurement bandwidth to allow for fast spin readout. We make use of Pauli spin blockade to perform the spin-to-charge conversion [36], maximally taking advantage of the large excited state energy splitting of $E_{ST} = 0.85$ meV and obtain single-shot spin readout. Finally, we demonstrate the integration of readout and qubit operation by performing all-electrically driven Rabi rotations on both qubits. Studying the control of a single hole qubit, we find a remarkably strong dependence of the resonance frequency on electric field and show a tunability of almost 1 GHz using only small electric potential variations.

7.2. RESULTS

7.2.1. SINGLE HOLE QUANTUM DOT AND PAULI SPIN BLOCKADE

A false-coloured SEM picture of the quantum dot device is depicted in Figure 7.1a. The device consists of a quadruple quantum dot system in a two-by-two array [2]. We tune the top two quantum dots into the many-hole regime, such that they can be operated as a single hole transistor. In order to perform high-bandwidth measurements of the sensor impedance, we make use of RF-reflectometry, where the SHT is part of a resonant LCR-circuit further consisting of an off-chip superconducting resonator together with the parasitic device capacitance. We apply a microwave signal to the tank circuit and measure the amplitude of the signal reflected by the LCR-circuit (see Figure 7.1a). The amplitude of the reflected signal $|S_{21}|$ depends on the matching of the tank cir-

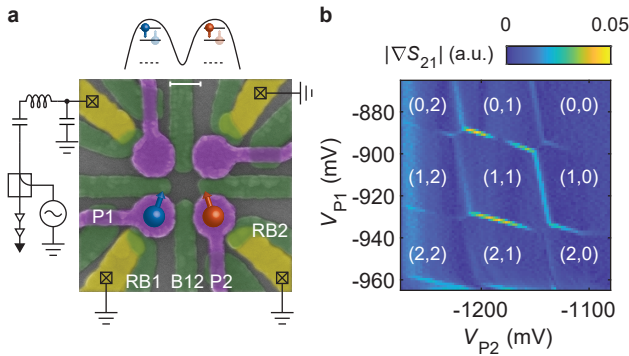


Figure 7.1: **Fabrication and operation of a planar germanium double quantum dot.** **a** False-coloured scanning electron microscope image of the quadruple quantum dot device. Ohmic contacts are indicated in yellow, a first layer of electrostatic barrier gates is indicated in green and the second layer of plunger gates is coloured in purple (for details, see Methods). The scale bar corresponds to 100 nm. We use the double quantum dot in the top channel as a single hole transistor (SHT) to sense changes in the charge occupation of the quantum dots formed under plunger gates P1 and P2. A schematic illustration of the electrostatic potential defining the two single-hole quantum dots is depicted above the figure. The charge sensor impedance is measured using reflectometry on a resonant circuit consisting of a superconducting resonator and the parasitic device capacitance. Barrier gates RB1 and RB2 can be used to control the tunnel rate of each quantum dot to its respective reservoir and gate B12 controls the interdot tunnel coupling. **b** Charge stability diagram of the double quantum dot system, where depletion of both quantum dots up to the last hole can be observed.

cuit impedance with the measurement setup and is therefore modulated by a change in the charge sensor impedance caused by the movement of a nearby charge.

We make use of the RF sensor to map out the charge stability diagram of the double quantum dot system defined by plunger gates P1 and P2. The tunnel coupling of the quantum dots to their reservoirs, as well as the interdot tunnel coupling can be tuned by gates RB1, RB2 and B12 respectively. Next, we tune the device to the single hole regime for both quantum dots (Fig. 7.1b and Figure 7.5), where (N_1, N_2) indicates the charge occupation, with N_1 (N_2) the hole number in the dot under P1 (P2). In our previous work [2], we further detail that we can deplete all four quantum dots in this device down to their last hole. In order to perform readout of the spin states, we make use of Pauli spin blockade (PSB), which is expected to be observed both at the $(1,1)$ - $(0,2)$ and $(1,1)$ - $(2,0)$ charge transitions. We define the virtual gates [37] detuning V_e and energy V_U (see Fig. 7.2a and Methods) and sweep across the $(1,1)$ - $(2,0)$ and $(1,1)$ - $(0,2)$ transitions in this gate space. As a result of its triplet character, the $|\downarrow\downarrow\rangle$ state has a negligible coupling to the $S(2,0)$ or $S(0,2)$ singlet charge states (Fig. 7.2b). When pulsing across the $(1,1)$ - $S(2,0)$ or $(1,1)$ - $S(0,2)$ anti-crossings, PSB prevents charge movement when the system is in the $|\downarrow\downarrow\rangle$ ground state. However, when the system resides in the singlet-like lower antiparallel spin state (in this case $|\downarrow\uparrow\rangle$, with Q2 being the qubit with lower Zeeman energy), charge movement to a doubly occupied quantum dot state is possible, therefore leaving the system in a $(0,2)$ or $(2,0)$ charge state. This results in a spin-to-charge conversion, which in turn can be picked up in the reflectometry signal from the SHT.

Indeed, we find that by sweeping the detuning voltage across the interdot transition from the $(1,1)$ into the $(0,2)$ charge region (Fig. 7.2d), tunnelling is blocked up to the reservoir transitions (indicated in white) when the system is initialised in the $|\downarrow\downarrow\rangle$ state. In this case we rely on the fast diabatic return sweep combined with fast spin relaxation compared to the sweep rate to prepare the system in the blocking $|\downarrow\downarrow\rangle$ state. When we inverse the sweeping direction, the system remains

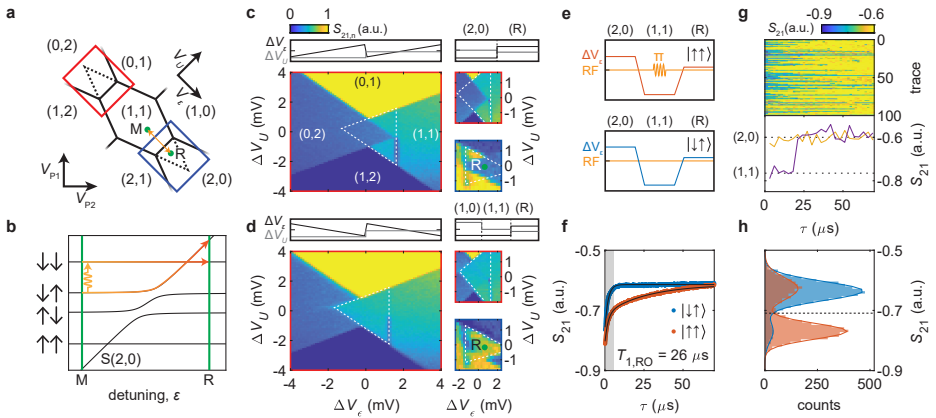


Figure 7.2: **Single-shot spin readout of a single hole.** **a** Schematic of a typical hole charge stability diagram with both possible regions of readout indicated in blue and red. The typical manipulation (M) and readout (R) points are indicated in green. **b** Two-hole energy diagram, with the five lowest lying energy states around the (1,1)-S(2,0) anticrossing. **c** Colour map of the normalised sensor response (normalisation in Methods) as a function of the applied gate voltages V_U and V_e . In the large panel, we linearly sweep V_e and step V_U , as indicated in the inset above the figure. The smaller panels on the right show the same effect for the (1,1)-(0,2) anticrossing (top, red box in **a**), and the (1,1)-(2,0) anticrossing (bottom, blue box in **a**), now using a two-level voltage pulse (details in Methods). **d** Similar colour map as in **c**, but with a reversed sweeping direction from (1,1) into the (0,2) region. The triangular spin blockade window is indicated by the dashed white line. The smaller panels on the right again demonstrate the same effect for both the (1,1)-(0,2) (top) as well as the (1,1)-(2,0) (bottom) anti-crossings, by first loading a random spin in one of the dots (details in Methods). **e** Schematic illustration of the three-level pulses used in panels **f-h**, indicating the detuning voltage ΔV_e in blue and red, and the RF-pulses in orange. **f** The averaged charge sensor response as a function of measurement time τ at R for $|\uparrow\uparrow\rangle$ initialisation (red) and $|\downarrow\downarrow\rangle$ initialisation (blue). The gray shaded area indicates the integration window for the threshold detection. **g** A sample of 100 single-shot traces (top), averaged for $3 \mu\text{s}$ per data point, with $\tau = 0$ the start of the readout phase. The bottom panel shows two single traces, where the purple (yellow) trace corresponds to the readout of a blocked (not blocked) spin state. Dashed lines correspond to the sensor signal for the different charge states. **h** Histogram of 5000 single-shot traces, integrating the signal for $5.5 \mu\text{s}$ as indicated in **f**. The blue (red) histogram corresponds to an initialisation in the $|\downarrow\downarrow\rangle$ ($|\uparrow\uparrow\rangle$) state. The dashed line corresponds to the optimised threshold for readout.

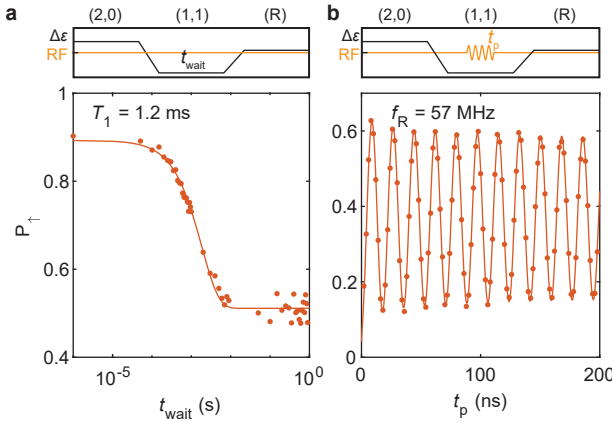


Figure 7.3: **Spin relaxation and coherent driving of a single hole.** **a** The system is initialised in the $|\downarrow\uparrow\rangle$ state after which the qubits idle at the measurement point. The spin-up fraction P_{\uparrow} of Q2 is measured as a function of waiting time t_{wait} and shows a typical T_1 -decay with a relaxation time of $T_1 = 1.2$ ms. **b** Driving of the single hole qubit Q2 shows coherent oscillations in P_{\uparrow} as a function of the microwave pulse length t_p . The coherent operation of Q1 is shown in Figure 7.8.

in the (0,2) charge states at the same values of V_e and V_U (Fig. 7.2c). After optimising the different tunnel rates in the device, we confirm the Pauli spin blockade at both the (1,1)-(2,0) and (1,1)-(0,2) anticrossings by loading a random spin before performing the readout, thereby not relying on a relaxation process for the initialisation (small panels of Fig. 7.2c,d). The diamond-shaped window of differential signal allows for a singlet/triplet readout of the system spin state and we select readout point R (see Figure 7.6). We note that the interdot transition line is shifted slightly towards positive detuning with respect to the reservoir transition lines. This is the direct result of a small voltage offset present across the device Ohmics, resulting in the unusual diamond-shaped spin readout window, but not limiting the readout. As holes in germanium do not have any valley states, the T(2,0) state is expected to be defined by the next quantum dot orbital. By increasing the bias voltage across the two quantum dots, we shift the interdot transition further. At large enough bias, the Pauli spin blockade window is capped as a result of the T(2,0) state becoming available in energy and from this we extract an excited state energy of $E_{ST} = 0.85$ meV, using a lever arm of $\alpha_e = 0.21$ as extracted from polarisation line measurements (Supplementary Figure 7.7).

7.2.2. QUBIT OPERATION

To coherently control the qubits, we implement a three-level voltage pulsing scheme (Fig. 7.2e) and operate at an external magnetic field of $B = 0.67$ T. We initialise the system by pulsing deep into the (2,0) region ($\alpha_e V_e > E_{ST}$), where the spins quickly relax into the (2,0) singlet state. Next, we ramp adiabatically into the (1,1) region, preparing the system into the $|\downarrow\uparrow\rangle$ state. At this point (M) we perform the qubit operations by applying microwave pulses to gate P1, taking advantage of the SOC-mediated EDSR. Rotating Q1 (Q2) will bring the system into the $|\uparrow\uparrow\rangle$ ($|\downarrow\downarrow\rangle$) state. Finally, the spin-state is read out by pulsing adiabatically into the readout window. Only the $|\downarrow\uparrow\rangle$ will allow a direct tunnelling into the (2,0) charge state, while tunnelling is blocked for all other states due to PSB.

Fig. 7.2f displays the charge sensor signal throughout the readout period, both for a $|\downarrow\uparrow\rangle$ ini-

tialisation (blue) as well as a $|\uparrow\uparrow\rangle$ initialisation (red) by applying a π -pulse to Q1. When no pulse is applied and the system is prepared in the $|\downarrow\downarrow\rangle$ state, a fast transition into the (1,1)-charge state, corresponding to a sensor signal of $S_{21} \approx -0.6$ can be observed. The remaining decay ($T_{\text{decay}} = 2 \mu\text{s}$) in this case can be attributed to the response of the SHT-signal to the voltage pulses on the gates. However, when the system is prepared in the $|\uparrow\uparrow\rangle$ state, a significantly slower relaxation into the (1,1) state is observed, due to the spin blockade combined with the slow $T_+(1,1)$ -S(2,0) relaxation. By fitting a double exponential decay, accounting for the SHT response, we extract a spin relaxation at the readout point of $T_{1,\text{RO}} = 26 \mu\text{s}$. A sample of 100 single-shot traces is plotted in Fig. 7.2g, together with two individual traces using a post-processing integration time of $3 \mu\text{s}$. A clear distinction of the (1,1) and (2,0) charge states can be observed from the sensor response. To determine the spin state of the qubits, we perform a threshold detection of the single-shot signal integrated from $\tau_0 = 1.0 \mu\text{s}$ up to $\tau_{\text{meas}} = 6.0 \mu\text{s}$ for maximised visibility, discarding the initial stabilisation of the SHT and optimising between the charge discrimination and spin relaxation. A histogram of 5000 single-shot events illustrates the clear distinction between the singlet ($S_{21} > -0.72$) and the triplet ($S_{21} < -0.72$) spin state readout (Fig. 7.2h). We find a spin readout visibility of $\nu = 56\%$ as obtained from the difference in spin-up fraction between the two prepared states. A large part of this reduced visibility is caused by relaxation of the blocked triplet state during the measurement, expected to amount to a signal reduction of $P_{\text{relax}} = 1 - e^{-\tau_{\text{meas}}/T_{1,\text{RO}}} = 0.21$. This gives good prospects for increasing the readout fidelity by optimising the spin relaxation, for instance by optimising the reservoir tunnel rates and moving to latched PSB readout mechanisms [38, 39]. Alternatively, by using high-Q on-chip resonators [40] the signal-to-noise ratio could be significantly improved, thereby lowering the required integration time and reducing the effective relaxation. The remaining triplet fraction of 0.11 that can be observed for the readout of the $|\downarrow\downarrow\rangle$ state could be attributed to an adiabaticity of the pulsing or a small coupling between the T(1,1) and S(2,0) states due to the SOC. This could be mitigated by further optimising the readout pulse sequence.

7

Now we probe the single spin relaxation time by initialising the system in the $|\downarrow\downarrow\rangle$ state and letting the system evolve at a detuning voltage $\Delta V_c = -7 \text{ mV}$ from the (1,1)-(2,0) anticrossing. Fig. 7.3a shows the spin-up fraction as a function of the waiting time t_{wait} , from which a single spin relaxation time of $T_{1,Q2} = 1.2 \text{ ms}$ can be extracted. This is substantially longer than reported before in planar germanium heterostructures [21], most likely as a result of the more isolated single hole spins as compared to the transport measurements with high reservoir couplings, and is also longer than all relevant time scales for qubit operation. Moreover, this relaxation time compares favourably to results obtained for holes in Ge nanowires [41], Ge hutwires [27] and other hole spins [42, 43].

To demonstrate coherent control of a single hole, we modulate the length of the driving microwave pulse and measure the spin-up fraction (Fig. 7.3b). A clear sinusoidal Rabi oscillation can be observed on Q2, with a Rabi frequency of $f_R = 57 \text{ MHz}$ (coherent operation of Q1 in Figure 7.8). We probe the phase coherence of both qubits by performing a Ramsey sequence in which we apply two $\pi/2$ -pulses, separated by a time τ in which we let the qubit freely evolve and precess at a frequency offset of $\Delta f = 7.4 \text{ MHz}$ and $\Delta f = 23.7 \text{ MHz}$ respectively. In Fig. 7.4b the Ramsey decay for Q1 and Q2 are plotted and we extract coherence times of $T_{2,Q1}^* = 380 \text{ ns}$ and $T_{2,Q2}^* = 140 \text{ ns}$. These coherence times are of comparable order, but slightly lower than previously reported numbers in the same heterostructure for a many-hole quantum dot [21]. In order to explain the origin of this, we measure the resonance frequency of both qubits as a function of the detuning voltage ΔV_c . We find a very strong dependence of the resonance frequency of both qubits on the detuning voltage over the entire range of voltages measured, with the g -factor varying between $g_{Q1} = 0.27 - 0.3$ and $g_{Q2} = 0.21 - 0.29$. This strong electric field dependence of the resonance frequency will increase the coupling of charge noise to the qubit spin states, which in turn will reduce phase coherence

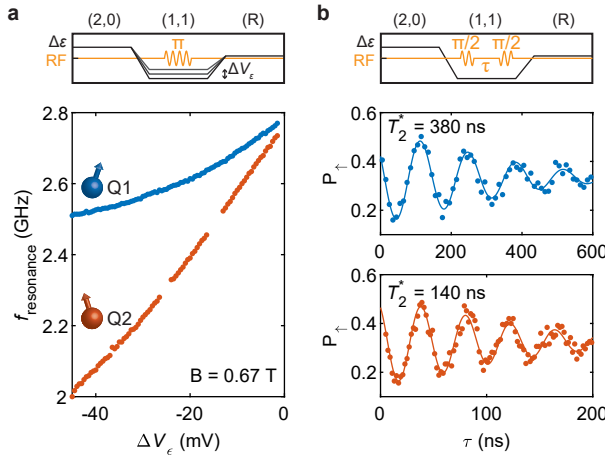


Figure 7.4: **Electric g-factor modulation and phase coherence of the qubit resonances.** **a** The resonance frequency of both qubits shows a strong modulation as a function of the detuning voltage ΔV_ϵ . **b** We perform a Ramsey experiment on both qubits to probe the phase coherence times, with $T_{2,Q1}^* = 380$ ns and $T_{2,Q2}^* = 140$ ns. The comparatively short phase coherence can be attributed to the strong dependence of $f_{\text{resonance}}$ to electric fields, coupling charge noise to the spin state, leading to increased decoherence.

[21]. The ratio in local slopes of the resonance frequency $\delta f_{Q2}/\delta f_{Q1} = 2$ is similar to the ratio in phase coherence of both qubits $T_{2,Q1}^*/T_{2,Q2}^* = 2.5$, consistent with charge-noise limited coherence. The strong modulation of the qubit resonance frequency by electric field could be explained from the strong SOC present [44, 45]. This is further supported by the Rabi frequency changing as a function of detuning voltage (see Figure 7.9), as is predicted to be a result of the strong SOC [44, 45]. We attribute the slightly different resonance frequency of Q1 and Q2 to an asymmetry in the potential landscape of the two dots. Although the strong g -factor modulation seems mainly a cause of decoherence in this case, careful optimisation of the electric field landscape could render a situation in which the qubit Zeeman splitting is well controllable, while maintaining a zero local slope for high coherence [45].

7.3. DISCUSSION

The demonstration that single hole spins can be coherently controlled and read out in single-shot mode, together with the spin relaxation times $T_1 > 1$ ms, defines planar germanium as a mature quantum platform. These aspects are demonstrated on a two-dimensional quantum dot array, further highlighting the advancement of germanium quantum dots. Moreover, controlling a single hole spin represents an important step towards reproducible quantum hardware for scalable quantum information processing.

METHODS

7.3.1. FABRICATION PROCESS

We grow strained Ge/SiGe heterostructures in an Epsilon 2000 (ASMI) reduced-pressure chemical vapor deposition reactor on a 100 mm n-type Si(001) substrate. The growth sequence comprises a 1.6- μm -thick relaxed Ge layer; a 1- μm -thick step-graded $\text{Si}_{1-x}\text{Ge}_x$ layer with final Ge composition

$x=0.8$; a 500-nm-thick strain-relaxed $\text{Si}_{0.2}\text{Ge}_{0.8}$ buffer layer; a 16-nm-thick strained Ge quantum well; a 22-nm-thick strain-relaxed $\text{Si}_{0.2}\text{Ge}_{0.8}$ barrier; a sacrificial Si cap layer <2 nm thick. Further details on the heterostructure are discussed in Ref. [31]. Ohmic contacts are defined by electron beam lithography, electron beam evaporation and lift-off of a 30-nm-thick Al layer. Electrostatic gates consist of a Ti/Pd layer with a thickness of 20 and 40 nm respectively for the barrier and plunger gate layer. Both layers are separated from the substrate and each other by 10 nm of ALD-grown Al_2O_3 .

7.3.2. EXPERIMENTAL SETUP

We use a Bluefors dry dilution refrigerator with a base temperature of $T_{\text{bath}} \approx 20$ mK to perform the measurements. Battery-powered voltage sources are used to supply DC-voltages on the gates. Additionally, AC-voltages generated by a Tektronix AWG5014C arbitrary waveform generator can be supplied to the gates through a bias-tee with a cut-off frequency of ≈ 10 Hz. Similarly, we can also apply a microwave signal generated by a Keysight PSG8267D vector source to gate P1 for qubit driving. Driving both qubits at the same power on gate P2, we observe significantly slower Rabi oscillations in Q1. From this we assume Q1 to be located under P1, and thus Q2 under P2, in correspondence with the trend in Rabi frequencies observed in a previous work [21].

We use an in-house built RF generator to supply the reflectometry signal. The signal is attenuated by 84 dB and applied to one of the sensor Ohmics via a Mini-Circuits ZEDC-15-2B directional coupler. The reflected signal is amplified by a Caltech CIRLF3 SiGe-amplifier at the 4K-stage of our fridge and an in-house built RF-amplifier at room temperature, and finally IQ-demodulated to give a measure of S_{21} .

7.3.3. MEASUREMENT DETAILS

The large panels of Fig. 7.2c and Fig. 7.2d are measured by continuously sweeping ϵ and stepping U , while measuring the sensor response. The smaller panels in Fig. 7.2c show the sensor response after applying a two-level voltage pulse to load the (2,0) or (0,2) charge configuration and vary the readout point across the map. The signal is then integrated for $10 \mu\text{s}$ at each pixel. The smaller panels in Fig. 7.2d show the sensor response after applying a three-level voltage pulse to first randomly load a spin in the second dot by pulsing across the (1,0)-(1,1) reservoir transition. Next, we pulse across the (1,1)-(0,2) or (1,1)-(2,0) interdot transition to perform the spin readout. The colour scale of the signal in Fig. 7.2c left and Fig. 7.2d left panels is normalised by $S_{21,n} = 10S_{21} + 3.5$. The top right panel in Fig. 7.2c is normalised by $S_{21,n} = 12.5S_{21} + 5.375$. The bottom right panel in Fig. 7.2c is normalised by $S_{21,n} = 12.5S_{21} + 5$. The top right panel in Fig. 7.2d is normalised by $S_{21,n} = 20S_{21} + 16.8$. The bottom right panel in Fig. 7.2d is normalised by $S_{21,n} = 25S_{21} + 20.75$, with $S_{21,n}$ the normalised sensor signal as plotted in Fig. 7.2 and $S_{21,n}$ the demodulated sensor signal strength in mV.

For the measurements in Fig. 7.2f-h and Fig. 7.3 and 7.4, typical adiabatic ramp times of $T_{\text{ramp}} \approx 1 \mu\text{s}$ are used.

7.3.4. VIRTUAL GATES

In order to allow independent control over the detuning and energy of the quantum dots more easily, we define the virtual gate axes of $V_\epsilon = V_{P2} - 0.5V_{P1}$ and $V_U = 0.5V_{P2} + V_{P1}$.

7.4. EXTENDED DATA

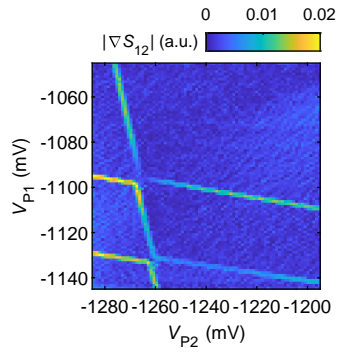


Figure 7.5: **Depletion of a hole double quantum dot in germanium.** Colour map of the sensor signal as a function of the voltages on plunger gates P1 and P2. No extra addition lines can be observed beyond $V_{P1} \approx -1100$ and $V_{P2} \approx -1260$, indicating the double quantum dot is fully depleted. This is the same anti-crossing as observed in Fig. 7.1b and the slight decrease of plunger gate voltages can be attributed to a time-dependent hysteretic drift as a result of extensive gate voltage sweeping.

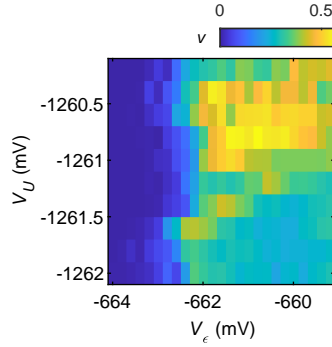


Figure 7.6: **Optimisation of the readout-point.** Colour map of the visibility of the readout ν , as defined by $\nu = P_{\text{blocked},\pi} - P_{\text{blocked},0}$, with $P_{\text{blocked},\pi}$ being the probability of measuring a blocked signal after applying a resonant π -pulse to Q1 and $P_{\text{blocked},0}$ the probability of measuring a blocked signal without applying any microwave pulses. A clear optimal spot for readout can be observed at $V_U = -1260.7$ mV, $V_\epsilon = -661.0$ mV.

7

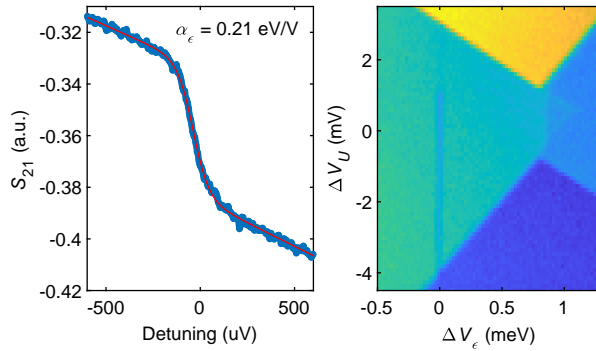


Figure 7.7: **Lever arm and excited state energy of the quantum dot.** **a** Polarisation line measurement of the (1,1)-(0,2) anticrossing. We fit the thermally limited polarisation line to a model including cross-talk to the charge sensor and the effect of the charge state on the sensor sensitivity [46]. Assuming a hole temperature of 100 mK as measured previously [47], we find a lever arm of $\alpha_\epsilon = 0.21$ eV/V, in good agreement with results obtained on similar devices. **b** We measure the excited state energy by applying a DC bias across the quantum dot ohmics, shifting the anti-crossing towards the negative detuning voltage. For large enough bias, the readout window is capped off, as a result of the excited state becoming available in energy. From this we deduce an excited state splitting of $E_{ST} = 0.85$ meV.

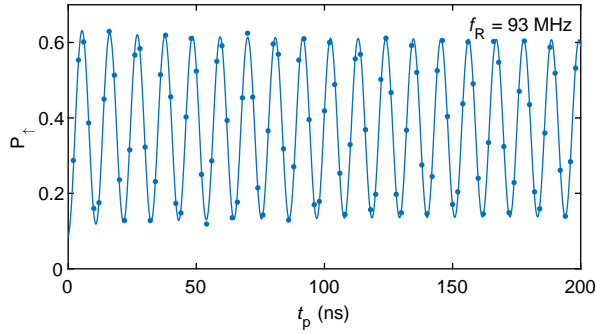


Figure 7.8: **Coherent operation of Q1.** We rotate Q1 by applying a resonant microwave pulse to gate P1 and observe fast Rabi oscillations, with a frequency of $f_R = 93$ MHz.

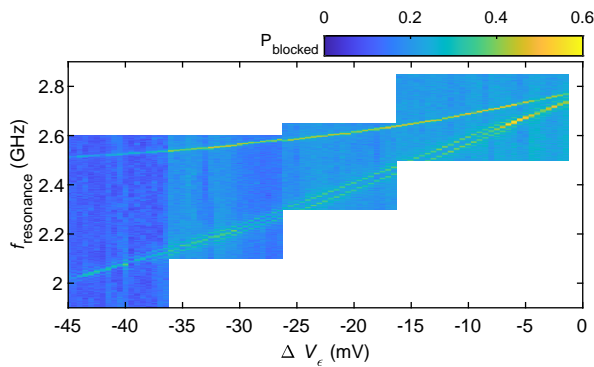


Figure 7.9: **Detuning dependence of the resonance frequency of Q1 and Q2.** Colour map indicating a blocked state fraction P_{blocked} as a function of the detuning voltage ΔV_ϵ of the manipulation point. We apply a microwave pulse to gate P2 with a duration of $t_p = 105$ ns, corresponding to an approximate 3π -pulse on Q2 and a π -pulse on Q1 at $\Delta V_\epsilon = -5$ mV. The resonance line corresponding to Q2, can be observed to split and recombine throughout the map, as a direct result of the Rabi frequency changing resulting in rotations exceeding a 3π -pulse.

REFERENCES

- [1] Loss, D. & DiVincenzo, D. P. Quantum computation with quantum dots. *Phys. Rev. A* **57**, 120–126 (1998).
- [2] Lawrie, W. I. L. *et al.* Quantum dot arrays in silicon and germanium. *Appl. Phys. Lett.* **116**, 080501 (2020).
- [3] Vandersypen, L. M. K. *et al.* Interfacing spin qubits in quantum dots and donors—hot, dense, and coherent. *npj Quantum Information* **3**, 34 (2017).
- [4] Veldhorst, M., Eenink, H. G. J., Yang, C. H. & Dzurak, A. S. Silicon CMOS architecture for a spin-based quantum computer. *Nature Communications* **8**, 1766 (2017).
- [5] Li, R. *et al.* A crossbar network for silicon quantum dot qubits. *Science Advances* **4**, eaar3960 (2018).
- [6] Itoh, K. M. & Watanabe, H. Isotope engineering of silicon and diamond for quantum computing and sensing applications. *MRS Commun.* **4**, 143–157 (2014).
- [7] Veldhorst, M. *et al.* An addressable quantum dot qubit with fault-tolerant control-fidelity. *Nat. Nanotech.* **9**, 981–985 (2014).
- [8] Morello, A. *et al.* Single-shot readout of an electron spin in silicon. *Nature* **467**, 687–691 (2010).
- [9] Yoneda, J. *et al.* A quantum-dot spin qubit with coherence limited by charge noise and fidelity higher than 99.9%. *Nat. Nanotech.* 102–106 (2017).
- [10] Yang, C. H. *et al.* Silicon qubit fidelities approaching incoherent noise limits via pulse engineering. *Nat Electron* **2**, 151–158 (2019).
- [11] Veldhorst, M. *et al.* A two-qubit logic gate in silicon. *Nature* **526**, 410–414 (2015).
- [12] Huang, W. *et al.* Fidelity benchmarks for two-qubit gates in silicon. *Nature* **1** (2019).
- [13] Watson, T. F. *et al.* A programmable two-qubit quantum processor in silicon. *Nature* **555**, 633–637 (2018).
- [14] Zajac, D. M. *et al.* Resonantly driven CNOT gate for electron spins. *Science* **359**, 439–442 (2018).
- [15] Bulaev, D. V. & Loss, D. Electric Dipole Spin Resonance for Heavy Holes in Quantum Dots. *Phys. Rev. Lett.* **98**, 097202 (2007).
- [16] Bulaev, D. V. & Loss, D. Spin Relaxation and Decoherence of Holes in Quantum Dots. *Phys. Rev. Lett.* **95**, 076805 (2005).
- [17] Pribiag, V. S. *et al.* Electrical control of single hole spins in nanowire quantum dots. *Nature Nanotechnology* **8**, 170–174 (2013).
- [18] Nowack, K. C., Koppens, F. H. L., Nazarov, Y. V. & Vandersypen, L. M. K. Coherent Control of a Single Electron Spin with Electric Fields. *Science* **318**, 1430–1433 (2007).
- [19] Maurand, R. *et al.* A CMOS silicon spin qubit. *Nature Communications* **7**, 13575 (2016).

- [20] Watzinger, H. *et al.* A germanium hole spin qubit. *Nature Communications* **9**, 3902 (2018).
- [21] Hendrickx, N. W., Franke, D. P., Sammak, A., Scappucci, G. & Veldhorst, M. Fast two-qubit logic with holes in germanium. *Nature* 1–5 (2020).
- [22] Hendrickx, N. W. *et al.* Gate-controlled quantum dots and superconductivity in planar germanium. *Nature Communications* **9**, 2835 (2018).
- [23] Hardy, W. J. *et al.* Single and double hole quantum dots in strained Ge/SiGe quantum wells. *Nanotechnology* **30**, 215202 (2019).
- [24] Froning, F. N. M. *et al.* Single, double, and triple quantum dots in Ge/Si nanowires. *Appl. Phys. Lett.* **113**, 073102 (2018).
- [25] Hendrickx, N. W. *et al.* Ballistic supercurrent discretization and micrometer-long Josephson coupling in germanium. *Phys. Rev. B* **99**, 075435 (2019).
- [26] Vigneau, F. *et al.* Germanium Quantum-Well Josephson Field-Effect Transistors and Interferometers. *Nano Lett.* **19**, 1023–1027 (2019).
- [27] Vukušić, L. *et al.* Single-Shot Readout of Hole Spins in Ge. *Nano Lett.* **18**, 7141–7145 (2018).
- [28] Mizokuchi, R., Maurand, R., Vigneau, F., Myronov, M. & De Franceschi, S. Ballistic One-Dimensional Holes with Strong g -Factor Anisotropy in Germanium. *Nano Lett.* **18**, 4861–4865 (2018).
- [29] He, L., Bester, G. & Zunger, A. Electronic Phase Diagrams of Carriers in Self-Assembled Quantum Dots: Violation of Hund’s Rule and the Aufbau Principle for Holes. *Phys. Rev. Lett.* **95**, 246804 (2005).
- [30] Liles, S. D. *et al.* Spin and orbital structure of the first six holes in a silicon metal-oxide-semiconductor quantum dot. *Nat. Comm.* **9** (2018).
- [31] Sammak, A. *et al.* Shallow and Undoped Germanium Quantum Wells: A Playground for Spin and Hybrid Quantum Technology. *Advanced Functional Materials* **29**, 1807613 (2019).
- [32] Lodari, M. *et al.* Light effective hole mass in undoped Ge/SiGe quantum wells. *Phys. Rev. B* **100**, 041304 (2019).
- [33] Schoelkopf, R. J., Wahlgren, P., Kozhevnikov, A. A., Delsing, P. & Prober, D. E. The Radio-Frequency Single-Electron Transistor (RF-SET): A Fast and Ultrasensitive Electrometer. *Science* **280**, 1238–1242 (1998).
- [34] Reilly, D. J., Marcus, C. M., Hanson, M. P. & Gossard, A. C. Fast single-charge sensing with a rf quantum point contact. *Appl. Phys. Lett.* **91**, 162101 (2007).
- [35] Barthel, C. *et al.* Fast sensing of double-dot charge arrangement and spin state with a radio-frequency sensor quantum dot. *Phys. Rev. B* **81**, 161308 (2010).
- [36] Ono, K., Austing, D. G., Tokura, Y. & Tarucha, S. Current Rectification by Pauli Exclusion in a Weakly Coupled Double Quantum Dot System. *Science* **297**, 1313–1317 (2002).
- [37] Hensgens, T. *et al.* Quantum simulation of a Fermi–Hubbard model using a semiconductor quantum dot array. *Nature* **548**, 70–73 (2017).

- [38] Studenikin, S. A. *et al.* Enhanced charge detection of spin qubit readout via an intermediate state. *Appl. Phys. Lett.* **101**, 233101 (2012).
- [39] Harvey-Collard, P. *et al.* High-Fidelity Single-Shot Readout for a Spin Qubit via an Enhanced Latching Mechanism. *Phys. Rev. X* **8**, 021046 (2018).
- [40] Zheng, G. *et al.* Rapid gate-based spin read-out in silicon using an on-chip resonator. *Nature Nanotechnology* **14**, 742–746 (2019).
- [41] Hu, Y., Kuemmeth, E., Lieber, C. M. & Marcus, C. M. Hole spin relaxation in Ge–Si core–shell nanowire qubits. *Nat. Nanotech.* **7**, 47–50 (2012).
- [42] Bogan, A. *et al.* Single hole spin relaxation probed by fast single-shot latched charge sensing. *Communications Physics* **2**, 1–8 (2019).
- [43] Gerardot, B. D. *et al.* Optical pumping of a single hole spin in a quantum dot. *Nature* **451**, 441–444 (2008).
- [44] Terrazos, L. A. *et al.* Theory of Hole-Spin Qubits in Strained Germanium Quantum Dots. (2020).
- [45] Wang, Z. *et al.* Suppressing charge-noise sensitivity in high-speed Ge hole spin-orbit qubits. (2019).
- [46] DiCarlo, L. *et al.* Differential Charge Sensing and Charge Delocalization in a Tunable Double Quantum Dot. *Phys. Rev. Lett.* **92**, 226801 (2004).
- [47] Petit, L. *et al.* Spin Lifetime and Charge Noise in Hot Silicon Quantum Dot Qubits. *Phys. Rev. Lett.* **121**, 076801 (2018).

8

SPIN RELAXATION BENCHMARKS AND INDIVIDUAL QUBIT ADDRESSABILITY FOR HOLES IN QUANTUM DOTS

We investigate hole spin relaxation in the single- and multi-hole regime in a 2x2 germanium quantum dot array. We find spin relaxation times T_1 as high as 32 ms and 1.2 ms for quantum dots with single- and five-hole occupations respectively, setting benchmarks for spin relaxation times for hole quantum dots. Furthermore, we investigate qubit addressability and electric field sensitivity by measuring resonance frequency dependence of each qubit on gate voltages. We can tune the resonance frequency over a large range for both single and multi-hole qubits, while simultaneously finding that the resonance frequencies are only weakly dependent on neighbouring gates. In particular, the five-hole qubit resonance frequency is more than twenty times as sensitive to its corresponding plunger gate. Excellent individual qubit tunability and long spin relaxation times make holes in germanium promising for addressable and high-fidelity spin qubits in dense two-dimensional quantum dot arrays for large-scale quantum information.

Qubits based on spin states are well established candidates for quantum information processing [2]. Pioneering studies were conducted on low-disorder gallium arsenide heterostructures [3, 4], but quantum coherence remained limited due to hyperfine interaction with nuclear spins. These interactions can be eliminated by using isotopically enriched group IV semiconductors as the host material [5]. In silicon this has led to landmark achievements, such as extremely long quantum coherence [6] and relaxation times [7], single qubit gates with fidelities beyond 99.9% [8, 9], execution of two-qubit gates [10, 11], quantum algorithms [12], and the operation of single qubit rotations [13] and two-qubit logic [14] above one Kelvin as a key step toward quantum integrated circuits [15–17].

In its natural form, germanium contains only 7.76% isotopes with non-zero nuclear spin and, like silicon, can be isotopically enriched [18] to eliminate nuclear spin dephasing. Recent advances in materials science enabled high mobility strained planar germanium (Ge/SiGe) heterostructures [19] for the fabrication of stable gate-defined quantum dots that can confine holes [20], which are predicted to have a multitude of favourable properties for quantum control [21, 22]. The inherent strong spin-orbit coupling of holes allows for fast qubit control [23–25] without integrating external components that complicate scalability, such as nano-magnets and microwave antennas. Moreover, holes do not suffer from valley degeneracy and their small effective mass of $m_h^* = 0.05 m_e^*$ [26] gives rise to large orbital splittings at the band center. These beneficial aspects thereby position holes in germanium as a promising material for quantum information [27].

While it has been demonstrated that both single- and multi-hole qubits can be coherently controlled and read out in planar germanium [25, 28], an open question remains which hole occupancy is most advantageous for quantum operation. Electron spin qubits in silicon have been operated with quantum dots containing one, three and even more electrons, with more electrons typically performing favourably in terms of driving speed when driven electrically due to greater wave function mobility [10, 29]. Here, we focus on single and multi-hole spin qubit operation in germanium and concentrate on two critical elements for quantum information with quantum dots: the spin relaxation time and the qubit addressability. We find that both the spin relaxation times of the single-hole ($T_{1,|n=1}\rangle$) and five-hole ($T_{1,|n=5}\rangle$) qubits are long, with the longest relaxation time for single-holes measured to be $T_{1,|n=1}\rangle = 32$ ms. Furthermore, we observe that single and multi-hole qubits exhibit a strong but comparable resonance frequency dependence on electric gate voltage. Interestingly, we find that while the qubit resonance frequency can be significantly tuned with the corresponding plunger gate, it is only weakly dependent on neighbour plunger gates. We thereby conclude that hole spin qubits can be locally addressed, crucial for the operation of dense qubit arrays.

8.1. DEVICE AND SETUP

The experiments are performed on a two-dimensional 2x2 quantum dot array fabricated using a multi-layer gate stack [30] (See Fig. 8.1a). Four plunger gates P_{1-4} define four quantum dots, whose interdot tunnel couplings are controllable via barrier gates B_{12-41} . Four metallic reservoirs O_{1-4} can be controllably coupled to each quantum dot via their respective barrier gates RB_{1-4} . We operate in a configuration whereby electrostatic gates P_1 , B_{12} and P_2 define one large quantum dot, serving as single-hole transistor (SHT) for charge sensing, shown in Fig. 8.1b. By connecting an inductor of $L \approx 2 \mu\text{H}$ inline with the ohmic O_1 , we form a resonant tank circuit at a frequency of $f_{O1} = 150.7$ MHz used for fast rf charge sensing [31, 32]. To optimise the reflection signal and minimise the inline resistance, we use a superconducting inductor made out of NbTiN. A second inline inductance connected to ohmic O_3 makes the device reconfigurable for any of the four dou-

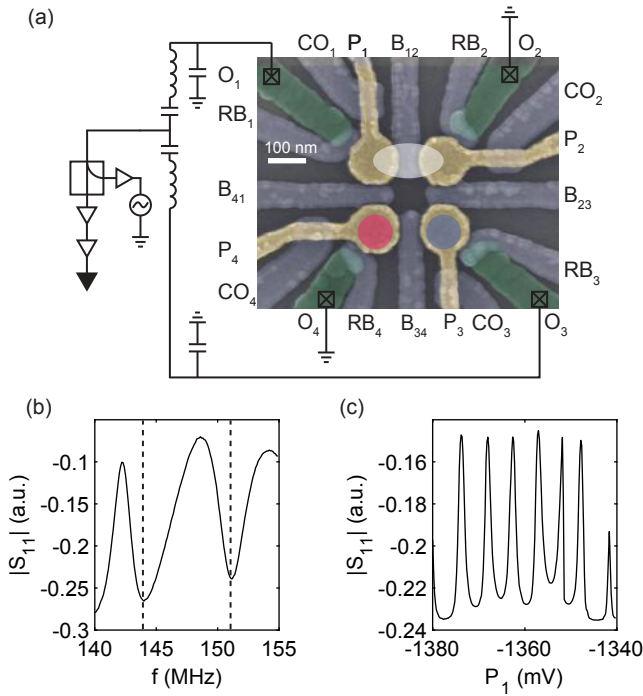


Figure 8.1: (a) Coloured scanning electron microscope image of a nominally identical 2x2 quantum dot array. Each quantum dot is defined by a plunger gate, P_{1-4} (yellow) and barrier gates B_{12-41} (blue) are used to set the tunnel coupling. In addition, each quantum dot is coupled to a reservoir, O_{1-4} (green), via a barrier gate RB_{1-4} . A cut off gate, CO_{1-4} , is present for good confinement of the quantum dots. Ohmics 1 and 3 are bonded to an inductor to create a tank circuit with the parasitic capacitance of the device to ground. A radiofrequency tone is applied to the ohmics and the reflected signal $|\Delta S_{11}|$ returns via a directional coupler and is read out. (b) Reflected signal of the two tank circuits. Two clear resonances occur at $f_{O1} = 150.7$ MHz and $f_{O3} = 143.3$ MHz for tank circuits connected to ohmics O_1 and O_3 respectively. (c) Single-hole transistor (SHT) Coulomb oscillations measured in the tank circuit response by applying a microwave tone of 150.7 MHz. A sensing quantum dot is formed underneath the plunger gates P_1 and P_2 , by opening the interdot barrier gate B_{12} .

ble quantum dot-sensor combinations, with a second tank circuit resonance at $f_{O3} = 143.3$ MHz. The reflected signal response to rf power delivered to the sample in a frequency range encompassing these two resonances is shown in Fig. 8.1b. Modulation of the channel resistance due to Coulomb oscillations in the SHT is shown in Fig. 8.1c. Next, we apply voltages to the plunger gates P_3 and P_4 to form quantum dots that load via the reservoir barriers RB_3 and RB_4 , respectively. By applying sawtooth wave pulses to the plunger gates and simultaneously applying the inverse pulses to the SHT plunger gates P_1 and P_2 , we can tune up the device to a double quantum dot of arbitrary occupancy while compensating the charge sensor in real time.

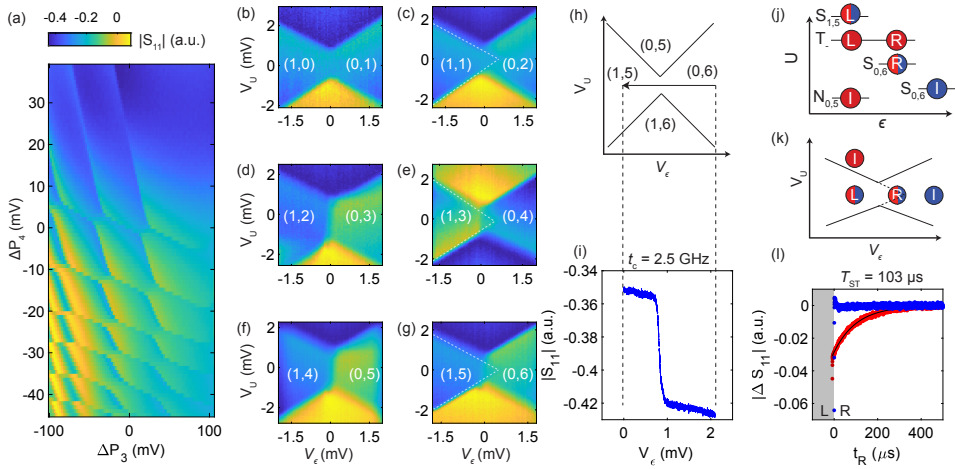


Figure 8.2: (a) Double quantum dot charge stability diagram obtained by rf-charge sensing in a reconfigurable quadruple quantum dot. A double quantum dot is formed under P_3 (blue) and P_4 (red) with controllable interdot tunnel coupling by tuning interdot barrier gate B_{34} and using rf-charge sensing we can clearly monitor the charge occupancy. The map is taken with 2000 averages. (b-g) Charge stability diagrams of charge anticrossings $(1,N-1) \leftrightarrow (0,N)$ for integer steps in N from 1 to 6. When N is odd (b,d,f), no spin blockade is present in the transitions. For even N (c,e,g), we observe spin blockade evidenced by triangular extensions of the charge addition lines (white lines are drawn in as a visual guide). (h-i) Interdot tunnel coupling measurement for the $(1,5) \leftrightarrow (0,6)$ transition. Sweep direction is negative in detuning axis to avoid spin blockade artifacts in spectrum. A tunnel coupling of $t_c = 2.5$ GHz is obtained and kept within 200 MHz of this value for all measurements in the work. (j) Cartoon of the initialization (I), loading (L) and readout (R) points of our pulse sequences in detuning ϵ and energy U space. The blue sequence loads the $|S_{(1,5)}\rangle$ singlet state which is not blocked on readout. The red sequence initializes in the $(0,5)$ charge state $N_{0,5}$ and loads a randomly oriented spin resulting in the singlet state or triplet state with equal probability (red), the latter of which results in a blocked signal. (k) Pulse sequences as a function of virtual detuning (V_e) and energy (V_U) gates, for the case of loading a singlet state (blue) and triplet/singlet state with equal probability (red). (l) Readout traces showing the signal difference between the spin blocked (red) and unblocked (blue) signals as a function of time spent in the read phase (t_R). Each trace is averaged 1000 times. The small deviation in the blue trace around $t_R = 0 \mu\text{s}$ is due to ringing in the applied AWG pulse. Loading a random spin under P_3 (red) leads to a singlet-triplet decay time of $T_{ST} = 103 \mu\text{s}$.

8.2. SPIN BLOCKADE FOR HOLE FILLINGS

Figure 8.2a shows the charge stability diagram for a sweep of gates P_3 versus P_4 over the first few charge addition lines in each quantum dot. We focus on the set of anticrossings for the first charge addition line of the quantum dot under P_3 of the form $(N_{P_3}, N_{P_4}) \iff (N_{P_3}-1, N_{P_4}+1)$, where $N_{P_{3(4)}}$ is the charge occupation of the quantum dot formed under $P_{3(4)}$, from double dot occupation $(1,0) \iff (0,1)$ to $(1,5) \iff (0,6)$. We define a virtual gate space in detuning V_c and energy V_U through a linear transformation of the gate voltages on P_3 and P_4 . We apply sawtooth wave pulses that sweep V_c from -2 mV to +2 mV and steps V_U from -2.5 mV to +2.5 mV with respect to the anticrossing. Figures 8.2b-g shows the resulting stability diagrams.

Pauli spin blockade is observed for $(N_{\text{odd}}, N_{\text{odd}}) \iff (N_{\text{even}}, N_{\text{even}})$ type transitions up to the sixth occupancy. This is consistent with a Fock-Darwin level filling observed for electrons in gallium arsenide [33] and holes in silicon [34] until the same charge occupancy. Working now with the $(1,5) \iff (0,6)$ anticrossing, we extract a lever arm $\alpha = 0.18$ from the thermally broadened polarization line using a hole temperature of 100 mK, which allows us to extract the tunnel couplings [35]. Figures 8.2h,i show the used pulse scheme and measured trace. The interdot coupling is kept constant within $t_c = 2.5 \pm 0.2$ GHz for all measurements. In Figures 8.2j, 8.2k, and 8.2l, we show the relevant pulse sequences in both energy-detuning and virtual gate space, as well as the resulting traces for Pauli spin blockade (PSB) readout respectively. Each pulse contains an initialization (I), load (L) and read (R) phase. Here we compare the partially blocked (red) and unblocked (dark blue) signals, allowing us to distinguish between the spin up and spin down states in the lower energy quantum dot. The small decay at the beginning of the unblocked trace is due to ringing in the AWG pulses. By loading a hole in P_3 with a random spin state, we expect to observe a blocked signal approximately half of the time. Monitoring the readout signal in the charge sensor as a function of time provides us with the spin relaxation at the readout position, which we find to be $T_{\text{ST}} = 103 \mu\text{s}$.

8.3. SPIN RELAXATION

We now assess the spin relaxation of the single- and five-hole qubits. All experiments were performed at a magnetic field $B = 0.67$ T, allowing for a comparison with previous germanium hole spin qubit experiments [25, 28] in a similar magnetic field regime. The Zeeman energy difference between our qubits manifests from spin-orbit induced changes in the g-factor of each qubit, lifting the antiparallel spin state energy degeneracy when an external magnetic field is applied. Figure 8.3a shows the pulse sequences used to measure the spin relaxation times of the hole spins in each quantum dot. Each pulse sequence consists of an initialization (I), load (L), and read (R) phase, with two ramps between the I and L phases (t_{IL}), and the L and R phases (t_{LR}). Using the first two sequences (red and blue in Fig. 8.3a) a randomly orientated spin is loaded into the quantum dot defined under P_4 or P_3 respectively. The Red and blue pulse sequences also contain an extra wait (W) step before initialization in the $(1,5)$ charge state to relax the spins to their ground state. This allows deterministic probing of the spin relaxation time of each dot, by varying the load wait time t_L .

The third pulse sequence (yellow in Fig. 8.3a) initializes the system in the singlet state with charge configuration $(N_{P_3}, N_{P_4}) = (0,6)$ ($|S_{(0,6)}\rangle$). The system is then tuned to the charge configuration $(N_{P_3}, N_{P_4}) = (1,5)$ ($|S_{(1,5)}\rangle$). We pulse with a ramp time $t_{\text{IL}} = 100$ ns, resulting in a diabatic movement through the charge anticrossing, and through fast charge relaxation we expect to initialize the $|\uparrow, \downarrow\rangle$ and $|\downarrow, \uparrow\rangle$ states randomly with equal probability. This initialization then allows us to efficiently measure both spin relaxation times in a single measurement, since the readout

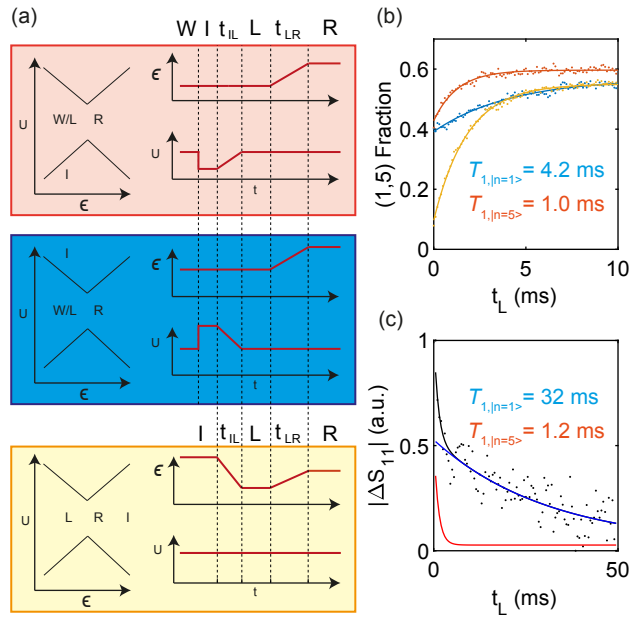


Figure 8.3: (a) Pulse sequences utilized for different loading protocols. Red loads a random spin in P_4 , blue loads a random spin in P_3 , and yellow loads either the $|S_{(1,5)}\rangle$ or a mixture of $|S_{(1,5)}\rangle$ and $|T_0\rangle$ depending on the adiabaticity of the IL pulse. (b) Deterministic loading of a single-hole in P_4 and P_3 (red, blue respectively) and mixed state loading (yellow). We extract spin relaxation times of $T_{1,|n=5\rangle} = 1.0$ ms and $T_{1,|n=1\rangle} = 4.23$ ms for each deterministically loaded quantum dot, which we fit as a double exponential for the mixed loading case. (c) Longest spin relaxation trace taken after minimizing reservoir-dot tunnel coupling. We extract two spin relaxation times of $T_{1,|n=1\rangle} = 32$ ms and $T_{1,|n=5\rangle} = 1.2$ ms.

signal is a linear combination of both spin relaxation decays, and is useful since it allows for fast measurements even when the quantum dot-reservoir couplings are low. Upon readout, the inherent spin orbit coupling in our system results in an avoided crossing between the $|T_{-}\rangle$ and $|S_{(0,6)}\rangle$ states, potentially limiting our readout fidelity. We therefore minimize the ramp time and operate with $t_{LR} = 100$ ns.

In Fig. 8.3b, we show the spin relaxation times of the quantum dots using the three sequences. We find $T_{1,|n=5}\rangle = 1.0$ ms and $T_{1,|n=1}\rangle = 4.23$ ms by fitting exponential decays to the individual measurements. The measurement corresponding to the sequence with randomly preparing a spin up state in one of the two quantum dots is fitted with a double exponential curve using the time constants of the individual decays, and we have left the amplitudes and asymptotes as free fitting parameters. We find approximately equal amplitudes for each decay, in correspondence with an equal loading of both anti-parallel spin states.

We can further increase the single-hole relaxation time by reducing the quantum dot-reservoir coupling. Using the barrier gate RB_3 , we tune the quantum dot-reservoir coupling of the single-hole quantum dot from 81.43 KHz to 27.45 KHz (see section 8.6.1). We note that these dot-reservoir couplings do not represent the actual tunnelling times at the point of measurement, which are expected to be orders of magnitude longer. The spin relaxation decay shown in Fig. 8.3c has been analysed using the above mentioned double exponential fit and we find an significantly increased single-hole spin relaxation time $T_{1,|n=1}\rangle = 32$ ms. By limiting the dot-reservoir tunnel coupling, we have demonstrated spin relaxation lifetimes significantly longer than results previously reported for planar germanium quantum dots ($T_{1,|n=1}\rangle = 1.2$ ms [28]), hut wires ($T_1 = 90$ μ s [36]), nanowires ($T_1 = 600$ μ s [37]), and even holes in gallium arsenide ($T_1 = 60$ μ s [38]) and silicon ($T_1 = 8.3$ μ s [39]) at similar magnetic fields. We expect that the main cause for the observation of longer spin relaxation times for single-hole spins compared to many hole spins originates from the tighter confinement of the quantum dot under P_3 . This leads to larger energy splittings to the excited states, a smaller degree of capacitive coupling to electrical fluctuations, and a smaller dot-reservoir coupling. Additionally, further reduction of the dot-reservoir tunnel coupling would likely improve the multi-hole spin relaxation time. Further investigation into the magnetic field dependence of T_1 could produce information about the spin relaxation mechanisms present and yield insights into means of further optimizing T_1 . However, our demonstration of T_1 up to 32 ms, shows encouraging spin relaxation times for quantum information processing, and that spin states in planar germanium define the benchmark for spin relaxation in hole based quantum dots.

8.4. QUBIT ADDRESSABILITY

The presence of spin-orbit coupling allows for electrical and coherent control of the spin states without the need for additional structures such as striplines or micromagnets [21, 22, 24, 25]. We investigate the individual tunability and addressability of the single- and multi-hole qubits. In Fig. 8.4a, we show results where we have applied a microwave tone of length $t_{mw} = 400$ ns to the gate P_4 . We observe two resonance frequencies at 3.33 GHz and 3.53 GHz in Fig. 8.4a, corresponding to an in-plane Zeeman energy difference $\Delta E_Z = 200$ MHz, as a result of the spin-orbit induced g-factor difference between each qubit. The difference in peak width is due to the delivery of microwave power via plunger gate P_4 , resulting in a power broadened resonance linewidth with respect to that of the spin under P_3 . Figures 8.4b,c show the dependence of each resonance frequency on the electrostatic gate voltages on the two relevant plunger gates P_3 and P_4 . We initialize in the $|S_{(0,6)}\rangle$ singlet state, then load in different points in the (1,5) charge state by changing the potentials applied to P_3 and P_4 . We then manipulate the spins by applying a microwave tone to

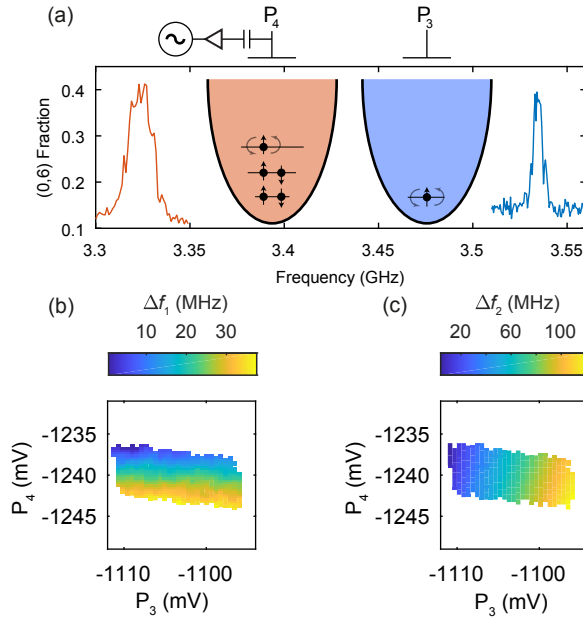


Figure 8.4: (a) Qubit resonance frequency of the five-hole (3.33GHz) and single-hole qubit (3.53 GHz). The magnetic field is set to $B = 667$ mT. A microwave tone is applied to the gate P_4 , which drives both hole spins, as indicated by the cartoon inset. We extract in-plane g -factors of $g_{|n=1\rangle} = 0.362$ and $g_{|n=5\rangle} = 0.383$ for plunger gate values $P_3 = 1098$ mV, $P_4 = 1236$ mV. (b) Five-hole (f_1) and (c) single-hole (f_2) resonance frequency dependence on gate voltage. We find a strong dependence of the resonance frequency on the respective plunger gate, but a significantly reduced dependence on the neighbouring plunger gate voltage.

P_4 and read out in the PSB window. The mechanism by which our resonance frequency changes is due to the modulation of the spin-orbit interaction via change in local electric fields, leading to a modulation of the g -factor of each qubit. The resonance frequency dependence on gate voltage is approximately linear. For the five-hole qubit we find a dependence on its plunger gate voltage $df_1/dP_4 = -4.78$ MHz/mV and we find $df_1/dP_3 = -0.155$ MHz/mV. For the single-hole qubit we find a slightly stronger dependence on its plunger gate voltage $df_2/dP_3 = 6.78$ MHz/mV and we find a cross talk, $df_2/dP_4 = -1.79$ MHz/mV. These values are comparable to those measured in a previous work on the same device under different electrostatic tuning parameters, and therefore we expect the coherence times of each qubit to be on the order of 300 ns as measured earlier [28]. This corresponds to a cross talk ratio of about 1/30 for the five-hole qubit and about 1/4 for the single-hole qubit. The cross talk for the single-hole qubit is comparable to the lever arm ratio (see section 8.6.2) $\alpha_{P_3/P_4}(f_2) = 0.11$. Remarkably, the five-hole qubit has a lever arm ratio $\alpha_{P_4/P_3}(f_1) = 0.07$, significantly larger than the resonance frequency cross talk ratio.

8.5. CONCLUSION

In summary, we have demonstrated benchmarks for spin relaxation in hole quantum dots and found $T_{1,|n=1\rangle} = 32$ ms for a single-hole qubit and $T_{1,|n=5\rangle} = 1.2$ ms for a five-hole qubit and con-

clude that spin relaxation is not a bottleneck for quantum computation with holes. We have shown the presence of Pauli-spin blockade at different hole fillings and found it to be consistent with a Fock-Darwin spectrum that only involves spin degeneracy. We find that both the single-hole and multi-hole qubit resonance frequency can be tuned over a large range. We find that the resonance frequencies are only weakly dependent on neighbouring gates, which results in good local addressability. The observation of the sign difference in the resonance frequency dependence on gate voltage and the strength of the cross talk ratio of the resonance frequencies may provide insights in the nature of the driving mechanism of holes in planar germanium. This is relevant for future work and a possible scenario is that the reduced cross talk of the five-hole qubit originates from an increased heavy-hole light-hole mixing. Such a change may affect the qubit resonance frequency dependence on the amplitude and orientation of the electric field, but further research is needed to investigate this. The long spin lifetimes and excellent individual qubit addressability are encouraging for the operation of hole qubits positioned in large two-dimensional arrays.

8.6. METHODS

8.6.1. TUNNEL RATE ANALYSIS

We measure the dot-reservoir tunnel coupling of the quantum dot under plunger gate P_3 . Before each measurement of spin relaxation in Figure 8.3, we pulse from the (0,5) charge state to the measurement point (1,5) charge state, and measure the sensor response. We observe an exponential decay, the time constant of which determines our dot reservoir tunnel coupling. We pulse the virtual energy gate U from the (0,5) to the (1,5) charge state. Figures 8.5a-b show the resulting sensor response as a function of time in the (1,5) charge state for the spin relaxation measured in figures 8.3b and 8.3c respectively. Due to the imperfect charge sensor compensation, we observe a short initial transient in the first few microseconds, followed by the actual charge state transient to which we fit an exponential decay, shown in the inset. We extract dot-reservoir load rates of 81.43 kHz to 27.45 kHz for the spin relaxation times measured in figures 8.3b and 8.3c respectively.

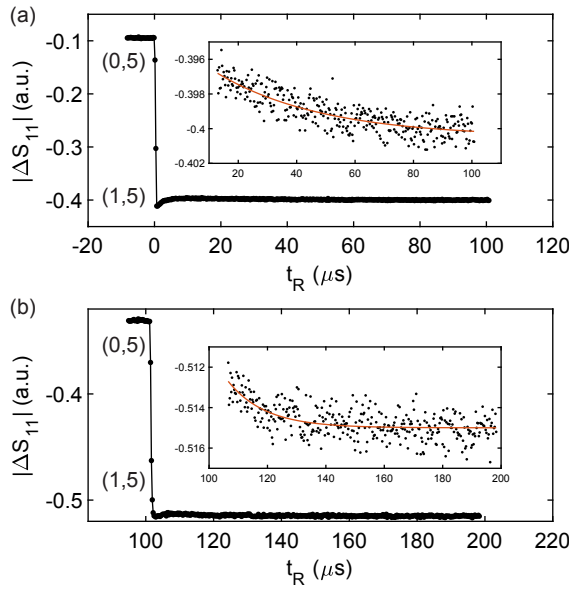


Figure 8.5: Dot-Reservoir coupling between the singly occupied quantum dot defined under the plunger gate P_3 . (a) A dot-reservoir coupling of 81.43 kHz is extracted from the dot loading transient for the spin relaxation measurement in figure 8.3b, and (b) 27.45 kHz for figure 8.33c.

8.6.2. RELATIVE LEVER ARM

We extract the relative lever arms of the plunger gates P_3 and P_4 to the quantum dot potentials underneath them. We take these values from the charge addition line slopes in the stability diagram in figure 8.2g. Here, the figure is taken using a virtual gate matrix space of detuning and energy (ϵ, U) which are defined as a linear combination of the voltages on gates P_3 and P_4 (V_{P3}, V_{P4}):

$$\begin{pmatrix} \epsilon \\ U \end{pmatrix} = \begin{pmatrix} 1 & -1.05 \\ 1.05 & 1 \end{pmatrix} * \begin{pmatrix} V_{P3} \\ V_{P4} \end{pmatrix}$$

By calculating the gradient of the single and multi hole qubit charge addition lines in figure 8.2g, we can solve for the changes in the plunger gate voltage space, and calculate the ratios for each quantum dot, giving $\alpha_{P_3/P_4} = 0.11$ and $\alpha_{P_4/P_3} = 0.07$.

REFERENCES

- [1] Lawrie, W. I. L. *et al.* Spin Relaxation Benchmarks and Individual Qubit Addressability for Holes in Quantum Dots. *Nano Lett.* **20**, 7237–7242 (2020).
- [2] Loss, D. & DiVincenzo, D. P. Quantum computation with quantum dots. *Physical Review A - Atomic, Molecular, and Optical Physics* **57**, 120–126 (1998).
- [3] Petta, J. R. *et al.* Coherent Manipulation of Electron Spins in Semiconductor Quantum Dots. *Science* **309**, 2180–2184 (2005).
- [4] Koppens, F. H. *et al.* Driven coherent oscillations of a single electron spin in a quantum dot. *Nature* **442**, 766–771 (2006).
- [5] Itoh, K. M. & Watanabe, H. Isotope engineering of silicon and diamond for quantum computing and sensing applications (2014).
- [6] Veldhorst, M. *et al.* An addressable quantum dot qubit with fault-tolerant control-fidelity. *Nature Nanotechnology* **9**, 981–985 (2014).
- [7] Yang, C. H. *et al.* Spin-valley lifetimes in a silicon quantum dot with tunable valley splitting. *Nature Communications* **4**, 1–8 (2013).
- [8] Yang, C. H. *et al.* Silicon qubit fidelities approaching incoherent noise limits via pulse engineering. *Nature Electronics* **2**, 151–158 (2019).
- [9] Yoneda, J. *et al.* A quantum-dot spin qubit with coherence limited by charge noise and fidelity higher than 99.9%. *Nature Nanotechnology* **13**, 102–106 (2018).
- [10] Veldhorst, M. *et al.* A two-qubit logic gate in silicon. *Nature* **526**, 410–414 (2015).
- [11] Zajac, D. M. *et al.* Resonantly driven CNOT gate for electron spins. *Science* **359**, 439–442 (2018).
- [12] Watson, T. F. *et al.* A programmable two-qubit quantum processor in silicon. *Nature* **555**, 633–637 (2018).
- [13] Yang, C. H. *et al.* Silicon quantum processor unit cell operation above one Kelvin. *arXiv 1902.09126* (2019).
- [14] Petit, L. *et al.* Universal quantum logic in hot silicon qubits. *Nature* **580**, 355–359 (2019).
- [15] Vandersypen, L. M. K. *et al.* Interfacing spin qubits in quantum dots and donors - hot, dense and coherent. *npj Quantum Information* **3**, 34 (2016).
- [16] Veldhorst, M., Eenink, H. G., Yang, C. H. & Dzurak, A. S. Silicon CMOS architecture for a spin-based quantum computer. *Nature Communications* **8** (2017).
- [17] Li, R. *et al.* A crossbar network for silicon quantum dot qubits. *Science Advances* **4**, eaar3960 (2018).
- [18] Itoh, K. *et al.* High purity isotopically enriched ⁷⁰Ge and ⁷⁴Ge single crystals: Isotope separation, growth, and properties. *Journal of Materials Research* **8**, 1341–1347 (1993).
- [19] Sammak, A. *et al.* Shallow and Undoped Germanium Quantum Wells: A Playground for Spin and Hybrid Quantum Technology. *Advanced Functional Materials* **29**, 1807613 (2019).

- [20] Hendrickx, N. W. *et al.* Gate-controlled quantum dots and superconductivity in planar germanium. *Nature Communications* **9**, 2835 (2018).
- [21] Bulaev, D. V. & Loss, D. Spin relaxation and decoherence of holes in quantum dots. *Physical Review Letters* **95**, 076805 (2005).
- [22] Bulaev, D. V. & Loss, D. Electric dipole spin resonance for heavy holes in quantum dots. *Physical Review Letters* **98**, 097202 (2007).
- [23] Maurand, R. *et al.* A CMOS silicon spin qubit. *Nature Communications* **7**, 13575 (2016).
- [24] Watzinger, H. *et al.* A germanium hole spin qubit. *Nature Communications* **9**, 3902 (2018).
- [25] Hendrickx, N. W., Franke, D. P., Sammak, A., Scappucci, G. & Veldhorst, M. Fast two-qubit logic with holes in germanium. *Nature* **577**, 487–491 (2020).
- [26] Lodari, M. *et al.* Light effective hole mass in undoped Ge/SiGe quantum wells. *Physical Review B* **100**, 041304 (2019).
- [27] Scappucci, G. *et al.* The germanium quantum information route. *arXiv 2004.08133* (2020).
- [28] Hendrickx, N. W. *et al.* A single-hole spin qubit. *arXiv 1912.10426* (2019).
- [29] Leon, R. C. *et al.* Coherent spin control of s-, p-, d- and f-electrons in a silicon quantum dot. *Nature Communications* **11**, 1–7 (2020).
- [30] Lawrie, W. I. L. *et al.* Quantum Dot Arrays in Silicon and Germanium. *Applied Physics Letters* **116**, 080501 (2020).
- [31] Schoelkopf, R. J., Wahlgren, P., Kozhevnikov, A. A., Delsing, P. & Prober, D. E. The radio-frequency single-electron transistor (RF-SET): A fast and ultrasensitive electrometer. *Science* **280**, 1238–1242 (1998).
- [32] Vukušić, L., Kukučka, J., Watzinger, H. & Katsaros, G. Fast Hole Tunneling Times in Germanium Hut Wires Probed by Single-Shot Reflectometry. *Nano Letters* **17**, 5706–5710 (2017).
- [33] Tarucha, S., Austing, D. G., Honda, T., van der Hage, R. J. & Kouwenhoven, L. P. Shell filling and spin effects in a few electron quantum dot. *Physical Review Letters* **77**, 3613–3616 (1996).
- [34] Liles, S. D. *et al.* Spin and orbital structure of the first six holes in a silicon metal-oxide-semiconductor quantum dot. *Nature Communications* **9**, 1–7 (2018).
- [35] DiCarlo, L. *et al.* Differential charge sensing and charge delocalization in a tunable double quantum dot. *Physical Review Letters* **92**, 226801 (2004).
- [36] Vukušić, L. *et al.* Single-Shot Readout of Hole Spins in Ge. *Nano Letters* **18**, 7141–7145 (2018).
- [37] Hu, Y., Kuemmeth, F., Lieber, C. M. & Marcus, C. M. Hole spin relaxation in Ge-Si core-shell nanowire qubits. *Nature Nanotechnology* **7**, 47–50 (2012).
- [38] Bogan, A. *et al.* Single hole spin relaxation probed by fast single-shot latched charge sensing. *Communications Physics* **2**, 1–8 (2019).
- [39] Bohuslavskiy, H. *et al.* Pauli blockade in a few-hole PMOS double quantum dot limited by spin-orbit interaction. *Applied Physics Letters* **109**, 193101 (2016).



9

A FOUR-QUBIT GERMANIUM QUANTUM PROCESSOR

The prospect of building quantum circuits [1, 2] using advanced semiconductor manufacturing positions quantum dots as an attractive platform for quantum information processing [3, 4]. Extensive studies on various materials have led to demonstrations of two-qubit logic in gallium arsenide [5], silicon [6–12], and germanium [13]. However, interconnecting larger numbers of qubits in semiconductor devices has remained an outstanding challenge. Here, we demonstrate a four-qubit quantum processor based on hole spins in germanium quantum dots. Furthermore, we define the quantum dots in a two-by-two array and obtain controllable coupling along both directions. Qubit logic is implemented all-electrically and the exchange interaction can be pulsed to freely program one-qubit, two-qubit, three-qubit, and four-qubit operations, resulting in a compact and high-connectivity circuit. We execute a quantum logic circuit that generates a four-qubit Greenberger-Horne-Zeilinger state and we obtain coherent evolution by incorporating dynamical decoupling. These results are an important step towards quantum error correction and quantum simulation with quantum dots

9.1. INTRODUCTION

Fault-tolerant quantum computers utilizing quantum error correction [1] to solve relevant problems [2] will rely on the integration of millions of qubits. Solid-state implementations of physical qubits have intrinsic advantages to accomplish this formidable challenge and remarkable progress has been made using qubits based on superconducting circuits [14]. While the development of quantum dot qubits has been at a more fundamental stage, their resemblance to the transistors that constitute the building block of virtually all our electronic hardware promises excellent scalability to realize large-scale quantum circuits [3, 4]. Fundamental concepts for quantum information, such as the coherent rotation of individual spins [15] and the coherent coupling of spins residing in neighbouring quantum dots [16], were first implemented in gallium arsenide heterostructures. The low disorder in the quantum well allowed the construction of larger arrays of quantum dots and to realize two-qubit logic using two singlet-triplet qubits [5]. However, spin qubits in group III-V semiconductors suffer from hyperfine interactions with nuclear spins that severely limit their quantum coherence. Group IV materials naturally contain higher concentrations of isotopes with a net-zero nuclear spin and can furthermore be isotopically enriched [17] to contain only these isotopes. In silicon electron spin qubits, quantum coherence can therefore be sustained for a long time [18, 19] and single qubit logic can be implemented with fidelities exceeding 99.9 % [20, 21]. By exploiting the exchange interaction between two spin qubits in adjoining quantum dots or closely separated donor spins, two-qubit logic could be demonstrated [6–12]. Silicon, however, suffers from a large effective mass and valley degeneracy [22], which has hampered progress beyond two-qubit demonstrations.

Holes in germanium are emerging as a promising alternative [23] that combine favourable properties such as a host material with a natural abundance of zero nuclear spin isotopes that can furthermore be enriched for long quantum coherence [24, 25], low effective mass and the absence of low-energy valley states [26] for relaxed requirements on device design, low charge noise for a quiet qubit environment [27], and low disorder for reproducible and well controlled quantum dots [28, 29]. In addition, strained germanium quantum wells defined on silicon substrates are compatible with semiconductor manufacturing [30]. Furthermore, hole states in general can exhibit strong spin-orbit coupling that allows for all-electric operation [13, 31–33] and that removes the need for microscopic components such as microwave striplines [6, 9, 12, 15] or nanomagnets [7, 8, 34, 35], which is particularly beneficial for the fabrication and operation of two-dimensional qubit arrays. The realization of strained germanium quantum wells in undoped heterostructures [36] has led to remarkable progress. In two year's time, germanium has progressed from the formation of stable quantum dots and quantum dot arrays [28, 29, 37], to demonstrations of single qubit logic [38], long spin lifetimes [39], and the realization of fast two-qubit logic in germanium double quantum dots [13].

9.2. A TWO-BY-TWO QUBIT QUANTUM DOT ARRAY

Here, we advance semiconductor quantum dots beyond two-qubit logic and execute a four-qubit quantum circuit using a two-dimensional array of quantum dots. We achieve this by defining the four-qubit system on the spin states of holes in gate-defined germanium quantum dots. Fig. 9.1a shows a scanning-electron-microscopy (SEM) image of the germanium quantum processor. The quantum dots are defined in a strained germanium quantum well on a silicon substrate [27] (Fig. 9.1b) using a double layer of electrostatic gates and contacted by aluminium ohmic contacts. A negative potential on plunger gates P1-P4 accumulates a hole quantum dot underneath that hosts qubits Q1-Q4, which can be coupled to neighbouring quantum dots through dedicated barrier gates. In addition, two quantum dots are placed to the side of the two-by-two array, and the total system comprises six quantum dots. Via an external tank circuit, we configure these additional

two quantum dots as radio frequency (rf) charge sensors for rapid charge detection. Using the combined signal of both charge sensors [37], we measure the four quantum dot stability diagram as shown in Fig. 9.1c. Making use of two virtual gate axes, we arrange the reservoir addition lines of the four quantum dots to have different relative slopes of approximately -1 , $+1$, -0.75 , 0.75 mV/mV for Q1, Q2, Q3, and Q4 respectively. Well defined charge regions (indicated as (Q1,Q2,Q3,Q4) in the white boxes) are observed, with vertical anticrossings marking the different interdot transitions.

For the qubit readout we make use of Pauli-spin blockade to convert the spin states into a charge signal that can be detected by the sensors. In germanium, however, the spin-orbit coupling can significantly lower the spin lifetime during the readout process, in particular when the spin-orbit field is perpendicular to the external magnetic field, reducing the readout fidelity [38, 40]. Here, we overcome this effect by making use of a latched readout process [41, 42]. During the readout process, shown in Fig. 9.1d and e, a hole can tunnel spin-selectively to the reservoir as a result of different tunnel rates of both quantum dots to the reservoir. After this process, the system is locked in this charge state for the (long) reservoir tunnel time T_{in} (details in Methods section). The high level of control in germanium allows tuning T_{in} to arbitrarily long time scales by changing the potential applied to the corresponding reservoir barrier gate. We set $T_{\text{in}, Q2} = 200 \mu\text{s}$ and $T_{\text{in}, Q4} = 2.4 \text{ ms}$ (Fig. 9.8), both significantly longer than the signal integration time $T_{\text{int}} = 10 \mu\text{s}$. Furthermore, we project all qubit measurements on the Q1Q2 and Q3Q4 readout pairs, such that the spin-orbit field is oriented along the direction of the external magnetic field $B_0 = 1.05 \text{ T}$ to minimize spin relaxation.

9.3. SINGLE QUBIT CONTROL

Coherent rotations can be implemented by applying electric microwave signals to the plunger gates that define the qubits, exploiting the spin-orbit coupling for fast driving [31, 33]. We initialize the system in the $|\downarrow\downarrow\downarrow\downarrow\rangle$ state by sequentially pulsing both the Q1Q2 and Q3Q4 double quantum dot systems from their respective $(0,2)_S$ states adiabatically into their $(1,1)_{T-}$ states. We then perform the qubit manipulations, after which we perform the spin readout as described above. We observe qubit resonances at $f_{Q1} = 2.304 \text{ GHz}$, $f_{Q2} = 3.529 \text{ GHz}$, $f_{Q3} = 3.520 \text{ GHz}$, and $f_{Q4} = 3.882 \text{ GHz}$, corresponding to effective g -factors of $g_{Q1} = 0.16$, $g_{Q2} = 0.24$, $g_{Q3} = 0.24$, and $g_{Q4} = 0.26$. We note that these g -factors can be electrically modulated using nearby gates as a means to ensure individual qubit addressability [39], as can also be observed in Fig. 9.3. Fig. 9.1f shows the single-shot spin-up probability P_{\uparrow} for each of the four qubits after applying an on-resonant microwave burst with increasing time duration t_p , resulting in coherent Rabi oscillations.

To quantify the quality of the single qubit gates, we perform benchmarking of the Clifford group [43] (Fig. 9.9a) and find single qubit gate fidelities exceeding 99 % for all qubits. The fidelity of Q3 reaches to 99.9 %, thereby comparing to benchmarks for quantum dot qubits in isotopically purified silicon [20, 21]. We find spin lifetimes between $T_1 = 1 - 16 \text{ ms}$ (Fig. 9.9b), comparable to values reported before for holes in planar germanium [39]. Furthermore, we observe T_2^* to be between 150-400 ns for the different qubits (Fig. 9.10a), but are able to extend phase coherence up to $T_2^{\text{CPMG}} = 100 \mu\text{s}$ by performing Carr-Purcell-Meiboom-Gill (CPMG) refocusing pulses (Fig. 9.10c), more than two orders of magnitude larger than previously reported for hole quantum dot qubits [13, 32, 33]. This indicates the qubit phase coherence is mostly limited by low-frequency noise, which is confirmed by the predominantly $1/f^\alpha$ noise spectrum we observe by Ramsey and dynamical decoupling noise spectroscopy (Fig. 9.11).

9.4. ONE, TWO AND THREEFOLD CONDITIONAL ROTATIONS

Universal quantum logic can be accomplished by combining the single qubit rotations with a two-qubit entangling gate. We implement a conditional rotation (CROT) gate [7–9, 12], where the

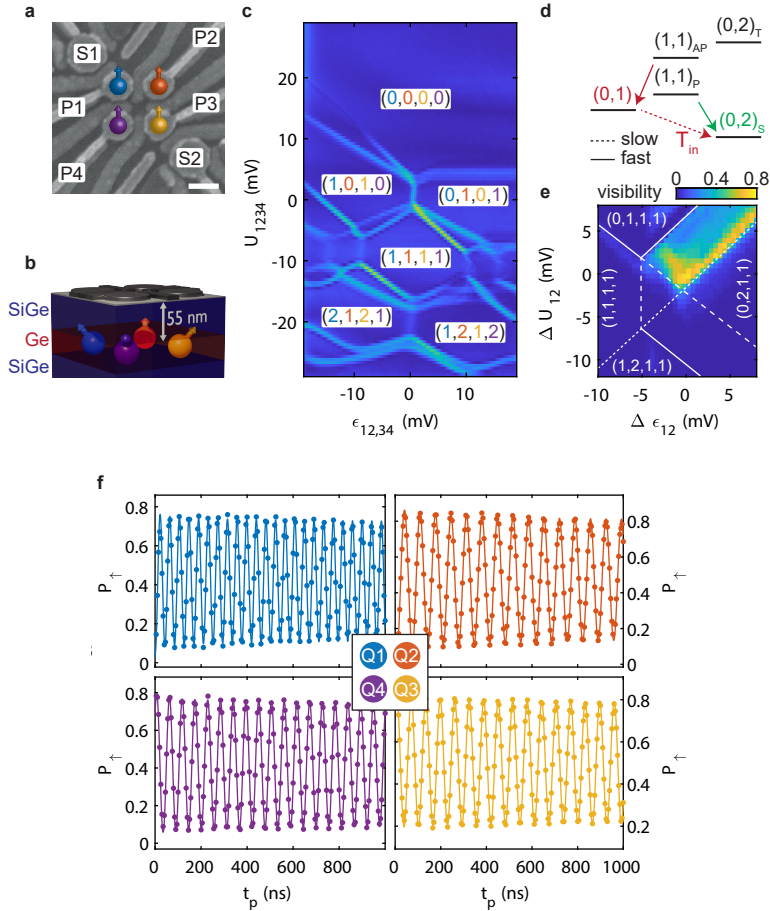


Figure 9.1: **Four germanium hole spin qubits.** **a**, Scanning electron microscope image of the four quantum dot device. We define qubits underneath the four plunger gates indicated by P1-P4. The qubits can be measured using the two charge sensors S1 and S2. The scale bar corresponds to 100 nm. **b**, Schematic drawing of the Ge/SiGe heterostructure. Starting from a silicon wafer, a germanium quantum well is grown in between two $\text{Si}_{0.2}\text{Ge}_{0.8}$ layers at a depth of 55 nm from the semiconductor/dielectric interface. **c**, Four quantum dot charge stability diagram as a function of two virtual gates. At the vertical and diagonal bright lines a hole can tunnel between two quantum dots or a quantum dot and its reservoir respectively. As a result of the virtual axes $\epsilon_{12,34}$ and U_{1234} , the addition lines of the different quantum dots have different slopes, allowing for an easy distinction of the different charge occupations indicated in the white boxes as (Q1, Q2, Q3, Q4). **d**, Energy diagram illustrating the latched Pauli spin blockade readout. When pulsing from the (1,1) charge state to the (0,2) charge state, only the polarized triplet states allow the holes to move into the same quantum dot, leaving an (0,2) charge state (green). Interdot tunnelling is blocked for the two antiparallel spin states and as a result the hole on the first quantum dot will subsequently tunnel to the reservoir leaving an (0,1) charge state (red), locking the different spin states into different charge states. **e**, Readout visibility as defined by the difference in readout between either applying no rotation and a π -rotation to Q2. The readout point is moved around the (1,1)-(0,2) anticrossing of the Q1Q2 system and a clear readout window can be observed bounded by the different (extended) reservoir transition lines indicated by the dotted lines. **f**, The qubits can be rotated by applying a microwave tone resonant with the Zeeman splitting of the qubit. Coherent Rabi rotations can be observed as a function of the microwave pulse length t_p for all qubits Q1-Q4.

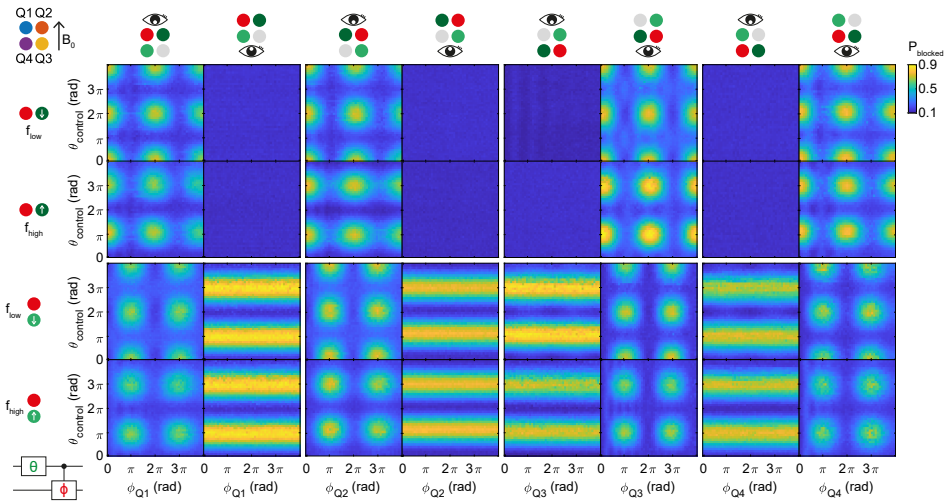


Figure 9.2: **Controlled rotations between all nearest-neighbour qubit pairs.** By selectively enabling the exchange interaction between each pair of qubits, we can implement two-qubit controlled rotations (CROT). The pulse sequence consists of a single preparation gate with length θ on the control qubit (labelled green), followed by a controlled rotation on one of the resonance lines of the target qubit (labelled in red). Both qubit pairs Q1Q2 and Q3Q4 are read out in single-shot mode and the position of the eye on top of each column indicates the respective readout pair. Each of the four main columns corresponds to conditional rotations on a different qubit as indicated by the red dot. Rows one and two show the results for the horizontal interaction (dark green), while rows three and four show the two-qubit interaction for the vertical direction (light green) with respect to the external magnetic field, as indicated in the top left. Rows one and three correspond to driving the lower frequency f_{low} conditional resonance line, while rows two and four show driving of the other resonance line f_{high} .

resonance frequency of the target qubit depends on the state of the control qubit, mediated by the exchange interaction J between the two quantum dots. The exchange interaction between the quantum dots is controlled using a virtual barrier gate (details in Methods), coupling the two quantum dots while keeping the detuning and on-site energy of the quantum dots constant and close to the charge-symmetry point. We demonstrate CROT gates between all four pairs of quantum dots in Fig. 9.2, proving that spin qubits can be coupled in two dimensions. Because the target qubit resonance frequency depends on the control qubit state, the conditional rotation is characterized by the fading in and out of the target qubit rotations as a function of the control qubit pulse length. For driving the two separate transitions, the pattern is shifted by a π rotation on the control qubit. When the control qubit is in a different readout pair as the target qubit (rows 3 and 4), we can independently observe the single qubit control, and two-qubit target qubit rotations in the two readout systems. By setting the pulse length equal to $\phi_Q = \pi$, a fast CX gate can be obtained within approximately $t_p = 100$ ns between all of the four qubit pairs.

The low effective mass and high uniformity in the material allow full control over the interdot coupling by dedicated tunnel barrier gates. To demonstrate this, we measure the qubit resonance frequency as a function of the eight possible permutations of the different basis states of the other three qubits, as illustrated in Fig. 9.3a,b. Without any exchange present, the resonance frequency of the target qubit should be independent on the preparation of the other three qubits, as schematically depicted in Fig. 9.3c. When the exchange interaction with one of the neighbouring quantum dots is enabled, the resonance line splits in two (Fig. 9.3de), allowing for the operation of the CROT gate. When both barriers to the nearest-neighbours are pulsed open at the same time, we observe the expected fourfold splitting of the resonance line (Fig. 9.3f-i). This allows performing a resonant i -Toffoli three-qubit gate (Fig. 9.3k and Fig. 9.12), which has theoretically been proposed as an efficient manner to create the Toffoli, Deutsch, and Fredkin gates [44]. We observe a difference in the efficiency at which the different conditional rotations can be driven, as can also be seen from the width of the resonance peaks in Fig. 9.3f-i. This is expected to happen when the exchange energy is comparable to the difference in Zeeman splitting and is caused by the mixing of the basis states due to the exchange interaction between the holes [45] (details in Methods). Finally, we open three of the four virtual barriers and observe the resonance line splitting in eight, corresponding to all eight permutations of the control-qubit preparation states (Fig. 9.3j). This enables us to execute a resonant four-qubit gate and in Fig. 9.3l we show the coherent operation of a three-fold conditional rotation (see Fig. 9.12 for the coherent operation of the other resonance lines). The good control over the interdot coupling thus enables a demonstration of the localized nature of the exchange interaction [3], coupling the different spins by electric gate pulses.

9

9.5. CONDITIONAL PHASE GATES BETWEEN NEIGHBOURING QUBIT PAIRS

While the demonstration of these conditional rotations can be beneficial for the simulation of larger coupled spin systems, the ability to dynamically control the exchange interaction allows for faster two-qubit operations. We efficiently implement controlled phase (CPHASE) gates [6, 8, 12] between the different qubit pairs by adiabatically pulsing the exchange interaction with the respective virtual barrier gate. We control the length and size of the voltage pulse (Fig. 9.13) to acquire a CZ gate, in which the antiparallel spin states accumulate a phase of exactly $\theta = \pi$ with respect to the parallel spin states. We demonstrate this in Fig. 9.4a,b, where we employ a Ramsey sequence to measure the conditional phase. After the exchange pulse U_{CZ} , we apply a software Z gate to both the target and control qubits to correct the individual single qubit phases. The virtual barrier pulses enable fast CZ gates between all neighbouring qubit pairs, all executed well within 10 ns (details in Table 9.2).

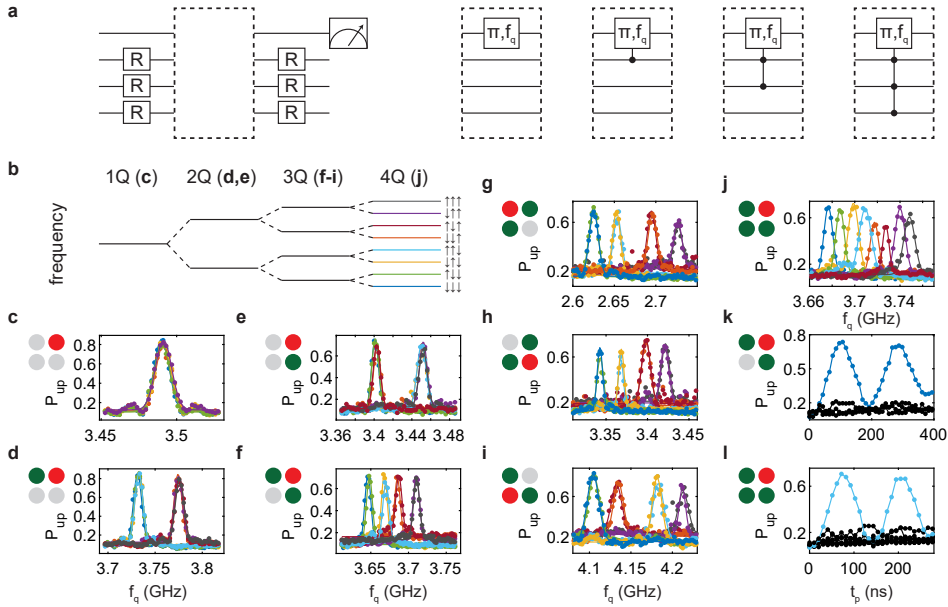


Figure 9.3: **Resonant one, two, three, and four-qubit gates.** **a**, Circuit diagram of the experiment performed in panels **c-l**. All eight permutations of the three control qubit eigenstates are prepared, with R being either no pulse or a π -pulse on the respective qubit. Next, the resonance frequency of the target qubit is probed using a π -rotation with varying frequency f_q . Finally, the prepared qubits are projected back and the target qubit state is measured. By changing the different interdot couplings J , we can switch between resonant single, two, three, and four-qubit gates as indicated in the dashed boxes. **b**, Turning on the exchange interaction between the different qubit pairs splits the resonance frequency in two, four, and eight for 1, 2 and 3 enabled pairs respectively. The colours of the line segments correspond to the colours in panels **c-l**. **c**, By turning all exchange interactions off, the qubit resonance frequency of Q2 is independent of the prepared state of the other three qubits, resulting in an effective single-qubit rotation. **d-e**, By turning on a single exchange interaction J_{12} (**d**) or J_{23} (**e**), the resonance line splits in two. The additional offset of the resonance frequencies is caused by electric modulation of the hole g -factor. **f-i**, Turning on both exchange interactions to the neighbouring quantum dots results in the resonance line splitting in four, for Q2 (**f**), Q1 (**g**), Q3 (**h**), Q4 (**i**) respectively. **j**, Turning on the exchange interactions between three pairs of quantum dots J_{12} , J_{23} , J_{41} splits the resonance line in eight. **k-l**, Resonant driving of the three-qubit gate (**k**) and the four-qubit gate (**l**) with Q2 being the target qubit, shows Rabi driving as a function of pulse length t_p , demonstrating the coherent evolution of the operation.

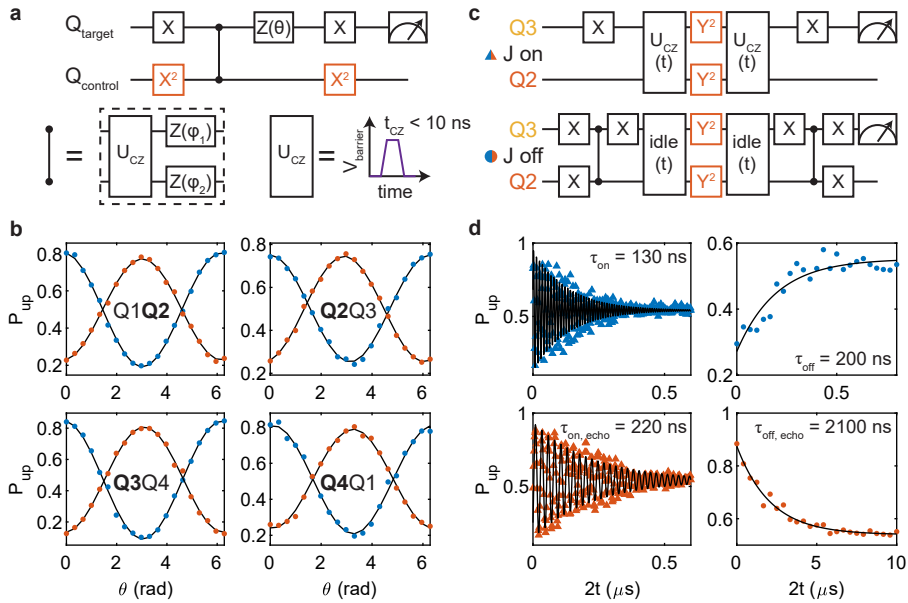


Figure 9.4: Controlled phase gate and dynamical decoupling. **a**, Circuit diagram of the experiment performed in panel **b**. The controlled phase gate is probed by performing a Ramsey sequence on the target qubit for both basis states of the control qubit. The phase of the second $\pi/2$ (X) gate is swept by performing an update of the microwave phase through quadrature modulation. Additionally, a phase update is performed on both the target and control qubit to compensate for any single qubit phases picked up as a result of the gate pulsing to achieve a controlled-Z (CZ) gate. **b**, The spin-up probability of the target qubit (in bold) as a function of the phase θ of the second X gate for the control qubit initialized in the $| \downarrow \rangle$ (blue) and $| \uparrow \rangle$ (red) state. Measurements for the inverted target and control qubits in Fig. 9.13c. By applying an exchange pulse and single qubit phase updates, we achieve a CZ gate at $\theta = 0$ rad. **c**, Circuit diagrams of the experiment performed in panel **d**. The phase coherence throughout the two-qubit experiment is probed using a Ramsey sequence, both for the case with J on (top) and off (bottom) and both with (orange) and without (blue) applying an echo pulse. **d**, Spin-up probability as a function of the experiment length, for the situation with exchange on (left, triangles) and off (right, circles). From the decay data we extract characteristic decay times τ of $\tau_{\text{on}} = 130$ ns, $\tau_{\text{on,echo}} = 220$ ns, $\tau_{\text{off}} = 200$ ns, and $\tau_{\text{off,echo}} = 2100$ ns (details in Methods).

To prepare our system for quantum algorithms, we implement decoupling pulses into the multi-qubit sequences to extend phase coherence [8], as demonstrated in Fig. 9.4c,d. We perform a CPHASE gate of length t between qubits Q2 and Q3 (Fig. 9.4d, left, triangles) and compare the decay of the resulting exchange oscillations for the situations with (orange) and without (blue) a Y^2 echo pulse. We observe an increased decay time of $\tau = 220$ ns for the decoupled CPHASE gate, as compared to $\tau = 130$ ns for a standard CPHASE gate. Next, we entangle Q2 and Q3 by forming the $|\Psi^+\rangle$ Bell state and let the system evolve for time $2t$ (Fig. 9.4d, right, circles). We then disentangle the system and measure the spin-up probability of Q3 as a function of the evolution time. Without the decoupling pulse, we observe a loss of the two-qubit coherence after a characteristic time $\tau = 200$ ns. However, by applying an additional Y^2 pulse to both Q2 and Q3, we can extend this time scale beyond $2 \mu\text{s}$, sufficient to perform a series of single and multi-qubit gates, owing to our short operation times.

9.6. DEMONSTRATION OF A FOUR QUBIT GREENBERGER-HORNE-ZEILINGER STATE

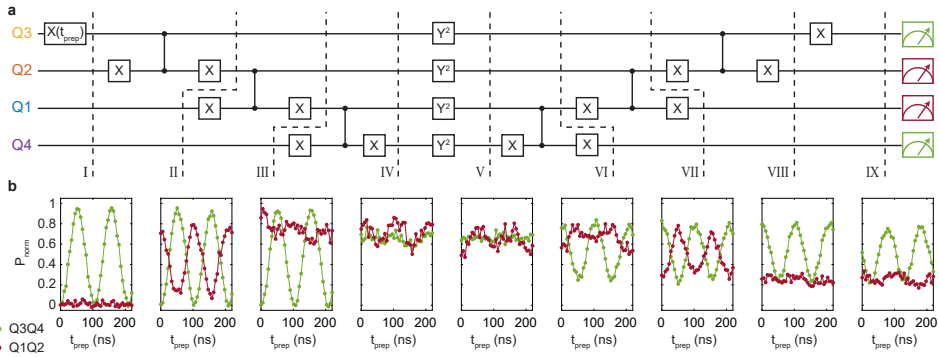


Figure 9.5: **Coherent generation of a four-qubit Greenberger-Horne-Zeilinger (GHZ) state.** **a-b**, A four-qubit GHZ state is created by applying three sequential two-qubit gates, each consisting of an X-CZ-X gate circuit. Next, a Y^2 decoupling pulse is applied, after which we disentangle the GHZ state again (circuit diagram in **a**). Pulses pictured in the same column are applied simultaneously. The initial state of Q3 is varied by applying a preparation rotation of length t . For different stages throughout the algorithm (dashed lines), we measure the non-blocked state probability as a function of t for both the Q1Q2 and Q3Q4 readout system, normalized to their respective readout visibility. At the end of the algorithm the qubit states correspond to the initial single qubit rotation, and the clear oscillations confirm the coherent evolution of the algorithm from isolated qubit states to a four-qubit GHZ state. (**b**).

We show this by coherently generating and disentangling a four-qubit Greenberger-Horne-Zeilinger (GHZ) state (Fig. 9.5). Making use of the fast two-qubit CZ gates, as well as a decoupling pulse on all qubits, we can maintain phase coherence throughout the experiment. We perform parity readout on both the Q1Q2 (red) and Q3Q4 (green) qubit system at different stages of the algorithm (I-IX). Both qubit systems are sequentially readout after each experiment and the observed blocked state fraction is normalized to the readout visibility. We prepare a varying initial state by applying a microwave pulse of length t to Q3, as visible at point I. After applying CZ gates between all four qubits, the system resides in an entangled GHZ type state at point IV/V, for a $\pi/2$ preparation pulse on Q3. The effective spin state oscillates between the antiparallel $|1010\rangle$ and $|0101\rangle$ states as a function of t_{prep} , resulting in a high readout signal for all t . The small oscillation

that can still be observed for the Q1Q2 system, is caused by a small difference in readout visibility for the two distinct antiparallel spin states. Next, we deploy a Y^2 decoupling pulse to echo out all single qubit phase fluctuations during the experiment (Fig. 9.14). After disentangling the system again, we project the Q3 qubit state by applying a final $X(\pi/2)$ gate, and indeed recover the initial Rabi rotation as a demonstration of the coherent evolution of a multi-spin entangled state (see Fig. 9.15).

The demonstration of a two-by-two array of four qubits shows that quantum dot qubits can be coupled in two-dimensions and multi-qubit logic can be executed. The hole states used are subject to strong spin-orbit coupling, enabling all-electrical driving of the spin state, beneficial for scaling up to even larger systems. In future experiments the performance of the qubit gates can be further optimized, by making use of tailored pulses and quantifying their performance using benchmarking sequences. The ability to freely couple one, two, three and four spins using electric gate pulses has great prospects both for performing high-fidelity quantum gates as well as studying exotic spin systems using analog quantum simulations. Furthermore, we envision that the low-disorder in planar germanium and the potential to leverage advanced semiconductor manufacturing will be beneficial for the realization of scalable qubit tiles [46–48] for fault-tolerant quantum processors.

9.7. METHODS

9.7.1. DEVICE FABRICATION

The device was fabricated on a Ge/SiGe heterostructure with a 55-nm-deep buried quantum well, grown in an industrial reactor by reduced vapour deposition, as detailed in [27, 36]. Ge quantum wells are fully compatible with a 300 mm semiconductor foundry line [23, 30]. Starting from a Si wafer, the heterostructure comprises a 1.6 μm relaxed Ge layer; a 1 μm step graded $\text{Si}_{1-x}\text{Ge}_x$ layer with a final Ge composition of $x = 0.8$; a 500 nm relaxed $\text{Si}_{0.2}\text{Ge}_{0.8}$ buffer layer; the 16-nm-thick compressively strained Ge quantum well; a 55 nm $\text{Si}_{0.2}\text{Ge}_{0.8}$ spacer layer and finally a sacrificial Si cap layer (< 2 nm). We define ohmic contacts by electron beam lithography and subsequent etching of the oxidized Si cap layer and deposition of a 30 nm Al contact layer [28]. Electrostatic gates are defined in two layers (20 nm and 40 nm Ti/Pd respectively), separated from both the substrate and each other by 7 nm of ALD-grown Al_2O_3 .

9.7.2. DEVICE SCREENING

After the devices are fabricated they undergo visual inspection as a first screening step. Devices that pass this step are wire bonded onto a printed circuit board (PCB) and cooled down to $T = 4.2$ K in a liquid helium cryostat. Channel turn-on and gate leakage is tested for channels through the north sensor, through the south sensor, and from the north to the south sensor (through the device area). In a fully automated transport measurement, all gates relevant to the respective channel are swept down to $V_{\text{gate}} = -1.5$ V, after which they are swept back up and down to $V_{\text{gate}} = 0$ V. These measurements are checked to confirm if (i) all channels turn on and (ii) all gates modulate the current as expected (exemplary data in Fig. 9.6b). Devices that pass all of these screenings are selected for cool down in a dilution refrigerator (see for device yield and test results Fig. 9.6a).

9.7.3. EXPERIMENTAL SETUP

Measurements are performed in a Bluefors dilution refrigerator with a base temperature of $T_{\text{base}} = 20$ mK. We use battery powered voltage sources to bias the electrostatic gates. Additionally, coaxial lines are connected to all plunger and barrier gates through an on-PCB bias-tee, which can be pulsed using a Keysight M3202A arbitrary waveform generator. Plunger gates P2, P3, and P4 are furthermore connected to a vector source (Rohde&Schwarz SGS100A for P3/P4 and Keysight PSG

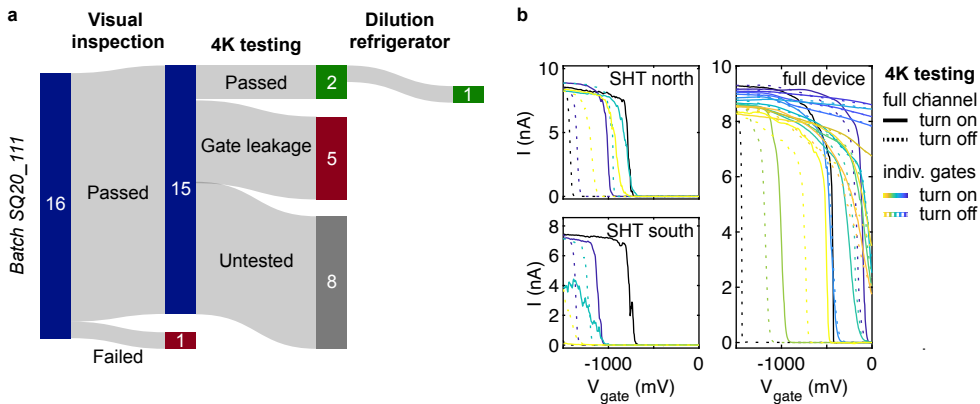


Figure 9.6: **Screening of qubit devices.** **a**, The qubit devices undergo a visual screening as well as a transport screening at a temperature of $T = 4.2$ K. Out of the full batch of 16 nominally identical devices, 15 passed visual inspection. Seven of these devices were tested at $T = 4.2$ K and two devices were found to pass all testing, of which one (the device presented in this work) was mounted in a dilution refrigerator. **b**, 4.2 Kelvin transport data of the device presented in this work. Three different channels are turned on by sweeping all gates down to $V_{\text{gate}} = -1500$ mV (black), thereby accumulating charge in the undoped strained Ge quantum well. Then the effect of the individual gates is tested by sweeping them up and down to $V_{\text{gate}} = 0$ V (coloured lines). All channels turn on and the gates affect the transport current as expected from the device layout.

E8257D for P2) through room-temperature diplexers with a stop band of $f = 400 - 1500$ MHz. We modulate the qubit driving pulses using the quadrature modulation inputs and use multiple vector sources to be able to drive all qubit resonance lines to overcome the limited output bandwidth of 400 MHz of the AWGs. Qubits Q2 and Q4 are driven using the vector source connected to P3, Q1 is driven from gate P4, and Q3 is driven from gate P2.

The charge sensors are connected to a resonant tank circuit consisting of an in-house made niobium-titanium-nitride (NbTiN) kinetic inductor with an expected inductance of $L = 2$ μH . We apply a resonant rf-tone at $f = 147.3$ MHz and $f = 139.9$ MHz for sensor S1 and S2 respectively. The reflected signal is split using a directional coupler mounted to the mK-plate of the fridge and amplified by a cryogenic amplifier at the 4 K stage. Next, the signal is demodulated using an in-house build demodulation setup and measured using a Keysight M3102A digitizer card. This is further detailed in Fig. 9.7 below. Both sensors can differentiate the different charge states in both the Q1Q2 and Q3Q4 qubit system. In this work, we only show the data of the sensor closest to the respective qubit pair.

The data in Fig. 9.5 are normalized with respect to the readout visibility as obtained from a Rabi measurement. We find $P_{\text{Q1Q2, not blocked}} = 0.15$, $P_{\text{Q1Q2, blocked}} = 0.78$, $P_{\text{Q3Q4, not blocked}} = 0.10$, and $P_{\text{Q3Q4, blocked}} = 0.93$.

9.7.4. VIRTUAL GATE MATRICES

In order to map out the transition lines of all four quantum dots in a single measurement, we define the following virtual gates [49] as linear combination of the physical gates $P_1 - P_4$, as well as

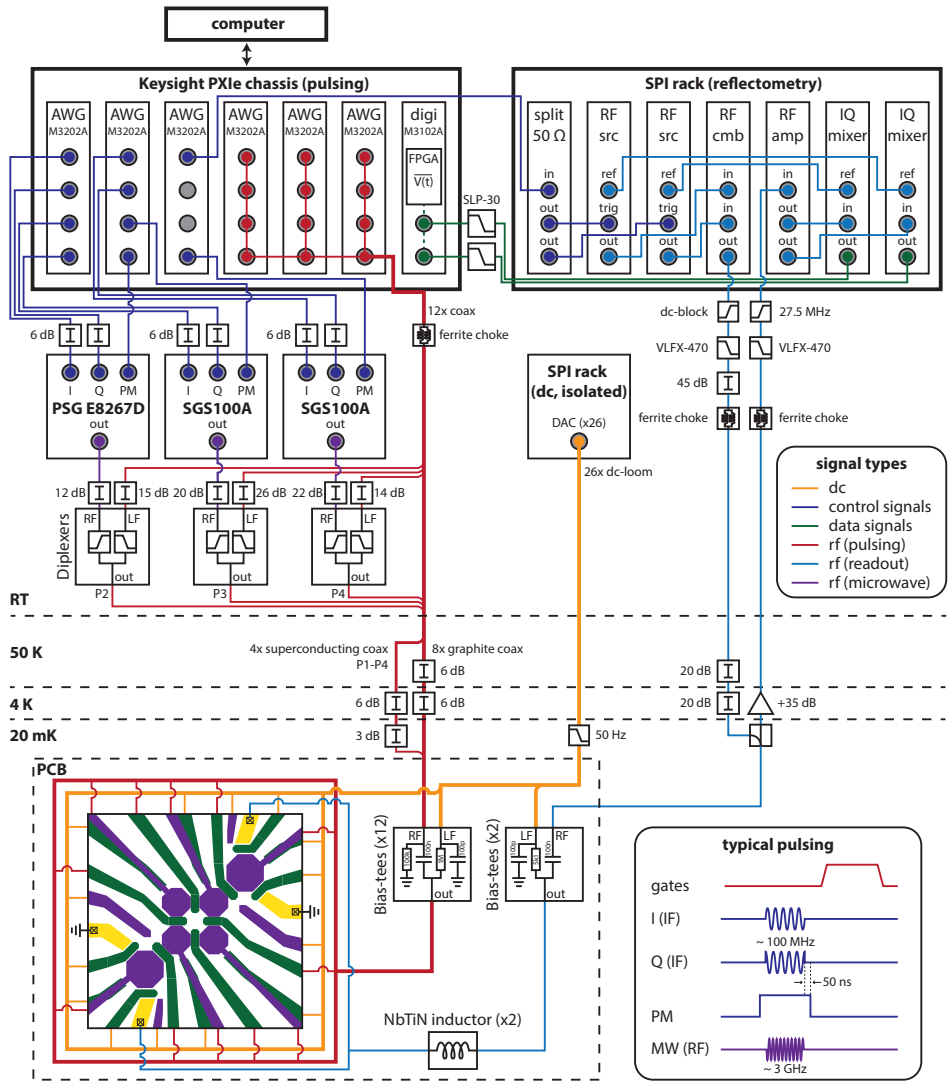


Figure 9.7: **Schematic of the measurement set-up.** Signals to gates are colour coded by signal type. Typical pulse lengths and shapes are shown in the bottom right inset.

the sensor plunger gates P_{S1} and P_{S2} . We write:

$$\begin{pmatrix} P_1 \\ P_2 \\ P_3 \\ P_4 \\ P_{S1} \\ P_{S2} \end{pmatrix} = \begin{pmatrix} 1 & 1 \\ -1 & 1 \\ 0.75 & 1 \\ -0.75 & 1 \\ -0.1 & -0.4 \\ -0.05 & -0.51 \end{pmatrix} \begin{pmatrix} \Delta\epsilon_{12,34} \\ \Delta U_{1234} \end{pmatrix}$$

with $\Delta\epsilon_{12,34}$ and ΔU_{1234} the virtual gates used in Fig. 9.1c.

In addition, we define a virtual gate system to allow independent control of the different inter-dot couplings and quantum dot detuning and on-site energy and write:

$$\begin{pmatrix} P_1 \\ P_2 \\ P_3 \\ P_4 \\ B_{12} \\ B_{34} \\ B_{23} \\ B_{41} \\ P_{S1} \\ P_{S2} \end{pmatrix} = \begin{pmatrix} 1.26 & 0.74 & 0.31 & -0.17 & -0.55 & 0 & 0 & -0.49 \\ -1.39 & 0.61 & -0.36 & -0.36 & -1.03 & 0 & -0.60 & 0 \\ 0.28 & -0.28 & 1.39 & 0.61 & 0 & -0.47 & -0.60 & 0 \\ -0.30 & -0.30 & -1.39 & 0.61 & 0 & -0.91 & 0 & -0.92 \\ 0 & 0 & 0 & 0 & 1.00 & 0 & 0 & 0 \\ 0 & 0 & 0 & 0 & 0 & 1.00 & 0 & 0 \\ 0 & 0 & 0 & 0 & 0 & 0 & 1.00 & 0 \\ 0 & 0 & 0 & 0 & 0 & 0 & 0 & 1.00 \\ -0.09 & -0.15 & 0.01 & -0.03 & 0 & 0 & 0 & 0 \\ 0 & 0 & -0.09 & -0.15 & 0 & 0 & 0 & 0 \end{pmatrix} \begin{pmatrix} \epsilon_{12} \\ U_{12} \\ \epsilon_{34} \\ U_{34} \\ vB_{12} \\ vB_{34} \\ vB_{23} \\ vB_{41} \end{pmatrix}$$

with ϵ_{mn} the detuning voltage and U_{mn} the voltage controlling the on-site energy of quantum dots m and n , vB_{mn} the virtual barrier gate controlling the coupling between quantum dots m and n , and P_n , B_{mn} and P_{S1-2} the various physical gates.

9.7.5. LATCHED READOUT MECHANISM

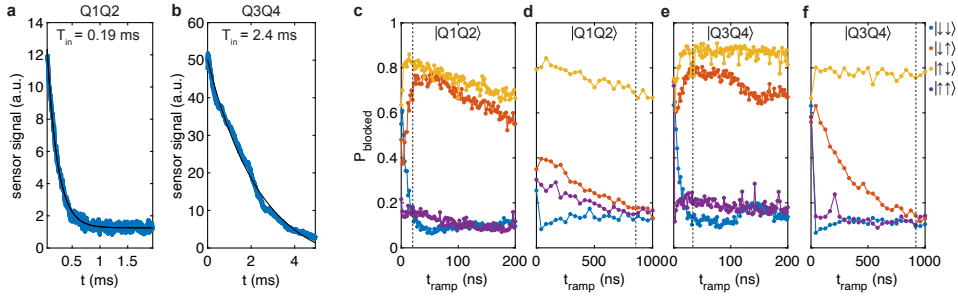


Figure 9.8: **Readout characteristics.** **a,b**, We measure the difference in charge sensor signal between the blocked and non-blocked states as a function of the measurement time at the readout point. An exponential decay can be observed related to the tunnel time T_{in} of Q2 (Q4) to the reservoir for the Q1Q2 (**a**) and Q3Q4 (**b**) readout system respectively. **c-f**, We vary the ramp time between the manipulation phase and the readout phase and measure the blocked state probability of the four different two qubit basis states by applying preparation π pulses to the relevant qubits, both for the Q1Q2 readout system (**a,b**) and the Q3Q4 readout system (**c,d**). By increasing the interdot coupling during the readout and elongating the ramp between the manipulation and readout point, we can switch between a parity readout (**a,c**) and a single state readout (**b,d**). The dashed line corresponds to the optimized readout ramp time used for the measurements in this manuscript.

To reduce readout infidelity as a result of spin relaxation, we make use of charge latching through the reservoir [41, 42]. We achieve this effect by pulsing into the area in the (0,2) charge region bounded by the extended (1,1)-(0,1) (fast) and the extended (1,1)-(1,2) (slow) transitions (dotted lines in Fig. 9.1e). When the interdot tunnelling into the (0,2) charge state is blocked, the hole in the first quantum dot will quickly tunnel into the reservoir. This locks the spin state in the metastable (0,1) charge state, with the decay to the (0,2) ground state governed by the slow tunnel rate T_{in} between the second quantum dot and the reservoir.

We operate in a parity readout mode where we observe both antiparallel spin states to be blocked (Fig. 9.8c,d), opposite to conventional parity Pauli spin blockade readout [50]. This may

be explained by the strong spin-orbit coupling mixing the parallel (1,1) states with the (0,2) state and causing strong relaxation of the upper parallel spin state. We note that both singlet-triplet readout for single state discrimination and parity readout are compatible with the execution of quantum algorithms [50]. However, by both increasing the interdot coupling and elongating the ramp between the manipulation and readout point, we can transition into a state selective readout where only the $|\downarrow\uparrow\rangle$ state results in spin blockade (Fig. 9.8e,f), with a slightly reduced readout visibility. Optimal parity readout is obtained for a ramp time of $t_{\text{ramp}} \approx 20$ ns, while single state readout is optimal at $t_{\text{ramp}} \approx 800$ ns.

Each charge sensor can detect transitions in both qubit pairs, but is most sensitive to their respective nearby quantum dots. We maximize the readout visibility as defined by the difference between the readout of a spin-up and spin-down state by scanning the readout level around the relevant anticrossing. This is illustrated for the Q1Q2 pair in Fig. 9.1e, where a clear readout window with maximum visibility can be observed bounded between the (extended) reservoir transitions of the two quantum dots.

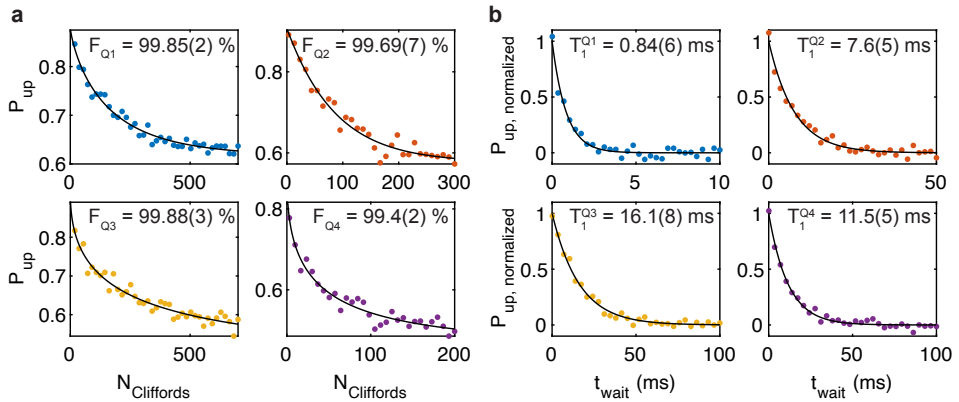


Figure 9.9: **Randomized benchmarking of the Clifford group and spin relaxation times of the different qubits.** **a**, We quantify the quality of the single qubit gates by performing randomized benchmarking of the single-qubit Clifford group [43]. The decay curve of the qubit state is measured as a function of the number of Clifford gates applied. Each data point consists of 1000 single shots for 30 different randomly selected Clifford sequences of length $N_{\text{Cliffords}}$. The decay is fitted to $P_{\text{up}} = a \exp(-N_{\text{Cliffords}}/m) + y_0$, with a the initial spin-up probability, m the decay parameter, and y_0 an offset. $F = 1 - \frac{m}{2 \cdot 1.875}$ is extracted based on the average single qubit gate length of $1/1.875$ Clifford gates. Error margins correspond to 1σ . **b**, The spin relaxation time T_1 is measured at the manipulation point by applying a π_X -pulse separated by a waiting time t_{wait} from the readout phase, as illustrated in the schematic on top. By fitting the normalized spin-up fraction to $P = \exp(-t_{\text{wait}}/T_1)$, we find spin relaxation times of $T_1^{\text{Q1}} = 0.84(6)$ ms, $T_1^{\text{Q2}} = 7.6(5)$ ms, $T_1^{\text{Q3}} = 16.1(8)$ ms, and $T_1^{\text{Q4}} = 11.5(5)$ ms. Error margins correspond to 1σ .

9.7.6. CONDITIONAL ROTATION GATES

We perform a series of qubit pulses, consisting of a single qubit control pulse (green) and a target qubit two-qubit pulse (red), as indicated in the diagram in Fig. 9.2. The length of both the control pulse θ_{control} as well as the target qubit pulse $\phi_{\text{Q1-Q4}}$ are varied, with $t_p(\phi = \pi) = 50 - 110$ ns (details in Table 9.1). The conditional rotations are performed on all four target qubits (four double columns) for both the horizontally interacting qubits (rows 1 and 2), as well as the vertically interacting qubits (rows 3 and 4), by driving the $|\downarrow\downarrow\rangle\text{-}|\uparrow\uparrow\rangle$ transitions with f_{low} (rows 1 and 3), as well as the inverse $|\uparrow\uparrow\rangle\text{-}|\downarrow\downarrow\rangle$ transitions with f_{high} (rows 2 and 4), with $|\text{Q}_{\text{target}}\text{Q}_{\text{control}}\rangle$. We then per-

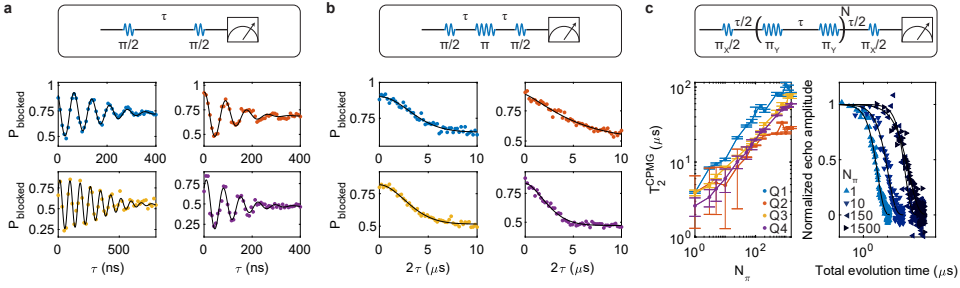


Figure 9.10: Ramsey, Hahn echo and Carr-Purcell-Meiboom-Gill (CPMG) measurements on the different qubits. **a**, The phase coherence time T_2^* is measured using a Ramsey sequence consisting of two $X(\pi/2)$ -pulses separated by a waiting time τ as illustrated in the schematic on top. By fitting the data to $P = \cos(2\pi\Delta f\tau + \phi_0) \exp(-(\tau/T_2^*)^\alpha)$, with Δf the frequency detuning, ϕ_0 a phase offset and α the power of the decay, we find spin dephasing times of $T_{2,Q1}^* = 201$ ns, $T_{2,Q2}^* = 146$ ns, $T_{2,Q3}^* = 445$ ns, and $T_{2,Q4}^* = 150$ ns for Q1-Q4 respectively. **b**, Using an additional $X(\pi)$ -pulse, low-frequency fluctuations of the qubit resonance frequency can be echoed out, allowing to probe the Hahn-echo decay time T_2^{Hahn} . Fitting the data to $P = \exp(-(\tau/T_2^{\text{Hahn}})^\alpha)$, we find Hahn echo times of $T_{2,Q1}^{\text{Hahn}} = 4.3\mu\text{s}$, $T_{2,Q2}^{\text{Hahn}} = 5.5\mu\text{s}$, $T_{2,Q3}^{\text{Hahn}} = 3.8\mu\text{s}$, and $T_{2,Q4}^{\text{Hahn}} = 2.9\mu\text{s}$. **c**, Using a CPMG sequence of repeated $Y(\pi)$ pulses, we can increase the echo bandwidth and extend the phase coherence to over $T_{2,Q1}^{\text{CPMG}} > 100\mu\text{s}$. The phase coherence can be observed to increase with the amount of refocusing pulses (left), with exemplary decay traces for Q1 plotted in the right panel.

form a measurement on both readout pairs by sequentially pulsing the Q1Q2 (left sub-columns), and the Q3Q4 qubit pairs (right sub-columns) to their respective readout points. When driving the $|\downarrow\downarrow\rangle - |\uparrow\uparrow\rangle$ transition of the qubit pairs used for readout (row 1), we apply an additional single-qubit π -pulse to the preparation qubit to preserve symmetry with the other measurements, as the control qubit also serves as the readout ancillary qubit.

9.7.7. SHIFT IN RABI FREQUENCY DUE TO EXCHANGE

When exchange interaction is present in the quantum dot system, the energy levels of the qubit are modified and the qubit basis states hybridize. Conditional driving of the spin states is a direct consequence of the shift of the energy levels, which allows for controlled multi-qubit gates as previously employed to drive two-qubit gates [6–8, 54]. The hybridization of the qubit states on the other hand gives rise to conditional Rabi frequencies that also depend on the strength of the exchange interaction [54]. Furthermore, the exchange interaction can become anisotropic in the presence of spin-orbit coupling [45]. When only considering the exchange interaction between neighbouring quantum dots, a general Hamiltonian can be written for the four quantum dots in the (1,1,1,1) charge regime as:

$$H = \sum_{\langle i,j \rangle} \mathbf{S}_i \cdot \overline{\mathcal{J}}_{ij} \mathbf{S}_j + \sum_{i=1}^4 (\mathcal{B} + \mathcal{B}_{ac} \cos(2\pi f t + \phi)) \cdot \mathbf{S}_i, \quad (9.1)$$

where the first sum runs along every neighbouring quantum dot pair $\langle i, j \rangle$ with the corresponding tensorial exchange interaction $\overline{\mathcal{J}}_{ij}$. We note that the term \mathcal{B} consists of both the Zeeman effect due to the external magnetic field, and the contribution due to the spin-orbit interaction. We also explicitly separate the static Zeeman interaction from the field induced by the electric driving.

We take \mathcal{D} to be the unitary matrix which diagonalizes Hamiltonian (9.1) for $\mathcal{B}_{ac} = 0$, e.g., $\mathcal{D}^\dagger H(\mathcal{B}_{ac} = 0) \mathcal{D} = \mathbf{I}$. Now, the effective Rabi amplitude between the eigenstates of the undriven

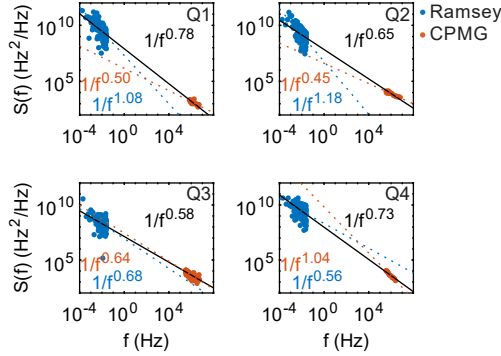


Figure 9.11: **Noise spectroscopy using Ramsey and CPMG measurements.** We measure the effective noise spectrum acting on the qubit, both tracing the resonance frequency using repeated Ramsey measurements [20] (in blue), as well as by using the filter function of a dynamical decoupling measurement [18, 51] (in red). Dashed blue and red lines are fits to the Ramsey and CPMG data respectively. The black line is a fit to the combined data set, where the weight of both sets is normalized for the amount of data points. The effective noise can be observed to increase towards low frequencies, consistent with the upwards trend of T_2^{CPMG} observed in Fig. 9.7c. The effective charge noise measured in this heterostructure is $S_{\text{cn}}(f) = 6 \mu\text{V}/\sqrt{\text{Hz}}$ at 1 Hz [27]. Combining this with a typical resonance frequency slope of $df/dV = 5 \text{ MHz/mV}$ [39], results in an effective resonance frequency noise power of $S(f) = 9 \cdot 10^8 \text{ Hz}^2/\text{Hz}$, comparable to what is observed experimentally, suggesting coherence is limited by charge noise in our system. The effect of charge noise could be mitigated by careful optimization of the electric field environment [52] or moving to a multi-hole charge occupancy, screening the influence of charge impurities [53], potentially enabling even higher fidelity operations. Alternatively, noise could originate in the nuclear spin bath present in natural germanium, which could be overcome by isotopically enriching the material.

Hamiltonian $|\xi\rangle$ and $|\zeta\rangle$ in the adiabatic limit of exchange is given by:

$$\Omega_{|\xi\rangle \rightarrow |\zeta\rangle} = \frac{1}{4} \langle \xi | \mathcal{D}^\dagger \mathcal{B}_{\text{ac}} \mathcal{D} | \zeta \rangle, \quad (9.2)$$

where the prefactor 1/4 is coming from the spin and the rotating wave approximation. Therefore, the Rabi amplitude depends on the exact form of the exchange interaction, as well as which transition is driven.

9

9.7.8. FITTING OF THE TWO-QUBIT DECAY DATA

In order to extract the decay time scale in Fig. 9.4d, we fit the exchange interaction data to the model function $P = A \cos(2\pi(f_0 + t\delta)t + \phi_0) \exp(-t/\tau) + y_0$, with amplitude A , frequency f_0 , phase offset ϕ_0 , and offset y_0 . We note that we allow for a small linear shift of the precession frequency δ , typically of size $\delta = 10 \text{ MHz}/\mu\text{s}$, as a result of pulse imperfections in these relatively large and extended exchange pulses. We observe a small creep towards the final pulse amplitude to be present, most likely caused by the skin effect in the coaxial lines, explaining the small observed frequency shift throughout the experiment. The data for the situation with no exchange present is fitted to the exponential decay $P = \exp(-t/\tau) + y_0$, from which we deduce the decay time scale τ .

9.7.9. SPECIFICATION OF THE CROT AND CZ GATE TIMES

The different two-qubit gate times are listed below both for the CROT (Table 1) as well as the CZ (Table 2) gates.

target	transition	control	$t_{\pi,\text{control}}$ (ns)	$t_{\pi,\text{target}}$ (ns)
1	$ \downarrow\downarrow\rangle- \downarrow\uparrow\rangle$	2	67	85
1	$ \downarrow\uparrow\rangle- \uparrow\uparrow\rangle$	2	67	95
1	$ \downarrow\downarrow\rangle- \downarrow\uparrow\rangle$	4	61	104
1	$ \downarrow\uparrow\rangle- \uparrow\uparrow\rangle$	4	61	108
2	$ \downarrow\downarrow\rangle- \downarrow\uparrow\rangle$	1	45	105
2	$ \downarrow\uparrow\rangle- \uparrow\uparrow\rangle$	1	41	105
2	$ \downarrow\downarrow\rangle- \downarrow\uparrow\rangle$	3	38	113
2	$ \downarrow\uparrow\rangle- \uparrow\uparrow\rangle$	3	38	100
3	$ \downarrow\downarrow\rangle- \downarrow\uparrow\rangle$	2	65	53
3	$ \downarrow\uparrow\rangle- \uparrow\uparrow\rangle$	2	65	83
3	$ \downarrow\downarrow\rangle- \downarrow\uparrow\rangle$	4	49	83
3	$ \downarrow\uparrow\rangle- \uparrow\uparrow\rangle$	4	45	68
4	$ \downarrow\downarrow\rangle- \downarrow\uparrow\rangle$	1	45	105
4	$ \downarrow\uparrow\rangle- \uparrow\uparrow\rangle$	1	45	120
4	$ \downarrow\downarrow\rangle- \downarrow\uparrow\rangle$	2	38	68
4	$ \downarrow\uparrow\rangle- \uparrow\uparrow\rangle$	2	38	74

Table 9.1: CROT driving times used in Fig. 9.2.

two-qubit system	t_{ramp} (ns)	t_{gate} (ns)
Q1Q2	3	6
Q2Q3	10	4
Q3Q4	10	5
Q4Q1	3	6

Table 9.2: CZ gate details.

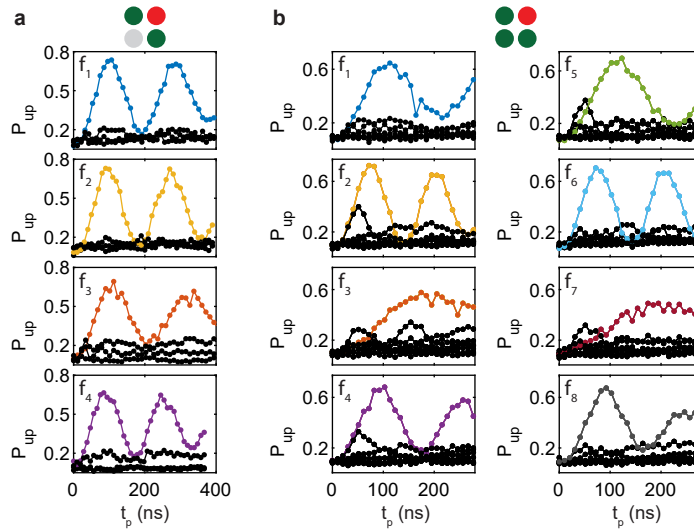


Figure 9.12: **Driving of all resonance lines of the coupled three and four qubit system.** **a**, Both the coupling between Q2 and Q1 as well as Q2 and Q3 are enabled, using the respective virtual barrier gates. This splits the resonance line in four, as shown in Fig. 9.3. Driving each of the separate lines, results in the conditional rotation of Q2 depending on the states of Q1 and Q3. We measure the spin up probability after driving each of the four resonance lines for time t_p , for all four permutations of the Q1 and Q3 basis states as initial state, following the colour scheme of Fig. 9.3. The driving power is adjusted for each of the transitions to synchronize the π -rotation times, with $a_{f_1} = 330$ mV, $a_{f_2} = 500$ mV, $a_{f_3} = 280$ mV, and $a_{f_4} = 400$ mV, for f_{1-4} from low to high. **b**, Similarly, by additionally opening up the coupling between Q3 and Q4 as well, the resonance line splits in four and we can drive all separate lines individually. The eight lines are driven using the same microwave power in this figure and a strong difference in rotation frequencies can be observed for the different transitions f_{1-8} from low to high. This also results in a small off-resonant driving effect for some of the lines.

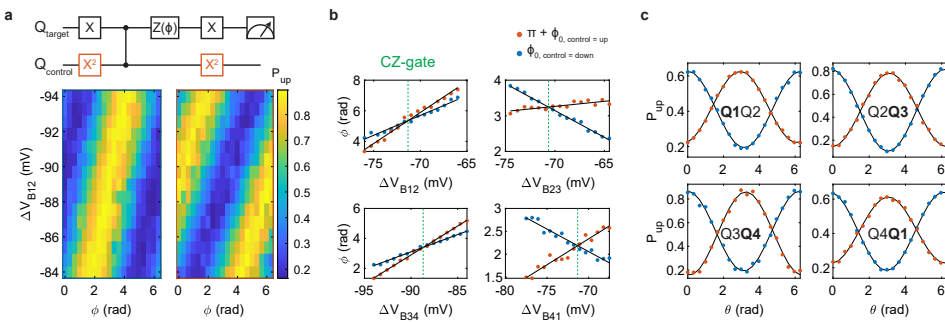


Figure 9.13: **Tuning of the CZ-gates.** **a,b**, The CZ-gates between all four qubit pairs are tuned using a Ramsey sequence (analogous to Fig. 9.4), where the spin-up probability is measured as a function of the phase ϕ of the final $\pi/2$ pulse as well as the depth of the exchange pulse V_{Bmn} , with m and n the relevant qubits (**a**). We choose to tune the height of the voltage pulse rather than its length, due to the limited temporal resolution of the exchange pulses (1 ns). The acquired phase ϕ_0 is obtained by fitting each line to $P = A \cos(\phi + \phi_0) + y_0$, with A the visibility and y_0 an offset. A CZ-gate is achieved when the difference in acquired phase is exactly $\Delta\phi = \pi$, for the situation where the control qubit is $|\downarrow\rangle$ (blue) compared to $|\uparrow\rangle$ (orange). The barrier gate voltage at which this occurs is obtained from the intersection of two locally linear fits to the extracted acquired phase (**b**). **c**, The CZ-gates between all four qubit pairs probed by a Ramsey sequence using the inverse qubits as target and control as compared to the data in Fig. 9.4b. The target qubit is marked in bold.

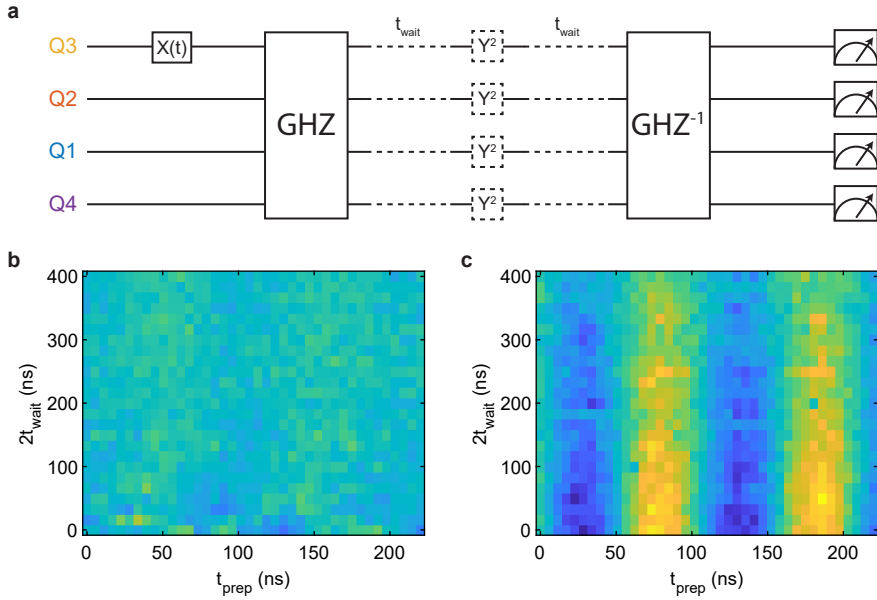


Figure 9.14: **Time evolution of the four-qubit GHZ state.** **a**, Circuit diagram of the experiments performed in panels **b,c**. We first apply a preparation pulse to Q3 and then generate a four qubit GHZ-state analogous to Fig. 9.5. Next we let the entangled system evolve for time t_{wait} , then apply an optional Y^2 decoupling pulse and finally disentangle the GHZ-state again. **b,c**, We vary both the waiting time and preparation time t_{prep} and plot the spin-up fraction of Q3 in the case without (**b**) and with (**c**) decoupling pulse. It can be clearly observed that without the echo pulse, the system has fully decohered at the end of the algorithm. However, by applying the decoupling pulse, the coherence of the entangled system can be maintained for a prolonged time scale, with a characteristic decay time of $\tau = 390$ ns.

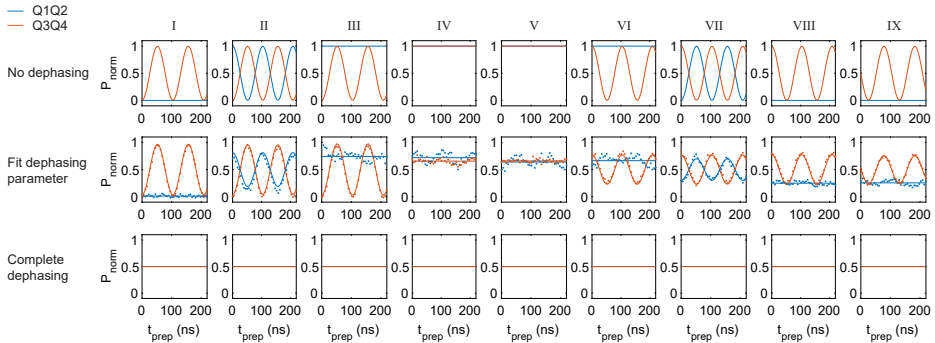


Figure 9.15: **Dephasing of the four-qubit GHZ state.** We model the quantum circuit performed in Fig. 9.5 and account for qubit decoherence by applying a depolarizing channel $\Lambda_\lambda(\rho) = \lambda\rho + \frac{1-\lambda}{d}\mathbb{1}$. We plot the expected measurement outcomes for qubit pairs Q1Q2 (blue) and Q3Q4 (orange). The top row corresponds to the case of perfect coherence in each panel. In the center row, we fit the depolarization parameter to the measurement data. The finite rotations visible in panels 4 and 5 in Fig. 9.5 can be reproduced by including gate errors in the model. Finally, the bottom row corresponds to a full depolarization of the state. If the qubit system is completely dephased at any point in time, no recovery of the signal can be observed in panel IX.

REFERENCES

- [1] Terhal, B. M. Quantum error correction for quantum memories. *Rev. Mod. Phys.* **87**, 307–346 (2015).
- [2] Reiher, M., Wiebe, N., Svore, K. M., Wecker, D. & Troyer, M. Elucidating reaction mechanisms on quantum computers. *PNAS* **114**, 7555–7560 (2017).
- [3] Loss, D. & DiVincenzo, D. P. Quantum computation with quantum dots. *Phys. Rev. A* **57**, 120–126 (1998).
- [4] Vandersypen, L. M. K. *et al.* Interfacing spin qubits in quantum dots and donors—hot, dense, and coherent. *npj Quantum Information* **3**, 34 (2017).
- [5] Shulman, M. D. *et al.* Demonstration of Entanglement of Electrostatically Coupled Singlet-Triplet Qubits. *Science* **336**, 202–205 (2012).
- [6] Veldhorst, M. *et al.* A two-qubit logic gate in silicon. *Nature* **526**, 410–414 (2015).
- [7] Zajac, D. M. *et al.* Resonantly driven CNOT gate for electron spins. *Science* **359**, 439–442 (2018).
- [8] Watson, T. F. *et al.* A programmable two-qubit quantum processor in silicon. *Nature* **555**, 633–637 (2018).
- [9] Huang, W. *et al.* Fidelity benchmarks for two-qubit gates in silicon. *Nature* **569**, 532–536 (2019).
- [10] He, Y. *et al.* A two-qubit gate between phosphorus donor electrons in silicon. *Nature* **571**, 371–375 (2019).
- [11] Mądzik, M. T. *et al.* Conditional quantum operation of two exchange-coupled single-donor spin qubits in a MOS-compatible silicon device. *Nature Communications* **12**, 181 (2021).
- [12] Petit, L. *et al.* Universal quantum logic in hot silicon qubits. *Nature* **580**, 355–359 (2020).
- [13] Hendrickx, N. W., Franke, D. P., Sammak, A., Scappucci, G. & Veldhorst, M. Fast two-qubit logic with holes in germanium. *Nature* **577**, 487–491 (2020).
- [14] Arute, F. *et al.* Quantum supremacy using a programmable superconducting processor. *Nature* **574**, 505–510 (2019).
- [15] Koppens, F. H. L. *et al.* Driven coherent oscillations of a single electron spin in a quantum dot. *Nature* **442**, 766–771 (2006).
- [16] Petta, J. R. *et al.* Coherent Manipulation of Coupled Electron Spins in Semiconductor Quantum Dots. *Science* **309**, 2180–2184 (2005).
- [17] Itoh, K. M. & Watanabe, H. Isotope engineering of silicon and diamond for quantum computing and sensing applications. *MRS Commun.* **4**, 143–157 (2014).
- [18] Muhonen, J. T. *et al.* Storing quantum information for 30 seconds in a nanoelectronic device. *Nat. Nanotech.* **9**, 986–991 (2014).
- [19] Veldhorst, M. *et al.* An addressable quantum dot qubit with fault-tolerant control-fidelity. *Nat. Nanotech.* **9**, 981–985 (2014).

- [20] Yoneda, J. *et al.* A quantum-dot spin qubit with coherence limited by charge noise and fidelity higher than 99.9%. *Nature Nanotechnology* **13**, 102–106 (2018).
- [21] Yang, C. H. *et al.* Silicon qubit fidelities approaching incoherent noise limits via pulse engineering. *Nat Electron* **2**, 151–158 (2019).
- [22] Zwanenburg, F. A. *et al.* Silicon quantum electronics. *Rev. Mod. Phys.* **85**, 961–1019 (2013).
- [23] Scappucci, G. *et al.* The germanium quantum information route. *Nature Reviews Materials* 1–18 (2020).
- [24] Itoh, K. *et al.* High purity isotopically enriched 70-Ge and 74-Ge single crystals: Isotope separation, growth, and properties. *J. Mater. Res.* **8**, 1341–1347 (1993).
- [25] Bulaev, D. V. & Loss, D. Spin Relaxation and Decoherence of Holes in Quantum Dots. *Phys. Rev. Lett.* **95**, 076805 (2005).
- [26] Lodari, M. *et al.* Light effective hole mass in undoped Ge/SiGe quantum wells. *Phys. Rev. B* **100**, 041304 (2019).
- [27] Lodari, M. *et al.* Low percolation density and charge noise with holes in germanium. *Mater. Quantum Technol.* **1**, 011002 (2021).
- [28] Hendrickx, N. W. *et al.* Gate-controlled quantum dots and superconductivity in planar germanium. *Nature Communications* **9**, 2835 (2018).
- [29] Lawrie, W. I. L. *et al.* Quantum dot arrays in silicon and germanium. *Appl. Phys. Lett.* **116**, 080501 (2020).
- [30] Pillarisetty, R. Academic and industry research progress in germanium nanodevices. *Nature* **479**, 324–328 (2011).
- [31] Bulaev, D. V. & Loss, D. Electric Dipole Spin Resonance for Heavy Holes in Quantum Dots. *Phys. Rev. Lett.* **98**, 097202 (2007).
- [32] Maurand, R. *et al.* A CMOS silicon spin qubit. *Nature Communications* **7**, 13575 (2016).
- [33] Watzinger, H. *et al.* A germanium hole spin qubit. *Nature Communications* **9**, 3902 (2018).
- [34] Pioro-Ladrière, M. *et al.* Electrically driven single-electron spin resonance in a slanting Zeeman field. *Nature Physics* **4**, 776–779 (2008).
- [35] Tokura, Y., van der Wiel, W. G., Obata, T. & Tarucha, S. Coherent Single Electron Spin Control in a Slanting Zeeman Field. *Phys. Rev. Lett.* **96**, 047202 (2006).
- [36] Sammak, A. *et al.* Shallow and Undoped Germanium Quantum Wells: A Playground for Spin and Hybrid Quantum Technology. *Advanced Functional Materials* **29**, 1807613 (2019).
- [37] van Riggelen, F. *et al.* A two-dimensional array of single-hole quantum dots. *Appl. Phys. Lett.* **118**, 044002 (2021).
- [38] Hendrickx, N. W. *et al.* A single-hole spin qubit. *Nature Communications* **11**, 3478 (2020).
- [39] Lawrie, W. I. L. *et al.* Spin Relaxation Benchmarks and Individual Qubit Addressability for Holes in Quantum Dots. *Nano Lett.* **20**, 7237–7242 (2020).

- [40] Danon, J. & Nazarov, Y. V. Pauli spin blockade in the presence of strong spin-orbit coupling. *Phys. Rev. B* **80**, 041301 (2009).
- [41] Yang, C. H. *et al.* Charge state hysteresis in semiconductor quantum dots. *Appl. Phys. Lett.* **105**, 183505 (2014).
- [42] Harvey-Collard, P. *et al.* High-Fidelity Single-Shot Readout for a Spin Qubit via an Enhanced Latching Mechanism. *Phys. Rev. X* **8**, 021046 (2018).
- [43] Knill, E. *et al.* Randomized benchmarking of quantum gates. *Phys. Rev. A* **77**, 012307 (2008).
- [44] Gullans, M. J. & Petta, J. R. Protocol for a resonantly driven three-qubit Toffoli gate with silicon spin qubits. *Phys. Rev. B* **100**, 085419 (2019).
- [45] Hetényi, B., Kloeffel, C. & Loss, D. Exchange interaction of hole-spin qubits in double quantum dots in highly anisotropic semiconductors. *Phys. Rev. Research* **2**, 033036 (2020).
- [46] Taylor, J. M. *et al.* Fault-tolerant architecture for quantum computation using electrically controlled semiconductor spins. *Nature Physics* **1**, 177–183 (2005).
- [47] Veldhorst, M., Eenink, H. G. J., Yang, C. H. & Dzurak, A. S. Silicon CMOS architecture for a spin-based quantum computer. *Nat. Commun.* **8**, 1766 (2017).
- [48] Li, R. *et al.* A crossbar network for silicon quantum dot qubits. *Science Advances* **4**, eaar3960 (2018).
- [49] Hensgens, T. *et al.* Quantum simulation of a Fermi–Hubbard model using a semiconductor quantum dot array. *Nature* **548**, 70–73 (2017).
- [50] Seedhouse, A. E. *et al.* Pauli Blockade in Silicon Quantum Dots with Spin-Orbit Control. *PRX Quantum* **2**, 010303 (2021).
- [51] Chan, K. W. *et al.* Assessment of a Silicon Quantum Dot Spin Qubit Environment via Noise Spectroscopy. *Phys. Rev. Applied* **10**, 044017 (2018).
- [52] Wang, Z. *et al.* Suppressing charge-noise sensitivity in high-speed Ge hole spin-orbit qubits. (2019).
- [53] Barnes, E., Kestner, J. P., Nguyen, N. T. T. & Das Sarma, S. Screening of charged impurities with multielectron singlet-triplet spin qubits in quantum dots. *Phys. Rev. B* **84**, 235309 (2011).
- [54] Russ, M. *et al.* High-fidelity quantum gates in Si/SiGe double quantum dots. *Phys. Rev. B* **97**, 085421 (2018).



10

SIMULTANEOUS DRIVING OF SEMICONDUCTOR SPIN QUBITS AT THE FAULT-TOLERANT THRESHOLD

Quantum computers will require the ability to perform quantum operations on large numbers of qubits with error rates below the fault tolerant threshold required for quantum error correction schemes [1]. Quantum dots define a promising platform due to their compatibility with semiconductor manufacturing, and high-fidelity operations beyond 99.9% have been realized with individual qubits [2], though investigations into the effect of operation of qubits simultaneously do not reach comparable values [3]. Here we present single qubit randomized benchmarking results in a two dimensional array of spin qubits, finding native gate fidelities as high as 99.990(1) %. We also characterize qubit performance during the simultaneous operation of N qubits, for which we define and utilize a novel benchmarking protocol called 'N-Copy benchmarking'. We find two- and four-copy fidelities of 99.905(8) % and 99.34(4) % respectively. We also find that benchmarking next-nearest neighbour pairs can return fidelities within the error margin of their single qubit cases, indicating that cross talk can be highly local in the absence of an exchange interaction. These characterizations of the single-qubit gate quality and the ability to operate simultaneously are crucial aspects for scaling up germanium based quantum information technology.

10.1. INTRODUCTION

Spin qubit approaches to quantum computing have made remarkable progress in the last few years. In both silicon and germanium [4, 5], two-dimensional approaches to scale up quantum dots have been the focus of multiple recent efforts [6, 7], as they provide greater qubit connectivity and enable the use of surface code architectures for quantum error correction [8]. For electrons in silicon, scaling qubits in the second dimension is challenging due to the need for components such as striplines and nanomagnets to enable qubit drive, and qubit realizations have been limited to linear arrays [9–11]. Instead, spin qubits based on holes in germanium can be driven all-electrically through the intrinsic strong spin-orbit coupling [12–14]. Furthermore, advances in strained germanium (Ge/SiGe) have yielded low charge noise and percolation density [15] and high hole mobility [16], indicative of a highly uniform platform. These advantages have resulted in the Ge/SiGe platform maturing rapidly over the last few years and led to demonstrations of long spin relaxation times [17], single hole qubits and singlet triplet qubits [14, 18] and universal operation on a 2x2 qubit array [19].

However, as spin qubits expand into two dimensions, the growing number of possible qubit cross talk interactions motivates careful characterization. In the present work, we make use of a 2x2 quantum dot array of hole spin qubits, to characterize the single qubit fidelities of our system, as well as characterizing their quality while driving two and four qubits simultaneously. We perform randomized benchmarking in the single qubit Clifford space, and investigate the dependence of fidelity on qubit Rabi period, finding that single qubit fidelities can be as high as 99.990(1)%. We then investigate the individual single qubit performance using a novel benchmarking technique we call N -copy benchmarking (See section 10.7). This technique applies the same Clifford operation to N qubits simultaneously, and results in a good approximation to simultaneous randomized benchmarking (SRB) [20] in the limit of low exchange interaction (See section 10.6). We find for $N=2$ and $N=4$, elementary gate fidelities of $F_{2Q}^{\pi/2} = 99.905(8)\%$ and $F_{4Q}^{\pi/2} = 99.34(4)\%$ respectively. We compare these experiments at two magnetic fields $B = 1$ T and $B = 0.65$ T and find that while individual qubit operation performs best at the lower magnetic field, multi-qubit operation performs better at a higher magnetic field, due to the relevance of qubit addressability.

10.2. RESULTS

Figure 10.1a shows a false-coloured scanning electron microscope (SEM) image of the device used in the experiment [19]. It consists of two gate layers and an ohmic layer, where ohmic contacts to the quantum well are created by diffused Al [21]. By applying potentials to the plunger gates P_1 - P_4 , we can define four quantum dots, each filled with a single hole spin such that we operate in the (1,1,1,1) charge regime (see section 10.5a). The tunnel couplings between these quantum dots can be tuned with the dedicated interdot barrier gates B12-41. We also define two larger quantum dots using P_{S12} and P_{S34} in the multiple hole regime, which we utilize as charge sensors. By applying a rf tone to the ohmic gates O_1 and O_3 via two off-chip inductors bonded in-line, we form a resonant tank circuit allowing us to perform fast rf charge sensing of our quantum dots to read out the spin states of our qubits, we perform spin-to-charge conversion in the form of Pauli spin blockade (PSB). Figure 1b depicts the two PSB readout pairs in our system, with the Q1Q2 system comprising of the two qubits Q1 and Q2 (orange, yellow), and the Q3Q4 system containing qubits Q3 and Q4 (purple, green). We make use of a latched readout mechanism [19, 22], whereby the dot-reservoir tunnel rate is limited significantly for one quantum dot per readout pair, which is depicted by a dashed arrow. We tune the tunnel rates of quantum dots Q2 and Q4 to be $\Gamma_{Q2} = 5$ kHz and $\Gamma_{Q4} = 0.416$ kHz respectively, and read out in an integration time of $10 \mu\text{s}$ such that we are well within the dot-reservoir limiting timescales. We apply an in-plane magnetic field B_{ext} to split the spin states. Two different magnetic fields were used in this experiment, of $B_{\text{ext}} = 1$ T and $B_{\text{ext}} =$

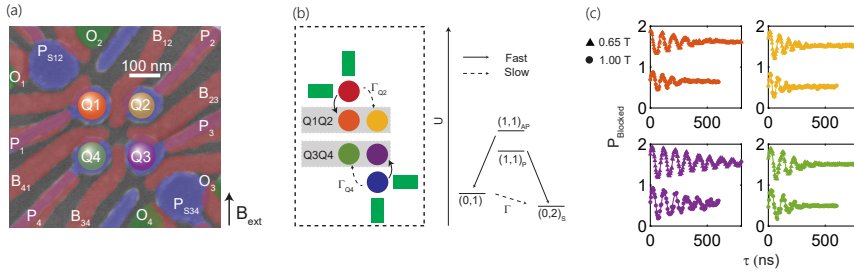


Figure 10.1: Heavy hole spin qubit array in germanium. (a) Scanning electron microscope (SEM) image of the device. The device is comprised of two lithographically defined layers of Ti:Pd constituting the plunger (blue) and barrier (red) gates, as well as an Al ohmic layer (green) forming low resistance ohmic contacts with the quantum well directly. An external magnetic field B_{ext} is applied in-plane with respect to the quantum well. (b) Latched spin blockade readout mechanism. We consider two separate readout systems Q1Q2 (red) and Q3Q4 (blue), each containing a double quantum dot pair and single hole transistor. By reducing the reservoir tunnel coupling to quantum dot Q2(4) $\Gamma_{Q2(4)}$, we are able to suppress the $(1,1)_T$ to $(0,2)_S$ transition longer than the typical singlet triplet relaxation rates [14], facilitating a readout integration window of $10 \mu\text{s}$. (c) Ramsey sequences on qubits Q1-4 respectively, at magnetic field $B = 1 \text{ T}$ (circles, lower) and 0.65 T (triangles, upper). Extracted spin dephasing times at 1 T for qubits Q1 (orange), Q2 (yellow), Q3 (purple) and Q4 (green) are $T_{Q1}^{2*} = 186 \pm 19 \text{ ns}$, $T_{Q2}^{2*} = 119 \pm 14 \text{ ns}$, $T_{Q3}^{2*} = 323 \pm 52 \text{ ns}$ and $T_{Q4}^{2*} = 147 \pm 26 \text{ ns}$. At 0.65 T the dephasing times increase to $T_{Q1}^{2*} = 276 \pm 22 \text{ ns}$, $T_{Q2}^{2*} = 166 \pm 14 \text{ ns}$, $T_{Q3}^{2*} = 472 \pm 31 \text{ ns}$ and $T_{Q4}^{2*} = 228 \pm 15 \text{ ns}$. Data for different magnetic fields is offset by unity for clarity.

0.65 T (Fig. 10.1c). These fields are chosen to provide a comparison between the different regimes of coherence, qubit drive response, and qubit resonance frequency spacing.

10.2.1. SINGLE QUBIT BENCHMARKING

In order to get a baseline reading of the individual qubit fidelities, we performed randomized benchmarking to estimate the average gate fidelity of each qubit [23]. Here, operations randomly selected from the Clifford group are applied to each single qubit, initialised in a known state, after which a final recovery Clifford C^{-1} is applied to bring the qubit back to its original state. Imperfections in the applied gates, and gradual qubit decoherence result in a decay of the recovered state probability as the number of applied Clifford operators is increased, allowing the extraction of a fidelity by fitting the decay [23]. Each element of the Clifford group can be constructed from a variety of generator gates. We construct our Clifford group from a minimal generator set $G_i \in \{X_{\pi/2}, Y_{\pi/2}\}$. We find this set advantageous since it contains on average 3.217 qubit $\pi/2$ rotations (generators) per Clifford, that differ only by a software phase shift. This means the estimated Clifford fidelity is a direct indicator of the generator fidelity, by equally weighting the generators of the same length [24].

Figures 10.2a-d show the randomized benchmarking sequences for Q1-4 respectively. A red (blue) measurement window indicates PSB readout on the Q1Q2 (Q3Q4) double quantum dot pair. Each qubit is initialised in the spin down state. For each sequence length N , 32 random permutations of N Cliffords are averaged to give the final trace, each of which is composed of 1500 single shot measurements. An exponential decay is fit to the resulting trace (see section 10.4.3), from which an average generator fidelity $F_{Q_i}^{\pi/2}$ can be extracted for each qubit.

Holes in germanium allow for very fast electrical driving, with Rabi frequencies exceeding hundreds of MHz [25, 26]. However, rapid qubit manipulation is not always optimal for coherent qubit

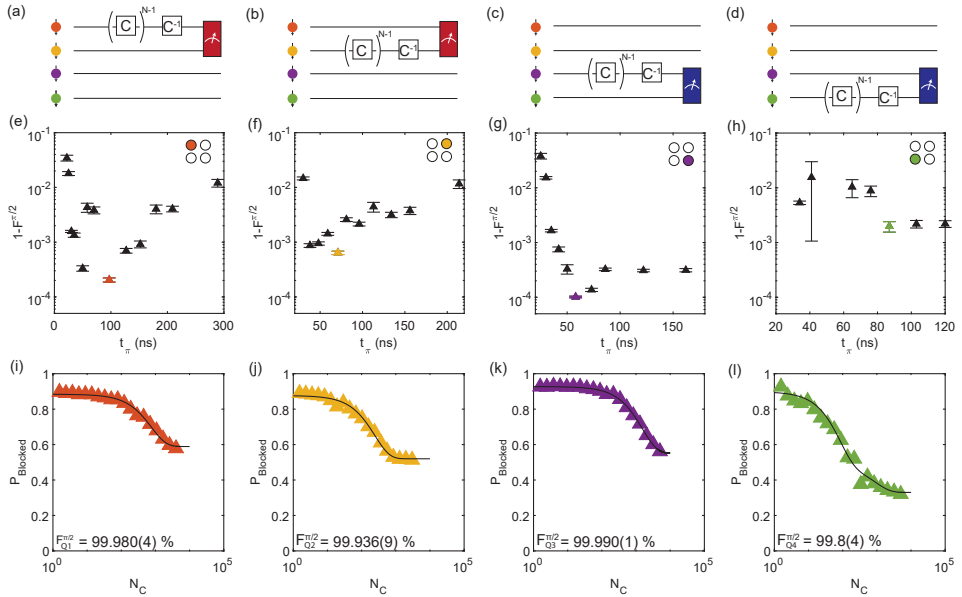


Figure 10.2: Single qubit randomized benchmarking at 0.65 T. (a-d) Random Clifford sequences applied to each qubit. Each qubit in the array is prepared in the spin down state. $N-1$ randomly selected Cliffords are applied to a single qubit, after which a recovery Clifford (C^{-1}) is applied bringing the system back to the $|\downarrow\rangle$ state. Each sequence is repeated 32 times with different random permutations of Cliffords. Readout occurs via PSB on one of the two readout pairs Q1Q2 (red) or Q3Q4 (blue). (e-h) Dependence of qubit fidelity on applied microwave power. An optimal power tuning occurs due to a trade-off between decoherence (low power) and errors introduced at high power including gate calibration errors and driving non-linearities. Error bars reflect the statistical error of the fitting. (i-l) Best single qubit benchmarks for each qubit. All native $\pi/2$ fidelities except $F_{Q4}^{\pi/2}$ exceed 99.9 %, with $F_{Q3}^{\pi/2}$ approaching four nines. These traces correspond to the respective highlighted points in (e-h).

control, with high powers leading to enhanced systematic errors in qubit operation arising from effects such as sample heating or pulse imperfections. Indeed we find a strong dependence of the single qubit fidelities on the drive speed. Figures 10.2e-h show the generator infidelities ($1 - F_{Q_i}^{\pi/2}$) as a function of qubit drive speed. Despite being able to drive qubit rotations in as fast as 10 ns, we find that the associated single qubit fidelity suffers as a result, visible by a sharp decrease in the fidelity for qubits Q1 and Q3. Fidelity in these cases could be limited by a number of mechanisms, such as quantum dot anharmonicities [27, 28] or systematic Pauli errors due to gate tuning.

Figures 10.2i-l show the randomized benchmarking data for the optimal Rabi periods. We extract generator fidelities above 99 % for each qubit in the array, with qubit Q3 performing the best with $F_{\pi/2}^{Q3} = 99.990(1)$ %. For single qubit randomized benchmarking, we expect a fully decohered state to exhibit a read out spin down probability of about 1/2. However in the presence of finite exchange and classical cross-talk between the active qubit and the readout qubit in the spin blockade pair, state leakage can occur to all four states in the two-qubit subspace, resulting in a readout signal of about $P_{\text{Blocked}} = 0.329$ (see section 10.5). We find that for the case of qubit Q4, the plateau of the spin blocked probability approaches the expected value of the fully depolarized two-qubit subspace for all driving powers.

To account for state leakage, an extra exponential is added for fitting randomized benchmarking traces for qubit Q4, yielding two characteristic decay constants (see section 10.4.3). From this analysis, we calculate a qubit fidelity $F_{Q4}^{\pi/2} = 99.8(4)\%$, and a leakage rate of $L_{Q4}^{\pi/2} = 0.07(2)\%$ per generator.

10.2.2. N -COPY RANDOMIZED BENCHMARKING

The operation of practical quantum computers will require multiple qubits to be controlled simultaneously [29]. Doing so however can affect performance to the detriment of the qubits due to both classical and quantum cross-talk [3]. We now turn to the characterization of single qubit fidelities using N -copy randomized benchmarking. Here, the same generation procedure described in the single qubit case is used to create a random sequence of single qubit Cliffords, which is applied to all qubits in the experiment. The recovery Clifford always brings the system back to the $|\downarrow\downarrow\rangle$ or $|\downarrow\downarrow\downarrow\downarrow\rangle$ state for two- or four-copy experiments respectively. It is important to distinguish between experiments wherein the driven qubits occupy the same measurement system (ES) ie. qubits Q1 and Q2 or Q3 and Q4, or different systems (ED) such as qubits Q1 and Q3. The measurement operators for ES and ED experiments will differ, leading to different decay behaviours (see section 10.7.2). We perform two-copy randomized benchmarking (2CRB) experiments with initial state $|\downarrow\downarrow\rangle$, since the fitting procedure is simplified and provides a good estimate of the true fidelity in the regime of low exchange (see section 10.8.2, and 10.9). Figures 10.3a-b show a complete characterization of the single, two- and four-copy benchmarking at a consistent Rabi period of $t_\pi = 96$ ns and magnetic field $B_{\text{ext}} = 0.65$ T. From this dataset, we can approximate the relative loss in fidelity in the ED case for each qubit due to the additional driving of another qubit by defining the quantity $\delta_{Q_i|Q_j} = \epsilon_{Q_i|Q_j} - \epsilon_{Q_i}$ where $\epsilon_{Q_i} = 1 - F_{Q_i}$ is the infidelity of qubit Q_i (Full numerical data available in section 10.10). For ES-2CRB, the resulting fidelity is related to the combined fidelities of both qubits in the system. We observe that qubits driven simultaneously with their nearest neighbours typically result in relatively larger error rates, while next nearest neighbour pairs can give error rates that are very low. For example, the relative loss of qubit Q3 due to the driving of qubit Q2 $\delta_{Q_3|Q_2} = 0.35\%$ is significant, while for the non-adjacent qubit pair Q3 and Q1, $\delta_{Q_3|Q_1}$ is immeasurable within the error bar and gave a simultaneous fidelity of $F_{Q_3}^{\pi/2} \approx F_{Q_3|Q_1}^{\pi/2} = 99.964(3)\%$. The same is true for the opposite configuration, where $\delta_{Q_1|Q_3}$ again is immeasurable within the error bar, and $F_{Q_1}^{\pi/2} \approx F_{Q_1|Q_3}^{\pi/2} = 99.97(1)\%$. Optimum Rabi periods for simultaneous driving also exist due to a trade-off between qubit coherence and frequency crowding. The fidelity of the Q3Q4

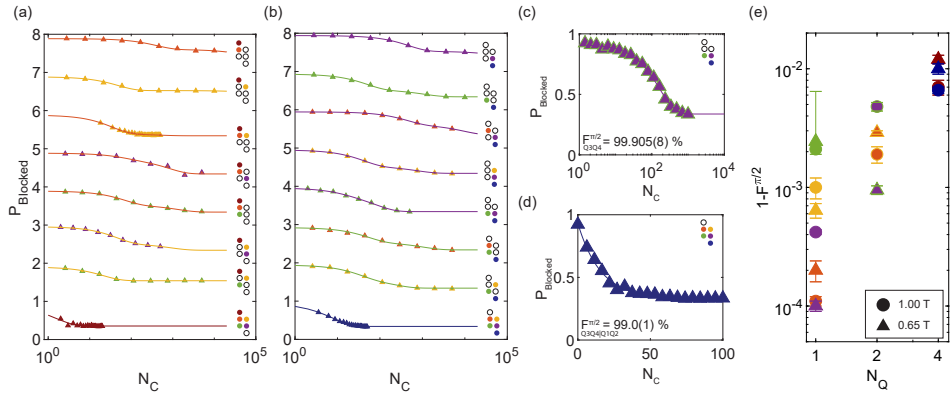


Figure 10.3: N -copy randomized benchmarking in a four qubit array. (a-b) Benchmarking characterization at $t_{\pi} = 96$ ns for single qubit randomized benchmarking, two- and four-copy randomized benchmarking experiments. (a) and (b) correspond to readout systems Q1Q2 and Q3Q4 respectively. For a pair of qubits, $N - 1$ randomly selected Clifford sequences are applied simultaneously followed by a recovery pulse, and read out via PSB. Line and marker color, as well as the corresponding cartoons indicate which qubits are being benchmarked, and which PSB readout pair is being probed. The additional coloured dot indicates which system is being read out, such that a red (blue) dot indicates readout of the Q1Q2 (Q3Q4) system. (c) Decay for an ES 2CRB trace at 0.650 T. The readout system is Q3Q4. Rabi period is set to $t_{\text{Rabi}} = 61$ ns for the qubits. A fidelity of $F_{Q3Q4}^{\pi/2} = 99.905(8)\%$ is extracted. (d) Four-copy randomized benchmarking at 0.650 T. The readout system is Q3Q4. The Rabi period for all qubits is set to $t_{\text{Rabi}} = 150$ ns. A fidelity of $F_{Q3Q4|Q1Q2}^{\pi/2} = 99.0(1)\%$ is extracted. (e) Summary of the fidelities, reported as the native average $\pi/2$ generator infidelity $1-F^{\pi/2}$ as a function of number of driven qubits N_q , such that $N_q=1$, $N_q = 2$ and $N_q = 4$ represent single qubit, ES two-copy and four-copy randomized benchmarking fidelities respectively. Data points for $B = 0.65$ T (triangles) and $B = 1$ T (circles) is compared. Colours are indicative of the qubits involved in the experiment. For $N_q = 2$, orange/yellow markers symbolize qubits Q1 and Q2, while purple/green markers symbolize qubits Q3 and Q4. Red and blue markers for $N_q = 4$ qubits represent all four qubits, read out in system Q1Q2 and Q3Q4 respectively.

system in a four-copy experiment, $F_{Q3Q4|Q1Q2}^{\pi/2} = 99.0(1)\%$, is optimal for a Rabi period of 150 ns. Further increase of the Rabi period does not yield better fidelities as the coherence of qubit Q4 is limiting this value. We find we can also improve the ES 2CRB fidelity of the adjacent qubit pair $F_{Q3Q4}^{\pi/2} = 99.905(8)\%$ by decreasing the Rabi period to 61 ns, (see fig. 10.3c), indicating that decoherence may have been the limiting process. The observation of high fidelity single qubit gates for ES and ED 2CRB, as well as four-copy benchmarking (4CRB) fidelities above 99%, shows promise for qubit operation in large scale spin qubit arrays.

Two different magnetic field settings were applied in this work to clarify the importance of spin coherence on the gate fidelities (see Fig. 10.1c). At lower magnetic fields, the effect of the spin-orbit coupling via the g-factor modulation of the qubits during driving is reduced, decreasing the susceptibility of the resonance frequency to charge noise [30]. Since the Rabi frequency is linear in magnetic field, the drive power has to be increased to compensate [31]. This leads to increased qubit cross-talk when driving qubits simultaneously and suggests the existence of an optimal magnetic field strength. Figure 10.3e summarises the randomized benchmarking results of this work, providing detailed information on the extracted average generator as a function of number of driven qubits N_Q . On average, the individual single qubit fidelities are higher at lower field, as are the fidelities for 2CRB. The power required to drive the systems at their optimal Rabi period however, was found to be inversely proportional with B_z as expected, and as such were observed to shift to longer Rabi periods. We observed that at the stronger magnetic field of 1 T, higher fidelities can be achieved for the four-copy case. We attribute this result to the faster achievable Rabi frequencies as well as larger qubit frequency splittings outweighing the relative loss in coherence. We expect that the magnitude of these classical cross talk effects can be reduced through pulse engineering techniques [32, 33], facilitating shorter Rabi periods when driving qubits. Additionally, the high g-factor tuneability of hole states observed in Ge/SiGe [14] and Si [34] could be exploited to reduce the cross talk effect by maximising the separation of the qubits' resonance frequencies [35].

10.3. CONCLUSION

We have characterized qubit operational fidelities in a two-dimensional spin qubit array. Single qubit fidelities of up to 99.990(1)% estimated using single qubit randomized benchmarking, are strongly dependent on Rabi period, leading to an optimal driving speed configuration in our qubits. We expect that pulse shaping will further increase this optimal drive speed if care is taken to reduce classical cross talk between qubits. The large g-factor tuneability of the platform could facilitate better resonant frequency spacings which could also lead to reduced cross talk. However, we still achieve ES 2CRB fidelities exceeding 99.9% for two adjacent qubits, and 99% for four-copy randomized benchmarking, defining the state-of-the-art for single qubit fidelities in quantum dot based spin qubits.

10.4. METHODS

10.4.1. DEVICE FABRICATION

The Ge/SiGe wafer is fabricated on a silicon substrate. We use reduced-pressure chemical vapour deposition to grow a 1.6 μm strain-relaxed Ge layer, a 1 μm reverse graded $\text{Si}_{1-x}\text{Ge}_x$ (x varies from 1 to 0.8), a 500 nm constant composition $\text{Si}_{0.2}\text{Ge}_{0.8}$, and a 16 nm compressively strained Ge quantum well. Finally on the quantum well we grow a 55 nm $\text{Si}_{0.2}\text{Ge}_{0.8}$ barrier followed by an oxidised Si cap layer (<2 nm). An ohmic contact layer is created by first defining it using electron beam lithography, etching away the oxidised cap, then depositing 30 nm of Al. This layer is then covered in 7 nm of Al_2O_3 via atomic layer deposition at 300 $^\circ\text{C}$. The gate stack is in two overlapping

layers of Ti:Pd (3/37 nm), separated by 7 nm of Al₂O₃.

10.4.2. GENERATION OF THE SINGLE-QUBIT CLIFFORD SET

We quantify the quality of the single-qubit gates on all qubits by performing randomized benchmarking using the Clifford group $C_1 = \{C_n \in U_1 | C_n P C_n^\dagger = P\}$ with the single-qubit Pauli group $P = \{I, X, Y, Z\}$. All 24 elements of the Clifford group are generated from a minimal set, $C_n = \prod_{g_i \in \mathcal{G}} g_i$ with $\mathcal{G} = \{X_{\pi/2}, Y_{\pi/2}\}$. The average number of elementary gates per Clifford is 3.217. All 24 Clifford gates are provided in section 10.6. While not the most efficient choice for elementary gates, this particular choice of set leads to uniform Clifford gates, whose elementary gates vary only by a $\theta = \pi/2$ phase-shift in the MW signal and are identical otherwise, beneficial for comparison and performing 2CRB protocols.

10.4.3. FITTING

Standard fitting of randomized benchmarking decays assumes a single exponential decay of the form $P_{\text{Blocked}} = aF^X + c$ where c should be equal to the average signal of the $|\downarrow, \downarrow\rangle$ and $|\uparrow, \downarrow\rangle$ subspace (where the first index corresponds to the qubit being benchmarked). Here F represents the circuit level fidelity, from which the Clifford fidelity $F_{Q_i}^C = 1 - (1 - F_{Q_i})/2$ and native gate fidelity $F_{Q_i}^{\pi/2} = 1 - (1 - F_{Q_i})/(2 \times 3.217)$ can be calculated. However, for qubit Q4, and for the high power regime of qubits Q1-3, we observe that the blocked signal plateaus to values corresponding to the fully decohered two-qubit subspace, indicating state leakage. In this case, we fit with two exponentials $P_{\text{Blocked}} = a_1 F_1^X + a_2 F_2^X + c$, where c is set to the average signal of the four two-qubit states in the readout pair. Here, F_1 and F_2 correspond to the two circuit level fidelities, representing a leakage rate and an actual qubit fidelity. In this case, we assign the lower of the two values to the qubit fidelity.

For ES 2CRB, we fit a single exponential, giving a result that is representative of the average fidelity of both qubits in the system. For ED 2CRB, we fit a single exponential when the plateau corresponds to a fully depolarized single-qubit subspace, and a double exponential when it decays to a fully depolarized two-qubit subspace representing leakage. In the latter case, the fidelity is always calculated from the faster of the two exponents. For 4CRB, a single exponential is fit. For all fits, we assign confidence intervals on the extracted gate fidelities and leakage at the 95% confidence level of the variance.

10.4.4. SIMULTANEOUS ELEMENTARY GATE TUNING

In order to tune the system for the case of two-simultaneously driven qubits, we first determine the non-simultaneously driven resonance frequency and Rabi frequency by applying a X_π pulse to each qubit separately and perform readout out via PSB. We then tune the values of t_π within 1 ns of each other and then set the desired simultaneous t_π as the average of the two single-qubit values of t_π . This constitutes a rough calibration of the qubits. To fine tune, we apply a $X_{2\pi}$ rotation on both qubit simultaneously, and sweep the frequency of both qubits. Fitting a two-dimensional Gaussian then gives the first iteration correction to the two qubits' resonance frequencies. We then perform the same experiment, but varying the amplitude of the MW power of both qubits. When driving four qubits simultaneously, the tuning procedure is extended to include both systems Q1Q2 and Q3Q4 in the tuning iteration.

10.5. INITIALIZATION AND READOUT

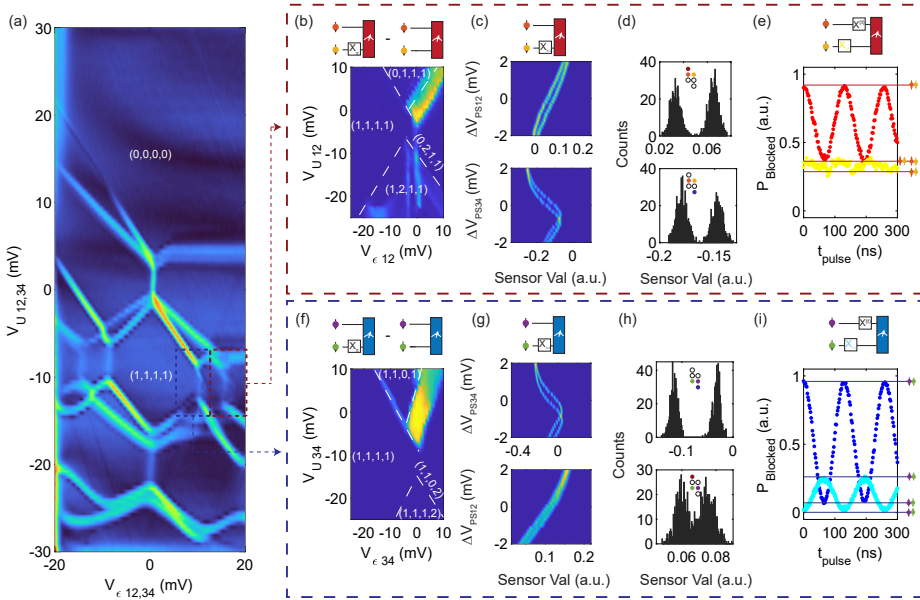


Figure 10.4: (a) Charge stability diagram of the 2×2 quantum dot array charge filling. The DC voltage point of the Digital-Analogue converters (DACs) is positioned within the $(1,1,1,1)$ charge filling regime. Anticrossings between the $(1,1,1,1)/(0,2,1,1)$ and $(1,1,1,1)/(1,1,0,2)$ charge transitions are shown in red and blue respectively. We use these anticrossings for spin to charge conversion and thus for readout of the qubit state. The axes $\epsilon_{12,34}$ and $U_{12,34}$ are virtual gates describing the combined detuning and energy of the two qubit pairs Q1Q2 and Q3Q4. (b) Readout calibration of the Q1Q2 system. While in the $(1,1,1,1)$ charge state, we prepare the qubit system in the $|\downarrow\downarrow\downarrow\downarrow\rangle$ state and apply a π -pulse to qubit Q2, bringing the system to the $|\downarrow\downarrow\uparrow\downarrow\rangle$ state. We then sweep the virtual detuning ($V_{\epsilon 12}$) and on-site energy ($V_{U 12}$) around the $(1,1,1,1)/(0,2,1,1)$ anticrossing. We then repeat the experiment without applying the X_{π} -pulse to Q2, and plot the difference of the two measurements, and pick the point of greatest visibility as the readout position. (c-d) Single shot readout calibration. (c) Sensor value plot as a function of virtual sensor plunger gate potential (V_{PS12}) for sensors one (upper, red) and two (lower, blue), for the Q1Q2 system. Qubit Q2 is brought into a superposition state by applying a $X_{\pi/2}$ -pulse, and the system is pulsed to the readout point from (b). We repeat 1000 single shot measurements, for each value of V_{PS12} and plot the resulting histogram of sensor response. A double-gaussian is fitted to the line cuts to find the sensor response to the blocked and non-blocked signals, and the plunger gate voltage for maximal separation between the gaussian peaks, is set. (d) The same experiment performed at the given V_{PS12} . A double gaussian is fit to the resulting histogram, and the single-shot threshold is calculated as the point of equal separation between the gaussian peaks. (e) Visibility of the two qubit subspace of the Q1Q2 system. Rabi oscillations are performed on Q1 with Q2 prepared either in the down state (red trace) or the up state (yellow trace). There is a small blocked fraction difference between the $|\downarrow\downarrow\rangle$ and $|\downarrow\uparrow\rangle$ states, and the $|\downarrow\downarrow\rangle$ state is less blocked than the $|\downarrow\uparrow\rangle$. (f-i) The same procedure as (b-e), but pertaining to the Q3Q4 system, $(1,1,1,1)/(1,1,0,2)$ anticrossing, with X_{π} - and $X_{\pi/2}$ -pulses on qubit Q4, instead.

10.6. CLIFFORD GATE SET

Table 10.1: single-qubit Clifford sequences and their composition via the minimal generator set. We benchmark by selecting a random sequence of Cliffords from the table below excluding C_1 , and calculate the recovery Clifford that projects the system back into it's original state. We only use a gate set containing $\pi/2$ rotations around the Bloch Sphere, so the gates $X_{\pi/2}$ and $Y_{\pi/2}$ are explicitly referring to a rotation of $\pi/2$ around the x-axis and y-axis of the Bloch sphere of a single-qubit respectively. A $Y_{\pi/2}$ rotation is just an $X_{\pi/2}$ rotation with a $\pi/2$ software phase correction. There are on average 3.217 generators per Clifford composition. The extracted fidelity then corresponds exactly to the $\pi/2$ rotation fidelity.

Clifford	Composition
C_1	I
C_2	$Y_{\pi/2}$
C_3	$X_{\pi/2}$
C_4	$Y_{\pi/2}X_{\pi/2}$
C_5	$X_{\pi/2}Y_{\pi/2}$
C_6	$Y_{\pi/2}Y_{\pi/2}$
C_7	$X_{\pi/2}X_{\pi/2}$
C_8	$Y_{\pi/2}X_{\pi/2}X_{\pi/2}$
C_9	$Y_{\pi/2}Y_{\pi/2}X_{\pi/2}$
C_{10}	$Y_{\pi/2}X_{\pi/2}Y_{\pi/2}$
C_{11}	$Y_{\pi/2}Y_{\pi/2}Y_{\pi/2}$
C_{12}	$X_{\pi/2}X_{\pi/2}X_{\pi/2}$
C_{13}	$X_{\pi/2}X_{\pi/2}Y_{\pi/2}$
C_{14}	$X_{\pi/2}Y_{\pi/2}Y_{\pi/2}$
C_{15}	$Y_{\pi/2}X_{\pi/2}Y_{\pi/2}Y_{\pi/2}$
C_{16}	$Y_{\pi/2}Y_{\pi/2}X_{\pi/2}Y_{\pi/2}$
C_{17}	$X_{\pi/2}X_{\pi/2}X_{\pi/2}Y_{\pi/2}$
C_{18}	$Y_{\pi/2}X_{\pi/2}X_{\pi/2}X_{\pi/2}$
C_{19}	$Y_{\pi/2}Y_{\pi/2}X_{\pi/2}X_{\pi/2}$
C_{20}	$X_{\pi/2}Y_{\pi/2}Y_{\pi/2}Y_{\pi/2}$
C_{21}	$Y_{\pi/2}Y_{\pi/2}Y_{\pi/2}X_{\pi/2}$
C_{22}	$Y_{\pi/2}Y_{\pi/2}Y_{\pi/2}X_{\pi/2}Y_{\pi/2}$
C_{23}	$Y_{\pi/2}X_{\pi/2}X_{\pi/2}X_{\pi/2}Y_{\pi/2}$
C_{24}	$Y_{\pi/2}X_{\pi/2}Y_{\pi/2}Y_{\pi/2}Y_{\pi/2}$

10.7. TWO-COPY RANDOMIZED BENCHMARKING

Here we derive the functional forms of two-copy randomized benchmarking. This involves randomized benchmarking by applying the same randomly selected Clifford to two qubits in the same readout system, simultaneously. We are therefore interested in the representation structure of the representation:

$$R^2(c)(\rho) = U_c^{\otimes 2} \rho U_c^{\dagger \otimes 2} \quad (10.1)$$

where c indexes a Clifford operation, ρ is an input state density matrix defining a two-qubit system, and U_c is the unitary representation of a given Clifford sequence indexed by c . The irreducible subrepresentations of this representation are as follows:

$$V_{tr,1} = \text{Span}\left\{\frac{1}{2}II\right\} \quad (10.2)$$

$$V_{tr,2} = \text{Span}\left\{\frac{1}{2\sqrt{3}}(XX + YY + ZZ)\right\} \quad (10.3)$$

$$V_{adj,1} = \text{Span}\left\{\frac{1}{2}IX, \frac{1}{2}IY, \frac{1}{2}IZ\right\} \quad (10.4)$$

$$V_{adj,2} = \text{Span}\left\{\frac{1}{2}XI, \frac{1}{2}YI, \frac{1}{2}ZI\right\} \quad (10.5)$$

$$V_{adj,3} = \text{Span}\left\{\frac{1}{2\sqrt{2}}(XY - YX), \frac{1}{2\sqrt{2}}(ZY - YZ), \frac{1}{2\sqrt{2}}(XZ - ZX)\right\} \quad (10.6)$$

$$V_3 = \text{Span}\left\{\frac{1}{2\sqrt{2}}(XX - YY), \frac{1}{2\sqrt{6}}(XX + YY - 2ZZ)\right\} \quad (10.7)$$

$$V_4 = \text{Span}\left\{\frac{1}{2\sqrt{2}}(XY + YX), \frac{1}{2\sqrt{2}}(ZY + YZ), \frac{1}{2\sqrt{2}}(XZ + ZX)\right\} \quad (10.8)$$

Here, the subscripts tr , and adj abbreviate *trivial* and *adjoint* respectively, as per the convention in ref. [], while the subscripts 3 and 4 simply enumerate two more non-equivalent representations. From these four representations, we can write down the functional form of such a protocol to be

$$p(m) \approx \text{Tr}\{A_{tr}M_{tr}^m\} + \text{Tr}\{A_{adj}M_{adj}^m\} + A_3f_3^m + A_4f_4^m \quad (10.9)$$

where m is the length of a sequence, A_{tr}, M_{tr} are 2×2 real matrices (associated to the trivial representations), A_{adj}, M_{adj} are 3×3 real matrices (associated to the adjoint representations), and A_3, f_3 and A_4, f_4 are real number associated to the third and fourth irreducible sub-representations respectively. It follows from standard RB theory that the conventional average fidelity of the channel Λ is given as:

$$\frac{4F_{\text{avg}}(\Lambda) - 1}{3} = \frac{1}{15}((\text{Tr}\{M_{tr}\} - 1) + 3\text{Tr}\{M_{adj}\} + 2f_3 + 3f_4) \quad (10.10)$$

The prefactors A_{rep} have matrix elements and real values given by

$$[A_{\text{rep}}]_{i,j} = |V_{\text{rep}}|^{-1} \text{Tr}\{P_{\text{rep},i}(E)\} \text{Tr}\{P_{\text{rep},j}(\rho)\} \quad (10.11)$$

$$A_3 = (1/2) \text{Tr}\{P_3(E)\} \text{Tr}\{P_3(\rho)\} \quad (10.12)$$

$$A_4 = (1/3) \text{Tr}\{P_4(E)\} \text{Tr}\{P_4(\rho)\} \quad (10.13)$$

for i, j indexing the number of copies of a given representation rep , $\rho \approx |00\rangle\langle 00| = (1/4)(II + IZ + ZI + ZZ)$ is the prepared initial state, and we observe the POVM element $E \approx |00\rangle\langle 00| = (1/4)(II + IZ + ZI + ZZ)$.

10.7.1. STRUCTURE OF THE MATRIX DECAYS

Two-copy RB differs from standard RB [23] and simultaneous RB [20] by the presence of matrix valued decay rates (encoded by the matrices M_{tr} and M_{adj}). To estimate the average fidelity we are interested in learning the trace of these matrices. This can be done in practice by assuming that the matrices $M_{\text{tr}}, M_{\text{adj}}$ are diagonalisable (note that this is a rather weak assumption). Then the matrix valued signal decomposes into a linear combination of exponentials with decay rates set by the eigenvalues. This is worth addressing in more detail. We begin by treating M_{tr} . If we assume that Λ is a trace preserving quantum channel, then certain entries of M_{tr} are fixed a priori. We concretely get that

$$M_{\text{tr}} = \begin{pmatrix} 1 & 0 \\ \alpha & f_{\text{tr}} \end{pmatrix} \quad (10.14)$$

where α and f_1 are real parameters. Note that only the diagonal parameter f_1 contributes to the average fidelity. The case of M_{adj} is more sophisticated, and has some novel features not earlier observed in benchmarking experiments. By construction M_{adj} is a 3×3 real matrix, which means it will have at least 1 real eigenvalue f_{adj} and two more eigenvalues that are either both real, or complex numbers that are each others complex conjugate. The telltale sign of the appearance of such a complex eigenvalue pair would be the appearance of damped oscillations in the 2CRB data. Note from figure 10.5 that we do in fact observe such oscillations in certain 2CRB experiments. Hence we will from now on assume that we are indeed in this scenario with two complex conjugate eigenvalues $\lambda_{\text{adj}}, \bar{\lambda}_{\text{adj}}$ and one real eigenvalue f_{adj} .

To gain further insight into M_{adj} it is worth making a natural extra assumption on the noise channel Λ . In particular we will assume that Λ is invariant under the interchange of two qubits. Examples of such channels include a global depolarizing channel and crosstalk due to exchange interaction (on which more later). Through a straightforward calculation we see that if Λ is invariant under the interchange of the two qubits, then $v = (1, 1, 0)/\sqrt{2}$ is an eigenvector of M_{adj} . Since this eigenvector is real, the associated eigenvector must also be. Complementary, the subspace spanned by $w_1 = (1, -1, 0)/\sqrt{2}, w_2 = (0, 0, 1)$ carries the pair of complex eigenvalues.

It is worth noting that this decomposition is robust against violations of the symmetry assumption we made above, as long as the complex eigenvalues are sufficiently far from being real. By this we mean that "the eigenvector carrying the real eigenvalue" will perturb continuously even under a symmetry breaking perturbation. This means the analysis above holds broadly even for quantum channels that do not respect the symmetry (as long as there are two complex eigenvalues). This is important as we expect the symmetry condition not to hold exactly in practice (for instance if the two qubits have different local error rates).

To summarise, under some mild assumptions the average fidelity takes the form:

$$\frac{4F_{\text{avg}}(\Lambda) - 1}{3} = \frac{1}{15} (f_{\text{tr}} + 3(f_{\text{adj}} + \lambda_{\text{adj}} + \bar{\lambda}_{\text{adj}}) + 2f_3 + 3f_4). \quad (10.15)$$

Where all parameters can in principle be extracted from decay experiments. However, what decays are visible depends on the choice of input state and output measurement (note that this not the case in standard RB, making 2CRB more difficult to execute and analyse even beyond the complexity of the representation structure). We have implemented several types of 2CRB, distinguished by different input states and measurements. We now discuss these in greater detail.

10.7.2. DIFFERENT TYPES OF TWO-COPY RB

With the information collected above we can further discuss the types of 2CRB experiments discussed in the main text. We distinguish three types of 2CRB, each with different input states ρ and

measurement operators E :

$$\rho \approx |00\rangle\langle 00| = (1/4)(II + IZ + ZI + ZZ), \quad E \approx |00\rangle\langle 00| = (1/4)(II + IZ + ZI + ZZ) \\ \text{(even, same-system (ES))}$$

$$\rho \approx |00\rangle\langle 00| = (1/4)(II + IZ + ZI + ZZ), \quad E \approx |0\rangle\langle 0| \otimes I = (1/2)(II + ZI) \\ \text{(even, different-system (ED))}$$

$$\rho \approx |01\rangle\langle 01| = (1/4)(II - IZ + ZI - ZZ), \quad E \approx |01\rangle\langle 10| = (1/4)(II - IZ + ZI + ZZ). \\ \text{(odd, same-system (OS))}$$

The logical fourth experiment (odd, different-system (OD)) was not performed, so we will not analyse it here. With these expressions for E, ρ we can directly calculate what the pre-factors A in equation 10.9 are in the ideal case for the three executed types of 2CRB:

$$A_{\text{tr}} = \frac{1}{4} \begin{pmatrix} 1 & 1/\sqrt{3} \\ 1/\sqrt{3} & 1/3 \end{pmatrix}, \quad A_{\text{adj}} = \frac{1}{12} \begin{pmatrix} 1 & 1 & 0 \\ 1 & 1 & 0 \\ 0 & 0 & 0 \end{pmatrix}, \quad A_3 = \frac{1}{12}, \quad A_4 = 0 \quad \text{(ES)}$$

$$A_{\text{tr}} = \frac{1}{4} \begin{pmatrix} 1 & 0 \\ 0 & 0 \end{pmatrix}, \quad A_{\text{adj}} = \frac{1}{12} \begin{pmatrix} 1 & 0 & 0 \\ 1 & 0 & 0 \\ 0 & 0 & 0 \end{pmatrix}, \quad A_3 = 0, \quad A_4 = 0 \quad \text{(ED)}$$

$$A_{\text{tr}} = \frac{1}{4} \begin{pmatrix} 1 & -1/\sqrt{3} \\ -1/\sqrt{3} & 1/3 \end{pmatrix}, \quad A_{\text{adj}} = \frac{1}{12} \begin{pmatrix} 1 & -1 & 0 \\ -1 & 1 & 0 \\ 0 & 0 & 0 \end{pmatrix}, \quad A_3 = \frac{1}{12}, \quad A_4 = 0 \quad \text{(OS)}$$

The first thing to note here is that in all three experiments $A_4 = 0$ in the absence of SPAM errors. Hence we do not expect to be able to reliably extract f_4 from the performed experiments. We will now discuss each experiment in more detail:

10.7.3. EVEN SAME-SYSTEM (ES) TWO-COPY RB

As can be seen above, in the ES experiment the matrices A_{tr} and A_{adj} are rank one. Hence it is not a priori clear we can reliably observe the full matrix decays (i.e. observe the eigenvalues of the matrix M). This is worth addressing in more detail. We begin by treating M_{tr} . Recall that under the assumption of gate-dependent trace preserving noise this matrix has a lower-triangular form (given by equation 10.14) Note that only the diagonal parameter f_1 contributes to the average fidelity. Using the expression for A_{tr} for the ES experiment we see that

$$\text{tr}(A_{\text{tr}}M_{\text{tr}}^m) = \frac{1}{4} \left(1 + (1/3)f_{\text{tr}}^m + \alpha(1 - f_{\text{tr}}^m)/(\sqrt{3}(1 - f_{\text{tr}})) \right) = af_{\text{tr}}^m + b \quad (10.16)$$

for some real constants a, b . Hence the trivial "sector" contributes only a single exponential decay to the model in equation 10.9. Moreover, in the high fidelity limit the constant a will be approximately $1/12$ for the ES experiment, which means that f_1 will typically be observable.

Next consider $\text{tr}\{A_{\text{adj}}M_{\text{adj}}^m\}$. Under the symmetry assumption made above we know that $v = (1, 1, 0)/\sqrt{2}$ is an eigenvector of M_{adj} with real eigenvalue f_{adj} . Note also that $A_{\text{adj}} = v^T v$ in the ES experiment, and thus that $\text{tr}\{A_{\text{adj}}M_{\text{adj}}^m\} = f_{\text{adj}}^m$. Hence in the absence of SPAM errors the ES experiment perfectly detects the one real decay in M_{adj} , and does not detect the two conjugate complex eigenvalues at all. Hence the presence of oscillations in the even experiment are only due to SPAM errors.

To summarize, in the ES 2CRB experiment, we expect the data to take the functional form

$$p(m)_{\text{even}} \approx a_{\text{tr}} f_{\text{tr}}^m + b_{\text{tr}} + A_3 f_3^m + a_{\text{adj}} f_{\text{adj}}^m \quad (10.17)$$

where $a_{\text{tr}}, b_{\text{tr}}, A_3, a_{\text{adj}}$ are real numbers encoding SPAM.

10.7.4. ODD SAME-SYSTEM (OS) TWO-COPY RB

The discussion of the odd same-system (OS) 2CRB experiment is largely analogous. Considering M_{tr} first, we see that

$$\text{tr}(A_{\text{tr}} M_{\text{tr}}^m) = \frac{1}{4} (1 + (1/3) f_{\text{tr}}^m - \alpha (1 - f_{\text{tr}}^m) / (\sqrt{3} (1 - f_{\text{tr}}))) = a f_{\text{tr}}^m + b \quad (10.18)$$

for some real constants a, b . Again in the high fidelity limit a will be approximately $1/12$ and we thus expect good visibility for f_{tr} . For M_{adj} we note that in the OS type experiment we have $A_{\text{adj}} = w_1^T w_1$ with $w_1 = (1, -1, 0) / \sqrt{2}$. This means the OS experiment does not observe the real eigenvalue f_{ad} (as the corresponding eigenvector is orthogonal). Instead we have that (by the realness of the overall signal)

$$\text{tr}\{A_{\text{adj}} M_{\text{adj}}^m\} = a_{\text{adj}} (\lambda_{\text{adj}}^m + \bar{\lambda}_{\text{adj}}^m) \quad (10.19)$$

for some real parameter a_{adj} . Thus in this experiment we expect a quite strong oscillating component in the signal. This is borne out in practice, see [10.5].

To summarise, in the OS two-copy experiment we expect the data to take the functional form

$$p(m)_{\text{odd}} \approx a_{\text{tr}} f_{\text{tr}}^m + b_{\text{tr}} + A_3 f_3^m + a_{\text{adj}} (\lambda_{\text{adj}}^m + \bar{\lambda}_{\text{adj}}^m) \quad (10.20)$$

where $a_{\text{tr}}, b_{\text{tr}}, A_3, a_{\text{adj}}$ are real numbers encoding SPAM.

10.7.5. EVEN DIFFERENT-SYSTEM (DS) TWO-COPY RB

Finally we discuss the case of ED 2CRB. This experiment has a significantly simpler decay structure (but as a consequence also collects less information about error processes). Note first that

$$\text{tr}\{A_{\text{tr}} M_{\text{tr}}^m\} = \text{tr}\left\{\frac{1}{4} \begin{pmatrix} 1 & 0 \\ 0 & 0 \end{pmatrix} \begin{pmatrix} 1 & 0 \\ \alpha & f_{\text{tr}} \end{pmatrix}\right\} = \frac{1}{4} \quad (10.21)$$

which means f_{tr} is not visible in this experiment. Furthermore, we see that $A_{\text{adj}} \propto (1, 0, 0)^T (1, 1, 0)$, and hence that

$$\text{tr}\{A_{\text{adj}} M_{\text{adj}}^m\} = a_{\text{adj}} f_{\text{adj}}^m \quad (10.22)$$

for some real parameter a_{adj} .

To summarise, in the ED two-copy experiment we expect the data to take the functional form

$$p(m)_{\text{odd}} \approx b_{\text{tr}} + a_{\text{adj}} f_{\text{adj}}^m \quad (10.23)$$

which means the ED experiment leads, under mild assumptions on the noise channel and SPAM, to a standard single exponential decay with offset.

10.8. TWO-COPY RB IN PRACTICE

In the previous section we discussed the general functional form of the different types of 2CRB, and how the extracted decay rates relate to the fidelity. In this section we will discuss in more detail how to extract these decay rates and also how to interpret them. There are three problems to deal with here. The first is the question of extracting the decay rates from the data $p(m)$. In the

next subsection we will discuss how to deal with this problem. The second problem is that none of the three performed types of 2CRB give access to the decay rate f_4 . This means that even if we perform all three experiments on the same pair of qubits we can not evaluate that average fidelity directly. We can partially deal with this question by arguing that (which we do in section 10.8.1) if one has access to all other decay rates ($f_{\text{tr}}, f_3, f_{\text{adj}}, \lambda_{\text{adj}}, \bar{\lambda}_{\text{adj}}$) one can derive a very sharp lower bound on the average fidelity proper. This allows us to give rigorous lower bounds on the average fidelity in the case where both the ES and OS two-copy experiments were performed (see 10.5).

Finally we deal with the question of how to interpret the decay rates themselves in the scenario where no rigorous statement on the average fidelity can be given (i.e. for qubit pairs where only the ES or ED experiment have been performed).

10.8.1. LOWER BOUND ON AVERAGE FIDELITY

Here we will give a proof of the claim that we can give a lower bound on the average fidelity, despite not being sensitive to the decay f_4 from Equation 10.15. This follows from the complete positivity of the channel Λ . Concretely we assume we have access (through experiment), to the decay rates $f_{\text{tr}}, f_3, f_{\text{adj}}, \lambda_{\text{adj}}, \bar{\lambda}_{\text{adj}}$ (i.e. only f_4 is missing). We will argue that f_4 is sharply lower bounded by the average infidelity $r(\Lambda) = 1 - F_{\text{avg}}(\Lambda)$. Key to this is the following general lemma, which might be of broader interest.

Theorem 1. *Let P, Q be commuting n -qubit Pauli operators and consider for a quantum channel Λ the Pauli transfer matrix element $2^n \text{Tr}\{P\Lambda(Q)\}$. We have*

$$|\delta_{P,Q} - 2^{-n} \text{Tr}\{P\Lambda(Q)\}| \leq 2 \frac{2^n + 1}{2^n} r(\Lambda). \quad (10.24)$$

Proof. Since P, Q commute, they are diagonal in a joint basis $\{|x\rangle\}_{x \in \{0,1\}^n}$. Since the average fidelity is invariant under unitary conjugation we can, without loss of generality, take this basis to be the computational basis. Writing $P|x\rangle = p(x)|x\rangle$ and $Q|x\rangle = q(x)|x\rangle$ for the eigenvalues of P, Q and noting that $\text{Tr}\{|x\rangle\langle x| \Lambda(|\hat{x}\rangle\langle \hat{x}|)\} \in [0, 1]$

$$\text{Tr}\{P\Lambda(Q)\} = \sum_{x \in \{0,1\}^n} p(x)q(x) \text{Tr}\{|x\rangle\langle x| \Lambda(|x\rangle\langle x|)\} + \sum_{x \in \{0,1\}^n} \sum_{\hat{x} \in \{0,1\}^n, \hat{x} \neq x} p(x)q(\hat{x}) \text{Tr}\{|x\rangle\langle x| \Lambda(|\hat{x}\rangle\langle \hat{x}|)\} \quad (10.25)$$

We begin by bounding the second term. We have

$$\left| \sum_{x \in \{0,1\}^n} \sum_{\hat{x} \in \{0,1\}^n, \hat{x} \neq x} p(x)q(\hat{x}) \text{Tr}\{|x\rangle\langle x| \Lambda(|\hat{x}\rangle\langle \hat{x}|)\} \right| \leq \left| \sum_{\hat{x} \in \{0,1\}^n} \text{Tr}\{|\hat{x}\rangle\langle \hat{x}| \Lambda(|x\rangle\langle x|)\} \right| \quad (10.26)$$

$$= \sum_{\hat{x} \in \{0,1\}^n} (1 - \text{Tr}\{|x\rangle\langle x| \Lambda(|x\rangle\langle x|)\}), \quad (10.27)$$

where we used that $\sum_{\hat{x}} \text{Tr}\{|\hat{x}\rangle\langle \hat{x}| \Lambda(|x\rangle\langle x|)\} = 1$. We can bound this directly directly by using Theorem 1 from [36], which states that

$$\sum_{x \in \{0,1\}^n} (1 - \text{Tr}\{|x\rangle\langle x| \Lambda(|x\rangle\langle x|)\}) \leq (2^n + 1)r(\Lambda) \quad (10.28)$$

For the first term we have two cases. If $P = Q$ then $p(x) = q(x)$ and thus $p(x)q(x) = 1$, which means we can lower bound the first term by $2^n - (2^n + 1)r(\Lambda)$. On the other hand if $P \neq Q$ we know that there are exactly 2^{n-1} values of x s.t $p(x)q(x) = 1$ and 2^{n-1} values of x s.t $p(x)q(x) = -1$ (since P, Q

must now be trace orthogonal). Labeling these two sets X_1, X_{-1} we see that

$$\sum_{x \in \{0,1\}^n} p(x)q(x) \text{Tr}\{|x\rangle\langle x| \Lambda(|x\rangle\langle x|)\} = \sum_{x \in X_1} \text{Tr}\{|x\rangle\langle x| \Lambda(|x\rangle\langle x|)\} - \sum_{x \in X_{-1}} \text{Tr}\{|x\rangle\langle x| \Lambda(|x\rangle\langle x|)\} \quad (10.29)$$

$$= \sum_{x \in X_{-1}} (1 - \text{Tr}\{|x\rangle\langle x| \Lambda(|x\rangle\langle x|)\}) - \sum_{x \in X_1} (1 - \text{Tr}\{|x\rangle\langle x| \Lambda(|x\rangle\langle x|)\}) \quad (10.30)$$

$$\leq \sum_{x \in X_{-1}} (1 - \text{Tr}\{|x\rangle\langle x| \Lambda(|x\rangle\langle x|)\}) + \sum_{x \in X_1} (1 - \text{Tr}\{|x\rangle\langle x| \Lambda(|x\rangle\langle x|)\}) \quad (10.31)$$

$$\leq (2^n + 1)r(\Lambda) \quad (10.32)$$

Putting these two cases together we obtain the lemma statement. \square

With this lemma we can directly lower bound f_4 in terms of the average infidelity $r(\Lambda)$:

$$f_4 = \frac{1}{24} \left(\text{Tr}\{(XY + YX)\Lambda(XY + YX)\} + \text{Tr}\{(XZ + ZX)\Lambda(XZ + ZX)\} + \text{Tr}\{(ZY + YZ)\Lambda(ZY + YZ)\} \right) \quad (10.33)$$

$$\geq \frac{1}{6} \left(6(1 - \frac{5}{2}r(\Lambda)) - 6\frac{5}{2}r(\Lambda) \right) \quad (10.34)$$

$$\geq 1 - 5r(\Lambda) \quad (10.35)$$

And thus by equation 10.15 we see that

$$1 - \frac{4}{3}r(\Lambda) \geq \frac{1}{15} (f_{\text{tr}} + 2f_3 + 3(f_{\text{adj}} + \lambda_{\text{adj}} + \bar{\lambda}_{\text{adj}}) + 3 - 15r(\Lambda)) \quad (10.36)$$

which after a rearranging of terms gives

$$r(\Lambda) \leq 3 \left(1 - \frac{1}{15} (f_{\text{tr}} + 2f_3 + 3(f_{\text{adj}} + \lambda_{\text{adj}} + \bar{\lambda}_{\text{adj}}) + 3) \right). \quad (10.37)$$

Note that this bound is asymptotically accurate, in the sense that if $f_{\text{tr}} = f_2 = f_{\text{adj}} = \lambda_{\text{adj}} = 1$ then $r(\Lambda) = 0$.

10.8.2. SYMMETRIC AND ANTI-SYMMETRIC INPUT STATES FOR TWO-COPY RB

We perform ES 2CRB on systems Q1Q2 (a) and Q3Q4 (b) for symmetric $|\downarrow\downarrow\rangle$ and anti-symmetric $|\uparrow\downarrow\rangle$ input states. The resulting decays give us access to every eigenvalue required to estimate the average fidelity of the system, bar one. However, as shown in section 10.8.1, we can place a rigorous lower bound on the average fidelity using Equation 10.37, assuming we have experimental access to the remaining eigenvalues. Figures 10.5 a and b show 2CRB experiments on combined systems Q1Q2 and Q3Q4 respectively. In these experiments, we perform two-copy randomized benchmarking for a symmetric input state $|\downarrow\downarrow\rangle$ (Yellow trace in (a), Cyan trace in (b)) and an anti-symmetric input state $|\uparrow\downarrow\rangle$ (red in (a), blue in (b)). We find that fitting a single exponent with one real decay rate to the symmetric input traces is sufficient, while for the anti-symmetric case, we fit three exponentials comprising one real decay and two complex conjugate decays, that give us access to decay rates λ_{adj} and $\bar{\lambda}_{\text{adj}}$ from equation 10.15. In the case of the real decay rates, the form of the symmetric input states in equation 10.17 should access all real decay rates, while for the anti-symmetric case, there will be no contribution to the decay from f_{adj} . We also have no a-priori reason to know which decay is represented by which eigenvalue. However, by choosing the lower of the real decays for substitution into equation 10.37, we can be certain that we are lower

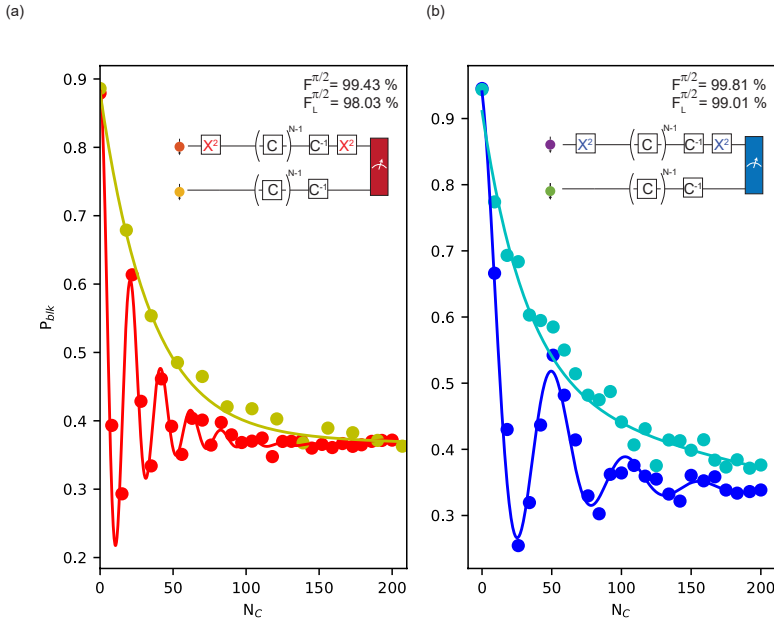


Figure 10.5: ES 2CRB of qubits Q1 and Q2 (a) and qubits Q3 and Q4 (b) at $B_{\text{ext}} = 0.65$ T for symmetric input state $|\uparrow\uparrow\rangle$ ((a),yellow and (b),cyan) and anti-symmetric input state $|\uparrow\downarrow\rangle$ ((a),red and (b),Blue). To prepare the antisymmetric space, we apply a X_π pulse to flip Q1(Q3) in the Q1Q2(Q3Q4) system before performing randomized benchmarking, then applying a second X_π pulse to the same qubit to project the final system back to the $|\uparrow\uparrow\rangle$ state. A rigorous lower bound on the fidelity $F_L^{\pi/2}$ can be obtained from the extracted decay rates of both symmetric and anti-symmetric experiments. The value $F^{\pi/2}$ represents the average native gate fidelity calculated using 10.15 assuming $f_4 = 0$.

bounding the fidelity. Tables 10.2 and 10.3 show the extracted decay rates for systems Q1Q2 and Q3Q4 respectively. By taking the lower of the real decays extracted from the symmetric and anti-symmetric starting state cases, we find lower bounds on the average fidelities of $F_{Q1Q2}^{\pi/2} \geq 98.03\%$ and $F_{Q3Q4}^{\pi/2} \geq 99.01\%$.

10.9. DIRECT COMPARISON OF TWO-COPY BENCHMARKING AND TWO-QUBIT SIMULTANEOUS RANDOMIZED BENCHMARKING

In this section we provide numerical evidence, beyond the formal bounds given above, that the decays numbers extracted from ES and ED 2CRB are representative of the average fidelity. We do this by directly comparing 2CRB (see section 10.7 to standard simultaneous randomized benchmarking (SRB) [20].

One drawback of SRB is the requirement that all Clifford gates are required to be identical in duration in order to avoid synchronization problems of simultaneous Clifford operations. In general these problems can be avoided by extending short Clifford gate sequences with an idling

Input State	Decay	Value
$ \downarrow\downarrow\rangle$	f_{tr}, f_{adj}, f_3	0.9722
$ \uparrow\downarrow\rangle$	f_{tr}, f_3	0.9798
$ \uparrow\downarrow\rangle$	λ_{adj}	0.9200+0.2779i
$ \uparrow\downarrow\rangle$	$\bar{\lambda}_{adj}$	0.9200-0.2779i

Table 10.2: Measured decay rates for system Q1Q2, for symmetric and anti-symmetric input states in the two-copy benchmarking experiment presented in Figure 10.5a.

Input State	Decay	Value
$ \downarrow\downarrow\rangle$	f_{tr}, f_{adj}, f_3	0.9709
$ \uparrow\downarrow\rangle$	f_{tr}, f_3	0.9770
$ \uparrow\downarrow\rangle$	λ_{adj}	0.9715+0.1110i
$ \uparrow\downarrow\rangle$	$\bar{\lambda}_{adj}$	0.9715-0.1110i

Table 10.3: Measured decay rates for system Q3Q4, for symmetric and anti-symmetric input states in the two-copy benchmarking experiment presented in Figure 10.5b.

time such that the duration of all Clifford gate sequences are equal. Fortunately, elementary gates based on single-qubit $\pi/2$ -microwave pulses with individual phase control allow the construction of all 24 single-qubit Clifford gates using two "real" and a up to two "virtual" Z-gates (see Ref. [3] and table 10.4). We use this compilation strategy for a direct comparison of 2CRB and standard SRB. For standard two-qubit SRB, random single-qubit Cliffords are chosen with the important caveat that each Clifford gate is chosen independently of the other qubit. We note here that the discussion regarding the simulation is independent of the Clifford compilation as derived above.

10.9.1. SIMULATION OF THE CLIFFORD GATE SUPEROPERATOR

In order to efficiently yet accurately simulate the two protocols, we first compute the full time-evolution superoperator for each combination of single-qubit Clifford gates on two qubits assuming quasistatic noise. Specifically, we solve the time-dependent Liouville–von Neumann equation for the density matrix ρ

$$i\hbar \frac{d}{dt} |\rho\rangle = [H(t)\rho - \rho H(t)], \quad (10.38)$$

where $\hbar = h/(2\pi)$ is the reduced Planck constant. Here, the system consisting of two germanium hole spin qubits is described by the Hamiltonian following [19, 37]

$$H(t) = \mu_B \mathbf{B}_1 \cdot \mathbf{S}_1 + \mu_B \mathbf{B}_2 \cdot \mathbf{S}_2 + \mathbf{S}_1 \cdot \mathcal{J} \mathbf{S}_2. \quad (10.39)$$

Here, \mathcal{J} is the tensorial form of the exchange interaction between qubits Q1 and Q2, μ_B is the Bohr magneton, h the Planck constant and $\mathbf{S}_j = (\sigma_x, \sigma_y, \sigma_z)^T/2$ is the vector consisting of the spin matrices acting on Qj. The effective magnetic field experienced by Qj is given by

$$\mathbf{B}_1 = (b_{Q1, f_{Q1}} \cos(2\pi f_{Q1} t + \phi_{Q1}) + b_{Q1, f_{Q2}} \cos(2\pi f_{Q2} t + \phi_{Q2}), 0, g_{Q1} B_z)^T \quad (10.40)$$

$$\mathbf{B}_2 = (b_{Q2, f_{Q1}} \cos(2\pi f_{Q1} t + \phi_{Q1}) + b_{Q2, f_{Q2}} \cos(2\pi f_{Q2} t + \phi_{Q2}), 0, g_{Q2} B_z)^T \quad (10.41)$$

which consists of the external magnetic field B_z multiplied by the in-plane g-factor g_{Qj} as well as contributions due to the spin-orbit interaction. Assuming an isotropic exchange interaction,

$\mathcal{J}_{jk} = J_{jk} \mathbb{1}_3$ and driving frequencies $f_{Qj} = \frac{\mu_B g_{Qj}}{h} B_z \gg J$ the dominating contribution of the exchange interaction is of the form $H_J = +\mathbf{S}_1 \cdot \mathcal{J} \mathbf{S}_2 \approx -\frac{J}{4} \mathbf{Z}\mathbf{Z}$ (see Ref. [38]). Single-qubit rotations are implemented via resonant driving $f_{Qj} = \frac{\mu_B g_{Qj}}{h} B_z$ with a Rabi frequency $\Omega_{Qj} = \frac{\mu_B}{2\hbar} b_{Qj, f_{Qj}}$. To utilize relevant parameters to the present experiment, we set $\Omega_{Q1} = \Omega_{Q2} = 10.6$ MHz. We simulate crosstalk such that each qubit is affected by both driving fields (one resonant and one is off-resonant) via the amplitudes $b_{Qj, f_{Q1}}$ and $b_{Qj, f_{Q2}}$. To simplify our simulations and maximize the crosstalk effect we set $b_{Qj, f_{Qk}} = 10.6$ MHz for $j, k = 1, 2$.

We solve Eq. (10.38) by iteratively computing the unitary propagator according to

$$U(t + \Delta t) = e^{-\frac{i}{\hbar} H(t + \Delta t)} U(t). \quad (10.42)$$

We discretize $H(t + \Delta t)$ into N segments of length Δt such that $H(t)$ is constant in the time-interval $[t, t + \Delta t]$. For all simulations, we choose $\Delta t = 10$ ps. Furthermore, we include quasistatic noise in the simulations by introducing classical fluctuations of $f_{Q1} \rightarrow f_{Q1} + \delta f_{Q1}$, $f_{Q2} \rightarrow f_{Q2} + \delta f_{Q2}$ which are assumed to be static on the time-scale of a single Clifford gate. The fluctuations follow a Gaussian distribution with mean $\mu = 0$, standard deviation $\sigma_{\delta f_{Qj}}$ and are estimated from the corresponding measured dephasing times $10.1 T_{2, Qj}^* = (2\sqrt{\pi} \sigma_{\delta f_{Qj}})^{-1}$ if not otherwise mentioned. To estimate the noisy density matrix we perform 250 noise implementations for each Clifford gate. In order to find the noisy superoperator, we repeat the simulations for a full basis set of initial density matrices ρ_{init} . The noisy superoperator is then constructed via the linear system

$$\begin{pmatrix} \rho_{\text{final}, 1} \\ \rho_{\text{final}, 2} \\ \vdots \\ \rho_{\text{final}, 16} \end{pmatrix} = \mathcal{L} \begin{pmatrix} \rho_{\text{init}, 1} \\ \rho_{\text{init}, 2} \\ \vdots \\ \rho_{\text{init}, 16} \end{pmatrix}, \quad (10.43)$$

where \mathcal{L} is the 16×16 -dimensional superoperator. The noisy superoperator in Liouville form is then constructed by transforming into the basis $\rho_1 = |0\rangle\langle 0|$, $\rho_2 = |0\rangle\langle 1|$, $\rho_3 = |0\rangle\langle 2|$, \dots , $\rho_{16} = |4\rangle\langle 4|$ following row ordering.

10.9.2. SIMULATION OF THE CLIFFORD EXPERIMENTS

With the superoperator in Liouville form of each Clifford gate, we can now model a randomized benchmarking experiment. We model each randomized benchmarking protocol using the following procedure.

1. Create a sequence of N -Cliffords chosen randomly on both qubits, and add the recovery Clifford to the sequence. For the standard two-qubit SRB protocol, Cliffords are picked at random and are uncorrelated between qubits. For the 2CRB protocol, the same Clifford is applied to both qubits. Repeat this K times.
2. Compute the final superoperator via multiplication of the corresponding two-qubit superoperator in Liouville form. This allows us to efficiently project onto the initialization and measurement at a later stage.
3. Chose an initial state and a measurement POVM to compute the expectation value for each sequence. Average over all K implementations.
4. Fit the final data.

10.9.3. COMPARISON BETWEEN THE RESULTS

Figures 10.6a,b and 10.6c,d show results for the simulated randomized benchmarking experiments for ES two-copy and simultaneous randomized benchmarking. It is clear from the study varying

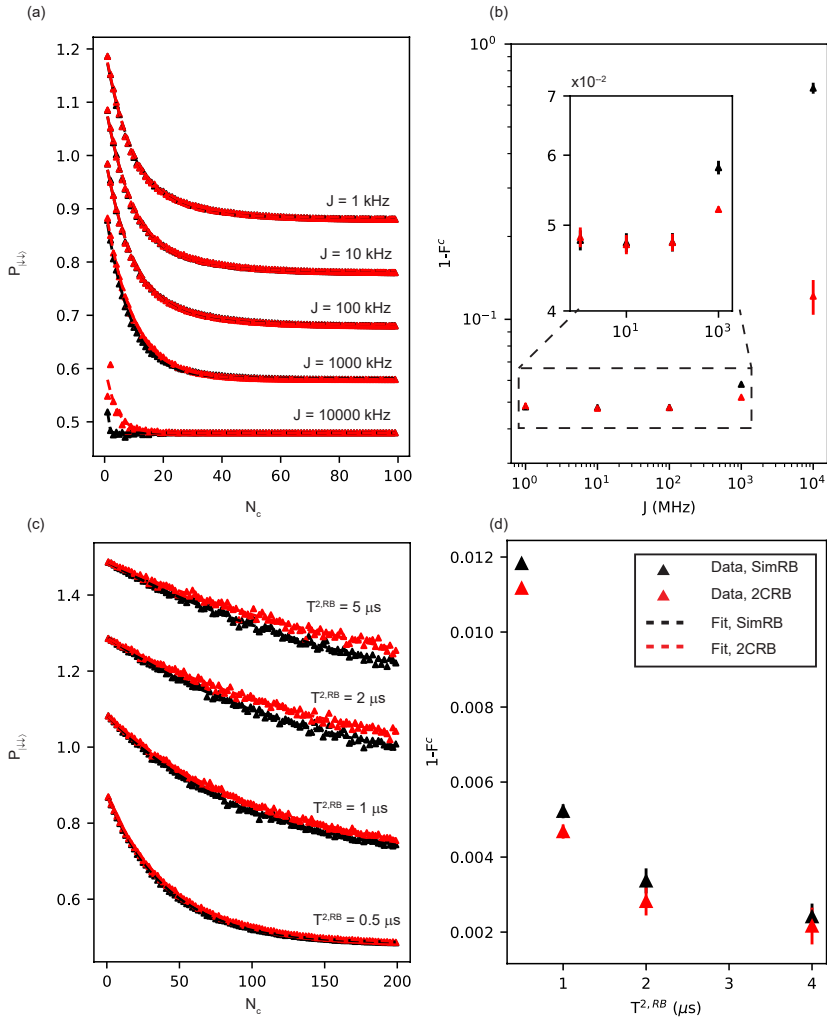


Figure 10.6: **Full Hamiltonian simulations comparing two-copy randomized benchmarking and simultaneous Randomized benchmarking.** (a) Effect of varying exchange for 2CRB (red) and SRB (black). Exchange is varied between 1 kHz and 10 MHz. For $J = 10$ MHz, single qubit gates become controlled rotations, resulting in a deviation from the characteristic decay form. (b) Summary of exponential fit Clifford fidelity for (a). For low values of J , 2QRB and SRB give fidelities within error bars of each other, while at higher J , 2CRB returns higher fidelities. (c) Effectively varying cross talk levels by changing the qubit dephasing times in the simulation, for $J = 260$ kHz, reflecting the expected residual exchange for qubit system Q1Q2. (d) Comparison of extracted Clifford fidelities for 2CRB and SRB at different dephasing times. While always returning slightly lower error rates, 2CRB appears to provide a good estimate of the average system fidelity.

classical cross talk noise via effective qubit coherence $T^{2, RB}$ in Figures 10.6c,d that ES 2CRB returns a higher fidelity than SRB as expected. However, in the limit of low exchange interaction, these fidelities can be very close, making ES 2CRB a good approximation to the fidelity of the system in our experiments.

Table 10.4: Single-qubit clifford compilation for a direct comparison between two-copy randomized benchmarking and simultaneous randomized benchmarking without idling times. We simulate both benchmarks by selecting a random sequence of Cliffords from the table below excluding C_1 , and calculate the recovery Clifford that projects the system back into it's original state. We use here a gate set containing $\pm\pi/2$ rotations around the Bloch Sphere, so the gates $X_{\pm\pi/2}$ and $Y_{\pm\pi/2}$ are referring to explicit rotations of $\pm\pi/2$ around the x-axis and y-axis of the Bloch sphere of a single-qubit. $Z_{\pm\pi/2}$ are rotations around the z-axis and implemented "virtually" via software correction of the signal generator. In this respect a $Y_{\pi/2}$ rotation is implemented identical to a $X_{\pi/2}$ rotation with a $\pi/2$ software phase correction.

Clifford	Composition
C_1	$X_{\pi/2}X_{-\pi/2}$
C_2	$X_{\pi/2}X_{\pi/2}$
C_3	$Y_{-\pi/2}Y_{-\pi/2}$
C_4	$X_{\pi/2}X_{-\pi/2}Z_{\pi/2}Z_{\pi/2}$
C_5	$X_{\pi/2}Y_{-\pi/2}$
C_6	$X_{\pi/2}Y_{\pi/2}$
C_7	$X_{-\pi/2}Y_{-\pi/2}$
C_8	$X_{-\pi/2}Y_{\pi/2}$
C_9	$Y_{-\pi/2}X_{\pi/2}$
C_{10}	$Y_{-\pi/2}X_{-\pi/2}$
C_{11}	$Y_{\pi/2}X_{\pi/2}$
C_{12}	$Y_{\pi/2}X_{-\pi/2}$
C_{13}	$Y_{-\pi/2}X_{\pi/2}Z_{-\pi/2}$
C_{14}	$Y_{-\pi/2}X_{-\pi/2}Z_{\pi/2}$
C_{15}	$X_{\pi/2}Y_{-\pi/2}Z_{\pi/2}$
C_{16}	$X_{\pi/2}Y_{\pi/2}Z_{-\pi/2}$
C_{17}	$X_{-\pi/2}X_{\pi/2}Z_{\pi/2}$
C_{18}	$X_{-\pi/2}X_{\pi/2}Z_{-\pi/2}$
C_{19}	$X_{\pi/2}Y_{-\pi/2}Z_{-\pi/2}$
C_{20}	$X_{\pi/2}Y_{\pi/2}Z_{\pi/2}$
C_{21}	$Y_{-\pi/2}X_{\pi/2}Z_{\pi/2}$
C_{22}	$Y_{-\pi/2}X_{-\pi/2}Z_{-\pi/2}$
C_{23}	$X_{\pi/2}X_{\pi/2}Z_{\pi/2}$
C_{24}	$X_{-\pi/2}X_{-\pi/2}Z_{-\pi/2}$

10.10. SUMMARY OF N -COPY BENCHMARKING DATA

Table 10.5: Extracted fidelities from figure 10.3a-b, a 2CRB experiment as well as single qubit RB and four qubit simultaneous driving error rates and leakage rates (when applicable) reported (in %). Qubits measured simultaneously in the same readout system (ES, see 10.7.2) have different measurement operators to those measured in different systems (DS), so the reported number is a combined system fidelity ($F_{Q1Q2} = F_{Q2Q1}$ and $F_{Q3Q4} = F_{Q4Q3}$ in the table). For this dataset, $t_\pi = 96$ ns. Leakage rates $L_{Q_i|Q_j}$ are reported in the case of single qubit RB or DS 2CRB when the decay plateau approaches the expected value of the fully depolarized two-qubit subspace, and are taken to be the longer of the two decay constants (see methods 10.4.3). The quoted errors correspond to the fitting error of the traces.

	Q1	Q2	Q3	Q4
1- F_{1Q}	0.0329 ± 0.0042	0.3155 ± 0.0310	0.0308 ± 0.0019	0.3224 ± 0.0446
L_{1Q}	-	-	-	0.0153 ± 0.0041
1- $F_{Q_i Q1}$	-	0.4018 ± 0.0130	0.0249 ± 0.0022	0.3087 ± 0.0690
1- $F_{Q_i Q2}$	0.4018 ± 0.0130	-	0.3791 ± 0.0300	0.4692 ± 0.0978
1- $F_{Q_i Q3}$	0.0301 ± 0.0048	0.3445 ± 0.0294	-	0.2778 ± 0.0298
1- $F_{Q_i Q4}$	0.2676 ± 0.0565	0.7324 ± 0.0388	0.2778 ± 0.0298	-
$L_{Q_i Q1}$	-	-	-	0.0175 ± 0.0065
$L_{Q_i Q2}$	-	-	0.0210 ± 0.0034	0.0741 ± 0.0213
$L_{Q_i Q3}$	-	0.0195 ± 0.0068	-	-
$L_{Q_i Q4}$	0.0273 ± 0.0092	-	-	-
1- F_{4Q}	9.8565 ± 0.9031		2.0007 ± 0.0428	

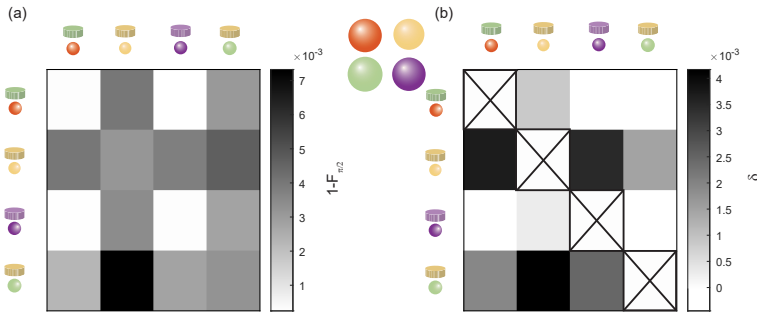


Figure 10.7: Table of infidelities and relative fidelity losses of the 2CRB experiment reported in Table 10.5 and Figure 10.3a-b. The plots can be interpreted by considering the qubit in question to be the column, and the qubit to be driven with to be the row. Qubits are represented diagrammatically by a coloured sphere, while the plunger gate from which they are driven is depicted above them by a coloured cylinder. (a) Absolute infidelity of the simultaneously driven qubits. Values on the diagonals represent the single-qubit fidelity in the non-simultaneously driven space. (b) relative fidelity loss δ of each qubit pair. Diagonals have no significance and are set to 0.

REFERENCES

- [1] Terhal, B. M. Quantum error correction for quantum memories. *Reviews of Modern Physics* **87**, 307–346 (2015).
- [2] Yoneda, J. *et al.* A quantum-dot spin qubit with coherence limited by charge noise and fidelity higher than 99.9%. *Nature Nanotechnology* **13**, 102–106 (2018).
- [3] Xue, X. *et al.* Benchmarking Gate Fidelities in a Si/SiGe Two-Qubit Device. *Physical Review X* **9**, 021011 (2019).
- [4] Vandersypen, L. M. K. *et al.* Interfacing spin qubits in quantum dots and donors—hot, dense, and coherent. *npj Quantum Information* **3**, 1–10 (2017).
- [5] Scappucci, G. *et al.* The germanium quantum information route. *Nature Reviews Materials* (2020).
- [6] Van Riggelen, F. *et al.* A two-dimensional array of single-hole quantum dots. *Applied Physics Letters* **118**, 44002 (2021).
- [7] Ansaloni, F. *et al.* Single-electron operations in a foundry-fabricated array of quantum dots. *Nature Communications* **11**, 1–7 (2020).
- [8] Fowler, A. G., Mariantoni, M., Martinis, J. M. & Cleland, A. N. Surface codes: Towards practical large-scale quantum computation. *Physical Review A - Atomic, Molecular, and Optical Physics* **86**, 032324 (2012).
- [9] Veldhorst, M. *et al.* A two-qubit logic gate in silicon. *Nature* **526**, 410–414 (2015).
- [10] Takeda, K. *et al.* Quantum tomography of an entangled three-spin state in silicon. *arXiv 2010.10316* (2020).
- [11] Sigillito, A. J. *et al.* Site-Selective Quantum Control in an Isotopically Enriched Si 28 /Si0.7Ge0.3 Quadruple Quantum Dot. *Physical Review Applied* **11**, 061006 (2019).
- [12] Watzinger, H. *et al.* Ge hole spin qubit. *Nature Communications* **9**, 1–6 (2018).
- [13] Hendrickx, N. W., Franke, D. P., Sammak, A., Scappucci, G. & Veldhorst, M. Fast two-qubit logic with holes in germanium. *Nature* **577**, 487–491 (2020).
- [14] Hendrickx, N. W. *et al.* A single-hole spin qubit. *Nature Communications* **11**, 1–6 (2020).
- [15] Lodari, M. *et al.* Low percolation density and charge noise with holes in germanium (2020). URL <https://doi.org/10.1088/2633-4356/abcd82>.
- [16] Sammak, A. *et al.* Shallow and Undoped Germanium Quantum Wells: A Playground for Spin and Hybrid Quantum Technology. *Advanced Functional Materials* **29**, 1807613 (2019).
- [17] Lawrie, W. I. *et al.* Spin Relaxation Benchmarks and Individual Qubit Addressability for Holes in Quantum Dots. *Nano Letters* **20**, 7237–7242 (2020).
- [18] Jirovec, D. *et al.* A singlet triplet hole spin qubit in planar Ge. *arXiv 2011.13755* (2020).
- [19] Hendrickx, N. W. *et al.* A four-qubit germanium quantum processor. *Nature* **591**, 580–585 (2021).

- [20] Gambetta, J. M. *et al.* Characterization of addressability by simultaneous randomized benchmarking. *Physical Review Letters* **109** (2012).
- [21] Lawrie, W. I. L. *et al.* Quantum Dot Arrays in Silicon and Germanium. *Applied Physics Letters* **116**, 080501 (2020).
- [22] Harvey-Collard, P. *et al.* High-Fidelity Single-Shot Readout for a Spin Qubit via an Enhanced Latching Mechanism. *Physical Review X* **8**, 021046 (2018).
- [23] Knill, E. *et al.* Randomized benchmarking of quantum gates. *Physical Review A - Atomic, Molecular, and Optical Physics* **77** (2008).
- [24] Cerfontaine, P. *et al.* Closed-loop control of a GaAs-based singlet-triplet spin qubit with 99.5% gate fidelity and low leakage. *Nature Communications* **11** (2020).
- [25] Wang, K. *et al.* Ultrafast Operations of a Hole Spin Qubit in Ge Quantum Dot. *arXiv 2006.12340* (2020).
- [26] Froning, F. N. *et al.* Ultrafast hole spin qubit with gate-tunable spin-orbit switch functionality. *Nature Nanotechnology* **16**, 308–312 (2021).
- [27] Crippa, A. *et al.* Electrical Spin Driving by g -Matrix Modulation in Spin-Orbit Qubits. *Physical Review Letters* **120**, 137702 (2018).
- [28] Scarlino, P. *et al.* Second-Harmonic Coherent Driving of a Spin Qubit in a Si/SiGe Quantum Dot. *Physical Review Letters* **115**, 106802 (2015).
- [29] Li, R. *et al.* A crossbar network for silicon quantum dot qubits. *Science Advances* **4**, 3960–3966 (2018).
- [30] Bulaev, D. V. & Loss, D. Electric dipole spin resonance for heavy holes in quantum dots. *Physical Review Letters* **98**, 097202 (2007).
- [31] Terrazos, L. A. *et al.* Theory of hole-spin qubits in strained germanium quantum dots. *Physical Review B* **103**, 125201 (2021).
- [32] Yang, C. H. *et al.* Silicon qubit fidelities approaching incoherent noise limits via pulse engineering. *Nature Electronics* **2**, 151–158 (2019).
- [33] Barends, R. *et al.* Superconducting quantum circuits at the surface code threshold for fault tolerance. *Nature* **508**, 500–503 (2014).
- [34] Liles, S. D. *et al.* Electrical control of the g -tensor of the first hole in a silicon MOS quantum dot. *arXiv 2012.04985* (2020).
- [35] Arute, F. *et al.* Quantum supremacy using a programmable superconducting processor. *Nature* **574**, 505–510 (2019).
- [36] Wallman, J. J. Bounding experimental quantum error rates relative to fault-tolerant thresholds (2015).
- [37] Hetényi, B., Kloeffel, C. & Loss, D. Exchange interaction of hole-spin qubits in double quantum dots in highly anisotropic semiconductors. *Phys. Rev. Research* **2**, 033036 (2020).
- [38] Meunier, T., Calado, V. E. & Vandersypen, L. M. K. Efficient controlled-phase gate for single-spin qubits in quantum dots. *Phys. Rev. B* **83**, 121403 (2011).

11

QUANTUM COHERENCE IN GERMANIUM HOLE SPIN QUBITS

"...and so do all who live to see such times. But that is not for them to decide. All we have to decide is what to do with the time that is given us."

Lord of the Rings: The Fellowship of the Ring

To operate a quantum computer, quantum information needs to be stored reliably [1]. This ability is compromised when qubits exchange energy with unaccounted for external systems. Quantum information loss can be quantified by two timescales: relaxation (T_1) and dephasing (T_2) rates of a spin state. For hole spin qubits in planar germanium (Ge/SiGe) [2], T_1 is not currently a limiting timescale, with relaxation rates exceeding 32 ms [3]. However, pure dephasing times (T_2^) have never exceeded a microsecond [4–6]. Here we study the magnetic field dependence of T_2^* for hole spin qubits between 0.1 T and 1 T. We find charge noise to be the dominant decohering process in this regime, and observe T_2^* as high as 1.9(1) μ s at low magnetic field, extendable to 504(10) μ s using refocussing techniques. Furthermore, we study the effect of the ^{73}Ge nuclear spin population, discovering that hole spin qubits in our device are sensitive to the nuclear spin bath. By developing a model to explain the decohering behaviour, we extract a nuclear quadrupole splitting for the ^{73}Ge nuclei of 4.17 kHz, and total hyperfine coupling strength of 34.4 kHz that we predict to limit spin dephasing times to $T_{2,\text{hf}}^* = 6.54 \mu$ s. These results simultaneously represent a milestone in achievable spin coherence in hole spin qubits, while also demonstrating their sensitivity to hyperfine coupling, providing concrete evidence of the necessity of isotopic purification.*

11.1. INTRODUCTION

Hole spin qubits in Ge/SiGe are leading candidates for quantum information processing [2]. Critical improvements in material growth [7], fabrication [8, 9] and tuning [10] have led to four-qubit quantum logic [4] and single qubit fidelities approaching 99.99% [11], marking the current state of the art for spin qubits in quantum dots. Hole spin qubits are attractive due to their strong spin-orbit interaction, facilitating a fast, all-electrical driving mechanism [12–14] that circumvents the requirement of microwave striplines or nanomagnets [15]. The implication of this relaxed requisite, alongside the low effective mass [16], absence of valley degeneracy, high material quality [17] and compatibility with existing complimentary semiconductor metal oxide technology, is that hole spin qubits in Ge/SiGe have an inherent scalability advantage over contemporary spin qubit platforms.

However, as with any mechanism that couples spin to charge, the spin-orbit interaction has consequences for coherence. The motion of charge present in all semiconductor devices can couple to the hole spin, resulting in dephasing. Furthermore, the effect of this noise becomes stronger at higher magnetic fields [12, 18], resulting in a trade-off between enhanced single qubit drive speeds and dephasing [11]. For hole spins in III-V heterostructure hosts however, nuclear spin dynamics dominate hole spin coherences up until very high magnetic fields [19, 20], and limit dephasing times to tens of ns [21, 22]. In contrast, since the concentration of spin-free isotopes in natural Ge is 92.24%, the decoherence due to nuclear spins is expected to be significantly weaker. Additionally, the hyperfine interaction of hole spins is highly anisotropic, resulting in an Ising-type coupling in the growth direction [23, 24]. Therefore, applying an in-plane magnetic field to break spin degeneracy strongly suppresses hyperfine interactions. This allows for lower magnetic field operation which reduces coupling to charge noise and increases coherence [6].

In the present work, we explore the quantum coherences of hole spin qubits defined in a Ge/SiGe heterostructure. We observe a clear inverse relationship between T_2^* and magnetic field strength, indicating that charge noise is limiting T_2^* . We measure unprecedented dephasing times for hole spin qubits of $T_2^* = 1.9(1) \mu\text{s}$ at the lowest magnetic field strength. We extend these coherences up to $T_2^{\text{CPMG}} = 504(10) \mu\text{s}$ using Carr-Purcell-Meiboom-Gill (CPMG) pulses. We also use CPMG pulse sequences as filter functions [25, 26], to sense the ^{73}Ge Lamor procession. Furthermore, a model is developed that characterizes the decohering behaviour, from which we estimate the hyperfine coupling strength as well as the nuclear quadrupolar splitting of the ^{73}Ge nuclear spin. An effective hyperfine limited dephasing time is estimated to be remarkably close to the longest measured T_2^* . This demonstrates the necessity of isotopic purification, marking a turning point for germanium hole spin qubits.

11.2. RESULTS

The device shown in Figure 11.1a is a 2x2 quantum dot array of heavy hole spin qubits (see section 11.4.1). We operate in the (1,1,1) charge state such that exactly one hole is present in each quantum dot. The charge state of the device is measured by monitoring the electrostatic potential using two radio-frequency single hole transistors (rf-SHT). Spin readout is performed via a spin-to-charge conversion technique based on Pauli spin blockade (PSB). Single-shot readout is performed by defining a threshold discriminating between the blocked and unblocked PSB readout signal detected by the rf-SHT (see section 11.4.3). The natural germanium quantum well (Fig. 11.1b) contains a 7.76% ^{73}Ge isotopic content, with nuclear spin number $I = 9/2$. Unlike electrons, hole wavefunctions confined within a quantum well are modulated by Bloch wavefunctions with p-type symmetry, which have nodes at nuclear sites. This results in a vanishing contact hyperfine interaction term. Additional hyperfine interactions arise from the dipole-dipole coupling between the hole spin (S) and nuclear spin (I), and from coupling between the hole angular mo-

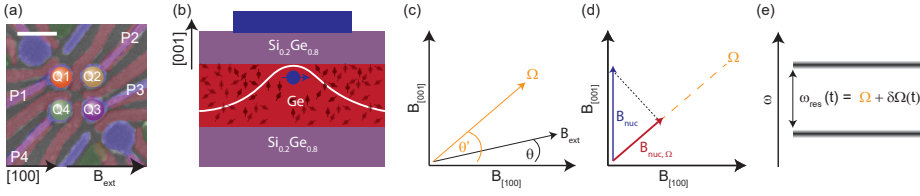


Figure 11.1: Device and hole spin noise mechanisms (a) False coloured scanning electron microscope image of the device used in this study. Plungers P1-P4 (blue) tune the potential such that there is a single hole occupying each quantum dot, Each hole constitutes a qubit, labelled Q1 (orange), Q2 (yellow) Q3 (purple) and Q4 (green). Scale is 100 nm. (b) Cross sectional sketch of the heterostructure. The blue rectangle represents a plunger gate, above a purple $\text{Si}_{0.2}\text{Ge}_{0.8}$ spacer layer. The red region indicates the Ge quantum well. A potential well created by applying a negative voltage to the plunger gate traps a single hole spin (blue). Ge in its natural form contains 7.76 % abundance of non-zero nuclear spins. (c) Schematic (not to scale) illustrating the effect of an out-of-plane misalignment of the magnetic field B_{ext} of angle θ . An angle θ' represents an effective misalignment angle, reflecting the large anisotropy of the g -factor. Ω represents the effective quantization axis due to the misaligned magnetic field. (d) Fluctuations of the Overhauser field B_{nuc} give rise to Zeeman noise via the projection of the out-of-plane component $B_{\text{nuc},\perp}$ onto Ω , $B_{\text{nuc},\Omega}$. (e) Electric field fluctuations due to local charge noise couples to the g -tensor via the spin-orbit interaction.

mentum (L) and I . Furthermore, random flip-flop events between nuclei lead to a fluctuating Overhauser field B_{nuc} experienced by the hole spin [27]. A magnetic field B_{ext} applied in the plane of the quantum well yields qubit g -factors of 0.16, 0.22, 0.22, 0.24 for qubits Q1-Q4 respectively (See section 11.5.1). We allow for an angle θ describing an out-of-plane misalignment in the magnetic field, resulting in two important consequences. First, the effective quantization axis of the qubit is no longer purely in plane. Secondly, due to the anisotropies of the hyperfine coupling and the g -tensor [14], small values of θ' result in enhanced hyperfine interaction strengths. We define an effective misalignment angle $\theta' = \arctan(g_{\perp}/g_{\parallel}) \tan(\theta)$ resulting in an effective quantization axis $\hat{\Omega} = (\sin \theta', 0, \cos \theta')$. The spin orbit interaction also facilitates a coupling of the g -factor of the hole spin and electrical noise, which can induce Zeeman noise by displacing or distorting the wavefunction of the qubit (Fig. 11.1e) [28]. The effect of these noise sources on the quantum coherence of hole spin qubits is studied in the following sections.

11.2.1. QUANTUM COHERENCES

We characterize the magnetic field dependence of the dephasing rates of the four hole spin qubits in our device. To extract T_2^* , we apply a $X_{\pi/2}$ -pulse, wait for a time τ , and finally apply a second $X_{-\pi/2}$ -pulse, resulting in a decay characterized by a time T_2^* . Figure 11.2a-d shows the extracted values of T_2^* as a function of magnetic field strength B_{ext} between 0.1 T and 1 T. We observe a clear $T_2^* \propto 1/B_{\text{ext}}$ dependence of the dephasing time. The longest $T_2^* = 1.9(1) \mu\text{s}$ is extracted at $B_{\text{ext}} = 0.1$ T for qubit Q3. This behaviour is consistent with the expectation that at larger magnetic fields, the dephasing is dominated by charge noise [12, 18]. Since the g -tensor of hole qubits depends strongly on electric fields [5, 29], and that charge noise primarily couples to the qubit via its electric field gradient, we deduce that charge noise is the dominant decohering mechanism for $B_{\text{ext}} > 0.1$ T.

The $1/f$ dependence of the charge noise spectral density permits the use of CPMG pulse sequences to extend the quantum coherence of the qubits. In such a sequence, a qubit is prepared in the spin down state, then brought to the equator of the Bloch sphere by applying a $X_{\pi/2}$ pulse. In this superposition state, the qubit will undergo random phase jumps as a result of environmental noise, and gradually lose phase coherence. This can be observed by waiting a time t , before projecting

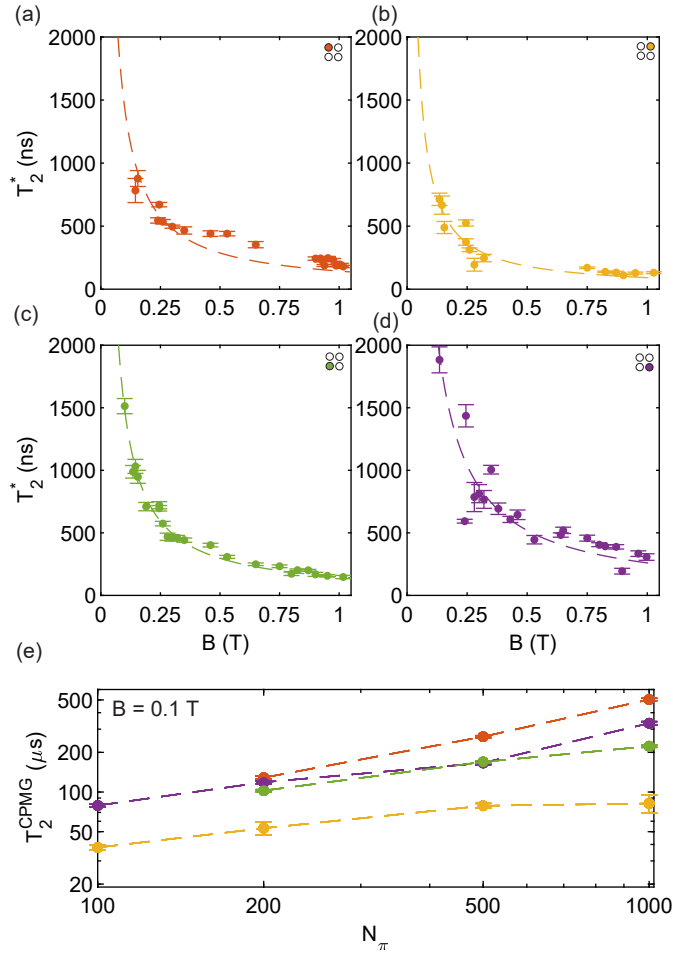


Figure 11.2: **Quantum Coherence of hole spin qubits in a 2x2 array as a function of magnetic field.** (a-d) Ramsey pulse sequences are applied to each qubit Q1 (red), Q2 (yellow) Q3 (purple) and Q4 (green) at magnetic fields between $B_{\text{ext}} = 0.1$ T and $B_{\text{ext}} = 1$ T. Each qubit shows a $T_2^* \propto 1/B$ dependence. Long dephasing times of $T_2^* = 1.9(1) \mu\text{s}$ are observed for qubit Q3 at a field of $B_{\text{ext}} = 0.135$ T. (e) Extending quantum coherence using a CPMG pulse sequence at external magnetic field strength $B_{\text{ext}} = 0.1$ T. Visibility after $N_\pi = 1000$ refocusing pulses vanishes, however coherence can be extended to $T_2^{\text{CPMG}} = 504(10) \mu\text{s}$ for qubit Q3. Error bars correspond to the 95% confidence intervals of the individual fits.

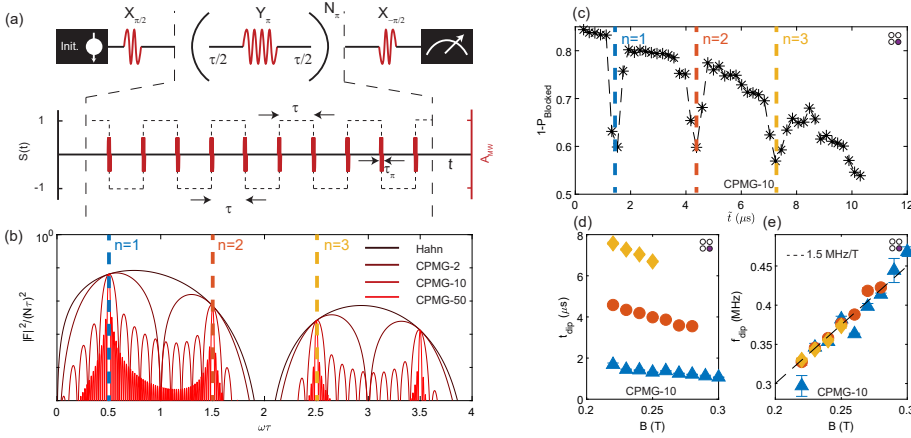


Figure 11.3: **Probing the ^{73}Ge nuclear spin precession using CPMG- N_π filter functions** (a) CPMG- N_π pulse sequence. A qubit is initialized in the spin down state, then brought to the cardinal +y axis of the Bloch sphere by applying a resonant $X_{\pi/2}$ pulse. Spin and charge Noise cause the qubit to gradually lose phase coherence. For quasi-static noise, the application of a Y_π pulse will invert the polarity $s(t)$ of the noise acting on the qubit, resulting in a recovery of phase coherence at a time $\tau/2$. Subsequent applications of a Y_π pulse will further increase the coherence of the qubit. A final $X_{-\pi/2}$ brings the qubit back to the spin down state. (b) CPMG- N_π transmission functions for various N_π . $|F|^2/(N_\pi\tau)^2$ for a single (Hahn echo), 2, 10 and 50 applied refocusing pulses is shown. Transmission maxima appear at $\omega\tau = (2n-1)/2$ for harmonic n . The first three harmonic positions are shown by dashed blue ($n=1$), orange ($n=2$) and yellow ($n=3$) lines. (c) An exemplary trace, showing the decay of qubit coherence for Q3 undergoing a CPMG-10 refocussing pulse sequence at $B_{\text{ext}} = 0.23$ T. Clear dips in coherence are seen in the measured probability of a blocked state $1-P_{\text{Blocked}}$, as marked by blue, red and yellow dashed lines. The frequencies corresponding to these dips are the first three harmonics of the ^{73}Ge nuclear spin precession frequency respectively. The temporal axis is defined $\tilde{t} = \tau + \tau_\pi$, where the Rabi period of the qubit is taken into account. (d) Magnetic field dependence on the temporal occurrence of each peak. (e) Corresponding frequency of each peak in (d), converted via the relation $f_{\text{dip}} = (2n-1)/2t_{\text{dip}}$ where $n = 1, 2, 3$ correspond to the principle, first and second harmonics respectively. The dotted line is the expected Larmor precession frequency of ^{73}Ge , $\gamma_{^{73}\text{Ge}} = 1.5$ MHz/T.

its state back onto the z-axis of the Bloch sphere by applying a $-\pi/2_X$ pulse. If the noise is quasi-static over a time period $t > \tau$, the effect can be effectively reversed by inserting a Y_π pulse between two time intervals of length $\tau/2$. This technique reverses the parity $s(t) \in \{-1, 1\}$ of the noise acting on the qubit, resulting in a phase coherent echo at time $t = \tau$. By increasing the number of Y_π pulses inserted into the total time window, the frequency spectrum of noise that is corrected for extends to higher frequencies, improving coherence. Figure 11.2e shows the dependence of quantum coherence on the number of refocusing pulses N_π at $B_{\text{ext}} = 0.1$ T. We achieve a record quantum coherence of $T_2^{\text{CPMG}} = 504(10)$ at $N_\pi = 1000$. Decaying visibility due to pulse imperfections, sample heating and decoherence during finite pulse times prevent us from measuring pulse sequences at larger N_π . Note that our data does not show a clear saturation of T_2^{CPMG} , indicating that longer coherence times are possible.

11.2.2. PROBING THE ^{73}Ge LARMOR PRESSION

Unlike electrons, the hyperfine interaction experienced by hole spins is highly anisotropic. The dipole-dipole interaction has a strong out-of-plane contribution A^\perp , and couples weakly in-plane A^\parallel [23]. A combination of density functional and $\mathbf{k} \cdot \mathbf{p}$ theory proves an Ising-type ($A^\parallel/A^\perp =$

−0.018) hyperfine interaction between the heavy hole qubit states and ^{73}Ge nuclear spins in a planar Ge/SiGe heterostructure [30]. Therefore, application of an in-plane magnetic field of modest strength should almost entirely suppress the hyperfine interaction. In order to investigate whether hole spin qubits are sensitive to the 7.73% ^{73}Ge population in the quantum well, we employ the CPMG- N_π sequence for frequency selective sensing. A CPMG- N_π pulse sequence (Fig. 11.3a) has a characteristic filter function $F(N_\pi, \omega\tau)$ given by [31]

$$F(N_\pi, \omega\tau) = \frac{8}{\pi\omega^2} \sin^4(\omega\tau/4) \frac{\sin^2(N_\pi\omega\tau/2)}{\cos^2(\omega\tau/2)} \quad (11.1)$$

where N_π is the number of refocusing pulses, and τ is the wait time between each pulse. Transmission maxima occur at frequencies

$$\omega = \frac{2n-1}{2\tau} \quad (11.2)$$

for integer n , making it possible to enhance sensitivity to an arbitrary frequency of noise. Figure 11.3b shows traces of the filter functions of several CPMG pulse sequences. Rapid dephasing of qubit coherence is expected when $\tau = (2n-1)/2\omega$ in the presence of a noise source with frequency ω . Figure 11.3c shows the coherence of qubit Q3 at $B_{\text{ext}} = 0.23$ T, using a CPMG-10 pulse sequence. Clear dips are visible in the data, corresponding to coherence loss at specific frequencies. By sweeping the magnetic field between $B_{\text{ext}} = 0.2$ and $B_{\text{ext}} = 0.3$ T, we track the shifting temporal position of these dips t_{dip} (Fig. 11.3d) and convert them to a frequency f_{dip} using Eq. 11.2. We fit for $n = 1, 2, 3$, depicted by blue triangle, red circle and yellow diamond markers, corresponding to the respective principle, first and second harmonics of the noise source (Fig. 11.3e). These data follow the Larmor precession frequency of the ^{73}Ge nuclear spin $\gamma_{^{73}\text{Ge}} = 1.5$ MHz/T, as represented by the black dashed line. We also confirm using a different qubit, and at a magnetic field strengths of up to 1 T, these harmonics still follow the same 1.5 MHz/T dependence (See Fig. 11.6). This suggests that the hole spin qubit coherence is affected by interactions with the nuclear spin bath, and motivates further investigation into the extent of these interactions.

11.2.3. SPIN DEPHASING DUE TO HYPERFINE NOISE

Isotopic purification has led to significant improvements in qubit metrics for silicon based electron spin qubits. For hole spin qubits in Ge/SiGe, it is unclear whether the dephasing effects of the nuclear spin bath are large enough to warrant isotopic purification. We therefore aim to quantify the expected dephasing time of hole spin qubits due to hyperfine noise in natural germanium quantum wells. The dephasing of a hole spin due to a noise spectral density $S(\omega)$, while undergoing a CPMG- N_π refocussing pulse sequence, is given by

$$C(N_\pi\tau) = \exp\left(-\int_{-\infty}^{\infty} d\omega \frac{S(\omega)}{\omega^2} F(N_\pi, \omega\tau)\right) \quad (11.3)$$

where $S(\omega)$ is the spectral density of the noise and $F(N_\pi, \omega\tau)$ is the filter function of a CPMG- N_π sequence described in Eq. 11.1. The spectral density can be divided up into two contributions $S(\omega) = S_{\delta\Omega}(\omega) + S_{hf}(\omega)$. The first term describes spectral diffusion of the hole spin, due to fluctuations in the Overhauser field as well as spin-orbit induced effects due to charge noise. We model this using an Ornstein-Uhlenbeck type process with characteristic fluctuation time constant τ_c , and interaction strength $\Delta\Omega$. We obtain a spectral density by evaluating

$$S_{\delta\Omega}(\omega) = \int \frac{dt}{2\pi} \langle \langle \delta\Omega(t) \delta\Omega \rangle \rangle. \quad (11.4)$$

$S_{hf}(\omega)$ represents the spectral contribution to $S(\omega)$ of hyperfine effects between the hole spin and the nuclear spin bath, defined to be

$$S_{hf}(\omega) = \int \frac{dt}{2\pi} e^{-i\omega t} \langle \{ \hat{h}_{\text{nuc}}(t), \hat{h}_{\text{nuc}} \} \rangle. \quad (11.5)$$

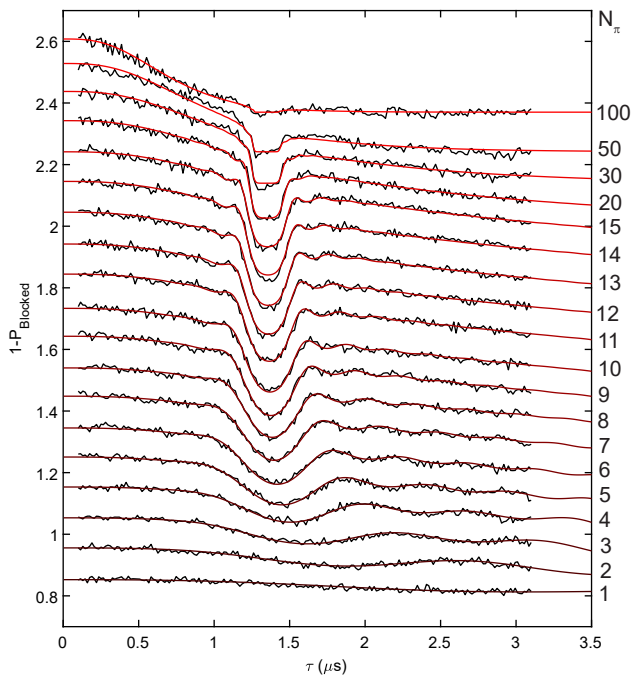


Figure 11.4: **Studying the hyperfine interaction induced dephasing time of a hole spin qubit.** (a) CPMG- N_π traces at $B_{\text{ext}} = 0.25$ T for qubit Q3 where N_π ranges from 1-15, 20, 30, 50 and 100 refocussing pulses. The data are offset for clarity.

Here, $\hat{h}_{\text{nuc}}(t) = \exp\{iH_{\text{nuc}}t\}\hat{h}_{\text{nuc}}\exp\{-iH_{\text{nuc}}t\}$ defines the time evolution of the transverse nuclear operator

$$\hat{h}_{\text{nuc}} = \sum_k \omega_k^\perp \cdot I_k \quad (11.6)$$

according to a nuclear spin hamiltonian

$$H_{\text{nuc}} = -\sum_k \omega_I I_k^Z + \frac{\omega_Q}{2} \sum_k (I_k^Z)^2 \quad (11.7)$$

where $\omega_I = \gamma_{73\text{Ge}}B_{\text{ext}}$, I_k^Z is the projection of the spin of the k 'th nucleus on the axis of B_{ext} , and ω_Q is the quadrupolar interaction strength. The term $\omega_k^\perp = \left(A_k^\perp \sin\delta\theta' \cos\delta\theta - A_k^\parallel \cos\delta\theta' \sin\delta\theta, A_k^\parallel\right)$, defines the hyperfine coupling strength of the k 'th nuclear spin perpendicular to the applied magnetic field, allowing for an out of plane misalignment angle θ of B_{ext} with respect to the plane of the quantum well. Evaluating Eq. 11.5 gives a spectral density contribution of the nuclear spin bath, parameterized by a hyperfine interaction strength σ_\perp and a quadrupolar interaction strength ω_Q . Figure 11.4 depicts CPMG- N_π pulse sequences at magnetic field $B_{\text{ext}} = 0.25$ T performed on qubit Q3, for varying N_π . The coherence dip due to interactions with the nuclear spin bath becomes more pronounced as $F(N_\pi\tau)$ becomes sharper around the ^{73}Ge precession frequency and the total time $N\tau$ spent sensitive to that frequency increases. Simultaneously fitting each trace (see section 11.4.2) assuming zero nuclear polarization, we extract $\tau_c = 292$ ns, $\Delta\Omega/2\pi = 54.4$ kHz, $\omega_Q/2\pi = 4.17$ kHz and $\sigma_\perp/2\pi = 34.4$ kHz.

The generality of our model prevents us from drawing strong conclusions about the quasi-static noise contributions to $\Delta\Omega/2\pi$, since it encompasses the combined effect of two decohering processes. These are Overhauser field fluctuations and g -tensor variations due to the presence of charge noise. Overhauser fields are expected to be weak in Ge/SiGe due to nuclear freezing effects that suppress nuclear flip-flop interactions [32], the low isotopic concentration of ^{73}Ge , and as discussed, is not believed to be the dominant source of noise down to magnetic field strengths of 0.1 T. Therefore it is likely this term primarily represents a charge noise dominated decohering effect on our system. The extracted quadrupole strength $\omega_Q/2\pi$ is higher than the measured bulk value of ~ 100 Hz [33], but significant increases in quadrupolar splitting of up to 26.9 kHz have been observed in strained ^{75}As nuclei in GaAs [34]. For magnetic fields in the limit of zero motional averaging $\gamma_{73\text{Ge}}B_{\text{ext}}T_2^* < 1$, the off-diagonal term $\sigma_\perp/2\pi$ will directly determine $T_{2,\text{hf}}^* \approx \sqrt{2}/\sigma_\perp = 6.54 \mu\text{s}$, which is very close to the measured value of $T_2^* = 1.03 \mu\text{s}$. We also note that the Zeeman noise strength $\Delta\Omega/2\pi$ is only marginally stronger. Additionally, by modelling the quantum dot as a cylindrical potential of radius 40 nm and depth 7 nm, we can estimate the out-of-plane misalignment angle to be $\theta = 0.09$. This relatively small value is a plausible misalignment within our experimental setup, and suggests that achieving the expected hyperfine suppression of an in-plane magnetic field is challenging in practice.

11.3. CONCLUSION

We have investigated the coherence of hole spin qubits defined in planar germanium. Dephasing is likely dominated by charge noise at magnetic field strengths $0.1 \text{ T} < B_{\text{ext}} < 1 \text{ T}$. At low field strength, dephasing timescales up to $1.9(1) \mu\text{s}$ are measured, extendable to $504(10) \mu\text{s}$ using dynamical decoupling techniques. We observed dephasing of hole spin qubits due to hyperfine coupling with the residual non-zero nuclear spin isotope ^{73}Ge . We developed a theoretical model of dephasing due to the effects of the nuclear spin bath on hole spin coherence, allowing for a small out-of-plane misalignment angle of the magnetic field to the quantum well. By simultaneously fitting coherence decays for hole spin qubits undergoing CPMG pulse sequences, we extract a pure hyperfine dephasing time $T_{2,\text{hf}}^* = 6.54 \mu\text{s}$ comparable to the charge noise limited value at the same

field. These findings constitute a novel and powerful tool for analysing nuclear spin noise mechanisms in quantum dot spin qubits, while also representing state-of-the-art coherence times for hole spin qubits. We envision that given the current rate of material improvement in planar germanium heterostructures, isotopic purification of the quantum well will further enhance quantum coherence metrics, positioning hole spins in planar germanium as a strong contender for future quantum technologies.

11.4. METHODS

11.4.1. DEVICE FABRICATION

The Ge/SiGe wafer is fabricated on a silicon substrate. We use reduced-pressure chemical vapour deposition to grow a 1.6 μm strain-relaxed Ge layer, a 1 μm reverse graded $\text{Si}_{1-x}\text{Ge}_x$ (x varies from 1 to 0.8), a 500 nm constant composition $\text{Si}_{0.2}\text{Ge}_{0.8}$, and a 16 nm compressively strained Ge quantum well. Finally on the quantum well we grow a 55 nm $\text{Si}_{0.2}\text{Ge}_{0.8}$ barrier followed by an oxidised Si cap layer (<2 nm) [7]. An ohmic contact layer is created by first defining it using electron beam lithography, etching away the oxidised cap, then depositing 30 nm of Al. This layer is then covered in 7 nm of Al_2O_3 via atomic layer deposition at 300 $^\circ\text{C}$. The gate stack is in two overlapping layers of Ti:Pd (3/37 nm), separated by 7 nm of Al_2O_3 [8].

11.4.2. FITTING METHODS

Ramsey sequences are fit to a sinusoid modulated by a decay envelope, of the form $P_{\text{Blocked}} = A \sin(2\pi f\tau + \phi) \exp\{-(\tau)^\alpha / T^{2*}\}$. CPMG- $N\pi$ decays are fit to an exponential decay function $P_{\text{Blocked}} = A \exp\{-(\tau)^\alpha / T^{2, \text{CPMG}}\}$. Coherence dips in figure 11.3c are fit to a function of the form $f = a \exp\left(-(\bar{\tau} - t_{\text{dip}})^2 / 2c\right) + d\bar{\tau} + e$ in the vicinity of each dip, yielding dip position t_{dip} and width $2c$ used as the error bars. Some data is post processed to aid fitting. Traces in figure 11.4 are fit to a general coherence function

$$P(\tau) = \beta + (P_0 - \beta) \exp\left[-\int_0^\tau d\omega \frac{S(\omega)}{\omega^2} F(N\pi, \omega\tau)\right] \quad (11.8)$$

where β is the measurement bias, $P_0 = P(0)$, and $S(\omega)$ is parameterized by $\Delta\Omega$, τ_c , ω_Q and σ_\perp as discussed in the main text. For each, β and P_0 are fit individually since these parameters can vary between experiment, while the parameters characterizing the noise spectral density are fit simultaneously to the set of traces.

11.4.3. READOUT

One ohmic lead of each charge sensor is connected in-line to a custom-fabricated niobium-titanium-nitride (NbTiN) kinetic inductor with expected inductance of $L = 2 \mu\text{H}$. The other lead is bonded to a DC-line that is grounded at room temperature. The parasitic capacitance of each charge sensor results in a tank circuit with resonant frequencies of $f = 147.3$ MHz and $f = 139.9$ MHz. Deviations in the reflected probe tone at these frequencies due to variations in sensor resistance provide a fast method for reading out the charge state of the capacitively coupled quantum dots.

Spin-to-charge conversion is achieved using a latched Pauli spin blockade method described in [4, 11].

11.5. EXTENDED DATA

11.5.1. HOLE SPIN QUBIT G-FACTORS

Figure 11.5a shows the measured values of qubit resonance frequency f as a function of applied magnetic field B between 0.1 T and 1 T. Figure 11.5b shows the extracted g -factors of each qubit from a linear fit.

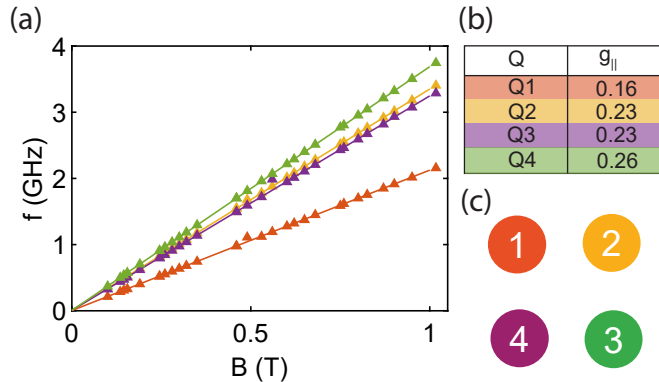


Figure 11.5: **Qubit resonance frequencies.** (a) Qubit resonance frequencies as a function of a magnetic field sweep between 0.1 T and 1 T. (b) Table of extracted in-plane qubit g -factors from a linear fit to (a). (c) Qubit schematic indicating placement and colour labelling.

11.5.2. OBSERVATION OF ^{73}Ge LAMOR PRECESSION AT HIGH FIELD

Additional experiments were performed on qubit Q1 at magnetic fields between 0.9 T and 1 T. Figure 11.6a shows the fitted values of t_{peak} at which coherence drops were measured using CPMG-50 pulse sequences. Figure 11.6b shows the converted frequency values, lying on the expected Lamor precession frequency of ^{73}Ge .

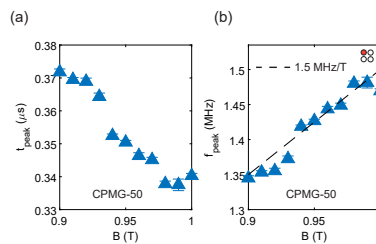


Figure 11.6: **Observation of Lamor precession at higher field strength.** (a) CPMG-50 pulse sequences applied to qubit Q1 result in coherence dips around at the wait time t_{peak} as a function of magnetic field strength between 0.9 T and 1.0 T. (b) Conversion to frequency indicates these coherence dips occur at the Lamor precession frequency of ^{73}Ge nuclear spins.

REFERENCES

- [1] DiVincenzo, D. P. The physical implementation of quantum computation. *Fortschritte der Physik* **48**, 771–783 (2000).
- [2] Scappucci, G. *et al.* The germanium quantum information route. *Nature Reviews Materials* (2020).
- [3] Lawrie, W. I. *et al.* Spin Relaxation Benchmarks and Individual Qubit Addressability for Holes in Quantum Dots. *Nano Letters* **20**, 7237–7242 (2020).
- [4] Hendrickx, N. W. *et al.* A four-qubit germanium quantum processor. *Nature* **591**, 580–585 (2020).
- [5] Hendrickx, N. W. *et al.* A single-hole spin qubit. *Nature Communications* **11**, 1–6 (2020).
- [6] Jirovec, D. *et al.* A singlet triplet hole spin qubit in planar Ge. *arXiv 2011.13755* (2020).
- [7] Lodari, M. *et al.* Low percolation density and charge noise with holes in germanium. *Materials for Quantum Technology* **1**, 011002 (2020).
- [8] Lawrie, W. I. L. *et al.* Quantum Dot Arrays in Silicon and Germanium. *Applied Physics Letters* **116**, 080501 (2020).
- [9] Hendrickx, N. W. *et al.* Gate-controlled quantum dots and superconductivity in planar germanium. *Nature Communications* **9**, 1–7 (2018).
- [10] Van Riggelen, F. *et al.* A two-dimensional array of single-hole quantum dots. *Applied Physics Letters* **118**, 44002 (2021).
- [11] Lawrie, W. I. L. *et al.* Simultaneous driving of semiconductor spin qubits at the fault-tolerant threshold. *arXiv:2109.07837 [cond-mat.mes-hall]* (2021).
- [12] Bulaev, D. V. & Loss, D. Electric dipole spin resonance for heavy holes in quantum dots. *Physical Review Letters* **98**, 097202 (2007).
- [13] Hendrickx, N. W., Franke, D. P., Sammak, A., Scappucci, G. & Veldhorst, M. Fast two-qubit logic with holes in germanium. *Nature* **577**, 487–491 (2020).
- [14] Watzinger, H. *et al.* Heavy-Hole States in Germanium Hut Wires. *Nano Letters* **16**, 6879–6885 (2016).
- [15] Vandersypen, L. M. K. *et al.* Interfacing spin qubits in quantum dots and donors—hot, dense, and coherent. *npj Quantum Information* **3**, 1–10 (2017).
- [16] Lodari, M. *et al.* Light effective hole mass in undoped Ge/SiGe quantum wells. *Physical Review B* **100**, 041304 (2019).
- [17] Sammak, A. *et al.* Shallow and Undoped Germanium Quantum Wells: A Playground for Spin and Hybrid Quantum Technology. *Advanced Functional Materials* **29**, 1807613 (2019).
- [18] Wang, X. J., Chesni, S. & Coish, W. A. Spin-echo dynamics of a heavy hole in a quantum dot. *Phys. Rev. Lett.* **109** (2012).
- [19] Stockill, R. *et al.* Quantum dot spin coherence governed by a strained nuclear environment. *Nature Communications* **7** (2016).

- [20] Huthmacher, L. *et al.* Coherence of a dynamically decoupled quantum-dot hole spin. *Physical Review B* **97**, 241413 (2018).
- [21] Petta, J. R. *et al.* Applied physics: Coherent manipulation of coupled electron spins in semiconductor quantum dots. *Science* **309**, 2180–2184 (2005).
- [22] Chekhovich, E. A. *et al.* Nuclear spin effects in semiconductor quantum dots. *Nature Materials* **12**, 494–504 (2013).
- [23] Philippopoulos, P., Chesi, S. & Coish, W. A. First-principles hyperfine tensors for electrons and holes in GaAs and silicon. *Physical Review B* **101**, 115302 (2020).
- [24] Fischer, J., Coish, W. A., Bulaev, D. V. & Loss, D. Spin decoherence of a heavy hole coupled to nuclear spins in a quantum dot. *Physical Review B* **78**, 155329 (2008).
- [25] Malinowski, F. K. *et al.* Notch filtering the nuclear environment of a spin qubit. *Nature Nanotechnology* **12**, 16–20 (2017).
- [26] Kerckhoff, J. *et al.* Magnetic Gradient Fluctuations from Quadrupolar ^{73}Ge in Si / Si Ge Exchange-Only Qubits. *PRX Quantum* **2**, 10347 (2021).
- [27] Coish, W. A. & Baugh, J. Nuclear spins in nanostructures. *Physica Status Solidi (B) Basic Research* **246**, 2203–2215 (2009).
- [28] Crippa, A. *et al.* Electrical Spin Driving by g -Matrix Modulation in Spin-Orbit Qubits. *Physical Review Letters* **120**, 137702 (2018).
- [29] Liles, S. D. *et al.* Electrical control of the g -tensor of the first hole in a silicon MOS quantum dot. *arXiv 2012.04985* (2020).
- [30] Philippopoulos, P. *Hyperfine and spin-orbit interactions in semiconductor nanostructures*. Ph.D. thesis, McGill University (2020).
- [31] Cywiński, Ł., Lutchyn, R. M., Nave, C. P. & Das Sarma, S. How to enhance dephasing time in superconducting qubits. *Physical Review B* **77**, 174509 (2008).
- [32] Madzik, M. T. *et al.* Controllable freezing of the nuclear spin bath in a single-atom spin qubit. *Science Advances* **6** (2020).
- [33] Verkhovskii, S. V. *et al.* Quadrupole Effects on ^{73}Ge NMR Spectra in Isotopically Controlled Ge Single Crystals. *Zeitschrift für Naturforschung - Section A Journal of Physical Sciences* **55**, 105–110 (2000).
- [34] Yusa, G., Muraki, K., Takashina, K., Hashimoto, K. & Hirayama, Y. Controlled multiple quantum coherence of nuclear spins in a nanometre-scale device. *Nature* **434**, 1001–1005 (2005).

12

CONCLUSION & OUTLOOK

12.1. CONCLUSION

The work in this thesis focused on two different qubit implementations: electron and hole spins in quantum dots. For the former, the main focus was on the Silicon MOS material platform, while the latter utilized a SiGe/Ge/SiGe heterostructure, where the quantum dot was defined in a germanium quantum well. The progress in these fields can be summarised as:

- **Development of a unified fabrication protocol for defining quantum dots in SiMOS, Si/SiGe and Ge/SiGe**

Chapter 3 presented a fabrication scheme for reliably creating quantum dot devices in three different group-IV based platforms. Specific fabrication steps are tailored to each platform based on fundamental challenges or advantages, however for the most part, the protocols were almost identical. A device fabricated on each platform using the relevant scheme was presented, showing that single charge occupancy was possible in all cases, for a three quantum dot linear array defined in SiMOS, a five quantum dot linear array defined in Si/SiGe, and a two-by-two quantum dot array defined in Ge/SiGe. The fabrication methods presented in this chapter were used to define every device studied in this thesis.

- **Demonstration of tuneable tunnel coupling in a SiMOS quantum dot array**

Chapter 4 showed that it was possible to tune interdot tunnel couplings in Silicon MOS. This is a major milestone in the platform, as the high effective mass of electrons, as well as poor material uniformity at the Si-SiO₂ interface has hindered the control of qubit-qubit interactions in SiMOS. However, by utilizing methods from the previous chapter in device fabrication, as well as improved material quality, tunnel couple control was possible for two adjacent quantum dots each occupied by a single electron spin. It was also demonstrated that control over the tunnel rates was possible, allowing for isolation of the quantum dots from their reservoirs, and retention of a single electron charge well outside the equilibrium occupation potentials.

- **Demonstration of universal two-qubit logic at elevated temperatures of electron spin qubits in SiMOS quantum dots**

Chapter 5 constituted a milestone in scalability for semiconductor spin qubits, by showing that a complete set of single and two-qubit gates could be coherently performed at temperatures of 1.1 K, more than an order of magnitude higher than conventional dilution refrigerator operating temperatures. Single qubit fidelities on the order of 99% were reported, and dephasing times did not respond to operation temperature between 0.4 K and 1.25 K.

- **Demonstration of CROT, CPHASE and SWAP gates in the same device using electron spin qubits in SiMOS quantum dots at 1.1 K.**

We further demonstrated a full suite of exchange interaction mediated two-qubit gates operated at elevated temperatures, and proposed composite two-qubit gates capable of overcoming limitations in control of the exchange interaction between electron spin qubits in quantum dots, defined in SiMOS. By applying charge noise models that reflect dephasing times in the present device, we predicted very high two-qubit gate fidelities possible in this platform when using composite gate sequences.

- **The first demonstration of a single hole spin qubit in a quantum dot**

Here, we switched gears to another platform, focus sing instead on exploring planar germanium quantum wells as a host for hole spin qubits. As a first step towards this goal, we demonstrate coherent control of a single hole spin qubit in a quantum dot, characterizing spin relaxation times, dephasing times, manipulation speed using EDSR, and g -factor tuneability. We find in particular that the resonance frequency of the qubit can be tuned over a broad range by varying the electrostatic potential of the gates capacitively coupled to the qubit.

- Demonstration of long spin lifetimes in a single hole spin.**
 Extending on previous work, we establish that spin relaxation times are limited by the coupling to nearby reservoirs. As a result, by making the tunnel barriers more opaque, we can extend spin lifetimes as high as 32 ms. We also show in this work that appreciable spin lifetimes above 1 ms can be achieved for hole spin qubits of higher charge occupation numbers, specifically for 5 hole spins in a quantum dot. We also investigate the dependence of hole spin qubit resonance frequency on the electrostatic potential environment, finding once again that the g -factor is highly sensitive to the electrostatic environment of the quantum dot.
- Universal control of a four qubit quantum processor, defined in a 2x2 array in planar germanium**
 Significant advances in Ge/SiGe material quality and stack design led to a lower-noise environment in which to define hole spin qubits. We fabricated a 2x2 quantum dot array with 2 charge sensors, and demonstrated coherent single-, two-, three- and four-qubit quantum logic, showcased in the demonstration of a 4-qubit GHZ state. This work set a new standard for spin qubit platforms, as it demonstrated the first two-dimensional array of semiconductor spin qubits, opening pathways towards quantum algorithms and simulations of unprecedented complexity.
- Demonstration of high single qubit fidelities in germanium hole spin qubits**
 On the same device, we performed single qubit randomized benchmarking, showing that with careful tuning of the driving power, native gate fidelities of up to 99.990(1)% are achieved. We also develop a novel randomized benchmarking protocol called n -copy benchmarking, that allows us to investigate single qubit fidelities while driving multiple qubits at once. Furthermore, the new protocol allows us to benchmark in such a way that we eliminate sensitivity to quantum crosstalk, allowing us to selectively quantify the effects of classical cross-talk errors. We find that single qubit fidelities can be as high as 99.967 % for two-copy benchmarking, and 99.34(4) % for the four copy case.
- Characterization of the hyperfine interaction strength for holes in natural germanium quantum wells**
 The final chapter of the thesis investigated the quantum coherence of hole spin qubits. We found a clear $T^{2*} \propto 1/B$ proportionality, suggesting that charge noise is the limiting mechanism for magnetic fields above 0.1 T. We also found that refocussing techniques could extend quantum coherence from $T^{2*} = 1.9 \mu\text{s}$ to $T^{2, \text{CPMG}} = 504 \mu\text{s}$. We also investigated the strength of the hyperfine interaction between the hole spins and ^{73}Ge nuclei in the natural germanium quantum wells. We find that this strength is comparable to the magnitude of the charge noise acting on the qubits. Given the present rate of material improvements, we foresee the hyperfine interaction becoming the limiting noise process for qubit coherence in the near future, necessitating efforts into isotopic purification of the germanium quantum well.

These efforts listed above constitute stepping stones for the field of quantum computing with spin qubits defined in quantum dots. They do however, raise some significant challenges for the field.

12.2. WHAT NEXT?

To repeat the mantra that shows up in just about every article in the field, quantum computing will require many qubits, controllable with a high degree of accuracy, in order to become a useful tool. Looking forward, we therefore examine here what is limiting a scale-up of semiconductor spin qubit based quantum computers.

12.2.1. IN GERMANIUM

Quantum computers comprising superconducting qubits have reached qubit numbers exceeding 50 qubits [1]. Trapped ion approaches have been demonstrated with tens of qubits [2]. Spin qubits, on the other hand, while very promising quantum computing candidates, have been limited to only a handful of qubits [3–6], performing simple quantum algorithms. This seems at odds with the common claims of scalability for semiconductor spin qubits, in particular spin states defined in quantum dots. One major hurdle, is the problem of interconnect scaling, known classically as Rent's rule.

We have discussed Rent's rule in the introduction chapter. The crux of the problem is that per additional qubit, current experimental demonstrations require multiple DC and AC lines per qubit, requiring routing between multiple interconnect layers within a dilution refrigerator. As a result, the realization of quantum computer comprising millions of qubits using contemporary device design is untenable. One strategy to mitigate this interconnect problem, is the on-chip integration of classical electronics. This approach, while elegant, introduces a new problem in that large amounts of heat will be dissipated at the mK stage, exceeding the cooling power of any modern dilution refrigerator. As we showed in chapter 5, operation of qubits at higher temperatures that greatly relieve the required cooling power, is indeed possible, for electron spins in SiMOS quantum dots. Given the universal advantage of hot qubit operation, similar efforts in Ge/SiGe would strengthen the platform as a scalable contender.

Several challenges present themselves in this effort. With an increase in operational temperature, the strength of charge noise will increase. For Ge/SiGe devices, charge noise already limits spin coherence as we saw in the previous chapter. This is further complicated by the fact that the low in-plane g-factor of holes in Ge/SiGe requires larger magnetic fields to achieve appreciable spin splittings, increasing the sensitivity of spin states to charge noise. One strategy to mitigate this could be to switch to an out-of-plane external magnetic field configuration, where the g-factor is much larger, requiring lower magnetic fields [7]. Such a configuration would require isotopic purification of the germanium quantum well, since the hyperfine interaction in the out-of-plane direction is enhanced. A second strategy could be to create 'squeezed' dots, where charge insensitive points are predicted to occur for quantum dots with a squeezed axis perpendicular to the applied magnetic field [8]. Such a configuration would allow in-plane configurations, and permit extremely fast Rabi oscillations at low power cost.

A second important avenue would be exploring shared control of qubits in quantum dots. Cross-bar style architectures that drastically reduce the required Rent exponent have been proposed [9]. While applicable to both platforms, hole spins, or indeed any qubit candidate exhibiting a strong spin orbit interaction, are favorably positioned for cross-bar architectures for two reasons. Firstly, striplines or micromagnets are no longer necessary for qubit manipulation, simplifying fabrication and design significantly. Secondly, the valence band pinning of the Fermi level in Ge facilitates p-type Ohmic contact for virtually any metal. This opens an avenue for charge sensor integration within quantum dot arrays (typical length scales of implantation straggle and thermal diffusion from annealing are typically larger than quantum dot size), by defining metallic islands flanking quantum dots throughout an array.

Improvements to the qubits themselves will be necessary to actually perform useful quantum operations on a larger quantum computer. Despite the impressive single qubit fidelities reported in chapter 10, two-qubit fidelities exceeding 99% have not been demonstrated for either electron spin qubits in SiMOS quantum dots, or hole spin qubits in Ge/SiGe. In both cases, spin dephas-

ing times at the exchange-on operational points are too short compared to gate operation times, in order to perform good two-qubit gates. This is likely due to the fact that at these operational points, the qubits are highly sensitive to detuning noise. These values could be improved by reducing charge noise values via material and fabrication improvements, or by operating in regimes where the qubits are insensitive to electric field fluctuations. A challenge in Ge/SiGe is the fact that symmetry point operation does not fully de-sensitize qubits to charge noise, indicating that a paradigm shift may be in order. This may come in the form of ‘squeezed dot’ geometries for charge insensitive operation [8], exploring different quantum well growth directions [10], or by other means.

We observed in the case of Ge/SiGe that control of the exchange interaction and cross-talk is vital for good qubit operational quality. A simple strategy to improve these issues could be to design arrays with larger interdot pitch, relying on the high mobility of the hole wavefunction to couple adjacent spins. Additionally, isotopic purification and an out-of-plane magnetic field would allow for larger frequency spacing between qubit resonance frequencies, tuneable via the electrostatic potentials on local gates. Another limiting factor for hole spin qubits in particular are the initialization and readout fidelities. The spin orbit interaction complicates these processes, and further efforts to understand and potentially tune the spin-orbit susceptibility of hole spin qubits may be key to increasing overall operational fidelity in the platform.

12.2.2. IN SILICON

The achievements in SiMOS included in this thesis have been important milestones for the platform, however difficulties still remain. The Si-SiO₂ interface disorder remains a major hurdle for the platform, as it hampers the control of qubit-qubit interactions, and results in poor uniformity between qubits. For SiMOS to continue as a viable platform, material improvements must be made on this front. Silicon as a host material however remains highly promising. Si/SiGe heterostructures such as those presented in chapter 3 have yielded extremely promising results, such as long coherence times, high single qubit fidelities, and recently, two-qubit fidelities exceeding 99%. At the time of writing, a six-qubit linear array of electron spin qubits in quantum dots has been fabricated using the methods developed in chapter 3, marking the largest array of quantum dot spin qubits to date. However, such linear arrays require micromagnets to create qubit addressability and artificial field gradients to permit qubit manipulation. This makes fabrication of spin qubit arrays in more than one dimension a major design challenge for the field, as two dimensional arrays of qubits are a requirement for many error correction codes. Additionally, crossbar architectures for silicon exist utilizing global ESR fields, however sufficient qubit addressability places challenging requirements on the fabrication of superconducting striplines [9].

Reliable valley splittings for electron spin qubits in silicon remains a challenge, particularly for Si/SiGe platform. A recent technique demonstrated that spiking the silicon quantum well with a small germanium fraction results in reliable valley splittings higher than 100 μeV , however, it is unclear how this will affect qubit properties. Therefore, characterization of qubits defined in such a heterostructure will be an important next step.

12.2.3. IN GENERAL

At the end of the day, improvements in host material quality and fabrication consistency determine how good a given qubit is. Additionally, improvements in one of these aspects alone cannot carry the burden. A wafer with high uniformity means nothing if the material is full of defects due to electron beam irradiation, while fabricating the perfect device won't work if the material is full of impurities or grain boundaries. For this reason, I believe that quantum wells in heterostruc-

tures are the most likely to succeed in advancing the field. It is also unlikely that devices fabricated in academic cleanrooms using electron beam lithography will ever achieve a standard of consistency in fabrication required to produce a truly scalable unit cell. However there seem to be some trends worth pursuing. Deeper quantum wells seem to improve charge noise and mobility in qubits [11]. This suggests that the majority of charge noise occurs at the surface of the heterostructure, likely due to a poor quality capping oxide, or atomic layer deposition oxide. Improvements of heterostructure engineering at these points may be the key to reducing charge noise. Additionally, positioning quantum wells even deeper may help.

Efforts to optimise the ratio of silicon and germanium in the various layers of heterostructure stacks are also underway. In Silicon quantum wells, the inclusion of germanium results in a valley splitting consistently greater than about 100 μeV , while in Ge/SiGe, the reduction of the stoichiometric ratio of silicon in the spacer layers results in very high mobilities [12]. It might just be me, but it seems like as a rule of thumb, the more germanium the better...

REFERENCES

- [1] Arute, F. *et al.* Quantum supremacy using a programmable superconducting processor. *Nature* **574**, 505–510 (2019).
- [2] Egan, L. *et al.* Fault-tolerant control of an error-corrected qubit. *Nature* **598**, 281–286 (2021).
- [3] Bradley, C. E. *et al.* A Ten-Qubit Solid-State Spin Register with Quantum Memory up to One Minute. *Phys. Rev. X* **9**, 031045 (2019).
- [4] Petit, L. *et al.* Universal quantum logic in hot silicon qubits. *Nature* **580**, 355–359 (2020).
- [5] Philips, S. G. J. *et al.* Universal control of a six-qubit quantum processor in silicon. *arXiv 2202.09252* (2022).
- [6] Hendrickx, N. W. *et al.* A four-qubit germanium quantum processor. *Nature* **591**, 580–585 (2020).
- [7] Miller, A. J. *et al.* Effective out-of-plane g-factor in strained-Ge/SiGe quantum dots. *arXiv 2102.01758* (2021).
- [8] Bosco, S., Benito, M., Adelsberger, C. & Loss, D. Squeezed hole spin qubits in Ge quantum dots with ultrafast gates at low power. *Phys. Rev. B* **104**, 115425 (2021).
- [9] Li, R. *et al.* A crossbar network for silicon quantum dot qubits. *Sci. Adv.* **4**, eaar3960 (2018).
- [10] Adelsberger, C., Benito, M., Bosco, S., Klinovaja, J. & Loss, D. Hole-spin qubits in Ge nanowire quantum dots: Interplay of orbital magnetic field, strain, and growth direction. *Phys. Rev. B* **105**, 075308 (2022).
- [11] Lodari, M. *et al.* Low percolation density and charge noise with holes in germanium. *Mater. Quantum Technol.* **1**, 011002 (2021).
- [12] Lodari, M. *et al.* Lightly-strained germanium quantum wells with hole mobility exceeding one million. *arXiv 2112.11860* (2021).

ACKNOWLEDGEMENTS

Choosing a place to commit four plus years of ones life is an objectively tough call. But I believe I made the right one with Delft. My time here has really cemented the fact that QuTech is a unique place to do science, and so I extend the most sincere gratitude to my promotor **Menno** for giving me the opportunity to work in such a fantastic place. Your ability to tackle the non-trivial and find pathways forward where I have seen dead-ends has been inspiring, and I am very grateful for your guidance. I am also deeply thankful for your support during periods of time where I was struggling with mental health complications - you showed sincere concern, never gave me a hard time for it, and pointed me in the right direction for external, professional help. Academia, unfortunately, seems to have a tendency to impart melancholy on it's disciples regardless of their capabilities. It is comforting to know that as the group grows in size and diversity, those who choose to work on the genuinely exciting science that takes place in Veldhorst lab, will be in good hands.

Thank you also to my copromotor **Giordano**. Whether it was a question about science or surfing, you have always been an approachable and helpful presence for me at QuTech. Congratulations on all your successes with germanium, which has become an exciting material to work with. Thanks also to **Lieven** for providing a collaborative and friendly environment within the spin-qubit community here in Delft. QuTech is lucky to have you in the drivers seat as scientific director.

Uprooting and moving country is a procedure with which nearly all who choose to pursue a PhD are painstakingly familiar. From a practical standpoint, it promotes the dissemination of knowledge and diversity - a process undeniably advantageous to the scientific process. However from a personal standpoint, it can take it's toll. As it turns out, in my case the place itself doesn't become home, rather the interactions within it. It was a slow process, but I was enormously lucky to have a beautiful group of people with which I felt a strong sense of belonging.

On that note, thank you to the "OG4", aka. Plant movers aka. **Luca, GJ** and **Nico**. **Luca**, you were one of my first and lasting connections in the Netherlands. You introduced me to the world of lifting mass - a world that, admittedly, I rapidly dissociated with. However your support and reliability during coffees, beers, dinners, lunches, 4PM Red-bulls, trips to Italy, Iceland, Spain and France has been a cornerstone of my life in Delft. **GJ**, you taught me most of what I now know about nano-fabrication, which was a critical skill for me during my PhD. Thank you for that, and also for all of the Movie nights, gaming nights with **BJ**, drinks, dinners, arriving at 9 O'clock on the toll of the Nieuwe Kerk bell to parties. Also, thanks for translating my propositions and summaries! I wish I could claim a better handle on Dutch after four and a half years but alas, here we are. **Nico**, I was hugely fortunate to be able to work with you these last few years. Your immense knowledge on seemingly everything lab-related was such a strong driving force in our group, and I hope that I've managed to acquire at least a small portion of it via osmosis. Thanks for all the beers, whiskys, vents, help, and best of luck in Zurich.

There are two important Matteo's to acknowledge here, however it turns out to be highly non-trivial to assign qualities that distinguish one from another, as they have identical initials, are both Italian, both work with diamond, and both play guitar. Even Roma and Romanga sound kind of

similar... Apparently I have a type. So, defaulting to order of appearance, **Matteo snr.**, we met on day one of my PhD in Delft. You were my office companion, my introduction to the QuTech band, and one of my primary external vents when things were going wrong. It was also a great comfort, to share experiences with you about the challenges of long-distance relationships. I am very happy that both of us have successfully outlasted the "long distance" component. Best of luck in the states, and I look forward to our paths crossing again.

Matteo jnr., you joined qutech a little later than I, so our overlap wasn't as long as I wish it could have been. But for sure we've made the most of the year-and-a-bit we've known each other. It's a rare thing to meet someone on such a similar musical page. Since bumping into you at one of the bebop jazz nights, we've spent a lot of time jamming, recording, and gigging, together or with the qutech band. Playing music with you has been a genuine highlight of my life in Delft. Best of luck with the rest of the PhD.

Floor, I'm really grateful to have learnt the ropes alongside you. A pessimist might describe our approaches to experiment as conflicting, however I like to think they were complementary. Regardless, working with you has led to a really nice portfolio of work that I'm very proud of. Thanks also for your support outside the lab, and being there for me when I needed to get something off my chest, or just grab a coffee.

I'd like to thank everyone in Veldhorst lab. I believe the mix of expertise and backgrounds really help lay the foundation for a very strong research group. Good luck to the next generation: **Chien, Marcel, Valentin, Hanifa, Francesco, Corentin, Timo, Sayr**, as well as everyone else in the group I've had the pleasure of working with: **Max R., Sander, Ruoy, Marco, David, Max K.** to name a few, but the sentiment extends to all alumni!

Zooming out, I'd also like to thank people in the extended Vandersypen and Scappucci groups with whom I've worked with or in close proximity to, for the last four years. Cheers to **Jelmer, Anne-Marije, Xiao, Stephan, Sjaak, Florian, Pablo, Tzu-kan, Sergey, Delphine, Tobias, Kostas, Udit, Tom, Gouji, Patrick, Alice, Andrea, Matteusz, Christian, Job, Alberto, Brian, Diego, Amir, Luka, Mario**, and everyone else in the local spin qubit community! A great deal of my time was spent in the cleanroom, fine-tuning fabrication recipes and creating devices. In Delft I always felt spoiled with the amazing fabrication tools and expertise available to me, and am immensely grateful to a huge number of people that made it all possible. First up, I'd like to thank my forerunners in the cleanroom, who did a huge amount of work towards developing reliable fabrication protocols. Thanks **Jelmer, Gabriel, Kanwal** and **Nima**, for really getting silicon fab off the ground. Next, I am greatly indebted to **Sergey, Gertjan** and **Nico** for investing so much time training me on the various tools and in the various techniques. Finally, thanks to the cleanroom staff who organise and maintain the cleanroom - cheers to **Marc, Marco, Hozanna, Charles, Anja, Arnold, Ewan, Eugene**, and **Pauline**. Thank you also to **Jason, Matt, Olaf, Jelle, Remco, Siebe, Mark** and **Nico**, who facilitated the smooth operation of all equipment outside the cleanroom, and provided rapid support whenever something wasn't sticking, cooling, conducting or beeping the way it should. I would also like to thank **Bill Coish, Pericles Philippopoulos** and **David Lintau**, for our collaboration on hole spin coherence in chapter 11. Additionally, thank you to **Jonas Helsen** for your help with all things randomized benchmarking, and to **Alex Hamilton** and **Matt Rendell** for hosting me in Sydney during my visit in 2019.

The common thread through much of my social life in Delft was music. I started joining an open jam night organized by **Chris** (thanks) at his house in the center of Delft, playing on possi-

bly the most out of tune piano in the known universe, sight reading chords to pop songs I'd heard maybe twice in my life. It was great fun, and I'd like to say thanks to those jam regulars **Jonas, James, Jochain, Holger, Filip, Albert, Alessio, Rob, Florian, Rama, Romy, Gurol, Gabi, Steven, Matteo, Maud, Vlad, Ege**, and many more, for making wednesday nights into an absolute blast. The same house that hosted the jam became my home for the remainder of my stay in Delft, where I had the privilege of living with **Deniz, Su** and **Raj**. You have all been wonderful companions, and I will always look back fondly on our house parties (and 5 am post-party debriefs), jam nights, summer afternoons in the hammock on the terrace, learning to hoola-hoop, BBQs, D&D nights, and loads more. OL24A was the cornerstone of my social life in Delft and I am so lucky to have shared it with you.

A huge shout out to the so called "Bebop crew", the real core of my social life in Delft. The local constituents of this community have been in constant flux since inception, but to **Almira, Deniz, GJ, Deepika, Milan, Sona, Luca, Stephan, Stefan, Nina, Milan, Tina, Theo, Kostas, Joana, Kristie, Kate, Matt, Quentin, Nicole**, and the extended family, you made Delft feel like home for me.

I was also fortunate to have been a part of several tabletop RPG campaigns that provided some much needed escapism, with the added bonus of improving my public speaking confidence. I also never had to DM - a mind-bendingly time-consuming job, particularly for people who, like me, struggle with improvisation. Therefore, a massive thanks goes to **Ata, Su, Tammy** and **Jonas**, for taking the time to prepare and deliver some absolutely fantastic campaigns and one-shots. Thanks also to the fellow players **Su, Deniz, Derin, Almira, Tammy, Boris, Hendrick, Edward, Irene, Jan** and **Wo** for all the stories and world building.

Qutech is a great place to work. That statement is further evidenced by the presence of a totally institute funded, inclusive and open band which I was so happy to have been a part of. Thanks to **Steven, Matteo, Matteo, Loek, Joe, Hans, Remco, Connor, Julia, Chris, Nico, Floor, Anne-Marije, Marina, Maia**, and **Gustavo** for all the rehearsals, Il pepperoncino dinners and gigs. And if someone could please show **Sayr** where the jazz scat setting is on the Roland, that would be swell.

Keeping sane throughout lockdowns, curfews and general pandemic related anxiety is absolutely not something one can take for granted. A huge thanks to **Su, Matteo, Luiz** and **Hans** for making those curfewed friday nights into a genuinely wonderful time, where we could learn new songs together, cook nice dinners, and find some comfort in an otherwise uncertain time.

Keeping in touch with people on the other side of the world in an awkward time zone can be quite tough, but somehow with **Declan, Jacob, Farley** and **Ellery** it has been possible. It was always a great comfort to be able to jump on discord and watch someones stream, or hang out. Special thanks to **Declan** for your countless hours of sacrificed sleep so that we could push through to the end of our many concurrent gaming projects. Also cheers to **Scott, Sonya, James D., Oliver, Sam, James B., Martin, Shanette** and **Ryan** who have been there in GMT+10, happy to be on the other side of a (albeit sporadic) catch-up call.

One of the perks of living in a small town is how naturally you get to know the people in your routines - every morning I bought a large flat white on the way to work. Morning chats with **Fleur, Emily** and **Leonie** always primed me for a good day. Also huge ups to the folks on the other side of the bar - miming along with instruments during the jazz nights with **Mike** and **Ruben**, chats on break with **Arnoud** and **Xavi**, mead tasting with **Edward** and **Baart**, D&D with **Edward** and **Su**, and general good vibes from all in the Delft hospitality community.

When I left Australia four-ish years ago, the move to Delft was an exciting, but lonely adventure that required a substantial adjustment time. At the time of writing, I have now moved once again, to Copenhagen, though this time not on my own. **Kaja** you have been a huge support to me over the last couple years, and I am so excited for our new chapter here in Denmark, and for all the chapters to come. Jeg elsker dig meget højt.

Finally, thanks to **Gran, Mum, Dad, Angus** and **Douglas**. It's been more than ten years now since I left WA, but the love and support I have felt throughout has always been my favorite fundamental constant - which I promise is a meaningful sentiment coming from a physicist.

CURRICULUM VITÆ

William Iain Leonard LAWRIE

21-09-1993 Born in Perth, Australia.

EDUCATION

2005–2010 High School
John Curtin College of the Arts, Fremantle

2012–2015 Bachelor of Science (Physics)
The University of Melbourne, Victoria, Australia

2012–2015 Diploma of Mathematical Sciences (Applied Mathematics)
The University of Melbourne, Victoria, Australia

2015–2017 Master of Science (Experimental Condensed Matter Physics)
The University of Melbourne, Victoria, Australia

2017- PhD. Candidate
Technical University of Delft, The Netherlands
Thesis: Spin Qubits in Silicon and Germanium
Promotor: Dr. M. Veldhorst
Co-promotor: Dr. G. Scappucci



LIST OF PUBLICATIONS

16. **W. I. L. Lawrie**, F. van Riggelen, N. W. Hendrickx, M. Russ, S. L. de Snoo, A. Sammak, G. Scappucci, M. Veldhorst *Quantum Coherence of Hole Spins in Planar Germanium*, In Preparation.
15. F. van Riggelen, **W. I. L. Lawrie**, G. Scappucci, M. Veldhorst M. Russ, N. W. Hendrickx, A. Sammak, M. Rispler, B. M. Terhal, G. Scappucci, M. Veldhorst *Phase flip code with semiconductor spin qubits*, arXiv preprint, arXiv:2202.11530 (2022).
14. S. G. J. Philips, M. T. Madzik, S. V. Amitonov, S. L. de Snoo, M. Russ, C. Volk, **W. I. L. Lawrie**, D. Brousse, L. Tryputen, B. Paquelet-Wutz, A. Sammak, M. Veldhorst, G. Scappucci, L. M. K. Vandersypen *Universal control of a six-qubit quantum processor in silicon*, arXiv preprint, arXiv:2202.09252 (2022).
13. **W. I. L. Lawrie**, M. Russ, F. van Riggelen, N. W. Hendrickx, S. L. de Snoo, A. Sammak, G. Scappucci, M. Veldhorst *Simultaneous driving of semiconductor spin qubits at the fault-tolerant threshold*, arXiv preprint, arXiv:2109.07837 [cond-mat.mes-hall] (2021).
12. N. W. Hendrickx, **W. I. L. Lawrie**, M. Russ, F. van Riggelen, S. L. de Snoo, R. N. Schouten, A. Sammak, G. Scappucci, M. Veldhorst *A Four-Qubit Germanium Quantum Processor*, Nature **591**, 580–585 (2021).
11. M. Lodari, N. W. Hendrickx, **W. I. L. Lawrie**, T. K. Hsiao, L. M. K. Vandersypen, A. Sammak, M. Veldhorst, G. Scappucci *Low percolation density and charge noise with holes in germanium*, Materials for Quantum Technology **1**, 001002 (2021).
10. F. van Riggelen, N. W. Hendrickx, **W. I. L. Lawrie**, M. Russ, A. Sammak, G. Scappucci, M. Veldhorst *A two-dimensional array of single-hole quantum dots* Applied Physics Letters, **118** (4) 044002 (2021).
9. **W. I. L. Lawrie**, N. W. Hendrickx, F. van Riggelen, M. Russ, L. Petit, A. Sammak, G. Scappucci, M. Veldhorst *Spin relaxation benchmarks and individual qubit addressability for holes in quantum dots* Nano Letters, **20** (10) 7237-7242 (2020).
8. L. Petit, M. Russ, H. G. J. Eenink, **W. I. L. Lawrie**, J. S. Clarke, L. M. K. Vandersypen, M. Veldhorst *High-fidelity two-qubit gates in silicon above one Kelvin* arXiv preprint, arXiv:2007.09034 (2020).
7. N. W. Hendrickx, **W. I. L. Lawrie**, L. Petit, A. Sammak, G. Scappucci, M. Veldhorst *A single-hole spin qubit*, Nature Communications **11** (1), 1–6 (2020).
6. L. Petit, H. G. J. Eenink, M. Russ, **W. I. L. Lawrie**, J. S. Clarke, L. M. K. Vandersypen, M. Veldhorst *Universal quantum logic in hot silicon qubits* Nature, **580** (7803), 355–359 (2020).
5. **W. I. L. Lawrie**, H. G. J. Eenink, N. W. Hendrickx, J. M. Boter, L. Petit, S. V. Amitonov, M. Lodari, B. Paquelet Wuetz, C. Volk, S. G. J. Philips, G. Droulers, N. Kalhor, F. van Riggelen, D. Brousse, A. Sammak, L. M. K. Vandersypen, G. Scappucci, M. Veldhorst *Quantum dot arrays in silicon and germanium*, Applied Physics Letters **116** (8) 080501 (2020).
4. L. Petit, H. G. J. Eenink, **W. I. L. Lawrie**, J. S. Clarke, L. M. K. Vandersypen, M. Veldhorst *Tunable coupling and isolation of single electrons in silicon metal-oxide-semiconductor quantum dots* Nano Letters, **19** (12), 8653-8657 (2019).

3. D. Holmes, **W. I. L. Lawrie**, B. C. Johnson, A. Asadpoordarvish, J. C. McCallum, D. R. McCamey, D. N. Jamieson *Activation and electron spin resonance of near-surface implanted bismuth donors in silicon* *Physical Review Materials* **3** (8) 083403 (2019).
2. D. N. Jamieson, **W. I. L. Lawrie**, S. G. Robson, A. M. Jakob, B. C. Johnson, J. C. McCallum *Deterministic Doping* *Materials Science in Semiconductor Processing* **62** 23-30, (2017).
1. D. N. Jamieson, **W. I. L. Lawrie**, F. E. Hudson, A. S. Dzurak, A. Morello, S. G. Robson, A. M. Jakob, B. C. Johnson, J. C. McCallum *Deterministic atom placement by ion implantation: Few and single atom devices for quantum computer technology* 2016 21st International Conference on Ion Implantation Technology (IIT), 1-6 (2016).